University of Florence

Dept. Civil and Environmental Engineering

International Doctorate in Civil and Environmental Engineering

Czech Technical University in Prague

Faculty of Civil Engineering

Doctoral Program in Physical and Materials Engineering

Modeling of Masonry Structures at Multiple Scales

SSD ICAR/08-09

DOCTORAL THESIS

Ph.D. Candidate:
Claudio Pagani

Doctoral Thesis Tutors:
Prof. Andrea Vignoli
Prof. Maurizio Orlando
Prof. Milan Jirásek, DrSc.
Dr. Luca Salvatori

Coordinator:
Prof. Claudio Borri

Firenze (Italy) and Prague (Czech Republic)
November 2017 - March 2021

University of Florence
Dept. of Civil and
Environmental Engineering
via di Santa Marta 3, 50139 Firenze

Czech Technical University in Prague
Faculty of Civil Engineering
Thákurova 7, 166 29 Praha 6

DECLARATION

Ph.D. student's name:	Claudio Pagani
Title of the doctoral thesis:	Modeling of Masonry Structures at Multiple Scales

I hereby declare that this doctoral thesis is my own work and effort written under the guidance of the tutors Prof. Andrea Vignoli, Prof. Maurizio Orlando, and Dr. Luca Salvatori from the University of Florence, Italy, and Prof. Milan Jirásek, DrSc., from the Czech Technical University in Prague, Czech Republic.

Firenze, Italy
March 31th, 2021

Signature

To Monica

Acknowledgements

I thank my doctoral tutors and both the University of Florence and the Czech Technical University in Prague to support my research.
I thank Prof. Andrea Vignoli and Prof. Maurizio Orlando for their support and wise suggestions.
I want to gratefully acknowledge Prof. Milan Jirásek for his guidance and enthusiastic encouragements and for having transmitted to me his passion for research.
The acknowledgments that Dr. Luca Salvatori deserves cannot be summarized in few lines. I will always be grateful to him for having believed in me and being my guide *per angusta ad augusta*.
I want to offer my special thanks to Dr. Martin Horák for all the support he gave me and for all he taught me about Computational Mechanics (while I reciprocated with FIFA lessons).
My grateful thanks are extended to the Department of Mechanics at CTU for the gentle hospitality. I wish to thank in particular Emma La Malfa and Florian Marconi for being special friends.
I would also like to extend my thanks to my great friends Andrea e Alice.
Finally, I wish to thank Monica for the strong support and encouragement throughout my study.

Abstract

Masonry represents the material used in the great majority of the world building heritage structures. Reliable tools for analysis of masonry structures are needed not only for seismic vulnerability assessment but also to properly design interventions to restore and strengthen existing buildings, which deserve to be preserved.

Masonry is a nonlinear, heterogeneous, and anisotropic material whose properties strongly depend on its microstructure, tipically composed of two phases, blocks and mortar, and on the way it is assembled. To simulate the mechanical behavior of masonry structures, numerous models have been developed, characterized by different detailing levels. For large structures, the need for computational efficiency leads to simplified models characterized by the subdivision of masonry walls in macro-elements. A notable example of this group of models is the equivalent-frame method, which consists of identifying the masonry wall with an ideal frame, where panels are modeled as beams characterized by proper mechanical behavior. The detailing level can be increased by considering each macro-element as a homogenized continuum, assuming that, at the scale of representation, masonry can be treated as a continuum having mechanical properties that reproduce the overall response of a certain portion of the heterogeneous microstructure. However, the formulation of a suitable constitutive law is not an easy task. It should phenomenologically reproduce the material mechanics, including tension cracking, shear sliding, compressive crushing, and many other aspects. Moreover, this approach requires a cumbersome identification of mechanical parameters that are not always easy to determine from basic experimental tests on the material. To consider the role of each constituent and the effects of their interactions, a microscale model can be set up, where blocks, mortar joints, and mortar-block interfaces are represented explicitly.

In this work, masonry structures are studied at several detailing levels. An issue affecting equivalent-frame models, namely the presence of irregularity in the wall opening layout, is addressed by comparing equivalent-frame results with finite-element ones, which are assumed to better represent the actual behavior of irregular walls. A parametric analysis on masonry piers, modeled as a homogenized continuum, is carried out, aimed to assess the influence of the heigth-to-width ratio and the vertical compression load on

the nonlinear static behavior. The focus is then shifted to finer scales. The localization analysis of an orthotropic macro-scale model in the framework of multi-surface plasticity is presented, deriving analytical localization conditions corroborated by finite element simulations. Finally, a microscale model for regular masonry is developed to analyze the localization properties of the representative volume element, also by investigating the role of its size and periodicity directions.

Sommario

La muratura rappresenta il materiale utilizzato nella grande maggioranza delle strutture del patrimonio edilizio mondiale. Strumenti affidabili per l'analisi delle strutture in muratura sono necessari non solo per la valutazione della vulnerabilità sismica ma anche per progettare adeguatamente gli interventi di ripristino e rafforzamento degli edifici esistenti, che meritano di essere preservati.

La muratura è un materiale non lineare, eterogeneo e anisotropo le cui proprietà dipendono fortemente dalla sua microstruttura, tipicamente composta da due fasi, blocchi e malta, e dalle modalità di assemblaggio. Per simulare il comportamento meccanico delle strutture in muratura sono stati sviluppati numerosi modelli, caratterizzati da diversi livelli di dettaglio. Per strutture di grandi dimensioni l'esigenza di efficienza computazionale porta a modelli semplificati caratterizzati dalla suddivisione delle pareti in muratura in macroelementi. Un importante esempio di questo gruppo di modelli è il metodo del telaio equivalente, che consiste nell'associare alla parete in muratura un corrispondente telaio ideale, dove i pannelli sono modellati come travi caratterizzate da un opportuno comportamento meccanico. Il livello di dettaglio può essere incrementato considerando ogni macroelemento come un continuo omogeneizzato, assumendo che, alla scala di rappresentazione, la muratura possa essere trattata come un continuo avente proprietà meccaniche che riproducono la risposta complessiva di una certa porzione della microstruttura eterogenea. Tuttavia, la formulazione di una legge costitutiva adeguata non è un compito facile. Dovrebbe riprodurre fenomenologicamente la meccanica del materiale, comprese la rottura a trazione per fessurazione, la rottura per scorrimento a taglio, lo schiacciamento per compressione e molti altri aspetti. Inoltre, questo approccio richiede una macchinosa identificazione di parametri meccanici che non sono sempre facilmente determinabili da prove sperimentali di base sul materiale. Per considerare il ruolo di ciascun costituente e gli effetti delle loro interazioni, è possibile realizzare un modello alla microscala, in cui i blocchi, i giunti di malta e le interfacce tra blocchi e malta sono rappresentati in modo esplicito.

In questo lavoro, le strutture in muratura vengono studiate a diversi livelli di dettaglio. Una questione aperta che riguarda i modelli a telaio equivalente, vale a dire la presenza di irregolarità nella geometria delle aper-

ture delle pareti murarie, viene affrontato confrontando i risultati ottenuti con il metodo del telaio equivalente con quelli di un'analisi ad elementi finiti, che si presume rappresenti meglio il comportamento effettivo delle pareti irregolari. Inoltre, viene eseguita un'analisi parametrica su pilastri in muratura, modellati come un continuo omogeneizzato, finalizzata a valutare l'influenza del rapporto altezza-larghezza e del carico di compressione verticale sul comportamento statico non lineare. L'attenzione viene quindi spostata su modellazioni con maggiore livello di dettaglio. Viene presentata l'analisi di localizzazione di un modello alla macroscala sviluppato nel framework della plasticità multi-superficie ortotropa, derivando condizioni analitiche di localizzazione, sucessivamente corroborate da simulazioni agli elementi finiti. Infine, viene sviluppato un modello alla microscala per murature regolari per analizzare le proprietà di localizzazione di volumi rappresentativi di muratura, indagando anche il ruolo della dimensione del volume rappresentativo e delle sue direzioni di periodicità.

Abstrakt

Zdivo je materiál použitý ve většině stavebních památek na celém světě. Spolehlivé nástroje pro analýzu zděných konstrukcí jsou zapotřebí nejen pro vyhodnocení jejich seismické zranitelnosti, ale také při návrhu opatření směřujících k obnovení či zvýšení únosnosti existujících budov, které si zaslouží ochranu.

Zdivo je nelineární, heterogenní a anizotropní materiál, jehož vlastnosti silně závisejí na základních stavebních jednotkách, tedy blocích (cihlách) a maltě, a na jejich prostorovém uspořádání. Pro simulaci mechanického chování zděných konstrukcí byla vyvinuta řada modelů, které se liší mírou rozlišení. Pro velké konstrukce vede snaha o výpočetní efektivitu ke zjednodušeným modelům, charakterizovaným rozdělením zděných stěn na makroprvky. Významným zástupcem této skupiny modelů je metoda ekvivalentního rámu. Její podstatou je nahrazení zděné stěny idealizovaným rámem, přičemž panely jsou modelovány jako nosníky charakterizované odpovídajícím mechanickým chováním. Míra rozlišení může být zvýšena tím, že se každý makroprvek uvažuje jako homogenizované kontinuum s vlastnostmi, které reprodukují celkovou odezvu určitého výseku heterogenní mikrostruktury. Formulace vhodného konstitutivního zákona ale není lehkou úlohou. Tento zákon by měl fenomenologicky reprodukovat mechanické chování materiálu, včetně vzniku tahových trhlin, smykového pokluzu, drcení v tlaku a dalších jevů. Navíc tento přístup vyžaduje těžkopádnou identifikaci mechanických parametrů, které není vždy snadné určit na základě běžných laboratorních testů materiálu. K popisu role základních stavebních jednotek a jejich interakce může posloužit model formulovaný na mikroúrovni, který explicitně bere v úvahu jednotlivé bloky, maltu a rozhraní mezi nimi.

Tato práce se zabývá zděnými konstrukcemi na několika úrovních rozlišení. Problémy s formulací modelů ekvivalentního rámu v případě nepravidelného rozmístění otvorů se zkoumají na základě porovnání výsledků pro ekvivalentní rámy s výsledky získanými metodou konečných prvků, o které lze předpokládat, že lépe postihuje skutečné chování nepravidelných stěn. Provedená parametrická analýza zděných pilířů modelovaných jako homogenizované kontinuum je zaměřena na posouzení vlivu tvaru a svislého tlakového zatížení na nelineární statické chování. Pozornost se pak přesouvá na jemnější úrovně rozlišení, na nichž se zkoumá lokalizace nepružného

přetváření, která ovlivňuje konstitutivní zákony pro modelování zdiva na makro a mikroúrovni. Provádí se lokalizační analýza ortotropního makroskopického modelu formulovaného podle teorie plasticity s více plochami plasticity, v jejímž rámci jsou odvozeny analytické podmínky lokalizace potvrzené simulacemi metodou konečných prvků. V závěru je vyvinut mikromechanický model pro pravidelné zdivo a pomocí něj se na reprezentativním objemu materiálu analyzují lokalizační vlastnosti, ovlivněné velikostí tohoto objemu a předpokládanými směry periodicity.

Contents

List of Figures

List of Tables

Chapter 1

Introduction

Masonry is among the first structural materials used by humankind, and it constitutes the great majority of structures of the world's building heritage.

Nevertheless, the modern mechanics of structures has been interested in studying two other materials that, after the industrial revolution, have strongly come on the scene as protagonists among building materials, namely steel and concrete. An in-depth study of masonry as a structural material has been developed only recently, starting from Heyman's pioneering work in 1966 (Heyman 1966). Previously, the masonry structure design was based on empirical rules, e.g., prescriptions on the maximum number of floors or the minimum thickness of walls. In contrast, only some isolated cases, notably the study of the cracking of the dome of San Pietro in Rome by Poleni in the mid-1700s (Poleni 1748), testify the use of rational procedures.

In the past, masonry buildings have always been conceived to carry only vertical loads, while the lateral actions induced by earthquakes were neglected. Consequently, the building heritage is fragile to seismic actions, as highlighted by recent earthquakes, e.g., the October 2016 Central Italy earthquake, or the most recent one in Durrës, Albania, in November 2019,

In Italy, the seismic issue awareness started to grow after the catastrophic events of the 1976 Friuli and 1980 Irpinia earthquakes. The need to address the problem of retrofitting and assessing the earthquake resistance of existing masonry buildings leads to a significant interest in studying masonry building mechanics under lateral forces. Many efforts have been made to determine efficient strengthening techniques to protect the building heritage and define a correct procedure for the seismic vulnerability assessment.

One of the first rational approaches was the POR method (Tomaževič 1978), which was extensively used for repair and strengthening work after the 1976 Friuli earthquake. This method adopted strong and simplistic assumptions by performing separate analyses for each building story and by checking the strength threshold on piers, modeled as beams. In parallel to this simplified modeling approach, other refined techniques arise. The most

common approach, starting from the work by Page et al. 1985, has been to consider masonry as a fictitious homogeneous continuum discretized by finite elements. Later, many attempts have been spent to find a suitable constitutive law for the macroscopic modeling of masonry.

In view of the large number of scientific publications in international journals, research on masonry mechanics is still an active field, especially in high-seismicity countries such as Greece, Portugal, and Italy. The scientific community is recently focused either on refining the existing methods and exploring new detailed ways of modeling the masonry mechanics. The refinement of simplified models leads to the formulation of the Equivalent-Frame method (Magenes 2000; Lagomarsino et al. 2013). On the other hand, the need for accounting for the material microstructure leads to the development of models at the microscale (Salvatori and Spinelli 2018), where the masonry constituents are explicitly modeled.

Nowadays, many modeling techniques of masonry structures involving different representation scales have spread in the scientific literature. The choice of the detailing level of representation depends on the dimensions and characteristics of the specimen to test or the purpose of the analysis. Each modeling approach still presents open issues, some of which will be discussed in the following paragraph.

1.1 Objectives of the research

The study of the effectiveness of the global analysis methods of masonry buildings is of key importance for their seismic vulnerability assessments. Therefore, reliable tools for analysis of masonry structures are also needed to properly design interventions to restore and improve existing building performances.

Analyses of large structures require simplified models able, at the same time, to effectively reproduce masonry mechanics and to speed up computation time. A widely-used approach is to consider walls as an assembly of macroelements, tipically the vertical elements, i.e., the piers, which bear vertical and horizontal loads; the horizontal elements, i.e., the spandrels, which couple the pier response; and the portions at the pier-spandrel intersections, namely the node panels. The effectiveness of these models relies on the proper mechanical behavior assigned to each macroelement.

Among the macroelement models, the Equivalent-Frame (EF) method is the most used model for practical computations. It relies on modeling a masonry wall with openings as an idealized frame composed of columns and beams, representing the masonry piers and spandrels, respectively. The material nonlinearities are accounted for by prescribing proper moment-curvature or shear-displacement constitutive laws, which define the strength and failure properties of each EF element. This method has many advan-

tages:

- The low computational burden, for the limited number of degrees of freedom of the computational model;
- The readability of the results, due to the familiarity that designers have with framed structures;
- The explicit endorsements by many building codes.

However, it is well known that the EF method suffers from several drawbacks. The strength and failure criteria for piers and spandrels provided by building codes are questionable. They do not account explicitly for relevant aspects, such as the applied vertical compression, the aspect ratio, or the material characteristics. Moreover, the EF model has difficulties in its application to buildings characterized by geometric irregularities in the distribution of openings since, in this case, the EF idealization of a given wall is more arbitrary. The objective is to find a rational way to overcome the EF model limits and keep using this simplified method for the seismic vulnerability assessment of masonry buildings.

Alternatively, the study of masonry structures can be performed through a homogenized continuum approach, where masonry is treated as a continuum having mechanical properties that reproduce the overall response of a certain portion of the heterogeneous microstructure. This approach is used for buildings characterized by geometric irregularity or, in general, whenever the masonry structure cannot be outlined as an equivalent frame. The key point is to define a constitutive model at the material point of the homogenized continuum. The stress-strain relationship should phenomenologically reproduce the mechanics of the underlying microstructure in terms of stiffness, strength, failure mechanisms, and localization properties. Numerous attempts have been made for simulating macroscopic masonry behavior by using stress-strain relations in the framework of plasticity (Lourenço, De Borst, et al. 1997), damage mechanics (Berto et al. 2002), smeared crack models (Lotfi and Shing 1991), or coupled damage-plasticity (Addessi, Marfia, et al. 2002). The main drawbacks of the homogenized continuum approach are

- The difficulties in reproducing the microstructural response with a single stress-strain relationship;
- The fact that it requires the definition of many mechanical parameters that are not easily evaluable in practice.

Lourenço's constitutive model is one notable example of macroscopic models for masonry structure analysis. Although it is one of the most widely used models, a thorough study of its localization properties lacks in literature. The study of the localization properties of a constitutive model is a

key aspect to assess its reliability in capturing the failure properties of the material that is supposed to simulate. The Lourenco's model assessment needs to be done on several stress scenarios, e.g. uniaxial stresses varying the stress angles, or shear tests varying the compression level. Since a such thorough experimental campaign is obviously missing, the reliability assessment can be performed only by comparing Lourenco's model response to the one of a detailed numerical model where the microstructure is explicitly represented.

In summary, the objectives of the research are:

- To study the drawbacks of simplified models for the seismic assessments of large masonry structure, and to propose a strategy to overcome their limits of application;

- To assess Lourenço's constitutive model for masonry through the study of its localization properties, and comparing them to the ones of a numerical model at the microscale.

1.2 Original contributions

A study on masonry structures at each level of representation, starting from the global building to the masonry microscale (Figure 1.1), is reported in this thesis, which is organized as follows.

In this Chapter, the motivation and the objectives of the work is presented, and the importance of the development of reliable mechanical models for masonry structures is highlighted.

In Chapter 2, a study of masonry mechanics at different detailing levels is reported. At the microstructural level, masonry response to basic stress states, namely vertical and horizontal tension and compression, shear stresses, and biaxial stresses, is discussed with reference to experimental tests taken from the literature. Then, we move the attention to the macroelement level, studying the masonry pier mechanics. The pier response under cyclic lateral actions is interpreted according to a novel procedure developed by the author. Finally, we analyze masonry mechanics at the global level, choosing as reference three experimental tests on full-scale masonry buildings, which allows us to discuss the strength mechanisms involved in a whole masonry building.

Chapter 3 is devoted to a review of mechanical models for masonry structure analysis at different detailing levels. For the wall level, the Equivalent-Frame and the articulated quadrilaterals method are discussed, considering their advantages and drawbacks. A review of pier models to be used within the Equivalent-Frame method is then reported. Subsequently, a series of constitutive laws suitable for the macroscopic representation of masonry is

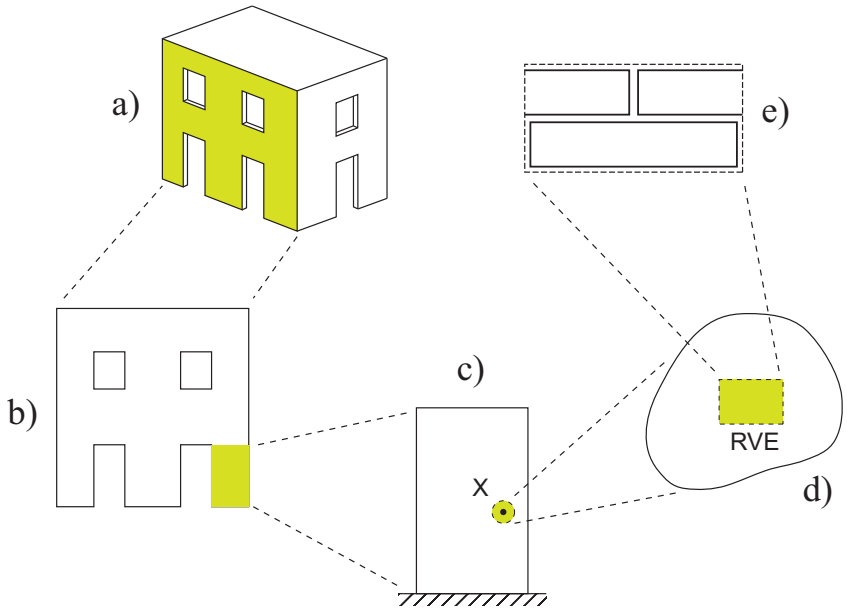

Figure 1.1: Overview of the representation scales for masonry structures analysis: a) global scale; b) wall scale; c) panel scale; d) macroscale; e) microscale.

discussed. Finally, we report some of the literature attempts for microstructural modeling, where the masonry constituents are explicitly modeled.

In Chapter 4, we report a study of an issue afflicting the Equivalent-Frame (EF) method applied to seismic analysis of masonry wall, namely the reliability of its results in the presence of irregularities in the opening layout. EF results are compared with finite-element ones, which are assumed to represent the actual behavior of irregular walls better. An EF solver is developed using more refined failure criteria for the masonry piers and strength criterion for the spandrels than the oversimplified ones suggested by building codes. Automated procedures are used to perform a large number of analyses, in which EF results and finite-element ones are compared. The difference in terms of predicted seismic vulnerability between the two models is correlated with a measure of the degree of irregularity of the walls. A geometric "confidence factor", increasing with the degree of irregularity, is proposed to account for the epistemic uncertainties in the EF modeling.

In Chapter 5, the nonlinear static behavior of masonry pier is studied through numerical analyses on a finite element model which treats masonry as a homogenized continuum. A parametric analysis, varying the aspect ratio and the actual compression-to-compressive strength ratio, is performed in order to explore pier response in a large range of conditions, and the relations between the nonlinear static quantities, namely lateral stiffness,

shear strength, and displacement capacity, and the parameters that influence them. The aim is to assess the reliability of the strength and failure criteria proposed by building codes on masonry piers and to provide a benchmark for the design of simplified pier models to be used as elements in the EF method.

In Chapter 6, the detailing level moves to the material point. We report a study on the localization properties of a macroscopic constitutive law suitable for masonry structures, namely a model in the framework of multi-surface orthotropic plasticity (Lourenço's model, Lourenço, De Borst, et al. 1997). The localization properties of Lourenço's model are determined under uniaxial stress and some biaxial stress states. The theoretical predictions are compared to numerical simulations, showing a perfect match in terms of localization surface directions.

In Chapter 7, the representation level of masonry further increases to the microstructural level. A microstructural model for regular masonry is set up, modeling its constituent explicitly as continua through a Rankine plasticity constitutive law. The model is able to reproduce the typical failure mechanisms. The localization angles computed within the RVE are compared to those of Lourenço's macroscopic model. Moreover, the variations of the RVE localization properties with its size and periodicity directions are assessed.

Finally, some general conclusions are drawn in Chapter 8.

The original scientific results of the present work can be outlined as follows:

- Wall scale:
  - Development of a new Equivalent-Frame model with more refined strength and failure criteria;
  - Proposal of a geometric confidence factor for the Equivalent-Frame model in case of irregular masonry walls;
- Panel scale:
  - Calibration of a finite element model on an experimental campaign on masonry piers;
  - Parametric study of the lateral behavior of masonry piers;
- Material point scale:
  - Characterization of the localization properties of a macroscopic model suitable for masonry, confirmed by numerical results;
- Microscale:
  - Development of an RVE model that reproduces the microstructural mechanics of masonry;

- Assessment of the influence of the RVE size and the change of periodicity directions.

Chapter 2

Mechanics of Masonry

Abstract

Masonry is a composite material formed as an assembly of blocks and mortar. The relevant size of its microstructure makes the masonry material as a structure within a structure. Therefore, a proper mechanical characterization of masonry needs to focus primarily at the microstructural level, whose properties influences masonry mechanics at greater scales. This chapter contains a review of the mechanical properties of masonry at different scales, namely the microscale, the macroelement level, and the building level.

A study of masonry mechanics at the microstructural level has been reported with reference to basic stress states, namely vertical and horizontal tension and compression, shear stresses, and biaxial states. Then, we moved the attention to the macroelement level, studying the masonry pier mechanics. We focused on the interpretation of the pier response under cyclic lateral actions according to a novel procedure developed by the author. The procedure is aimed to retrieve some relevant quantities describing the pier cyclic response from experimental shear-displacement graphs. The procedure is applied to three experimental tests exhibiting different failure modes and leads significant results regarding the characterization of the stiffness and strength degradation and energy dissipation. Finally, we analyze masonry mechanics at the global level, choosing as reference three experimental tests on full-scale masonry buildings, which allow us to discuss the strength mechanisms involved in a whole masonry building.

2.1 Introduction

Masonry is constituted by an arrangement of blocks, which can be natural or artificial, linked to each other by mortar joints. Two main kinds of masonry can be distinguished depending on the regularity of the block dimensions and arrangement. Regular-textured masonry is made of rows of identical blocks placed next to each other. Head and bed mortar joints fill respectively vertical and horizontal interspaces between blocks. On the other hand, irregular masonry is a disordered as-

sembly of blocks whose dimensions and possibly shapes are not equal to each other. Surveys on the building heritage show a great variety of masonry typologies based on composition (block and mortar materials), texture and building techniques.

Moreover, since the standard dimensions of blocks are in the range of $5 \div 50$ cm, the microstructural size is relevant compared to the structure dimensions. This fact leads to the consideration that the microstructure, namely the material structure within the building structure, cannot be neglected. The existence of nested structures within a material is not a peculiarity of masonry only; however, unlike other materials, the microstructural dimensions are relevant for masonry.

Regarding its mechanical properties, masonry is characterized by:

- Low or null tensile strength in the direction orthogonal to mortar bed joints;
- Significant vertical compression strength;
- Shear strength based on a frictional mechanism or brick cracking due to induced tensile stresses.

Although failure can occur due brick failure, mortar layers represent the masonry planes of weakness. For regular masonry, mortar layer orientations represent its privileged direction, so that masonry can be considered an orthotropic material. Therefore, the stress inclination with respect to material axes acquires importance.

Obviously, the described microstructure properties have consequences in masonry response at higher scales. At the wall scale, the masonry facade can be subdivided into three kinds of panels according to their structural function. By virtually extending the lines of opening edges, we can identify vertical and horizontal stripes of masonry, defined respectively as "piers" and "spandrels". The panels at the intersection of piers and spandrels are defined as "node panels". Restricting our attention to pier panels, which are the ones that bear vertical and horizontal loads, it is worth studying its behavior under lateral actions. Different failure mechanisms can be recognized. The pier response under flexure is characterized by base section partialization due to the absence of vertical tensile strength. In the case of low vertical compression, the panel tends to overturn around its toe, and it is said to fail due to rocking. On the other hand, for high compression loads, compression stresses localize in the panel's toe, and the failure mechanism is associated with toe crushing. Alternatively, the crack pattern at failure can be characterized by a stepped localized path or a diagonal crack. The latter cases belong to the category of shear failure mechanisms. The failure mode determination depends on the relative values of the internal actions (vertical compression, bending moment, shear force) and its mechanical parameters (compression strength, cohesion, friction coefficient, etc.).

Regarding the lateral behavior of masonry piers, it is particularly worth studying its cyclic response. Experimental tests show that piers under cyclic lateral loading exhibit

- Lateral stiffness degradation;
- Shear strength degradation;
- Permanent lateral displacements;
- Energy dissipation.

Despite the importance of the assessment of these quantities, the literature lacks its thorough study. In this chapter, we report a novel proposal to interpret cyclic test results on masonry piers. The procedure aims to define the evolution of the relevant quantities describing the cyclic behavior and give them a physical interpretation.

Extending our attention at the global scale, it is interesting to evaluate the overall behavior of the wall panels and see how they collaborate in the strength mechanism of a whole masonry building. Several experimental campaigns have been performed to study the seismic response of full-scale masonry buildings in recent years. From their observation, we can get many information and suggestions to interpret masonry building behavior.

The chapter is organized as follows. The mechanics of masonry at the microscale subjected to elementary stress states is viewed in Section 2.2. The discussion is restricted to regular masonry, although similar reasonings could also be derived in the case of irregular masonry. The response of regular masonry structures in terms of compression, tension, and shear is described respectively in Sections 2.2.1, 2.2.2, and 2.2.3, while the behavior towards biaxial stress states is reported in Section 2.2.4. In Section 2.3, we report the interpretation of masonry pier mechanics under lateral cyclic loading, according to a new procedure developed by the author. The evolution of the relevant quantities describing the cyclic behavior and their differences among piers with different failure modes will be shown. Then, Section 2.4 is devoted to studying the mechanics of masonry walls. We report three experimental tests made on full-scale masonry buildings, which allow us to express some significant considerations. Finally, concluding remarks are discussed in Section 2.5.

2.2 Masonry mechanics at the microscale

2.2.1 Compression strength

The compressive strength of masonry has been the subject of systematic investigations since the second half of the twentieth century. Since masonry structures are mainly stressed by compression, the interest of scientific community was primarily directed to the study of compressive strength (Hilsdorf 1969; McNary and Abrams 1985; Binda et al. 1988).

The main aspects that influence compression strength are (Hendry 1981; Tassios 1986):

- Compression strength and the geometry of blocks;
- Compression strength of mortar;
- Stiffness of blocks and mortar;
- Thickness of bed joints;
- Arrangement of blocks;
- Hygroscopicity of blocks.

Experimental tests show that the stress-strain curve in compression for brickwork lies in between the two curves related to bricks and mortar (Hendry 1981). Units exhibit high stiffness and strength and brittle behavior. In contrast, mortar shows low stiffness and strength but high strain capacity until its failure.

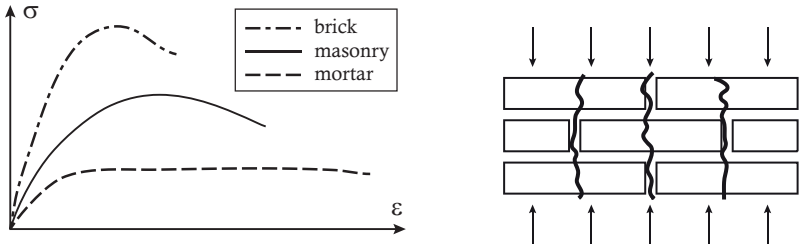

(a) Typical stress-strain curves for masonry and its constituents.

(b) Brickwork failure mechanism.

Figure 2.1: Masonry behavior under vertical compression.

As Figure 2.1a shows, the behavior of masonry in compression is intermediate in terms of stiffness, strength, and ductility compared to the ones of its constituents. The stiffness of the composite material can be intuitively determined as a weighted average of its constituents. On the other hand, failure mechanisms are more complex and need a detailed description since, in this case, the interactions between blocks and mortar play a key role.

In fact, if we consider a couple of bricks with a mortar layer between them subjected to compression orthogonal to the bed joint, they tend to expand laterally due to the Poisson effect. This expansion is greater for mortar since it is softer than blocks. The differential lateral expansion is prevented by friction between the constituents and horizontal actions arise to recover lateral strain compatibility. Therefore, mortar joints turn out to be in a triaxial compression state, while lateral tension stresses rise in blocks. Compression tests on masonry specimens show the formation of vertical cracks due to the failure of bricks in tension in the orthogonal direction to external compression (Figure 2.1b).

The horizontal tensile stresses in bricks due to vertical compression can be quantified analytically. In the following reasoning, two hypotheses are assumed: (i) linear elastic behavior of constituents and (ii) non-shifted vertical arrangements of blocks. Although they are not realistic, the actual nonlinear behavior is not far from what is obtained using these simplifications, as confirmed by experimental tests.

Let us consider a portion of masonry constituted by blocks of length l_b and height h_b, and bed joints of thickness h_j, subjected to uniaxial compression stress orthogonal to the bed joints. Let x and y be, respectively, the horizontal and vertical axis. We restrict our attention to the plane xy for the sake of simplicity.

The system is subjected to vertical compression σ_y, that generate horizontal stress $\sigma_{b,x}$ in blocks, considered positive if tensile, and $\sigma_{j,x}$ in mortar, considered positive if compressive, see Figure 2.2.

Lateral strains in blocks and mortar are given by

$$\varepsilon_{b,x} = \frac{1}{E_b}\sigma_{b,x} + \frac{\nu_b}{E_b}\sigma_y \tag{2.1}$$

$$\varepsilon_{m,x} = -\frac{1}{E_j}\sigma_{j,x} + \frac{\nu_j}{E_j}\sigma_y \tag{2.2}$$

where the subscripts b and j indicate the Young moduli E and Poisson ratios ν for

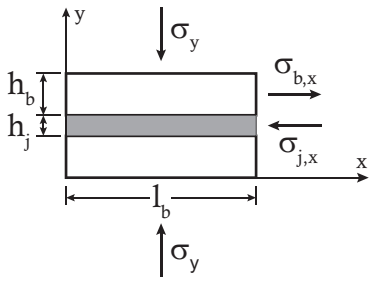

Figure 2.2: Stresses on a portion of masonry due to external compression stress.

blocks and mortar respectively.

The lateral strains of bricks and mortar must be equal for compatibility, namely

$$\varepsilon_{b,x} = \varepsilon_{j,x} \tag{2.3}$$

Moreover, the equilibrium in x direction reads

$$\sigma_{b,x}\, h_b\, t_b = \sigma_{j,x}\, t_b\, h_j \tag{2.4}$$

Combining the preceding equations we obtain the relation between the horizontal stress in blocks $\sigma_{b,x}$ and the vertical compression σ_z, that is

$$\sigma_{b,x} = \varsigma\, \sigma_y \tag{2.5}$$

where

$$\varsigma = \frac{\nu_b \dfrac{h_j}{h_b}\left(\dfrac{\nu_j}{\nu_b} - \dfrac{E_j}{E_b}\right)}{1 - \nu_j + \dfrac{E_j}{E_b}\dfrac{h_j}{h_b}(1 - \nu_b)} \tag{2.6}$$

The horizontal stress in mortar $\sigma_{j,x}$ is determined through (2.4) as

$$\sigma_{j,x} = \frac{h_b}{h_j}\sigma_{b,x} \tag{2.7}$$

Typical values of the ratio between elastic moduli of mortar and bricks range from 1:3 to 1:10 for high to low-quality mortar, while the ratio between Poisson ratios range from 1 to 3. Therefore, the coefficient ς is always positive and the predicted sign of stresses in bricks and mortar are correct. It is worth observing the dependence of the coefficient ς on the ratio between the thickness of bed joints h_j and the height of blocks h_b. Figure 2.3a shows this relation for three different Young modulus ratios (1:3, 1:5, and 1:10) and given Poisson ratios (ν_b=0.15 and ν_m=0.30). We can see that the coefficient ς, and thus the horizontal tension in blocks for a given vertical compression, increases for increasing thickness ratio and for low values of Young modulus ratios (for instance, in case of low-quality mortar). Therefore, we can conclude that, in linear elasticity, vertical compression induces horizontal tensile stresses in blocks that increase when the thickness of bed joints increases, keeping fixed the height of the blocks.

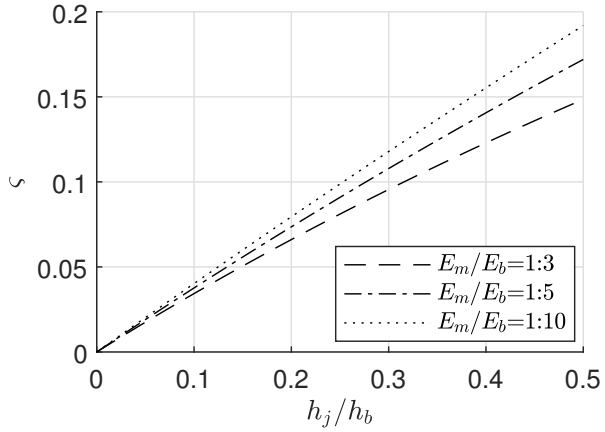

(a) Influence on the coefficient ς.

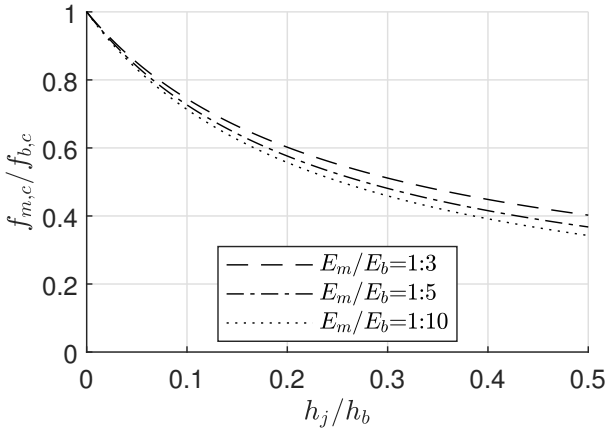

(b) Influence on the ratio between compression strength of masonry $f_{m,c}$ and blocks $f_{b,c}$.

Figure 2.3: Influence of the ratio between bed joint thickness h_j and block height h_b (with $\nu_b = 0.15$, $\nu_j = 0.30$, and λ=1:10).

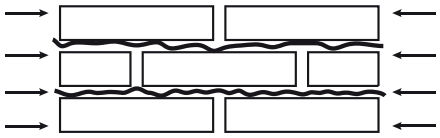

Figure 2.4: Brickwork failure in compression along bed joint direction.

Experimental compression tests on masonry prisms (McNary and Abrams 1985) show that mortar induces tensile stresses in bricks, representing the main cause of failure in compression. These stresses increase in a non-proportional way with compression stresses due to the nonlinear deforming properties of mortar bed joints.

Further analytical results regarding the compression strength of masonry could be obtained by means of other simplifying hypotheses. Let us assume that failure of masonry in compression occurs when a suitable failure criterion is reached in bricks, for instance

$$\frac{\sigma_y}{f_{b,c}} + \frac{\sigma_{b,x}}{\lambda f_{b,c}} = 1 \tag{2.8}$$

where a simplified Mohr-Coulomb criterion is assumed, and

$$\lambda = \frac{f_{b,t}}{f_{b,c}} \tag{2.9}$$

is the ratio between the strength in tension f_t and compression f_c for bricks. Substituting (2.5) into (2.8) we get

$$\sigma_y = \frac{1}{1 + \frac{\varsigma}{\lambda}} f_{b,c} \tag{2.10}$$

When the compression stress σ_y reaches the compression strength of masonry $f_{m,c}$, we obtain

$$\frac{f_{m,c}}{f_{b,c}} = \frac{1}{1 + \frac{\varsigma}{\lambda}} \tag{2.11}$$

from which we can analyze the influence of geometric and elastic parameters of masonry on its compression strength. Figure 2.3b shows the negative influence on masonry compression strength of high ratio h_j/h_b between thicknesses of the constituents. High values of the ratio h_j/h_b generates higher transversal tension which reduces the overall compression strength compared to the one of the blocks. The strength reduction is greater with softer mortar.

In case of uniaxial compression in the horizontal direction (Figure 2.4), failure occurs by bed-joints splitting due to lateral expansion of the masonry panel (Page 1981; Dhanasekar et al. 1985). The behavior is explained analogously to the case of compression in the vertical direction.

2.2.2 Tensile strength

The strength mechanism of masonry in tension depends on the tensile direction relative to the bed joints.

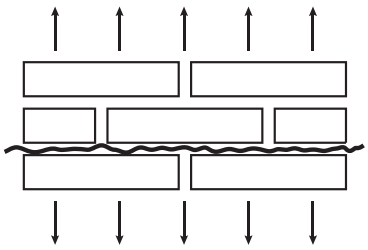

Figure 2.5: Portion of masonry subjected to tension orthogonal to bed joints.

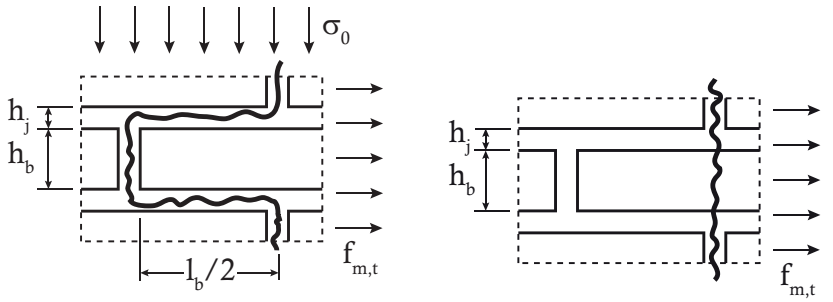

(a) Shear sliding of blocks on bed joints.

(b) Tensile cracking of blocks.

Figure 2.6: Strength mechanisms in horizontal tension.

If tension acts orthogonally to bed joints (Figure 2.5), failure is determined when the tensile strength in mortar joints is reached. Hence, the tensile strength of masonry $f_{m,t}$ could be expressed as a percentage of mortar tensile strength $f_{j,t}$, namely

$$f_{m,t} = \alpha f_{j,t} \tag{2.12}$$

The parameter α strongly depends on the quality of mortar joints, and it can greatly vary both in time and space. Its value depends on time because mortar is affected by degradation caused by weathering or temperature variations; it depends on space since the workforce cannot guarantee uniformity of mortar quality in the whole structure and temperature and humidity conditions during curing may affect mortar properties. Moreover, the tensile strength of mortar is, generally, a factor of ten lower than other strength parameters, and it shows a great scatter in experimental tests (Van der Pluijm 1999). Due to its strong variability and low value, vertical tensile strength is not reliable, and it is preferably not taken into account in structural computations. The parameter α is, therefore, considered as zero.

If the tensile direction is oriented along bed joints, two different mechanisms can be activated (Tassios 1986):

- shear sliding of blocks on bed joints (Figure 2.6a);
- block cracking in tension (Figure 2.6b).

In the first case, the horizontal tensile strength of masonry is given by the friction mechanism on the interface between bricks and mortar. The strength derived by this mechanism is usually called "pseudo"-tensile strength since it is not related to the tensile strength of any of its constituents (see Figure 2.6a).

If we consider a Coulomb friction strength mechanism and we neglect the tensile strength of mortar head joints, we can write the equilibrium in the horizontal direction as

$$2(h_b + h_j) f_{m,t} = l_b \, (c + \mu \, \sigma_0) \tag{2.13}$$

where c and μ represent the cohesion and the friction coefficient, and σ_0 is the vertical compression.

The horizontal tensile strength of masonry is then

$$f_{m,t} = \tilde{c} + \tilde{\mu} \, \sigma_0 \tag{2.14}$$

where

$$\tilde{c} = \frac{c}{\tan \phi} \ , \qquad \tilde{\mu} = \frac{\mu}{\tan \phi} \tag{2.15}$$

and

$$\tan \phi = \frac{2(h_b + h_j)}{l_b} \tag{2.16}$$

The angle ϕ is the average inclination angle of the stair-shaped crack forming in the head joint and in the superposition zone between two consecutive blocks (half the brick length in the case depicted).

It is worth noting that this mechanism is similar to failure due to shear sliding, that will be discussed later in Section 2.2.3.

In case of failure due to block cracking in tension (Figure 2.6b), masonry strength is strictly related to the brick tensile strength. Neglecting tensile strength of head joints, the horizontal equilibrium reads

$$2(h_b + h_j) f_{m,t} = h_b \, f_{b,t} \tag{2.17}$$

and then

$$f_{m,t} = \frac{1}{2(1 + \frac{h_j}{h_b})} \, f_{b,t} \tag{2.18}$$

Hence, the strength of masonry in horizontal tension decreases if the thickness of bed joints increases and reduces to

$$f_{m,t} = \frac{f_{b,t}}{2} \tag{2.19}$$

in case of thin bed joints, namely $h_j \ll h_b$.

In the case of uniaxial tension inclined by a generic angle relative to mortar bed joints, experimental tests (Dhanasekar et al. 1985) show mixed failure modes between bed-joint separation, typical of vertical tension, and shear sliding/brick cracking, distinctive of horizontal tension. It is worth noting that, since many different mechanisms can occur depending on the tensile direction and transversal compression, it not possible to define a fixed tensile strength for the material.

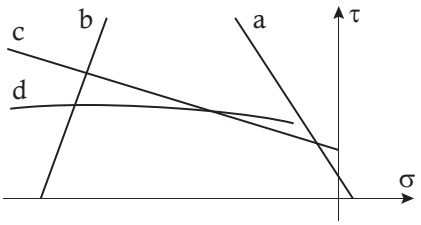

Figure 2.7: Shear failure modes of masonry (from Mann and Müller 1977).

2.2.3 Shear strength

Normal stresses to mortar bed joints influence the masonry shear strength, as shown by several experimental campaigns (Mann and Müller 1977; Mann and Muller 1982; Atkinson et al. 1989; Van der Pluijm 1999).

Mann and Müller 1977 distinguished four failure modes and represented their strength domain in a $\sigma - \tau$ graph (Figure 2.7).

The observed failure mechanisms are the following:

- Tensile bond failure (a);
- Block compressive failure (b);
- Interface sliding failure (c);
- Block tensile failure (d).

These four modes can be grouped as failure due to bending (a,b) and failure due to shear (c,d).

Bending failure occurs in the extreme cases of a low or high level of normal compression, determining respectively tensile failure at the brick-mortar interface (a, Figure 2.8a) or brick crushing in compression (b, Figure 2.8b). In contrast, shear failure occurs in the mid compression range. Two possible mechanisms, depending on relative values of mechanical properties between bricks and mortar, can occur: shear sliding at the brick-mortar interface (c, Figure 2.8c) or brick cracking due to the overcoming of tensile strength (d, Figure 2.8d).

Bending modes

Both mechanisms associated with the bending mode group can be explained by analyzing the response of brick subjected to normal and shear stress, without considering tensile strength at the interface with mortar bed joints.

A masonry block of length l_b, thickness t_b and height h_b is subjected to shear and compression stresses on its top surface. The shear strength τ is reached when the compression stresses in the reactive zone of thickness t_b and length a reach the compression strength of units $f_{b,c}$ (Figure 2.9).

Vertical equilibrium equation is the following

$$\sigma_0 \, l_b \, t_b = f_{b,c} \, a \, t_b \tag{2.20}$$

from which the dimension a of the reacting zone is determined, namely

$$a = \frac{\sigma_0}{f_{b,c}} l_b \tag{2.21}$$

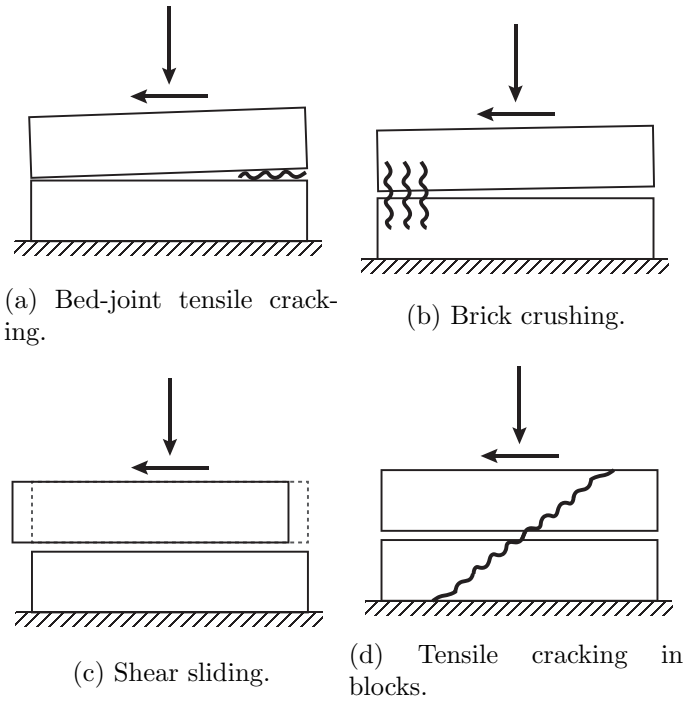

(a) Bed-joint tensile cracking.

(b) Brick crushing.

(c) Shear sliding.

(d) Tensile cracking in blocks.

Figure 2.8: Shear failure modes of masonry.

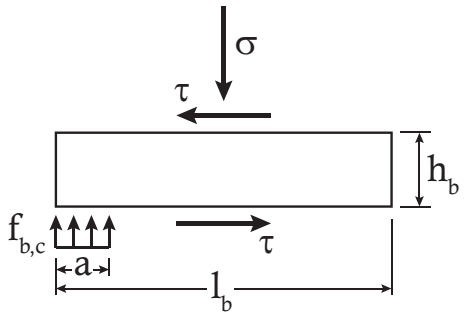

Figure 2.9: Geometry and actions of a masonry unit in bending mode for shear strength.

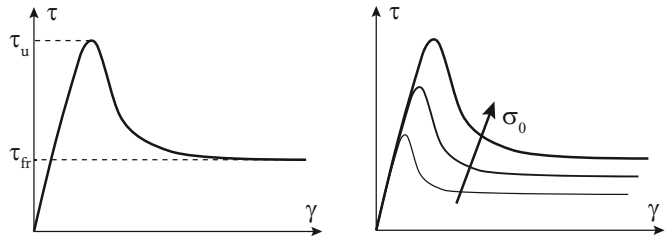

(a) Typical shape of a stress-strain curve.

(b) Influence of compression stress on shear strength.

Figure 2.10: Stress-strain curves of direct shear tests on bricks with shear sliding failure (from Van der Pluijm 1999).

The rotational equilibrium reads

$$\tau \, l_b \, t_b \, h_b = \sigma_0 \, l_b \, t_b \, \frac{l_b - a}{2} \tag{2.22}$$

By combining (2.20), (2.21), and (2.22), we obtain the following expression

$$\tau = \frac{\sigma_0}{2} \frac{l_b}{h_b} \left(1 - \frac{\sigma_0}{f_{b,c}} \right) \tag{2.23}$$

that define the relation between the shear strength in bending mode and the geometric and mechanical properties of bricks and the compression stress σ_0.

Shear modes

In case of shear sliding along the interface between blocks and mortar (curve c of Figure 2.7), shear stress-strain diagrams from experimental tests have the typical shape reported in Figure 2.10a (Van der Pluijm 1999). The stress-strain relationship is linear until the decohesion peak is reached, after which the shear stress diminishes rapidly at a certain stable stress level. As shown in Figure 2.10b, compression stresses greatly influences both the peak and the residual strength. Coulomb's friction criterion is a suitable model for this kind of shear failure. Therefore, the strength criterion can be written as

$$\tau = c + \mu \, \sigma_0 \tag{2.24}$$

where c is the cohesion and μ is the friction coefficient, both material properties to be determined by direct shear experimental tests.

The brick cracking failure mode is usually interpreted as caused by the overcome of tensile strength in bricks. Turnšek and Čačovič 1971 adopted a Rankine failure criterion, stating that failure occurs when the maximum principal stress reaches the tensile strength. By restricting the analysis in the two dimensional space, the stress state of a brick subjected to a vertical compression stress σ_0 and a shear stress τ is

$$\boldsymbol{\sigma} = \begin{bmatrix} 0 & \tau \\ \tau & -\sigma_0 \end{bmatrix} \tag{2.25}$$

The maximum principal stress is

$$\sigma_I = -\frac{\sigma_0}{2} + \sqrt{\left(\frac{\sigma_0}{2}\right)^2 + \tau^2} \tag{2.26}$$

When $\sigma_I = f_{b,t}$, we obtain the shear stress as

$$\tau = f_{b,t}\sqrt{1 + \frac{\sigma_0}{f_{b,t}}} \tag{2.27}$$

that represent the shear strength in case of brick-cracking failure mode.

Shear strength domain

The analytical formulas for shear strength derived in the previous paragraphs show a dependence on the compression stress σ_0, as observed in experimental tests. Therefore, it is interesting to determine the shear strength as a function of the compression stress, where the shear strength is evidently determined as the minimum value among the ones corresponding to each mechanism, namely

$$\tau = \min \begin{cases} \dfrac{\sigma_0}{2}\dfrac{l_b}{h_b}\left(1 - \dfrac{\sigma_0}{f_{b,c}}\right) \\ c + \mu\,\sigma_0 \\ f_{b,t}\sqrt{1 + \dfrac{\sigma_0}{f_{b,t}}} \end{cases} \tag{2.28}$$

The shear strength τ, normalized with respect to the block compressive strength $f_{b,c}$, is represented in Figure 2.11 as a function of the compression ratio $\sigma_0/f_{b,c}$, for the case of a brick with standard height h_b and length l_b of 5.5 cm and 25 cm respectively, having a compressive $f_{b,c}$ and tensile $f_{b,t}$ strength of 10 MPa and 1 MPa, and, for the sliding shear strength mechanism, the cohesion c as 0.5 MPa and the friction coefficient μ as 0.4. For the chosen parameter set, we can see that flexural failure occurs for low and high compression ratios, which determine respectively rocking and crushing mechanisms. On the other hand, the intermediate range of the vertical stress ratios determines shear failure. The shear sliding mechanism occurs for lower vertical compression and brick cracking for higher ones.

The relative position between the curves depends on the geometric and mechanical properties of the block. For instance, the bending-mechanism parabolic curve can be lower than the other curves in case of low compression strength or a high ratio h_b/l_b (slender blocks). In this case, the block would fail in bending for any σ_0.

2.2.4 Biaxial stress states

Masonry panels subjected to in-plane loads, such as masonry piers or spandrels, are generally in a state of biaxial stress. The study of the masonry response concerning biaxial stresses through experimental tests was conducted by many authors, notably by Page 1981 and Dhanasekar et al. 1985.

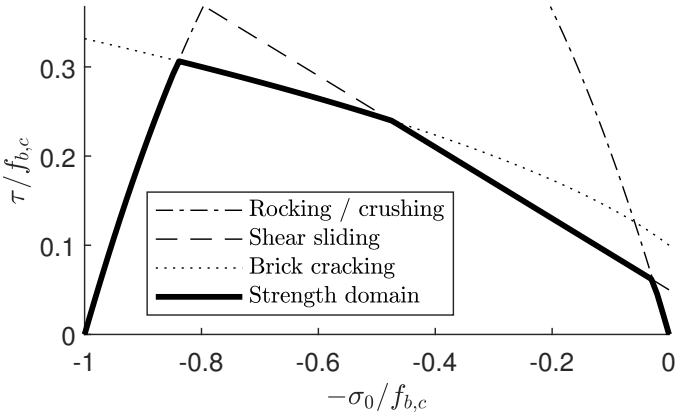

Figure 2.11: Shear strength domain of masonry.

Masonry behavior depends both on the stress state and the bed-joint orientation relative to the principal directions. Therefore, biaxial failure must be described in terms of three variables: the principal stresses σ_1 and σ_2, and their respective orientations to the bed joint, namely θ and $\theta + \pi/2$. The failure surface in the plane $\sigma_1 - \sigma_2$ obtained by Page 1981 is shown in Figure 2.12, where each curve represent the failure surface relative to a given bed joint orientation.

For most values of σ_1 and σ_2, the bed joint direction slightly influences masonry strength, which turns out to be greater than compression strength in uniaxial compression. In these cases, failure occurs with brick cracking in a plane parallel to the masonry mid-plane.

However, the bed joint angle plays an important role when one principal stress dominates on the other since the problem gets closer to the case of uniaxial compression. In this case, in fact, failure occurs by cracking and sliding of joints or a combined mechanism involving bricks and joints, depending on the bed joint angle.

Dhanasekar et al. 1985 extended the experimental tests to the case of tension-compression and biaxial tension. In these cases, failure was due to cracking and sliding of bed joints, involving tensile strength of mortar or the friction mechanism between brick and joints depending on the bed-joint angle, as already discussed in Section 2.2.2.

2.3 Mechanics of masonry piers

Experimental observations on the seismic behavior of masonry walls suggest a subdivision of the wall in this set of elements (Figure 2.13):

- Masonry piers, the vertical elements which bear the vertical and horizontal loads and mainly influence the seismic behavior of the entire building;
- Masonry spandrels, the horizontal elements that couple the response of the two adjacent piers;
- Node panels, the portions at the intersection between piers and spandrels.

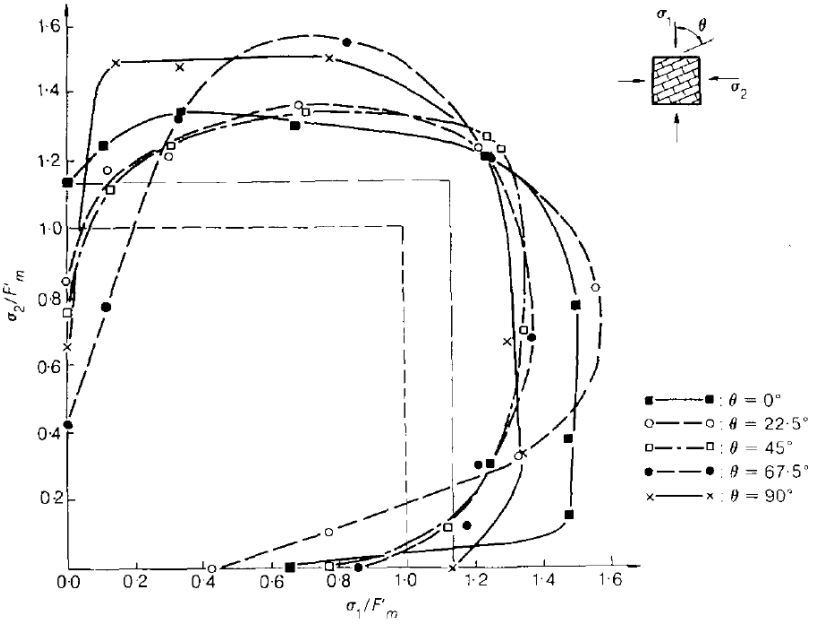

Figure 2.12: Failure surface in biaxial compression (from Page 1981).

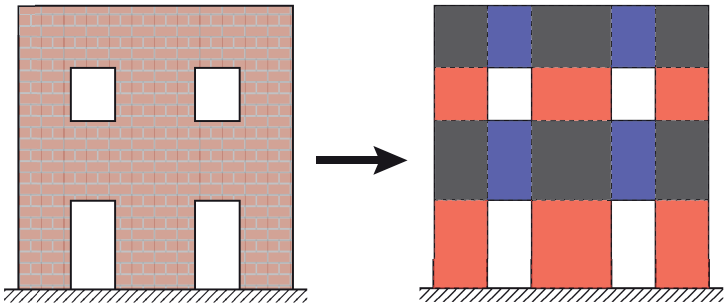

Figure 2.13: Subdivision of a masonry wall in piers (in red), spandrels (in blu), and node panels (in black).

Since the mechanism failure under seismic actions generally involves masonry piers and spandrels only, the study on the mechanics of node panels has been neglected. They are usually considered infinitely stiff and resistant in numerical analyses.

The behavior of masonry spandrels can vary depending on their construction technique. We can distinguish the following typologies:

- Weak spandrels, providing no coupling capability between masonry piers, for instance, the ones supported by timber lintels or shallow masonry arches;
- Strut spandrels, when one tension-resistant element, such as reinforced concrete beam or tie-rod, is present and spandrels react as compressive struts;
- Strong spandrels, having tension-resistant elements positioned at both ends and, therefore, a bending and shear strength.

The spandrel typology highly influences the masonry pier boundary conditions, resulting in a static scheme ranging from cantilever, in the case of weak spandrels, to doubly rotation fixed, in the case of strong spandrels.

The scientific community has only recently begun to pay attention to the study of masonry spandrels (Rinaldin, Amadio, and Gattesco 2017). The experimental test campaigns conducted so far (Gattesco et al. 2008; Graziotti et al. 2012; Beyer and Dazio 2012) have shown the influence on their cyclic response of the present axial force, whose amount is uncertain in an existing building. Due to the lack of deep knowledge of spandrel mechanics and its lower influence on the wall seismic response, we restrict our attention to the study of masonry piers, which, on the other hand, have been extensively studied in the past.

The experimental test of reference is the shear-compression test, in which the masonry pier is subjected to a given vertical load and an imposed lateral displacement.

The masonry pier is generally put on a concrete foundation slab. The vertical and horizontal loads are applied through two vertical and one horizontal actuators linked to a stiff steel beam positioned on the top of the pier. The vertical actuators have the role of imposing the top boundary condition. Generally, the top rotation is fixed by checking that the two vertical actuators have the same vertical displacement during the test, realizing a double-bending static scheme (Magenes and Calvi 1997; Anthoine et al. 1995; Magenes, Galasco, et al. 2010). However, masonry piers have also been tested in a cantilever static scheme (Magenes, Morandi, et al. 2008), i.e., having free top rotation, or in intermediate conditions with variable shear-span heights (Petry and Beyer 2014).

The lateral loading protocol is more frequently cyclic; namely, the horizontal actuator imposes a cyclic displacement with increasing amplitude. Each cycle is generally repeated three times (Silva et al. 2014; Magenes, Galasco, et al. 2010; Almeida et al. 2012). In other cases the top displacement is imposed monotonically, namely the lateral displacement is increased until failure (Vasconcelos and Lourenço 2009; Lourenço, Oliveira, et al. 2005; Borri et al. 2012).

The main result of these experimental tests is the base shear - top displacement graph, which gives information on the lateral behavior of masonry piers. A piecewise-linear function outlines monotonic test graphs according to a given piecewise linearization procedure, which is usually considered the same as the one used for entire masonry buildings, as described in Frumento, Magenes, and Morandi

2009 and reported in the following. The idealized graph is composed of a first linear branch, followed by a limited constant-force one. The first branch is defined as the secant at 70% of the shear peak and its slope represent the specimen's lateral stiffness. The ordinate value of the second branch defines the pier shear strength, and it is defined according to an energy equivalence criterion between the real and ideal graphs. The second branch limit, which gives the displacement capacity, is defined as the displacement corresponding to a 20% strength reduction of the shear peak in the softening part of the graph. These quantities, namely the lateral stiffness, the shear strength, and the displacement capacity, characterize the lateral monotonic behavior of masonry piers. However, we can derive the monotonic quantities even from cyclic tests by considering an equivalent monotonic graph, which is constructed by connecting the peak point of each cycle.

As highlighted in Beyer, Petry, et al. 2014, the specimen response is influenced by the loading protocol. It was shown that cyclic tests led to slightly lower strength and significantly lower displacement capacity compared to monotonic tests. This reduction is higher in the case of piers failing in shear (Wilding, Dolatshahi, et al. 2017).

However, from cyclic tests, we get some additional information regarding the evolution of the monotonic quantities during the test. In fact, shear-displacement graphs from cyclic experimental tests show:

- Lateral stiffness degradation;
- Shear strength degradation;
- Development of permanent lateral displacements;
- Energy dissipation.

These aspects are caused by the formation and progressive development of tensile cracks, compression crushing, or shear sliding, occurring in the specimen at the microscale level.

Several studies of lateral stiffness degradation and energy dissipation can be found in the literature. The cyclic stiffness decay was described as a function of the lateral drift (Zepeda et al. 2000; Vasconcelos and Lourenço 2009) or of a measure of the observed physical damage, called damage index I_d (Tomaževič 1999; Zimmermann et al. 2011). The lateral stiffness for each loading cycle was computed as the slope of the line connecting the maximum and minimum peak points in the force-displacement graph. An expression of the lateral stiffness degradation was proposed by Zimmermann et al. 2011, describing the decay as a negative exponential function of the damage index

$$\frac{K^{(i)}}{K_e} = \exp\left(-\beta\, I_d^{(i)}\right) \tag{2.29}$$

where K^i is the stiffness at cycle i, K_e is the initial stiffness, and β is a fitting parameter.

The dissipation of energy has been described by means of the ratio between the cumulative dissipated energy and the cumulative input energy (Shing et al. 1989), namely

$$I_E^{(i)} = \frac{1}{E_{inp}} \sum_{j=1}^{i} E_{dis}^{(j)} \tag{2.30}$$

where E_{dis}^{j} is the area of the j-th hysteretic cycle, with $0 \leq j \leq i$, and E_{inp} is the total elastic energy absorption of the equivalent elastic-perfectly plastic model.

However, the way the dissipated energy ratio I_E is computed depends on the test loading protocol. Since the dissipated energy is cumulative, obtained as the sum of the ones of all previous cycles, the ratio I_E is particularly influenced by the number of repeated same-amplitude cycles, and the comparison between tests from different experimental campaigns cease to make sense. Moreover, studies on strength degradation and the evolution of permanent lateral displacement have never been performed so far.

2.3.1 Proposal for the interpretation of cyclic tests on masonry piers

In the following, a procedure for the interpretation of cyclic test results on masonry piers is described, aimed to measure stiffness and shear degradation and the evolution of the dissipated energy and permanent displacement. The procedure is composed of four steps:

1. Determination of the monotonic quantities from the cyclic graph envelope;
2. Subdivision of the force-displacement diagram into cycles;
3. Subdivision each cycle into loading-unloading branches;
4. Determination of the relevant quantities for each branch.

First, the monotonic quantities are obtained from the cyclic diagram envelope as for monotonic experimental tests. This is done for both lateral displacement directions, and the corresponding quantities are denoted with the subscripts + and − (Figure 2.14a). Then, the force-displacement diagram is subdivided into a sequence of n cycles, where each cycle is defined as a set of four branches (Figure 2.14b), namely:

- First loading branch (L+);
- First unloading branch (U+);
- Second loading branch (L-);
- Second unloading branch (U-).

The subdivision between loading and unloading branches is determined when the displacement variation changes its sign; on the other hand, the transition from unloading branches to loading ones is done when the lateral force crosses the zero value in the diagram. The loading branches of cycle i are outlined through the aforementioned bilinearization procedure, from which we obtain the lateral stiffnesses ($K_{L+}^{(i)}$ and $K_{L-}^{(i)}$), the lateral strengths ($V_{+}^{(i)}$ and $V_{-}^{(i)}$), and the displacement capacities ($d_{c,+}^{(i)}$ and $d_{c,-}^{(i)}$). The latter quantities are measured from the zero displacement value so that they are comparable with the monotonic values (d_c^+ and d_c^-). Other relevant quantities are: the unloading stiffnesses ($K_{U+}^{(i)}$ and $K_{U-}^{(i)}$); the permanent displacements ($d_{p,+}^{(i)}$ and $d_{p,-}^{(i)}$), defined as the difference between the displacement at the end of the unloading branch and the displacement at the beginning of the previous loading branch; the cumulative permanent displacement

$$d_{p,cum}^{(i)} = \sum_{j=1}^{i} \left(d_{p,+}^{(j)} + d_{p,-}^{(j)} \right) \tag{2.31}$$

The dissipated energy associated with the i-th cycle, $E_{dis}^{(i)}$, is defined as the envelope area of all the cycles j, with $j \leq i$ (Figure 2.14a).

The monitored quantities are then normalized to obtain adimensional parameters that can be used for the cyclic response comparison of different specimens.

We define the displacement index I_D as the ratio between the lateral displacement of the given cycle i, say $d_c^{(i)}$, and the maximum lateral displacement at the end of the test, namely

$$I_D^{(i)} = \frac{\left|d_c^{(i)}\right|}{d_{c,max}} \tag{2.32}$$

where $d_{c,max} = \max_{j=1}^{n} d_c^{(j)}$. The displacement index I_d describes the test evolution, ranging from 0 when it starts to 1 at the end of the test. The stiffness degradation index at the cycle i is defined as the ratio between the actual stiffness and the initial elastic stiffness, namely

$$I_K^{(i)} = \frac{K^{(i)}}{K_e} \tag{2.33}$$

The strength degradation index is obtained as

$$I_V^{(i)} = \frac{V^{(i)}}{V_{r-tc}} \tag{2.34}$$

where the actual strength is normalized by means of the shear strength associated to the rocking or toe-crushing failure mechanism. We define the permanent displacement index as the ratio between the permanent displacement and the maximum lateral displacement, that is

$$I_P^{(i)} = \frac{d_P^{(i)}}{d_{c,max}} \tag{2.35}$$

and the dissipation energy index as

$$I_E^{(i)} = \frac{E_{dis}^{(i)}}{E_{ref}} \tag{2.36}$$

where the reference energy used for normalization is the dissipated energy by the equivalent elastic-perfectly plastic model, namely

$$E_{ref} = V_y^+ \left(d_c^+ - \frac{V_y^+}{K^+}\right) + V_y^- \left(d_c^- - \frac{V_y^-}{K^-}\right) \tag{2.37}$$

The methodology presented above is used for the interpretation of experimental test results. Several aspects may influence the masonry pier response under lateral loads, namely the compression ratio between the actual and ultimate vertical load, the in-plane aspect ratio, the static scheme, and the masonry typology in terms of constituent dimensions and mechanical properties. Among the aforementioned parameters, the compression ratio plays a key role in the determination of pier lateral behavior. As already discussed in Section 2.2.3, we distinguish three zones in the shear-axial force failure domain, that is low, medium, and high compression zone, which lead to three different strength failure mechanisms and cyclic responses. In the following, we take advantage of the experimental test results of three different specimens characteristic of the shear domain zones.

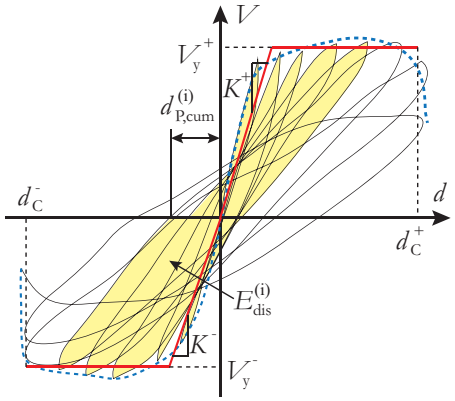

(a) Monotonic quantities, dissipation energy, and cumulative permanent displacement.

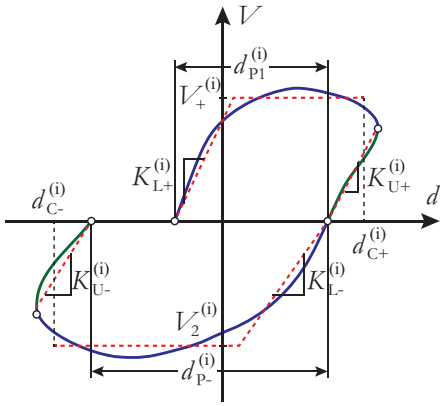

(b) Relevant quantities for loading and unloading branches of each cycle.

Figure 2.14: Interpretation of cyclic test diagrams.

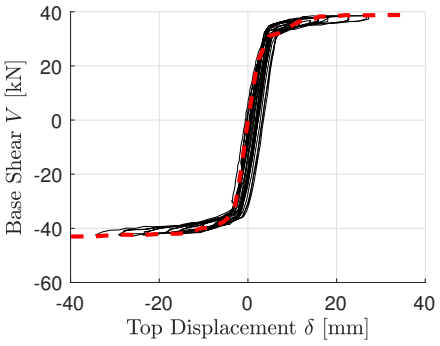

(a) Test 1 (Vasconcelos and Lourenço 2009).

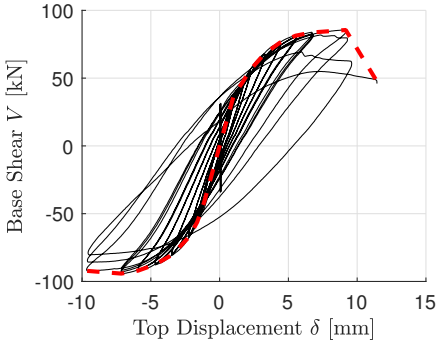

(b) Test 2 (Magenes, Galasco, et al. 2010).

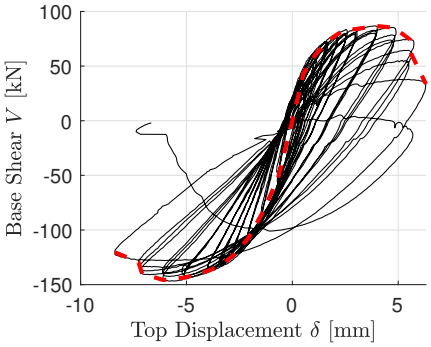

(c) Test 3 (Silva et al. 2014).

Figure 2.15: Shear-displacement graphs of the selected experimental tests.

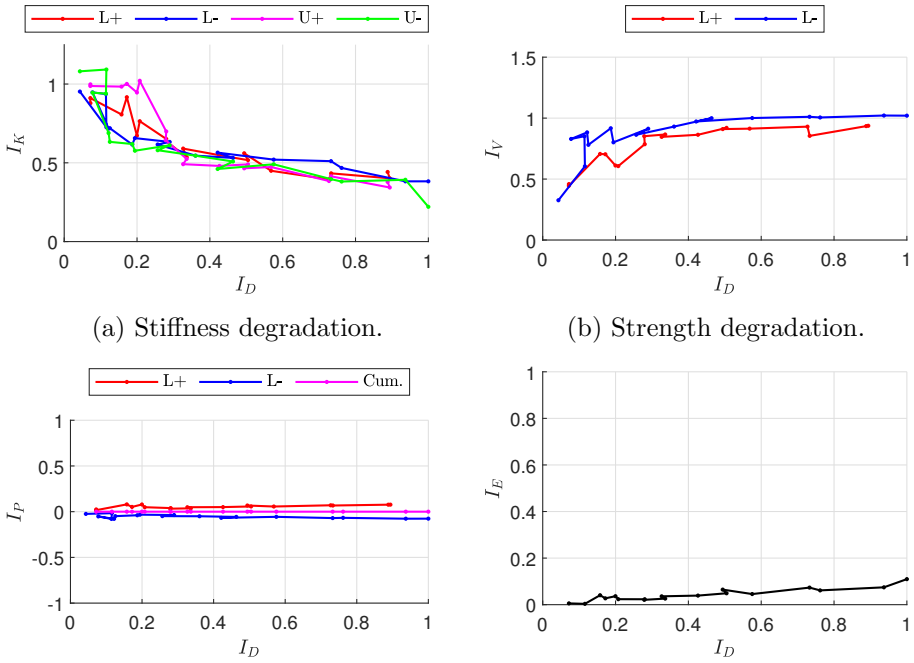

(a) Stiffness degradation.

(b) Strength degradation.

(c) Permanent displacements.

(d) Energy dissipation.

Figure 2.16: Cyclic behavior of Test 1.

The first specimen (Vasconcelos and Lourenço 2009) was tested with a low compression ratio (about 0.7%) and exhibited a rocking failure mechanism. In this case, after the shear strength limit is reached, the panel rocks alternatively about each base toe, and the lateral displacement grows, keeping the lateral force constant. If the panel toe is not damaged, the unloading process goes through the same path as the loading one; the panel returns to the initial position and starts to overturn in the opposing direction, repeating the same mechanism. An S-shaped graph characterizes the shear-compression diagram (Figure 2.15a), and the cyclic behavior is almost nonlinear elastic. The stiffness degradation index (2.16a) shows a steep decay in the first part of the test. In the late stage, both the lateral stiffness and the strength (2.16b) are almost constant. Figures 2.16c and 2.16d show that the rocking mechanism is characterized by small permanent displacements and low energy dissipation.

The second specimen (Magenes, Galasco, et al. 2010), tested with a compression ratio of 17%, exhibits shear failure and a shear-displacement diagram with remarkable energy dissipation (Figure 2.15b), caused by progressive degradation of brick-mortar interfaces. The indices describing the cyclic behavior indicate a significant stiffness decay (2.17a), the development of large permanent displacements (2.17c) and high amount of dissipation energy (2.16d). Significant shear degradation occurs only in the last cycles (2.17b), associated with an increase in permanent displacements and dissipated energy.

As reported in some databases (Vanin, Zaganelli, et al. 2017; Morandi et al.

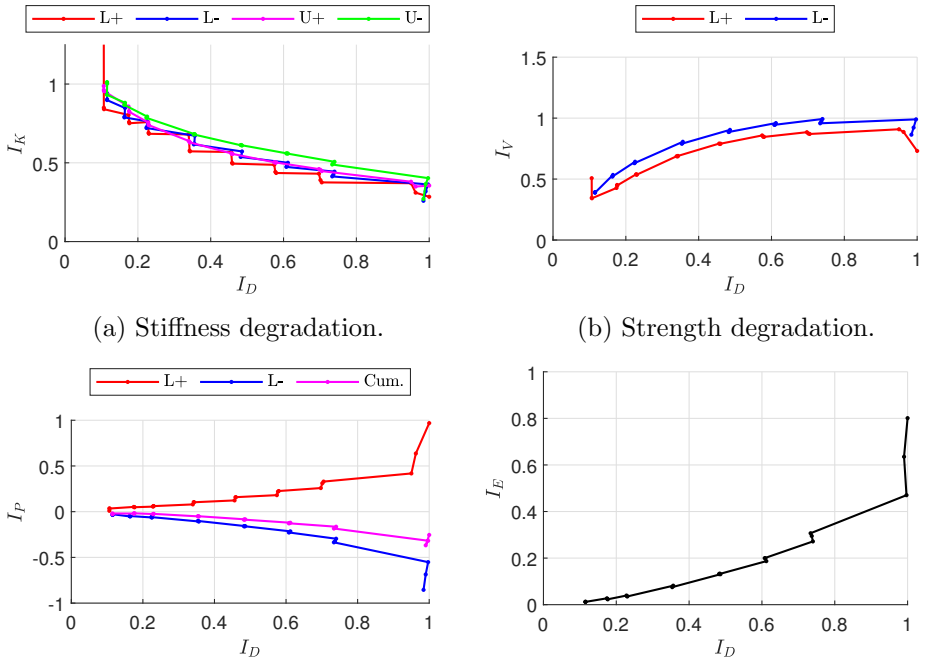

(a) Stiffness degradation.

(b) Strength degradation.

(c) Permanent displacements.

(d) Energy dissipation.

Figure 2.17: Cyclic behavior of Test 2.

2018), specimens have never been tested under compression ratios over 60%. Therefore, a thorough investigation of the behavior of piers in the high-compression range has never been done. However, to describe some aspects of this failure type, we can select a specimen exhibiting a toe-crushing mechanism even if the compression ratio is not very high, i.e., 0.415%. As we can see from Figure 2.15c, the graph shows large dissipation energy due to a progressive hysteretic cycle degradation. In this case, the stiffness and strength degradation (Figures 2.18a and 2.18b), the permanent displacement formation (Figure 2.18c), and energy dissipation (Figure 2.18d) are more notable and steeper with respect to Test 2.

In conclusion, the cyclic behavior highly depends on the compression ratio. The behavior is almost nonlinear elastic for low-compressed piers, with low energy dissipation and strength degradation. Stiffness and strength degradation, permanent displacements evolution, and dissipated energy increase with the compression load due to the progressive shear damaging for mid-range compressions or the toe-crushing mechanism in case of high compression ratios.

2.4 Mechanics of masonry walls

Masonry is the oldest and most widespread material used for building constructions. In the past, masonry buildings have always been conceived to carry only vertical loads, while the lateral actions induced by earthquakes were neglected. In Italy, the seismic issue awareness started to grow after the catastrophic events of

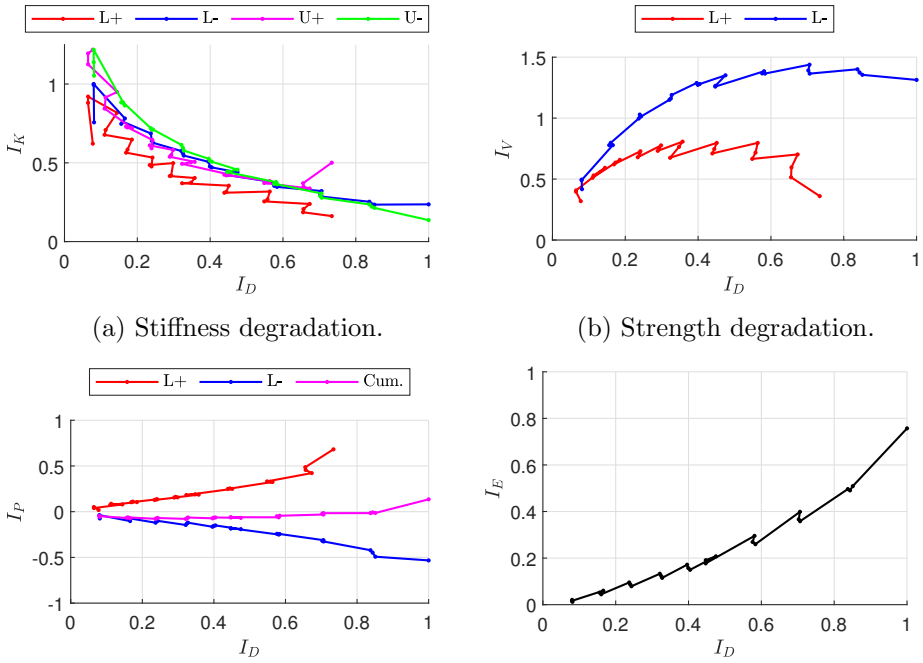

(a) Stiffness degradation.

(b) Strength degradation.

(c) Permanent displacements.

(d) Energy dissipation.

Figure 2.18: Cyclic behavior of Test 3.

the 1976 Friuli and 1980 Irpinia earthquakes. The need to address the problem of retrofitting and assessing the earthquake resistance of existent masonry buildings leads to a significant interest in studying masonry building mechanics under lateral forces. Many efforts have been made to determine efficient strengthening techniques to protect the building heritage and define a correct procedure for the seismic vulnerability assessment. The development of these methods needs a proper validation on experimental tests. For this purpose, several experimental campaigns have been performed on full-scale masonry buildings in recent years.

One of the most notable test is the one conducted by the University of Pavia (Magenes, Kingsley, et al. 1995) on a full-scale, two-story unreinforced masonry building. Almost all numerical models for masonry structures have been tested and calibrated on it. The building consisted of four solid brick walls with 250 mm thickness, with plan dimensions 6.0 m x 4.4 m, and height 6.4 m. Contrarily to the two transversal walls, the two longitudinal walls contained openings, and they were called the "door wall" and the "window wall". The seismic forces were simulated by the cyclic quasi-static application of four concentrated horizontal forces, through displacement-controlled screw jacks, applied at the two longitudinal walls at the floor levels. Due to the weak coupling given by the flexible floors and the equal displacement applied at both longitudinal walls, the two walls constituted two independent structural systems that worked mainly in their plane.

The response of each wall was summarized in plots of base shear versus top displacement, and the in-plane crack pattern at each cycle was monitored. Initially, cracking was limited to first-floor spandrels, leading to a decoupling of masonry pier

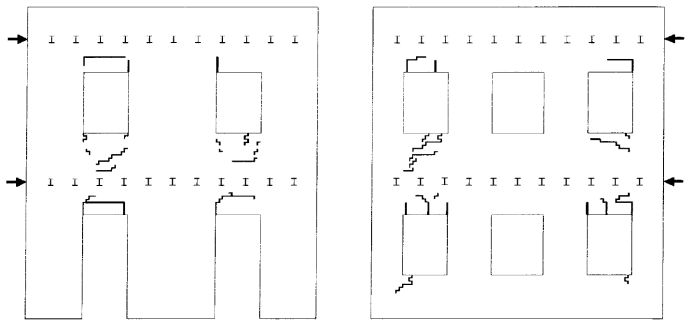

(a) Crack distributions at the end of the third cycle.

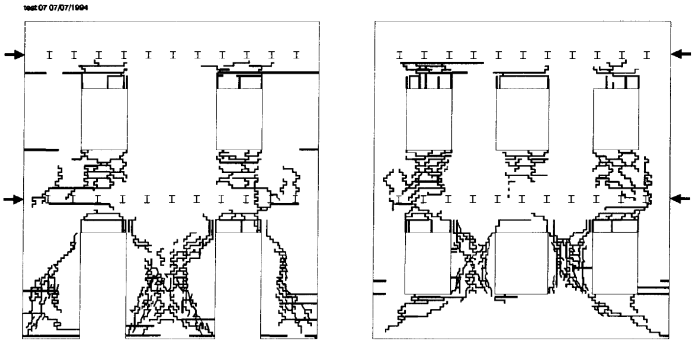

(b) Crack distributions at the end of the test.

Figure 2.19: Experimental test on a full-scale masonry building (from Magenes, Kingsley, et al. 1995).

response (Figure 2.19a). At later stages, the response of the two walls was quite different (Figure 2.19b). The damage due to shear mechanisms was concentrated in the two central first-floor piers in the window wall. The exterior piers in the window wall exhibited a rocking mode, showing no diagonal cracks. In contrast, the exterior piers in the door wall failed in shear, presenting diagonal shear cracking only in one direction. The latter is due to the overturning effect of horizontal forces, which generates a compression increase in the pier located downhill of the seismic force direction and a compression decrease in the opposite wall. The maximum base shear reached was approximately 150 kN in the door wall and 140 kN in the window wall, achieved at a drift (ratio between the top displacement and the building height) of 0.2%. The test was terminated at the maximum drift of 0.4% when significant damage occurred in the walls.

The Pavia test investigated the in-plane mechanisms of masonry walls. However, under seismic actions, masonry buildings exhibit complex behavior that often leads to local failure mechanisms, namely the ones that involve only a limited part of the structure, i.e., a wall, that fails due to a mechanism that acts out of its plane. These phenomena usually occur in case of bad connection between floors and walls or between orthogonal walls or poor masonry quality.

Out-of-plane mechanisms were noticed in an experimental test conducted on a full-scale masonry building at the EUCENTRE laboratory in Pavia (Kallioras

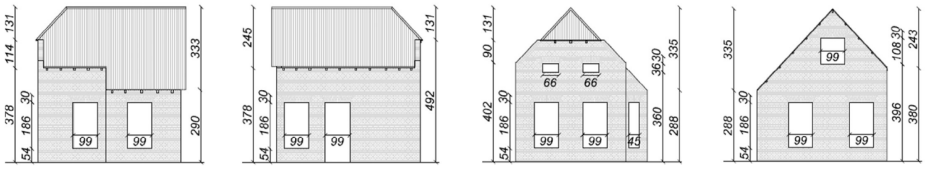

(a) West wall. (b) East wall. (c) North wall. (d) South wall.

Figure 2.20: Geometry of the specimen tested at EUCENTRE (from Kallioras et al. 2018).

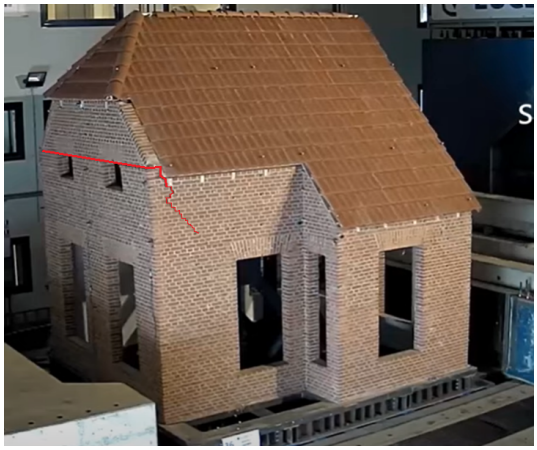

Figure 2.21: Cracks due to out-of-plane mechanism in the North wall.

et al. 2018). The structure was characterized by the typical features of Dutch masonry buildings, such as solid clay-crick walls, flexible floors, and steep-pitched roofs with high gables. The building was subjected to an incremental dynamic test in the direction perpendicular to roof trusses and floor beams. The specimen had an irregular plan configuration, with overall footprint dimensions of 5.8 m in the shaking direction and 5.3 m in the transverse one, and a total height of 6.2 m. The walls are characterized by different opening layout, particularly in the two longitudinal walls, the ones parallel to the ground shaking direction, namely the West wall (Figure 2.20a) and East wall (Figure 2.20b). The transversal walls have different roof-end typologies: a half-hipped roof with a clipped gable for the North wall (Figure 2.20c) and a full-height gable for the South wall (Figure 2.20d).

The specimen exhibited an out-of-plane overturning mechanism on both north and south gables, even at low-level input motions. Horizontal cracks were found in the North wall just above the openings along the entire façade (Figure 2.21). Good interlocking between intersecting walls guaranteed the interaction between in-plane and out-of-plane responses, as testified by the crack extension in the upper-left corner of the West wall.

The experimental campaign performed by Magenes, Penna, Senaldi, et al. 2014 reported interesting results on the effect of out-of-plane mechanisms and gives information on how to improve the seismic resistance of masonry structures. Shake table tests were carried out on two full-scale two-story buildings, having the same

(a) L-shaped steel profile. (b) Masonry ring beam.

Figure 2.22: Strengthening techniques used in the experimental test by Magenes, Penna, Senaldi, et al. 2014.

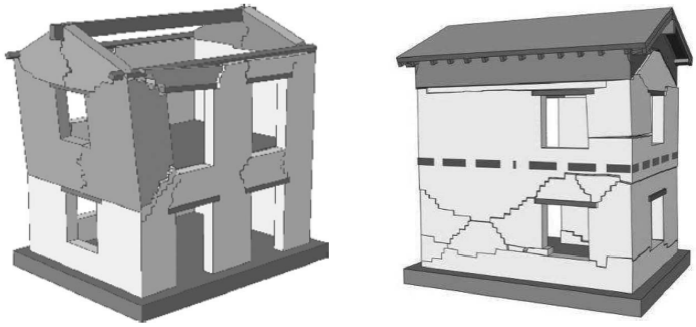

(a) Building 1. (b) Building 2.

Figure 2.23: Damage pattern of the buildings tested (from Magenes, Penna, Senaldi, et al. 2014).

geometry and materials (undressed double-leaf stone masonry with timber floor and roof) but different construction details. The first specimen (Building 1) represented a vulnerable building without any antiseismic detail or device. The second prototype (Building 2) has the same configuration as Building 1, but the connections among walls and between floors and walls were improved. At the floor level, a continuous L-shaped steel profile was put at the internal side of the walls and connected by threaded bars to steel plates on the facades (Figure 2.22a). At the roof level, the strengthening technique consisted of a reinforced masonry ring beam put on the top of the masonry walls (Figure 2.22b). The experimental campaign was aimed to understand the dynamic behavior of unstrengthened masonry buildings and evaluate the effectiveness of some strengthening strategies.

Buildings were subjected to shake table tests at EUCENTRE. The motion direction was parallel to the East and West walls. Building 1 attained a near-collapse condition because of the occurrence of an out-of-plane mechanism of the North wall gable, which also involved the spandrels of the intersecting walls (Figure 2.23a). The improvement of the wall connections in Building 2 proved to be very effective since no out-of-plane mechanism was monitored, and box-type global mechanisms occurred (Figure 2.23b). The ring beam presence significantly improved the spandrel coupling effect on piers, enhancing both its lateral strength (up to 40% greater than Building 1) and its deformation capacity.

2.5 Remarks

Masonry, as heterogeneous, anisotropic, and nonlinear material, deserves particular attention for the description of its mechanical properties. Its microstructural size is not negligible, so that it influences masonry mechanics even at greater scales. In this chapter, we reported a review of masonry mechanics at the microscale, at the scale of piers, and the wall level.

The study of masonry mechanics at the microscale is conducted reporting its response under basic stress scenarios, namely vertical and horizontal tension and compression, shear stresses, and biaxial stresses. The study has been restricted to regular masonry, although similar reasonings can be formulated in the case of irregular texture. A simple analysis of a small portion of masonry under vertical compression shows that this failure mechanism is associated with the brick failure in horizontal tension formed due to the presence of a softer medium, namely the mortar layers. The tensile behavior of masonry has been discussed. It has been shown its strong dependence on the tensile direction relative to the bed joints. For tension acting orthogonal to bed joints, failure is determined when the mortar tensile strength is reached. Therefore, since the tensile strength of mortar is poor and has a strong variability, the masonry tensile strength in that direction is usually neglected in practical computations. Conversely, the tensile strength parallel to bed joints is not negligible, as it activates a frictional mechanism on the interface between bricks and mortar bed joints. Then, we discussed the strong influence of the vertical compression on the shear behavior. Shear failure mode can vary between rocking, shear sliding, brick tensile cracking, or tow crushing, for increasing the vertical stress amounts.

Then, we discussed masonry piers mechanics with a focus on their cyclic behavior. A novel procedure for the cyclic response interpretation of masonry piers has been proposed. It is aimed to describe the evolution of the stiffness and strength degradation, permanent displacement increase, and energy dissipation during cyclic experimental tests. It has been shown that panels characterized by different failure modes exhibit a different evolution of the aforementioned parameters. In particular, the behavior is almost nonlinear elastic for low-compression piers, with low energy dissipation and strength degradation. Increasing the vertical compressions, all the evolution parameters increase due to the progressive shear damaging for mid-range compressions or the toe-crushing mechanism in case of high compressions.

Finally, three experimental tests on full-scale masonry buildings performed at the University of Pavia have been reviewed. If the out-of-plane mechanisms were prevented, strength mechanisms involve masonry walls in their plane. In this case, piers exhibit the typical flexural and shear failure modes, depending on their aspect ratio and their position within the structure with respect to the seismic load direction. The coupling effect of spandrels and how the pier behavior changes after spandrel strength degradation have been shown. Conversely, tests show that without any antiseismic details aimed to prevent out-of-plane overturning, building collapse without involving the wall in-plane resources.

Chapter 3

Mechanical Models for Masonry Structure Analysis

Abstract

This chapter is devoted to a review of mechanical models for masonry structure analysis. Since masonry is a heterogeneous material whose constituent dimensions strongly influence its mechanics, a refined representation would require the explicit modeling of its components. Increasing the specimen size, however, the computational burden increases and can become unsustainable for large structures. At larger scales, masonry structure analysis needs simplified models to speed up computation and obtain manageable results. Therefore, several modeling techniques characterized by different detailing level rises in the literature.

For the wall level, the Equivalent-Frame and the articulated quadrilaterals methods are discussed, considering their advantages and drawbacks. A review of pier models to be used within the Equivalent-Frame method is then reported. Subsequently, a series of constitutive laws suitable for the macroscopic representation of masonry is discussed. Finally, we report some of the literature attempts for microstructural modeling, where the masonry constituents are explicitly modeled.

3.1 Introduction

The mechanical modeling of masonry is a challenging task. Its main characteristic can be summarized as follows. The masonry material is:

- *Heterogeneous*, as it is composed by two phases, namely blocks and mortar;
- *Anisotropic*, as masonry has preferential directions based on the way it is assembled;
- *Nonlinear*, due to its limited strength values in shear and compression, and its negligible tension strength.

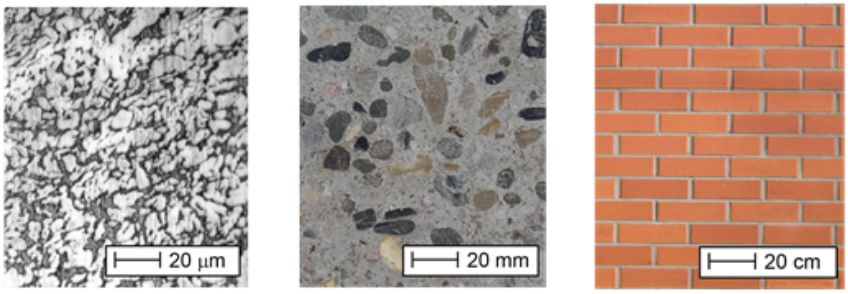

(a) Steel. (b) Concrete. (c) Masonry.

Figure 3.1: Comparison of microstructural dimensions between materials.

Masonry can be defined as a "structure within a structure" since its mechanical response strongly depends on its constituents and how they are arranged. The existence of nested structures within a material is not a peculiarity of masonry only (Figure 3.1); however, unlike other materials, the microstructural dimensions is relevant in the case of masonry. Steel microstructure is composed of grains having a characteristic size of a few μm; concrete consists of a binding medium in which are embedded particles and aggregates having a size of the order of a few cm. On the other hand, regular brick sizes are 25 cm $\times$ 12 cm $\times$ 5.5 cm, which are not negligible when compared to the structural element dimensions.

The strong influence of the microstructure on masonry mechanics leads many authors to develop models where the constituents are explicitly modeled (Oliveira and Lourenço 2004; Pina-Henriques and Lourenço 2006; Minga et al. 2018). In this case, blocks, mortar, and block-mortar interfaces are characterized by proper constitutive laws aimed to represent the mechanics of each constituent or their interactions separately.

We can further increase the detailing level by observing the granulometric composition of the material. We can explain masonry mechanical behavior by considering the microscopic interactions between the grains of the constituents. However, this scale of representation is too refined for technical applications. It cannot be used in practical situations, even though it can explain some of the constituent microscopic properties (Li et al. 2004; Diamond and Landis 2007).

When large portions of masonry are at study, however, explicit modeling of its constituents requires an impractical amount of discretization elements and computer resources. At this scale, in fact, masonry material is generally interpreted as a homogenized continuum. The reproduction of the microstructural mechanisms is fully devoted to the definition of a proper constitutive law, which can be formulated in the framework of plasticity (Page et al. 1985; Lourenço, De Borst, et al. 1997), damage mechanics (Berto et al. 2002), smeared crack models, or coupled damage-plasticity models (Addessi, Marfia, et al. 2002).

However, these macroscopic phenomenological models require a large amount of data. Since they need to phenomenologically reproduce the microstructural mechanics in all their complexity with a single stress-strain relationship, they require many parameters for their definition that are not easy to extract from basic experimental tests on the material. A case in point is Lourenço's model (Lourenço, De Borst, et al. 1997), for which sixteen mechanical parameters are required.

Therefore, large structure analyses require simplified models able at the same time to effectively reproduce masonry mechanics and to speed up computation time. A widely-used approach is to consider walls as an assembly of macroelements (*macroelement modeling*). They can be distinguished between the vertical elements, i.e., the piers, which bear vertical and horizontal loads; the horizontal elements, i.e., the spandrels, which couple the pier response; and the portions at the pier-spandrel intersections, namely the node panels. The effectiveness of these models relies on the proper mechanical behavior assigned to each macroelement. The articulated-quadrilaterals method (Caliò et al. 2012) belongs to the same model family. In this case, building walls are discretized in quadrilateral elements, calibrated to reproduce the masonry failure mechanisms at the macroelement level, namely rocking, toe-crushing, diagonal cracking, and shear sliding.

In summary, masonry mechanics can be modeled at different detailing levels:

- *Microscale*, when the masonry constituents are explicitly taken into account;
- *Macroscale*, when we consider masonry as a homogenized continuum.
- *Macroelement scale*, when a mechanical behavior is assigned to large portions within a wall.

In this chapter, a review of the most widely-used modeling techniques for masonry at all scales of representation is reported. The study of masonry at scales that are smaller than the dimensions of its constituents is not relevant from a structural point of view, and it will be neglected.

Here, we limit our attention to the in-plane behavior of masonry walls under the assumption of out-of-plane mechanisms prevention. As shown in Section 2.4, if the out-of-plane mechanisms are not prevented in a masonry building, they are the first ones to occur, and buildings collapse without the activation of in-plane mechanisms. The out-plane mechanisms are generally studied with specific models, such as limit analysis (Shawa et al. 2012; Doherty et al. 2002; Abrams et al. 2017). The study of the in-plane mechanisms is tipically done separately from the verification of the absence of out-of-plane mechanism, under the assumptions that they are decoupled. The coupling effect of in-plane and out-plane mechanisms is still an open issue.

In Section 3.2, we report a review of modeling techniques at the wall level, namely the Equivalent-Frame method and the articulated-quadrilateral model. The Equivalent-Frame method requires the definition of specific models for its macroelements. A review of the macroelement models for masonry piers is reported in Section 3.3. The family of homogenized continuum models suitable for masonry structures is then discussed in Section 3.4. In Section 3.5, the attention is then focused on microscale modeling. Finally, a final discussion is reported in Section 3.6.

3.2 Wall level

Masonry is a composite material having particular mechanical characteristics, as described in Chapter 2. Since the 80s (Page et al. 1985), finite element methods have been used for the analysis of masonry structure. However, these refined models are time-consuming and require a large amount of data. Since they suffer from mesh dependency, they require many parameters for regularization that are not easy to extract from basic experimental tests of the material. Moreover, these models

are susceptible to mechanical parameters and require careful calibration to obtain reliable results.

Therefore, the need for simplified models arises for large structures. In the following sections, we present the characteristics of the Equivalent-Frame method and the one based on the articulated quadrilaterals, which are widely used in the professional practice for the seismic vulnerability assessment of masonry buildings. The main advantage of these models is the low detailing level of representations of the masonry structures, since they are based on the subdivision of each masonry wall into panels. Since the constitutive behavior is assigned at this representation level, the resulting model has a lower number of degrees of freedom with respect to other modeling techniques, and the required computation time for analyses is highly reduced.

3.2.1 Equivalent-Frame

The Equivalent-Frame (EF) method relies on modeling a masonry wall with openings as a frame composed of columns and beams (Figure 3.2). Let us consider a wall with openings in a masonry building. By virtually extending the lines of opening edges, we can identify vertical and horizontal stripes of masonry, which are defined respectively as "piers" and "spandrels". The panels at the intersection of piers and spandrels are defined as "node" panels.

Once the subdivision of the masonry wall in macroelements is made, the reliable prediction of its overall behavior relies on the proper modeling of each member response. A review of modeling strategies for EF macroelements is reported in Section 3.3. The nonlinear behavior is usually concentrated in piers and spandrels. Node panels are considered zones where damage cannot occur, and they are modeled as infinitely stiff and resistant. In the numerical implementation, the latter assumptions are taken into account by inserting rigid offsets to pier and spandrel beams. Generally, the determination of the flexible portion of piers accounts for the height of adjacent openings. A commonly adopted criterion defines the pier vertical limits at the intersection of its axis with the virtual lines having a 30° inclination on horizontal direction starting from the adjacent opening corner (Dolce 1991).

Compared to other modeling techniques, the EF method has advantages in terms of readability of results (for the familiarity that designers have with framed structures) and computational time (for the reduced number of degrees of freedom of the models). For these reasons, EF is, to date, the most used modeling technique in professional practice.

The scientific community has proposed numerous EF methods, starting from the POR method (Tomaževič 1978), which was extensively used for repair and strengthening work after the 1976 Friuli earthquake. This method adopted strong and simplistic assumptions. Each floor is analyzed separately, under the assumption of infinite stiffness and strength of spandrels and keeping constant the axial force in wall elements during the analysis. Moreover, an elastic-perfectly plastic constitutive law for the elements was assumed, with a strength limit given only by the shear mechanism. Axial force in piers was determined by vertical loads only, neglecting the effects of horizontal actions, which can determine compression variations. Moreover, since the analysis was carried out storey-by-storey, the method gave rise to unbalanced solutions in relation to the entire wall, and the effect of force redistributions in the whole wall after element damaging was not taken into

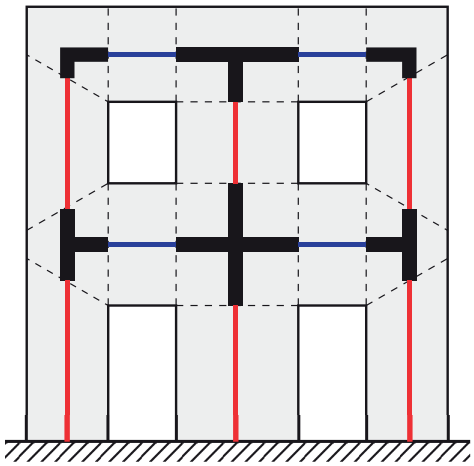

Figure 3.2: Subdivision of a masonry wall in piers (in red) and spandrels (in blue) by the EF method.

account.

The method was partially improved by Braga and Dolce 1982, formulating the PORFLEX method, which introduced failure in spandrels, different mechanisms (tension, compression, and shear) for strength failure of piers, and the variation of axial force with increasing of the horizontal load. However, the limit of the preceding techniques, i.e., to perform a separate analysis at each storey, has not been removed.

The first method which analyzed the entire masonry wall under lateral loads in the nonlinear field as an equivalent frame was the SAM method (Magenes and Calvi 1996; Magenes and Della Fontana 1998). Piers and spandrels were formulated as elastic-plastic columns and beams with flexural and shear deformability ad strength defined by two failure mechanisms (flexural and shearing), expressed as internal forces. The collapse of piers was determined when their lateral drift overcame a given threshold, which depends on the failure type: 0.5% for shear failure and 1.0% for flexural failure.

Another EF method that is worth mentioning is the one implemented in the commercial software TREMURI (Lagomarsino et al. 2013). It introduced some advanced features like the explicit modeling of flexible horizontal diaphragms, useful for modeling timber floors in historical buildings, and the formulation of a refined macroelement model, which will be discussed in Section 3.3.

Despite the advantages of this kind of modeling, the EF method has some controversial aspects that need to be mentioned. This method is difficult to apply to walls characterized by an irregular layout of openings. In this case, the schematization of a wall in an equivalent frame is arbitrary, not unique, and left to the analist imagination and sensitivity. Furthermore, the reliability of the results obtained with this model on walls with irregular geometry of the openings is questionable. A study of the reliability of the EF method in case of an irregular set of openings is presented in Chapter 4.

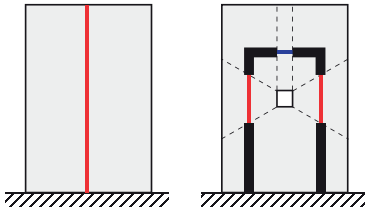

(a) The "small-opening paradox".

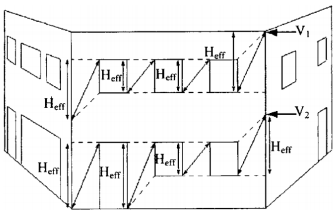

(b) Definition of pier effective height based on development of compression strut (from Moon et al. 2006).

Figure 3.3: Controversial aspects of the EF method.

A reckless application of the EF method can lead to paradoxes. Let us consider a wall without openings that can be modeled by the EF method as a cantilever. If we consider the same wall, having a small opening inside, its corresponding equivalent is extremely different as it has tiny flexible portions of piers and spandrels (Figure 3.3a). In other words, small variations in the wall geometry lead to a large variation in its response. This fact represents an undesirable feature for a structural model.

Another aspect that is often neglected in defining the frame geometry is the seismic action direction. Experimental evidence shows that the effective portion of the pier is determined by the opening located downstream with respect to the seismic action. Moon et al. 2006 proposed a method in which the effective height of a pier is defined as the height over which a compression strut is likely to develop, changing its geometry depending on the load direction (Figure 3.3b). However, this consideration is not easy to implement for the analysis of a three-dimensional structure. In fact, in some cases, i.e., the case of shape irregularity of floor plans, torsional effects can lead to inversions of the seismic load direction for some walls with respect to the global one assigned in the pushover analysis.

3.2.2 Articulated quadrilaterals

The Articulated-Quadrilateral (AQ) model (Caliò et al. 2012) is based on a plane nonlinear discrete element, able to simulate the behavior of masonry walls in their own plane.

This model differs to the EF method for the concept of panel discretization (Figure 3.4). While in the EF method each member represents a macroelement, i.e., a pier or a spandrel, in the AQ model a masonry wall can be subdivided into a larger number of discrete elements, also to accommodate the irregular pattern of openings or at the user's discretion (Figure 3.5b).

The quadrilateral element (Figure 3.5a) is composed of rigid edges with two diagonal nonlinear springs, having a proper stiffness to simulate panel shear stiffness, non-reacting in tension and having a compression strength calibrated to reproduce the diagonal-cracking shear mechanism of the panel. The flexure and shear-sliding mechanism are simulated through a finite number of vertical and horizontal springs at the top and bottom interfaces, respectively. Vertical springs have linear-elastic behavior limited by tensile and compressive strength. Failure is treated differently in tension and compression. Once the compressive ultimate displacement is reached,

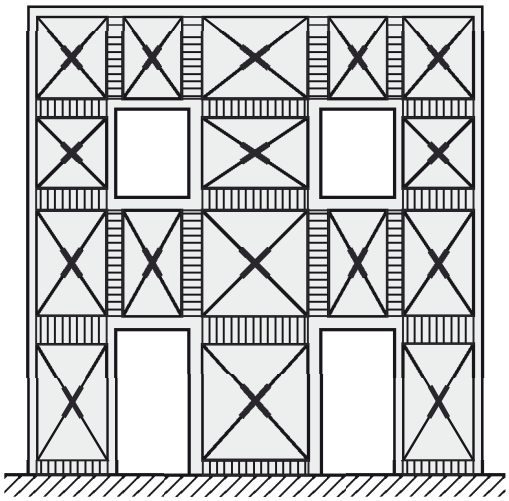

Figure 3.4: Subdivision of a masonry wall in articulated quadrilaterals.

the spring is removed by the model since the corresponding fiber is crushed. On the other hand, when the tensile limit is attained, the vertical spring is not removed since it would bear further compressive loads once the lateral load is inverted. Horizontal springs are modeled as rigid-plastic governed by the Mohr-Coulomb yielding criterion. From a kinematic point of view, the quadrilateral element has four degrees of freedom, three of which are associated with the in-plane rigid-body motion and a fourth derived from the shear deformability.

This model has some advantages and drawbacks. Like other simplified approaches, it can analyze a masonry structure with a low computational cost. Moreover, masonry walls with irregular opening layout can be geometrically divided into elements since every wall panel (pier, spandrel, and node panel) is modeled with the same articulated quadrilateral element. Besides, the model can account for the

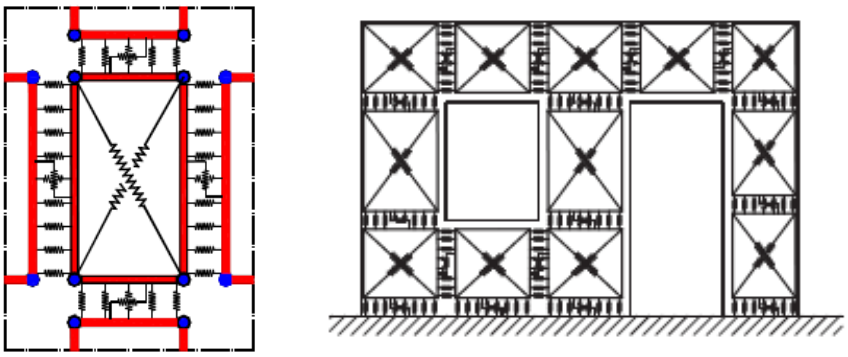

(a) The basic element. (b) Wall discretization.

Figure 3.5: Articulated-Quadrilateral model (from Caliò et al. 2012).

effect of seismic load direction. In fact, if we consider a masonry pier having aside openings of different heights, the pier elements can result as confined by other elements in one direction, while they are contact-free due to the opening void in the other one.

However, the arbitrariness of the wall discretization represents a drawback. Unlike the finite element method where the results tend to the exact solution with mesh refining, the AQ model response can be very different with different subdivisions, since element spring strengths are calibrated on experimental tests adopting AQ elements having specific dimensions.

3.3 Macroelements

In Equivalent-Frame models, the effectiveness of the overall response relies on the proper modeling of each macroelement.

The scientific community has focused its attention mainly on the masonry piers since they are the components that more strongly influence the seismic response of masonry structures. Masonry piers have been tested in numerous experimental campaigns in the last three decades (Magenes and Calvi 1992; Tomaževič and Lutman 1996). The interpretation of the masonry pier mechanics, which has been discussed in Section 2.3, is now consolidated in the scientific community.

Conversely, the interpretation of the spandrel's behavior under seismic actions is still an open issue. Unlike masonry piers, spandrels have been subjected to experimental campaigns only recently (Gattesco et al. 2008; Beyer and Dazio 2012), and the evaluation of their behavior is still under discussion. Moreover, the spandrel response is strongly influenced by the compression acting along its horizontal axis, which difficult to assess in a real masonry structure. For these reasons, spandrel models are usually the same ones chosen for masonry piers, with the only difference of having the reference frame rotated at a right angle.

Specific models for spandrels have been developed only recently. Cattari, Lagomarsino, et al. 2008 proposed a failure criterion based on the equivalent tensile strength originated by the interlocking phenomena at the interface between the spandrel end sections and the contiguous masonry. Another notable model is the one formulated by Calderoni et al. 2011, in which the spandrel is modeled as an "arched strut" having two failure mechanisms, namely, toe crushing and tensile cracking.

Node panels are generally considered infinitely rigid and resistant, as confirmed by experimental evidence showing that elastic and inelastic strains are concentrated in piers and spandrels.

In this section, we restrict our attention to masonry pier models within the Equivalent-Frame method. Two main families of modeling techniques can be found in literature: the *beam* approach and the *multi-spring* approach.

In the *beam* approach (Figure 3.6b), the beam theory is used to model the panel. Nonlinearities can be considered as smeared along the beam axis, lumped to its ends, or, in some cases, by correcting according to some criteria the linearly-computed internal forces.

On the other hand, in the *multi-spring* approach (Figure 3.6c), both elastic and inelastic strains are concentrated in springs that are connected by rigid bodies. Similarly to the beam models, the springs can be properly nonlinear or linear with strength and failure criteria.

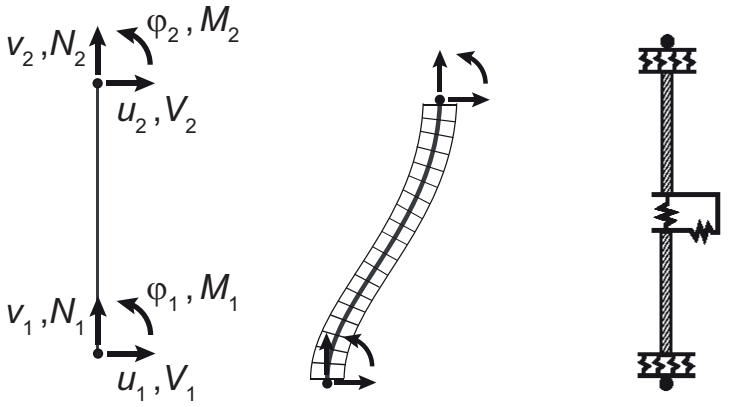

(a) Macroelement generalized forces and degrees of freedom.

(b) Beam approach.

(c) Multi-spring approach.

Figure 3.6: Macroelement models.

In the following, we consider the vector $\boldsymbol{p}$ as the one that groups the global generalized displacements, composed of the in-plane displacements and the rotation about the out-of-plane axis of the bottom and top nodes. Moreover, we consider $\boldsymbol{P}$ as the vector of global generalized forces, that groups axial and shear forces and bending moments at the end nodes of the beam, namely

$$\boldsymbol{p} = \begin{bmatrix} u_1 \\ v_1 \\ \varphi_1 \\ u_2 \\ v_2 \\ \varphi_2 \end{bmatrix}, \qquad \boldsymbol{P} = \begin{bmatrix} V_1 \\ N_1 \\ M_1 \\ V_2 \\ P_2 \\ M_2 \end{bmatrix} \tag{3.1}$$

where the meaning of the symbols is explained in Figure 3.6a.

3.3.1 Beam elements

Piecewise linear beams

The simplest and the most common approach, which is implemented in a large number of EF solvers (Lagomarsino et al. 2013; Pagani, Salvatori, et al. 2017), is the piecewise-linear model, in which we first compute the elastic internal forces as

$$\boldsymbol{P} = \boldsymbol{K}_e \, \boldsymbol{p} \tag{3.2}$$

where $\boldsymbol{K}_e$ is the Timoshenko beam stiffness matrix, given by

$$\boldsymbol{K}_e = C \begin{bmatrix} 0 & \frac{A\,H^2}{I}(1+\Phi) & 0 & 0 & -\frac{A\,H^2}{I}(1+\Phi) & 0 \\ 12 & 0 & 6H & -12 & 0 & 6H \\ 6H & 0 & (4+\Phi)\,H^2 & -6H & 0 & (2-\Phi)\,H^2 \\ 0 & -\frac{A\,H^2}{I}(1+\Phi) & 0 & 0 & \frac{A\,H^2}{I}(1+\Phi) & 0 \\ -12 & 0 & -6H & 12 & 0 & -6H \\ 6H & 0 & (2-\Phi)\,H^2 & -6H & 0 & (4+\Phi)\,H^2 \end{bmatrix} \tag{3.3}$$

where

$$C = \frac{EI}{(1+\Phi)\,H^3} \qquad \Phi = \frac{12EI}{GA_sH^2} \tag{3.4}$$

where E and G are the Young and shear moduli, respectively; A, A_s and I are the panel cross-section area, the shear area, and the moment of inertia, respectively; H is the height of the panel. The shear deformation parameter Φ represents the ratio between bending and shear stiffnesses. When its value vanishes, the stiffness matrix reduces to the one according to the Euler-Bernoulli beam theory.

After the linear prediction, some verifications are made aiming to correct the internal forces vector $\boldsymbol{P}$. First of all, it is checked whether the pier has reached the compression limit, after which the pier is considered as collapsed. The ultimate compressive load is given by

$$P_u = f_c\,A \tag{3.5}$$

where f_c is the compressive strength.

Then, we perform a check on the lateral drift θ, defined as

$$\theta = \frac{u_2 - u_1}{H} + \frac{\varphi_2 + \varphi_1}{2} \tag{3.6}$$

The failure criterion on the lateral drift is an open issue, since in several building codes, e.g., the Eurocode 8 (EN 1998-3 2005), it is roughly defined as a function of the strength mechanism only. According to this formulation, the ultimate lateral drift (θ_u) is given by

$$\theta_u = \begin{cases} 1.0\% & \text{flexural failure} \\ 0.5\% & \text{shear failure} \end{cases} \tag{3.7}$$

This definition does not account for many aspects which are significant for the determination of pier failure, such as the aspect ratio $\lambda = H/L$, being L the in-plane dimension of the cross-section, or the compression ratio $p = P/P_u$, or the material of which the pier is composed of. Moreover, it leads to a paradox. For high compression loads, masonry piers exhibit a toe-crushing (a flexural type) strength mechanism. Therefore, the ultimate drift is predicted as a value higher than the one corresponding to panels failing in shear, associated with lower compression loads. In contrast, numerous studies, notably Orlando et al. 2016, or the parametric study carried out in Chapter 5, have shown that the drift capacity decreases for high compression loads.

Recently, the Italian Building Code has implemented a new definition of the

ultimate drift which considers the influence of the compression ratio, namely

$$\theta_u = \left\{ \begin{array}{ll} 1.0\% & p \leq 0.2 \\ 1.25\% \cdot (1-p) & p > 0.2 \end{array} \right\} \quad \text{flexural failure} \qquad \text{shear failure} \tag{3.8}$$

which fixes the above-mentioned issue.

If the drift limit is overcome, the element loses the capacity to bear any lateral load, i.e., it becomes a strut, and the internal forces vector is accordingly modified.

If the failure criteria are not satisfied, the pier behavior is considered linear with strength cut-off defined by some simplified strength criteria, based on mechanical or phenomenological hypotheses proposed in the literature and codes.

Nonlinear beams

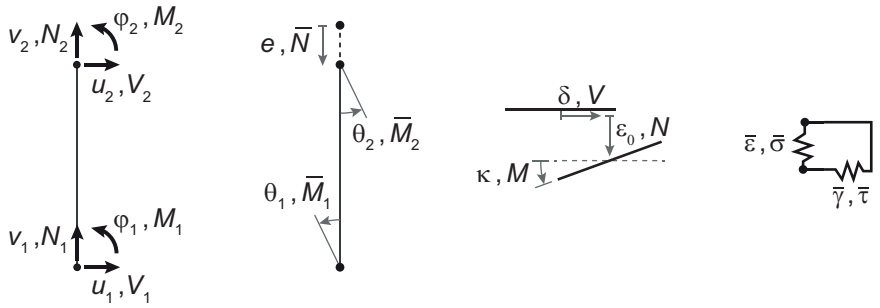

(a) Global level. (b) Element level. (c) Section level. (d) Fiber level.

Figure 3.7: Detailing levels in nonlinear beam models.

In linear models, nonlinearities are considered by properly correcting the internal forces, which are computed linearly from the beam displacements. In contrast, in nonlinear beam models, we consider a properly nonlinear relation between displacements and internal forces

$$\boldsymbol{P} = \tilde{\boldsymbol{P}}(\boldsymbol{p}) \tag{3.9}$$

Nonlinear beam models can be distinguished in two categories depending on their finite-element formulation. The classical displacement-based (DB) approach assumes compatible displacement and strains along the elements, using polynomial interpolation functions, which satisfy the continuity conditions. An alternative approach is represented by the force-based (FB) formulation, in which the stress field is interpolated along the element. This approach yields to a more complex procedure, but it leaves more freedom to the displacement field, which is not obliged to respect the prescribed shape functions.

It is worth defining some quantities that are useful for the description of both DB and FB formulations. Inside the beam element, there are four different levels at which we can define the kinematic and static quantities.

At the global level (Figure 3.7a), we have the displacements $\boldsymbol{p}$ and the internal forces $\boldsymbol{P}$, already defined in (3.1).

At the element level (Figure 3.7b), we define the element deformations $\boldsymbol{q}$ and forces $\boldsymbol{Q}$ as

$$\boldsymbol{q} = \begin{bmatrix} \theta_1 \\ \theta_2 \\ e \end{bmatrix} \qquad \boldsymbol{Q} = \begin{bmatrix} \bar{M}_1 \\ \bar{M}_2 \\ \bar{N} \end{bmatrix} \tag{3.10}$$

where θ_1 and θ_2 are the nodal rotations and e is the axial elongation. Similarly, $\bar{M}_1$ and $\bar{M}_2$ are the bending moments at the end nodes and $\bar{N}$ is the axial force.

At the section level (Figure 3.7c), the sectional deformations and internal actions are defined as

$$\boldsymbol{d} = \begin{bmatrix} \varepsilon_0 \\ \delta \\ \kappa \end{bmatrix} \qquad \boldsymbol{S} = \begin{bmatrix} N \\ V \\ M \end{bmatrix} \tag{3.11}$$

where ε_0 is the axial strain, δ the shear strain, and κ the curvature, while N, V, and M are respectively the axial force, the shear force, and the bending moment.

Finally, we can imagine the beam section as made up of a set of fibers (Figure 3.7d), having their fiber strains $\boldsymbol{\varepsilon}$ and stresses $\boldsymbol{\sigma}$ as

$$\boldsymbol{\varepsilon} = \begin{bmatrix} \bar{\varepsilon} \\ \bar{\gamma} \end{bmatrix} \qquad \boldsymbol{\sigma} = \begin{bmatrix} \bar{\sigma} \\ \bar{\tau} \end{bmatrix} \tag{3.12}$$

where $\bar{\varepsilon}$ and $\bar{\gamma}$ are the fiber normal and shear strains, and $\bar{\sigma}$ and $\bar{\tau}$ are the normal and shear stresses of the fiber.

$\boldsymbol{p}$	$\xrightarrow{\boldsymbol{d}=\boldsymbol{B}\,\boldsymbol{p}}$	$\boldsymbol{d}$	$\xrightarrow{\boldsymbol{\varepsilon}=\boldsymbol{G}\,\boldsymbol{d}}$	$\boldsymbol{\varepsilon}$
				$\downarrow$
				$\boldsymbol{\sigma} = \tilde{\boldsymbol{\sigma}}(\boldsymbol{\varepsilon})$
				$\downarrow$
$\boldsymbol{P}$	$\xleftarrow{\boldsymbol{P}=\int_0^H \boldsymbol{B}^T \boldsymbol{S}}$	$\boldsymbol{S}$	$\xleftarrow{\boldsymbol{S}=\int_A \boldsymbol{G}^T \boldsymbol{\sigma}}$	$\boldsymbol{\sigma}$

Table 3.1: Flowchart for the DB approach.

In the DB approach (Bažant and Bhat 1977; Hellesland and A. Scordelis 1981; A.C. Scordelis 1984; Belmouden and Lestuzzi 2009), we interpolate the displacement field along the beam through shape functions. Namely, the displacements $\boldsymbol{u}(x)$, where x is the abscissa varying from 0 to the beam length H, are given by

$$\boldsymbol{u}(x) = \begin{bmatrix} u_x \\ u_y \end{bmatrix} = \boldsymbol{N}(x)\,\boldsymbol{p} \tag{3.13}$$

It can be demonstrated (Bazoune et al. 2003) that the shape function matrix $\boldsymbol{N}$ for the Timoshenko beam is given by

$$\boldsymbol{N} = \begin{bmatrix} 0 & N_{a,2} & 0 & 0 & N_{a_5} & 0 \\ N_{b,1} + N_{s,1} & 0 & N_{b,3} + N_{s,3} & N_{b,4} + N_{s,4} & 0 & N_{b,6} + N_{s,6} \end{bmatrix} \tag{3.14}$$

where

$$N_{a,2} = 1 - \frac{x}{H} \tag{3.15}$$

$$N_{a,5} = \frac{x}{H} \tag{3.16}$$

$$N_{b,1} = \frac{1}{1+\Phi}\left[1 - 3\left(\frac{x}{H}\right)^2 + 2\left(\frac{x}{H}\right)^3\right] \tag{3.17}$$

$$N_{b,3} = \frac{H}{1+\Phi}\left[\frac{x}{H} - 2\left(\frac{x}{H}\right)^2 + \left(\frac{x}{H}\right)^3 + \frac{\Phi}{2}\left(2\frac{x}{H} - \left(\frac{x}{H}\right)^2\right)\right] \tag{3.18}$$

$$N_{b,4} = \frac{1}{1+\Phi}\left[3\left(\frac{x}{H}\right)^2 - 2\left(\frac{x}{H}\right)^3\right] \tag{3.19}$$

$$N_{b,6} = \frac{H}{1+\Phi}\left[-\left(\frac{x}{H}\right)^2 + \left(\frac{x}{H}\right)^3 + \frac{\Phi}{2}\left(\frac{x}{H}\right)^2\right] \tag{3.20}$$

$$N_{s,1} = \frac{\Phi}{1+\Phi}\left(1 - \frac{x}{H}\right) \tag{3.21}$$

$$N_{s,3} = -\frac{H\Phi}{1+\Phi}\frac{1}{2}\frac{x}{H} \tag{3.22}$$

$$N_{s,4} = \frac{\Phi}{1+\Phi}\frac{x}{H} \tag{3.23}$$

$$N_{s,6} = -\frac{H\Phi}{1+\Phi}\frac{1}{2}\frac{x}{H} \tag{3.24}$$

The section strains $\boldsymbol{d}$ can be obtained directly from the global displacements $\boldsymbol{p}$ by means of

$$\boldsymbol{d}(x) = \boldsymbol{B}(x)\,\boldsymbol{p} \tag{3.25}$$

where the matrix $\boldsymbol{B}$ given by

$$\boldsymbol{B} = \begin{bmatrix} 0 & \frac{\mathrm{d}N_{a,2}}{\mathrm{d}x} & 0 & 0 & \frac{\mathrm{d}N_{a,5}}{\mathrm{d}x} & 0 \\ \frac{\mathrm{d}N_{s,1}}{\mathrm{d}x} & 0 & \frac{\mathrm{d}N_{s,3}}{\mathrm{d}x} & \frac{\mathrm{d}N_{s,4}}{\mathrm{d}x} & 0 & \frac{\mathrm{d}N_{s,6}}{\mathrm{d}x} \\ \frac{\mathrm{d}^2N_{b,1}}{\mathrm{d}x^2} & 0 & \frac{\mathrm{d}^2N_{b,3}}{\mathrm{d}x^2} & \frac{\mathrm{d}^2N_{b,4}}{\mathrm{d}x^2} & 0 & \frac{\mathrm{d}^2N_{b,6}}{\mathrm{d}x^2} \end{bmatrix} = \tag{3.26}$$

(3.27)

$$= \begin{bmatrix} 0 & -\frac{1}{H} & 0 & 0 & \frac{1}{H} & 0 \\ -\frac{\Phi}{(1+\Phi)H} & 0 & -\frac{\Phi}{2(1+\Phi)} & \frac{\Phi}{(1+\Phi)H} & 0 & -\frac{\Phi}{2(1+\Phi)} \\ \frac{6(2x-H)}{(1+\Phi)H^3} & 0 & \frac{6x-(4+\Phi)H}{(1+\Phi)H^2} & -\frac{6(2x-H)}{(1+\Phi)H^3} & 0 & \frac{6x-(2-\Phi)H}{(1+\Phi)H^2} \end{bmatrix} \tag{3.28}$$

Then, we can obtain the fiber strains under the assumption of plane conservation of beam sections. If we consider an abscissa s along the beam sections, having

value as zero at the centroid position, we have

$$\boldsymbol{\varepsilon}(x, s) = \boldsymbol{G}(s)\, \boldsymbol{d}(x) \tag{3.29}$$

where

$$\boldsymbol{G}(s) = \begin{bmatrix} 1 & 0 & s \\ 0 & 1 & 0 \end{bmatrix} \tag{3.30}$$

Then, we are able to find the stress by defining the relation between stresses and strains at the fiber level, namely

$$\boldsymbol{\sigma} = \tilde{\boldsymbol{\sigma}}(\boldsymbol{\varepsilon}) \tag{3.31}$$

The constitutive law is usually defined separately for normal and shear actions. Raka et al. 2015 considered a plasticity model for the axial stress-strain relation, characterized by limited strength in tension and a hardening-softening law in compression, while the shear response is described through a phenomenological force-deformation law, with no interaction between shear and axial-bending behaviors. In the beam model formulated by Addessi, Mastrandrea, et al. 2014, a piecewise linear function has been used for the axial response, with no-stress in tension and a stress limit in compression. The shear behavior is formulated in the plasticity framework, with shear-sliding effects occurring in the compressed portion of the cross section.

The beam actions at the section level are retrieved by using equilibrium as

$$\boldsymbol{S}(x) = \int_A \boldsymbol{G}^T(s)\, \boldsymbol{\sigma}\, \mathrm{d}A \tag{3.32}$$

Similarly, we obtain the global internal forces by integrating along the beam axis, namely

$$\boldsymbol{P} = \int_0^H \boldsymbol{B}^T(x)\, \boldsymbol{S}(x)\, \mathrm{d}x \tag{3.33}$$

Structural analysis is most frequently done using a displacement-based finite element formulation for its simplicity and general effectiveness. Therefore, a displacement-based element is convenient and easy to implement in this kind of framework (Table 3.1).

However, all that glitters is not gold. Fine discretization is needed in the case of localized inelastic strains. A typical case is the rocking mechanism of masonry piers, for which the whole part of the body remains elastic, and a large rotation is concentrated at the pier base.

For this reason, recent efforts to develop more robust and efficient beam elements have shown a trend towards FB formulations (Taucer et al. 1991; Spacone et al. 1996; Neuenhofer and Filippou 1998) that rely on force interpolation functions that strictly satisfy the equilibrium of forces along the element. This approach can be implemented in a global displacement-based formulation, although it requires a more complex algorithm for retrieving internal forces during the element state determination (Addessi and Ciampi 2007). The FB approach is computationally efficient, and coarser spatial discretizations can be used than the ones needed for DB elements.

The element displacements $\boldsymbol{q}$ and forces $\boldsymbol{Q}$, defined in (3.10), are related to the global ones by means of

$$\boldsymbol{q} = \boldsymbol{B}\, \boldsymbol{p} \qquad \boldsymbol{P} = \boldsymbol{B}^T\, \boldsymbol{Q} \tag{3.34}$$

where $\boldsymbol{B}$ is a kinematic operator that removes the rigid modes from the global displacement vector $\boldsymbol{p}$, given by

$$\boldsymbol{B} = \begin{bmatrix} \frac{1}{H} & 0 & 1 & -\frac{1}{H} & 0 & 0 \\ \frac{1}{H} & 0 & 0 & -\frac{1}{H} & 0 & 1 \\ 0 & -1 & 0 & 0 & 1 & 0 \end{bmatrix} \tag{3.35}$$

Then, the section stress field is interpolated along the beam as

$$\boldsymbol{S}(x) = \boldsymbol{b}(x)\,\boldsymbol{Q} \tag{3.36}$$

where the equilibrium matrix $\boldsymbol{b}$ is

$$\boldsymbol{b}(x) = \begin{bmatrix} 0 & 0 & 1 \\ \frac{1}{H} & \frac{1}{H} & 0 \\ \frac{x}{H} - 1 & \frac{x}{H} & 0 \end{bmatrix} \tag{3.37}$$

where we have assumed the absence of distributed load along the beam, leading to constant axial and shear forces, and to a linear variation of bending moments along the element. The relation between section stresses and strains is the same as in the displacement-based element, namely

$$\boldsymbol{S}(x) = \int_A \boldsymbol{G}^T \boldsymbol{\sigma}(\boldsymbol{G}\,\boldsymbol{d}(x))\,\mathrm{d}A \tag{3.38}$$

However, in the force-based element, we need to find the inverse relation, which involves the section flexibility matrix $\boldsymbol{f}(x)$, the inverse of the section stiffness matrix $\boldsymbol{k}(x)$, given by

$$\boldsymbol{k}(x) = \int_A \boldsymbol{G}^T \frac{\partial \boldsymbol{\sigma}}{\partial \boldsymbol{\varepsilon}} \boldsymbol{G}\,\mathrm{d}A \tag{3.39}$$

Therefore, we can write

$$\boldsymbol{d} = \boldsymbol{f}\,\boldsymbol{S} = \boldsymbol{f} \qquad \text{where } \boldsymbol{f} = \boldsymbol{k}^{-1} \tag{3.40}$$

By applying the principle of virtual work, the vector of nodal displacements can be retrieved, namely

$$\boldsymbol{q} = \int_0^H \boldsymbol{b}^T\,\boldsymbol{d}\,\mathrm{d}x \tag{3.41}$$

that can be expressed also as

$$\boldsymbol{q} = \boldsymbol{F}\,\boldsymbol{Q} \tag{3.42}$$

where

$$\boldsymbol{F} = \int_0^H \boldsymbol{b}^T\,\boldsymbol{f}\,\boldsymbol{b}\,\mathrm{d}x \tag{3.43}$$

which represents the inverse of the element stiffness matrix $\boldsymbol{K}$.

$\boldsymbol{p}$	$\xrightarrow{\boldsymbol{q}=\boldsymbol{B}\,\boldsymbol{p}}$	$\boldsymbol{q}$	$\xleftarrow{\boldsymbol{q}=\int_0^H \boldsymbol{b}^T\boldsymbol{d}}$	$\boldsymbol{d}$	$\xrightarrow{\boldsymbol{\varepsilon}=\boldsymbol{G}\,\boldsymbol{d}}$	$\boldsymbol{\varepsilon}$
		$\downarrow$		$\uparrow$		$\downarrow$
		$\boldsymbol{Q}=\boldsymbol{F}^{-1}\boldsymbol{q}$		$\boldsymbol{d}=\boldsymbol{K}_s^{-1}\boldsymbol{S}$		$\boldsymbol{\sigma}=\tilde{\boldsymbol{\sigma}}(\boldsymbol{\varepsilon})$
		$\downarrow$		$\downarrow$		$\downarrow$
$\boldsymbol{P}$	$\xleftarrow{\boldsymbol{P}=\boldsymbol{B}^T\boldsymbol{Q}}$	$\boldsymbol{Q}$	$\xrightarrow{\boldsymbol{S}=\boldsymbol{b}\,\boldsymbol{Q}}$	$\boldsymbol{S}$	$\xleftarrow{\boldsymbol{S}=\int_A \boldsymbol{G}^T\boldsymbol{\sigma}}$	$\boldsymbol{\sigma}$

Table 3.2: Flowchart for the FB approach.

Therefore, the element state determination requires two nested inversions of stiffness matrices at both section end element level, as shown in the flowchart reported in Table 3.2. The element state determination is more complex than for the classical DB formulation. Details about its implementation can be found in Addessi and Ciampi 2007.

For both DB and FB beam elements, the numerical response depends on the number of integration points, which determines an internal length associated with each element section, say $H_i = w_i H$, where H is the beam length and w_i is the integration weight associated to each integration point. Therefore, these models need regularization techniques to have objective localization of inelastic strains. Two families of regularization techniques have been proposed in the literature: the first one is based on modifying the integration scheme at the beam level to have the desired internal characteristic length (Scott and Fenves 2006; Addessi and Ciampi 2007), while the second one is based on mesh-adjusted fracture energy parameters (Pugh et al. 2014; Vásquez et al. 2016).

3.3.2 Multi-spring approach

Experimental tests show that cracking zones tend to concentrate at element ends when failure mechanisms are of the flexure type, while a diagonal crack forms in the middle of the panel in case of shear failure. This observation leads to the development of elements with lumped nonlinearities using elements composed of several nonlinear springs connected by rigid links (Rinaldin, Amadio, and Macorini 2016; Penna et al. 2014). Springs are placed at the two ends of the masonry element for describing the flexural behavior and in the middle for representing the response in shear.

The advantage of the multi-spring approach, when compared to beam models, is the even lower computational effort due to the concentration of nonlinearities into a limited number of springs.

Penna et al. 2014 formulates a worth-mentioning model which have been implemented in the academic version of the commercial software TREMURI. It is a nonlinear multi-spring model, in which internal forces are computed as

$$\boldsymbol{P} = \boldsymbol{K}_{ms}\,\boldsymbol{p} - \boldsymbol{P}^* \tag{3.44}$$

where $\boldsymbol{K}_{ms}$ is the stiffness matrix of the multi-spring element, and $\boldsymbol{P}^*$ is the nonlinear term that properly corrects internal forces accounting for cracking, toe-crushing

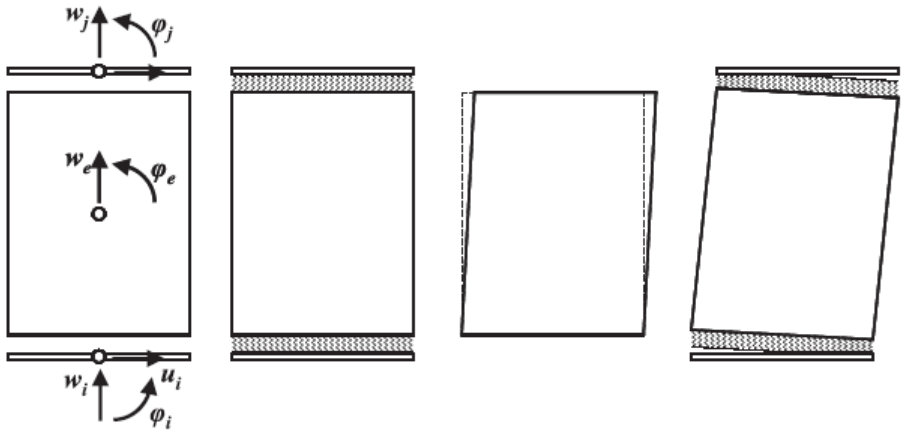

Figure 3.8: Kinematic of the multi-spring element (from Penna et al. 2014).

and shear damage conditions. The panel consists of three parts: a central body accounting for shear deformation only and two interfaces which model the axial and bending behavior. The macroelement kinematics can be described by means of eight degrees of freedom, six of which are the nodal displacement components (u_1,v_1,ϕ_1,u_2,v_2,ϕ_2) and two internal components (w_e, ϕ_e). The spring's kinematic variable in charge of modeling the panel shear behavior is a function of the displacement components u_1, u_2, and ϕ_e. Two damage variables for each cross-section edge was introduced to perform the nonlinear correction associated with the toe-crushing phenomena and to update the compressive stiffness associated with the bending–rocking behavior. For the shear behavior, other two internal variables were considered: the shear-sliding plastic displacement and a damage variable, accounting for shear strength degradation. Element collapse can be defined at a certain threshold of the lateral strength decay based on experimental results. Alternatively, it can also be defined at the macroelement level by setting its lateral stiffness as zero when the lateral drift limit is reached. In this case, in the further load steps, the element is transformed into a strut able to bear vertical loads only.

3.4 Homogenized continuum

Homogenized continuum models assume that, at the scale of representation, masonry can be treated as a continuum having mechanical properties that averagely reproduce the response of the heterogeneous material. Each material point of the homogenized continuum represents a certain portion of masonry containing blocks and mortar joints (Figure 3.9). The effectiveness of these models relies on the selection of a proper constitutive law that phenomenologically reproduces the stress-strain relation of this portion of masonry structure, which can be written in the following form

$$\boldsymbol{\sigma} = \tilde{\boldsymbol{\sigma}}(\boldsymbol{\varepsilon}, \boldsymbol{\alpha}) \tag{3.45}$$

where $\boldsymbol{\alpha}$ represents the internal variables describing the material point state.

Assuming the definition of an accurate stress-strain relationship, the advantage of homogenized continuum models is that a coarse finite element mesh can be used,

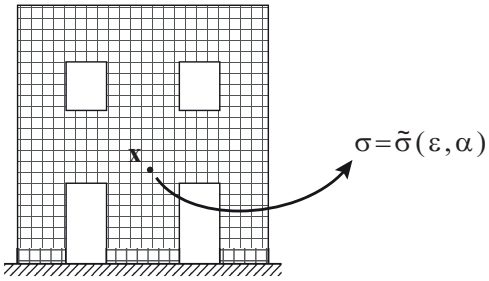

Figure 3.9: Homogenized continuum model.

with elements encompassing several bricks and joints. This leads to a lower computational burden compared to a more accurate microscale modeling, allowing its application even for large masonry structures. However, constitutive laws typically depend on numerous parameters that are difficult to retrieve from experimental tests on masonry specimens.

3.4.1 Nonlinear elasticity models

Nonlinear elasticity models treat masonry under the simplified assumptions of elastic material non-reacting in tension (Maier and Nappi 1990; Angelillo 1994; Lucchesi et al. 2008). Therefore, no internal variables are accounted in the model and the constitutive law reduces to

$$\boldsymbol{\sigma} = \tilde{\boldsymbol{\sigma}}(\varepsilon) \tag{3.46}$$

The solution of the boundary value problem relies on a problem of minimization of a potential with inequality constraints. Although several elegant solutions have been found in the literature for such a complex problem, this approach cannot simulate the post-peak behavior and the cyclic response of masonry structures, which is a strong limitation for a proper assessment of the seismic vulnerability.

3.4.2 Plasticity models

The use of plasticity models for masonry structure analysis can be justified based on experimental evidence. First of all, the shear-sliding mechanism exhibits the classic frictional behavior, characterized by the development of permanent displacements and a strength limit, which depends on transversal compression. Compressive crushing can also be modeled in a plasticity framework since the crushed portion of masonry can exhibit permanent compressive strains.

However, the interpretation of the tensile cracking as plastic is questionable. In fact, experimental tests show that, in case of tensile failures, either the blocks detach from mortar or a crack forms through blocks, leading to the creation of voids or macro-cracks. The interpretation of this mechanism through plasticity would generate permanent displacements in the numerical model that can lead to paradoxes. For instance, if we consider a cyclic tensile loading that activates plastic flow in the loading branch, the material would start reacting even at the beginning of the loading inversion, which contrasts with the stress-free crack opening/closure mechanism.

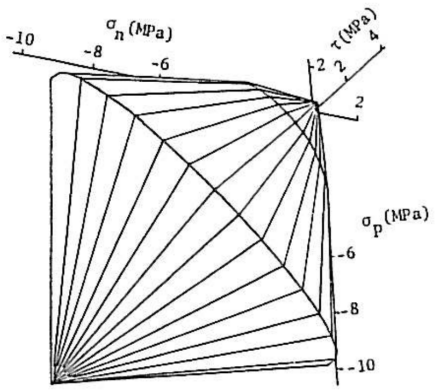

Figure 3.10: Yielding surface proposed by Page et al. 1985.

Nevertheless, many plasticity models have been developed in the literature for masonry structure analysis. One of the first significant papers was the one by Page et al. 1985. Previous experimental tests done on masonry specimens subjected to biaxial stress states (Page 1981) suggested a yielding surface composed of three elliptic cones in the σ_n-σ_p-τ space, where n and p are the axes respectively normal and parallel to mortar bed joints (Figure 3.10). Depending on the position of the stress state on the yielding surface, a failure mode was individuated among tension failure normal or parallel to bed joints, shear failure, and biaxial tension or compression; then, at each step of the iterative-incremental procedure, the tangent stiffness matrix and stress components were edited according to prescribed patterns depending on the failure mode. Plastic strain evolution was related to stress by power laws at all stress levels.

Lourenço, De Borst, et al. 1997 developed an orthotropic model in the framework of multisurface plasticity, with the yield function described as the composition of two different surfaces for the tensile and compressive behavior (Figure 3.11). The model was developed for the plane-stress case so that the non-zero components of the stress tensor are σ_x, σ_y, and τ_{xy} in a Oxy reference frame.

An orthotropic Rankine-type yielding function was considered for tensile stresses, namely

$$f_t = \frac{(\sigma_x - \sigma_{t,x}) + (\sigma_y - \sigma_{t,y})}{2} + \sqrt{\left(\frac{(\sigma_x - \sigma_{t,x}) - (\sigma_y - \sigma_{t,y})}{2}\right)^2 + \alpha\tau_{xy}^2} \quad (3.47)$$

where α is a parameter describing the effect of shear stresses on tensile yielding, and $\sigma_{t,x}$ and $\sigma_{t,y}$ are the yielding tensile stresses related to the material axes x and y, which degrade according to an exponential softening function as a function of a scalar internal variable κ_t.

The adopted failure surface in compression corresponds to a Hill-type yield function,

$$f_c = \frac{\sigma_x^2}{\sigma_{c,x}^2} + \frac{\beta\sigma_x\sigma_y + \gamma\tau_{xy}^2}{\sigma_{c,x}\sigma_{c,y}} + \frac{\sigma_y^2}{\sigma_{c,y}^2} - 1 \quad (3.48)$$

where parameters β and γ control respectively the coupling of normal stresses and shear contribution, and $\sigma_{c,x}$ and $\sigma_{c,y}$ are the compressive strengths along the

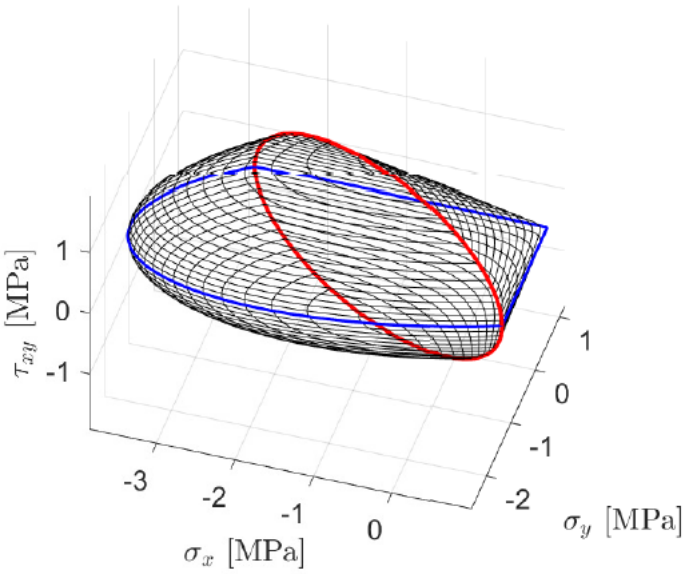

Figure 3.11: Composite yielding domain of Lourenço's model (Lourenço, De Borst, et al. 1997). The red and the blue lines represent respectively the intersection of the two yielding surfaces and the intersection of the domain with the $\tau_{xy} = 0$ plane.

material axes, depending on the hardening parameter κ_c according to a hardening-softening law.

Regularization of strain localization is done by introducing mesh-adjusted fracture energies, two (one in tension and one in compression) independent quantities for each material axis. More details will be presented in Chapter 6, devoted to the localization analysis of this model.

3.4.3 Damage models

Damage models can well represent masonry mechanics from a macroscopic point of view. Both tensile cracking and compressive crushing mechanism can be seen as a progressive weakening of a portion of the body.

The damage model proposed by Mazars et al. 2015, although originally formulated for concrete structures, has also been used for masonry structures (Facchini and Betti 2016; De Falco et al. 2018). The model is based on an isotropic formulation and a scalar damage variable, a function of two independent internal variables related to tensile and compressive damage. The constitutive law is given by

$$\boldsymbol{\sigma} = (1 - \omega)\, \boldsymbol{D}_e : \boldsymbol{\varepsilon} \tag{3.49}$$

The scalar damage parameter ω is defined by

$$\omega = 1 - \frac{(1 - A)Y_0}{Y} - A \exp(-B(Y - Y_0)) \tag{3.50}$$

where Y is the damage-driving variable and Y_0 is its initial threshold, given by

$$Y = r\,Y_t + (1-r)\,Y_c \tag{3.51}$$
$$Y_0 = r\,\varepsilon_{0t} + (1-r)\,\varepsilon_{0c} \tag{3.52}$$
$$\tag{3.53}$$

The triaxial factor r varies from 0 in case of triaxial compression to 1 in case of triaxial tension, and it is defined as

$$r = \frac{\sum_I \langle \bar{\sigma}_I \rangle}{\sum_I |\bar{\sigma}_I|} \tag{3.54}$$

where $\bar{\boldsymbol{\sigma}} = \boldsymbol{D}_e\,\boldsymbol{\varepsilon}$ is the so-called "effective stress", the subscript I denote principal components, and the Macauley brackets $\langle . \rangle$ denote the "positive part" operator. The variables A and B influence the shape of the damage evolution and are function of the triaxial factor r and four material parameters (A_t, A_c, B_t, and B_c). The variables Y_t and Y_c are the maximum values reached by the equivalent strains ε_t and ε_c during the loading process, given by

$$\varepsilon_t = \frac{I_\varepsilon}{2(1-2\nu)} + \frac{\sqrt{J_\varepsilon}}{2(1+\nu)} \tag{3.55}$$
$$\varepsilon_c = \frac{I_\varepsilon}{5(1-2\nu)} + \frac{6\sqrt{J_\varepsilon}}{5(1+\nu)} \tag{3.56}$$

where I_ε is the first invariant of the strain tensor and J_ε is three times the second invariant of the deviatoric part of the strain tensor, namely

$$I_\varepsilon = \varepsilon_1 + \varepsilon_2 + \varepsilon_3 \tag{3.57}$$
$$J_\varepsilon = \left[(\varepsilon_1 - \varepsilon_2)^2 + (\varepsilon_2 - \varepsilon_3)^2 + (\varepsilon_3 - \varepsilon_1)^2\right]/2 \tag{3.58}$$

The damage variable ω is different from 0 when one of the thermodynamic varibles (Y_t or Y_c) overcomes the corresponding initial threshold (ε_{0t} or ε_{0c}). Figure 3.12 shows the threshold of damage initiation of the Mazars model in the $\sigma_1 - \sigma_2$ plane for $\sigma_3 = 0$.

Berto et al. 2002 proposed an orthotropic damage model where damage was treated as a fourth-rank tensor. The stress-strain relation reads

$$\boldsymbol{\sigma} = (\boldsymbol{I} - \boldsymbol{\Omega}) : \boldsymbol{D}_e : \boldsymbol{\varepsilon} \tag{3.59}$$

The basic assumption of this model is the identification of material principal axes as principal axes of damage. The damage tensor $\boldsymbol{\Omega}$ depends on four independent damage parameters, accounting for damage in tension and compression in each principal direction. The exponential damage evolution is induced when the effective stress is outside of a limit surface of allowable stress states (Figure 3.13), which turns to be similar to the experimental limit surface obtained by Page et al. 1985 (Figure 3.10).

3.4.4 Smeared crack models

Another framework which is widely used for the homogenized continuum approach is the smeared crack model (Lotfi and Shing 1991; Pagani, Salvatori, et al. 2017;

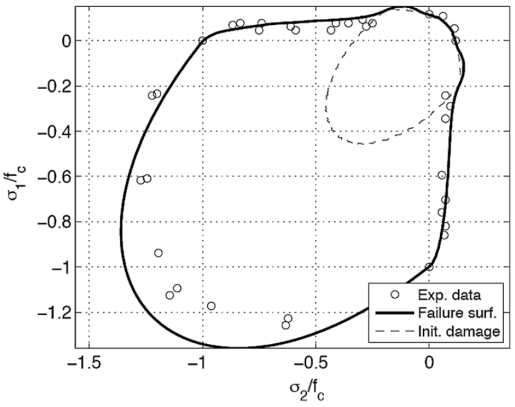

Figure 3.12: Threshold of damage initiation in the plane $\sigma_3 = 0$ (from Mazars et al. 2015).

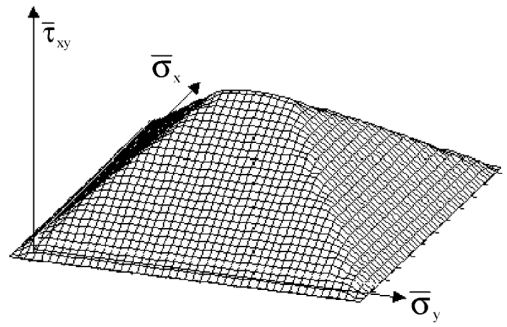

Figure 3.13: Limit surface assumed from the damage model proposed by Berto et al. 2002.

Billi et al. 2019) Similarly to plasticity, smeared crack models are based on the strain decomposition in elastic and inelastic part, which here are called cracking strain, namely

$$\boldsymbol{\varepsilon} = \boldsymbol{\varepsilon}_e + \boldsymbol{\varepsilon}_c \tag{3.60}$$

and the elastic strains are related to stress by generalized Hooke law

$$\boldsymbol{\sigma} = \boldsymbol{D}_e : \varepsilon_e \tag{3.61}$$

A crack opens when the maximum principal stress reaches the tensile strength f_t. Once a crack occurs, the material is considered orthotropic, having as orthotropy axes the normal and tangential directions of the crack surface.

Originally, the crack direction was assumed to remain fixed, and shear tractions across the crack were treated using the so-called retention factor (Suidan and Schnobrich 1973). To consider the possibility of developing several cracks with different directions, the multiple fixed crack model was formulated (Gupta and Akbar 1984). Later, the rotating crack model was proposed, which allows the formation of up to three mutually orthogonal cracks that keep aligned with the strain principal directions. Consequently, neither shear tractions nor shear crack strains appear in the formulation.

To understand the fundamentals of this model, let us consider the case of a single crack, having the vector $\boldsymbol{n}$ as normal. The corresponding crack strain tensor in tensorial notation reads

$$\boldsymbol{\varepsilon}_c = \varepsilon^c_{nn}\, \boldsymbol{n} \otimes \boldsymbol{n} \tag{3.62}$$

where ε^c_{nn} represents normal strain (in the sense of smeared crack opening) in direction perpendicular to the crack. The stress-strain law (3.61) turns into

$$\boldsymbol{\sigma} = \boldsymbol{D}_e : (\boldsymbol{\varepsilon} - \varepsilon^c_{nn}\, \boldsymbol{n} \otimes \boldsymbol{n}) \tag{3.63}$$

The key point of this model is to determine the unknown normal crack strain ε^c_{nn} at the integration point level from the cohesive law

$$\sigma_{nn} = f_t(\varepsilon^c_{nn}) \tag{3.64}$$

where $\sigma_{nn} = \boldsymbol{n} \cdot \boldsymbol{\sigma} \cdot \boldsymbol{n}$ is the normal traction on the crack plane and $f_t(\varepsilon^c_{nn})$ is the relation, identifiable by experiments, that links tensile strength to normal crack strains. The latter equation can be solved by the Newton method or even in closed form if the cohesive law is linear of piecewise linear.

The so-called Total Strain Rotating Crack model, implemented in the commercial software DIANA (Diana 2012), belongs to the latter-described framework, and it is the constitutive model used by the author for modeling of masonry piers through the homogenized continuum approach in Chapter 4 and 5.

3.4.5 Coupled damage-plasticity models

As discussed in the previous sections, some masonry failure mechanisms can be modeled in the plasticity framework and others through damage models. From a microscopic point of view, plasticity is due to intergranular displacements. It accounts for inelastic deformations during the loading process, and it can be used to model shear sliding and crushing mechanisms. On the other hand, damage is linked to the growth and coalescence of voids and microcracks that contribute

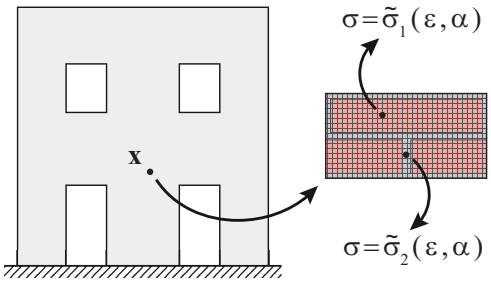

Figure 3.14: Microscale modeling.

to progressive material weakening, and it can well represent tensile cracking of masonry. Therefore, this calls for the use of models that combine the frameworks of damage and plasticity.

As on example, Addessi, Marfia, et al. 2002 developed a model where the mechanical properties degradation was taken into account through an isotropic damage scalar variable, which depends on two underlying variables describing the behavior in tension and compression. The model is completed by introducing plasticity effects. The plastic flow is controlled by the effective stress tensor and a yielding function characterized by isotropic hardening and different thresholds in tension and compression. The stress-strain law was postulated in the form

$$\boldsymbol{\sigma} = (1-\omega)^2 \, \boldsymbol{D}_e : (\boldsymbol{\varepsilon} - \boldsymbol{\varepsilon}_p) \tag{3.65}$$

The evolution of the damage variable ω is governed by the loading-unloading function which defines the damage limit domain. To regularize strain localization and avoid mesh-dependent results, a nonlocal model for the damage variable was proposed, based on the introduction of the damage Laplacian.

3.5 Microscale modeling

As already discussed, the prediction of the response of masonry is a challenging task. In fact, masonry is a heterogeneous anisotropic nonlinear material composed of two phases, bricks and mortar, characterized by different characteristics. Macroscale models can represent a valid approach, but their effectiveness relies on the definition of the constitutive law, which is not easy to formulate. It should phenomenologically reproduce the material mechanics, including tension cracking, shear sliding, compressive crushing, and many other aspects. Moreover, this approach requires a cumbersome identification of mechanical parameters that are not always easy to determine from basic experimental tests on the material.

To take into account role of each constituent and the effects of their interactions, a microscale model can be set up, where blocks, mortar joints, and mortar-block interfaces are represented explicitly (Figure 3.14). This detailed representation is suitable to model small masonry specimens as it requires large computation time.

However, the micromodeling approach can be used in multiscale simulations. The microscale model response can be used just to pre-calculate the parameters of a homogenized continuum model (Sejnoha et al. 2008; Cavalagli et al. 2011), or it

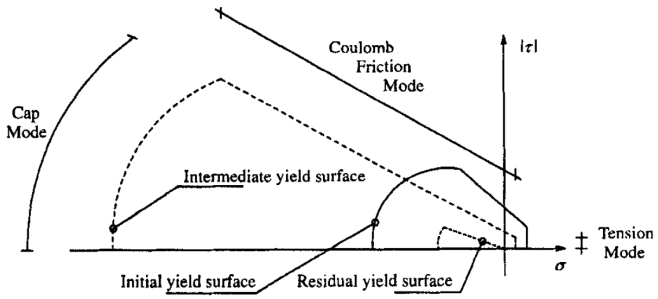

Figure 3.15: Interface cap model proposed by Lourenço and Rots 1997.

can be used simultaneously with a macroscale model which interactively obtains macroscopic stresses from the microscale during the analysis, realizing a proper multiscale model (Massart et al. 2007; Salerno and De Felice 2009; De Bellis and Addessi 2011).

The more direct approach for microscale modeling considers bricks and mortar as continua and requires a stress-strain law for each. A case in point is the model proposed by Massart et al. 2007 in which an isotropic damage model was adopted for both bricks and mortar. In the same spirit, a microscale model based on Rankine plasticity is proposed in Chapter 7.

However, the most common approach is to consider the mortar joints as an interface in which all the nonlinearities are concentrated, justified by the fact that they are the weakest component. This consideration leads to models where bricks are represented as linear elastic or rigid bodies, and the attention is focused on the formulation of the interface stress-strain law.

The interface model proposed by Gambarotta and Lagomarsino 1997 is based on damage mechanics, and it takes into account both mortar damage and brick-mortar decohesion. The interface mean strain is based on an additive decomposition of elastic and inelastic strains, where the inelastic contributions are the inelastic extension and sliding of the mortar joint. The inelastic strain evolution depends on two internal variables: the joint damage variable, which increases the opening and sliding compliances of mortar joints, and the shear strength, which is the internal force in the compressed joint limiting or locking the sliding. The interface model exhibits a brittle response under tensile stresses, and it is characterized by frictional dissipation and stiffness degradation under compressive stresses.

Lourenço and Rots 1997 developed an interface model in the framework of multisurface plasticity. The yielding domain was delimited by three surfaces devoted to capturing different failure mechanisms (Figure 3.15): a tension cut-off for tensile failure, a Coulomb-friction envelope for shear-sliding failure, and a cap model for crushing in compression. Exponential softening laws were adopted for tensile and shear yielding surfaces. In contrast, a parabolic hardening function followed by an exponential softening one was chosen to describe the evolution of the compressive surface. Although the adoption of plasticity for modeling tensile failure of masonry is questionable, as pointed out in Section 3.4, the model can reproduce the lateral behavior of masonry walls.

An interface model based on the combination of plasticity and damage was proposed by Minga et al. 2018. A multisurface plasticity criterion was considered,

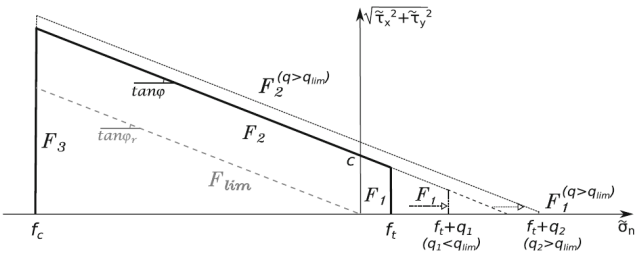

Figure 3.16: Multisurface yielding criterion proposed by Minga et al. 2018.

characterized by a Coulomb criterion limited by two caps, respectively, in tension and compression (Figure 3.16). The effects of strength and stiffness degradation are introduced through an isotropic damage tensor whose evolution is dictated on plastic work. Due to the algorithmic decoupling of plasticity and damage, no further local iterations are required after the plastic stress return, resulting in an efficient model that can be used even for relatively large masonry structures.

The model formulated by Salvatori and Spinelli 2018 considers a different constitutive behavior depending on the phase (cohesive, non-cohesive, crushed) in which the interface stands. Interfaces start in a cohesive phase where the stress-strain law is linear elastic. The transition from cohesive to non-cohesive phase is triggered at the violation one of three different conditions representing the elastic threshold for tension, compression, and shear. The non-cohesive phase is characterized by a nonlinear elastic behavior in the normal-to-interface direction, with compression limit and no tensile strength, and elastic-perfectly plastic behavior in the parallel-to-interface direction, with Mohr-Coulomb yielding criterion and non-associated flow. The transition to the crushed phase occurs when the deformation normal to the interface falls behind an ultimate threshold. Eventually, in the crushed phase, the interface does not transmit internal actions. A great advantage of this model is the requirement of a reduced number (seven) of mechanical parameters. Moreover, the interface kinematics follow a corotational approach that allows the treatment of large displacements and rotations of blocks while still considering small deformations of interfaces.

3.6 Remarks

This chapter is devoted to the review of mechanical models for masonry structure analysis. Since masonry is a heterogeneous material whose constituents dimensions strongly influence its mechanics, a refined representation would require the explicit modeling of its components. Enhancing the specimen size, however, the computational burden increases and can become unsustainable for large structures. At larger scales, in fact, masonry structure analysis needs simplified models to speed up computation and obtain manageable results. Therefore, several modeling techniques characterized by different detailing level rises in the literature.

The need for rapid and simplified computations of masonry buildings in professional practice led to the development of the equivalent-frame and the articulated quadrilaterals methods, both based on the subdivision of walls into macroelements.

The two methods require the assignment of proper mechanical behavior to each macroelement.

Restricting the attention to masonry piers of the EF method, two main modeling techniques can be found in literature: the beam approach and the multi-spring approach. The beam model features have been discussed, focusing on the difference between the displacement- and force-based beam formulations. Instead, multi-spring elements are based on a lumped approach, where both elasticity and nonlinearities are considered through nonlinear springs connected by rigid links. A few examples of the latter approach taken from the literature have been described.

Then, increasing the detailing level, masonry can be seen as a homogenized continuum. The effectiveness of these models relies on selecting a proper constitutive law that phenomenologically reproduces the microstructural mechanics. The chapter discusses several attempts performed by many authors in defining a suitable stress-strain relationship for masonry in the framework of nonlinear elasticity, plasticity, damage mechanics, smeared cracking, or coupled damage-plasticity.

However, only an explicit representation of the constituents can account for material heterogeneity and the interactions between masonry components. This consideration leads several authors to develop microstructural models, whose main characteristics have been discussed in the paper.

Chapter 4

Irregular Opening Layouts in Unreinforced Masonry Walls: Equivalent Frame and Finite Element Simulations

Abstract

The Equivalent-Frame (EF) method, compared to other modeling techniques, has advantages in terms of readability of results and computational efficiency. Since it is explicitly endorsed by building codes, it is widely used in the professional practice. However, in presence of irregularities in the layout of openings, a common circumstance in existing structures, it is difficult to univocally identify the equivalent frame and the reliability of the results obtained for the most irregular cases is doubtful. Here, the issue of irregularity is treated by comparing EF results with finite-element ones, which are assumed to better represent the actual behavior of irregular walls. An EF solver is developed, by using more refined failure criteria for the masonry piers and strength criterion for the spandrels than the oversimplified ones suggested by building codes. Automated procedures are used to perform a large number of analyses, in which EF results and finite-element ones are compared. The difference in terms of seismic vulnerability between the two models is correlated with a measure of the degree of irregularity of the walls. A geometric confidence factor, increasing with the degree of irregularity, is proposed to account for the epistemic uncertainties in the EF modeling.

4.1 Introduction

Seismic analysis of masonry buildings is often dealt with the equivalent-frame (EF) method (Magenes and Calvi 1996, Pugi 2000, Lagomarsino et al. 2013), where masonry piers and spandrels are modeled as one-dimensional elements representing

Figure 4.1: Examples of irregular opening layouts.

respectively columns and beams of the equivalent frame. Among others, the Italian Building Code (IBC 2008) suggests the adoption of this model for masonry structures, stating that "in the presence of coupling elements, the analysis can be performed by frame models, in which the intersections between vertical and horizontal elements can be considered as infinitely rigid". Compared to other modeling techniques, the EF method has advantages, both in terms of readability of results (for the familiarity that designers have with framed structures) and computational terms (for the reduced number of degrees of freedom of the models). For these reasons, EF is, to date, the most used modeling technique in professional practice. However, the method has intrinsic problems for structures with irregular geometric configurations such as misaligned openings or irregularities in their dimensions. These circumstances make the identification of a frame difficult or ambiguous. The IBC states that "ordinary masonry structures must have walls with vertically aligned openings" and that "in the absence of more accurate assessments, only wall portions that have vertical continuity from the level being tested to the foundation, shall be taken into account in the structural model". The IBC, therefore, sets limits only for one geometric irregularity type (for new buildings), and gives very restrictive modeling indications by requiring only the continuous ground-to-story portions of piers to be taken into account.

In the Italian building heritage, irregularities in the layout and size of the openings are widespread in both monumental and minor buildings (Fig. 4.1). In the presence of such irregularities, finding an equivalent frame may be difficult and arbitrary. Commercial computer programs based on EF modeling are often able to generate a frame from any wall with openings algorithmically. However, the reliability of the results obtained in the most irregular cases is doubtful.

In addition to the geometric problem of irregular walls (Parisi and Augenti 2013), the strength and failure criteria for piers and spandrels provided by building codes and implemented in commercial computer programs are an additional issue in the EF models. Some considerations on openings in infill walls are discussed in Margiacchi et al. 2016.

As to the piers, the ultimate displacement is a function of the panel height and the failure mode. It does not explicitly consider the aspect ratio of the wall, its static scheme, the material, or the axial loading. Moreover, the ultimate displacement exhibits a discontinuity at the transition between the failure modes as it jumps from 0.008 h in the case of flexural failure (0.006 h for existing buildings) to 0.004

h in the case of shear failure, being h the height of the pier.

As to the spandrels, the strength is evaluated very roughly by considering the spandrel as a 90-degree-rotated pier, despite the masonry orthotropy. Moreover, according to the IBC, the strength vanishes in the absence of tensile-resistant elements such as steel ties or reinforced concrete curbs. Finally, the IBC does not describe the post-peak behavior, whether it is fragile, with softening, or ductile (and in this case, to what amount).

As to the geometric irregularities of masonry walls, the following questions are addressed here:

- Should the results of equivalent-frame models be corrected in the presence of irregularity to account for the limits of this modeling approach in that case?
- Is it possible to define an applicability threshold for the equivalent-frame approach?

To answer these questions, the following scheme is followed:

1. A geometric measure of a wall irregularity level is proposed.
2. Each wall is modeled through nonlinear continuum (discretized by FEM) and EF approaches.
3. For a regular configuration, the parameters of both numerical models are calibrated so that their nonlinear static response in terms of stiffness, strength, and displacement capacity is equivalent to an experimental test used as a reference.
4. It is assumed that the nonlinear continuum approach is also valid in the presence of geometric irregularities.
5. The error of the EF in terms of capacity peak ground acceleration (PGA) is estimated as the difference between EF and FEM.
6. Automatic analyses are carried out to obtain a statistically significant number of analyses.
7. A correlation between the measure of irregularity and the corresponding EF error is sought.
8. Based on such correlation, a confidence factor on the EF predictions and a criterion for providing an applicability threshold are proposed.

Compared to a previous paper (Berti et al. 2017), this piece of work solves some issues by using an ad-hoc-developed software for the EF analyses to overcome the limits of commercial software and building codes highlighted above and to fully automatize the procedure, allowing a much larger number analysis so that statistically significant conclusions can be drawn.

The chapter is organized as follows. In Section 4.2, the proposed irregularity measure is recalled. In Section 4.3, the analysis procedure is presented. In Section 4.4, some details on the two numerical modeling techniques employed and the calibration parameters are provided. In Section 4.5, the results of two groups of analysis are shown. The first one is aimed to define the influence on the EF error of different kinds of irregularities; the second one consists of statistical analyses on a large number of randomly generated walls. The final result is a quantification of the correlation between irregularity measure and EF error. This relation is used

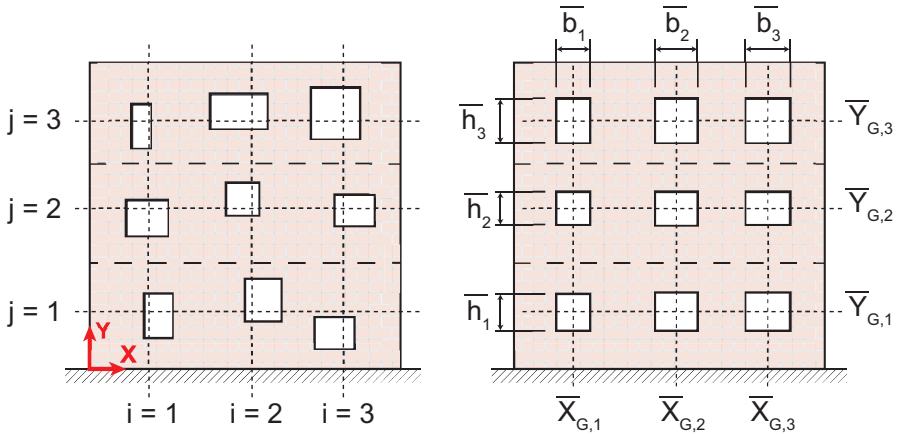

Figure 4.2: Wall with irregular opening layout (left) and its ideal regularization (right), which the irregularities are measured from.

to determine the modeling confidence factor, which aims to estimate the EF error based on the wall geometry only. Finally, some concluding remarks are reported in Section 4.6.

4.2 Irregularity measure

The recurring typologies of irregularities are identified as in Berti et al. 2017. A rectangular wall with N stories and M rectangular openings per story is considered. The levels are numbered from the ground ($j = 1$) to the top ($j = N$), vertical opening-alignments, from the left ($i = 1$) to the right ($i = M$). Considering a Cartesian reference frame, with origin in the lower-left corner of the wall, horizontal rightward X axis and vertical upward Y axis, let $(X_{G,ij}, Y_{G,ij})$ be the position of the centroid of the i-th level j-th opening, b_{ij} its width, and h_{ij} its height. To define irregularities and corresponding measures, we refer to an ideal regularized configuration of the openings (Fig. 4.2), where the alignments and dimensions of the openings are the means of the corresponding geometrical properties in the original irregular configuration.

Horizontal and vertical alignments are defined by

$$\bar{Y}_{G,j} = \frac{\sum_{i=1}^{M} Y_{G,ij}}{M} \qquad (j\text{-th horizontal alignment}) \tag{4.1}$$

and

$$\bar{X}_{G,i} = \frac{\sum_{j=1}^{N} X_{G,ij}}{N} \qquad (i\text{-th vertical alignment}) \tag{4.2}$$

and regularized opening widths and heights are

$$\bar{h}_j = \frac{\sum_{i=1}^{M} h_{ij}}{M} \qquad (j\text{-th story}) \tag{4.3}$$

and

$$\bar{b}_i = \frac{\sum_{j=1}^{N} b_{ij}}{N} \qquad (i\text{-th vertical alignment}) \tag{4.4}$$

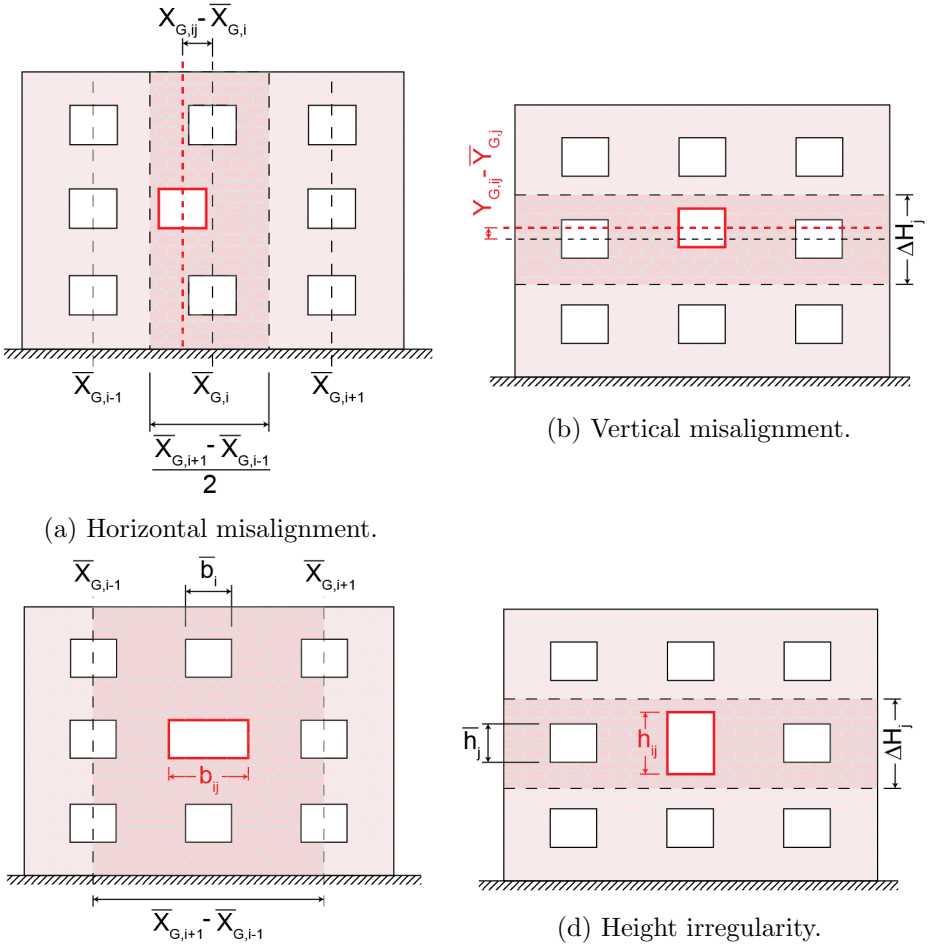

(a) Horizontal misalignment.

(b) Vertical misalignment.

(c) Width irregularity.

(d) Height irregularity.

Figure 4.3: Types of irregularity in opening layouts.

Horizontal misalignment (Fig. 4.3a) occurs when the centroid abscissa of an opening $X_{G,ij}$ differs from the vertical alignment of the i-th vertical opening array $\bar{X}_{G,i}$. The index measuring such misalignment can be estimated as the ratio between the absolute value of the actual misalignment, normalized with respect of the distance between the ideal vertical boundaries of the vertical opening array,

$$I_{X,ij} = \frac{2\,|X_{G,ij} - \bar{X}_{G,i}|}{\bar{X}_{G,i+1} - \bar{X}_{G,i-1}} \tag{4.5}$$

with the conventional assumptions $\bar{X}_{G,0} = -\bar{X}_{G,1}$ and $\bar{X}_{G,M+1} = 2L - \bar{X}_{G,M}$, being L the total width of the wall.

Vertical misalignment (Fig. 4.3b) occurs when the centroid ordinate of an opening $Y_{G,ij}$ differs from the horizontal alignment of the j-th story $\bar{Y}_{G,j}$. The index measuring the entity of such misalignment can be estimated as the ratio between the absolute value of the actual misalignment, normalized with respect to

the inter-story height ΔH_j, namely

$$I_{Y,ij} = \frac{|Y_{G,ij} - \bar{Y}_{G,j}|}{\Delta H_j} \tag{4.6}$$

Irregularity in width (Fig. 4.3c) occurs when an opening width b_{ij} differs from the average one of the i-th vertical opening alignment $\bar{b}_i$. The corresponding index may be assessed as the difference between those widths, rated in absolute value and normalized with respect of the distance between the adjacent vertical alignments

$$I_{W,ij} = \frac{|b_{i,j} - \bar{b}_i|}{\bar{X}_{G,i+1} - \bar{X}_{G,i-1}} \tag{4.7}$$

with $\bar{X}_{G,0} = 0$ and $\bar{X}_{G,M+1} = L$.

Irregularity in height (Fig. 4.3d) occurs when the opening height h_{ij} differs from the average one in the j-th story $\bar{h}_j$. The corresponding index may be assessed as the difference between the two heights, rated in absolute value and normalized with respect of the inter-story distance,

$$I_{H,ij} = \frac{|h_{i,j} - \bar{h}_j|}{\Delta H_j} \tag{4.8}$$

4.3 Analysis procedure

The EF method is the most used modeling technique in professional practice. Structural checks of masonry structures usually take advantage of the EF method combined with nonlinear static analysis through the N2 method (Fajfar and Fischinger 1988), as endorsed by numerous Building Codes.

The N2 method requires a nonlinear static analysis, where the structure is first subjected to vertical loading, say $\bar{\boldsymbol{f}}_0$, and then to a set of lateral forces, which mimic the seismic action. The lateral loading is proportional to a predefined force pattern, say $\bar{\boldsymbol{f}}$. Hence, the external forces acting on the structure are

$$\boldsymbol{f}_{ext}(\mu) = \bar{\boldsymbol{f}}_0 + \mu \bar{\boldsymbol{f}} \tag{4.9}$$

where μ is a scalar multiplier, which, during the process, must be set so that the displacement of a control node increases monotonically. The goal is to obtain a curve, also called the "push-over curve", which relates the control-node displacement d_c to the scalar multiplier μ. The structural capacity is then compared to the seismic demand according to a specific procedure that involves the equivalence to a single-degree-of-freedom oscillator.

In this chapter, the seismic vulnerability index taken as the reference is the peak-ground-acceleration capacity, for simplicity indicated as a_g in the following, defined as the minimum value of the peak ground acceleration that leads the structure to fail according to the N2 method.

Since masonry buildings can be assessed according to different modeling techniques, their seismic vulnerability can differ according to the modeling choice. The EF model may be affected by significant errors as it can overestimate the seismic capacity, in particular when it is applied to walls with irregular opening layouts.

In this chapter, we are concerned with determining the link, if any exists, between the index of irregularity, a function of the wall geometry, and the error made

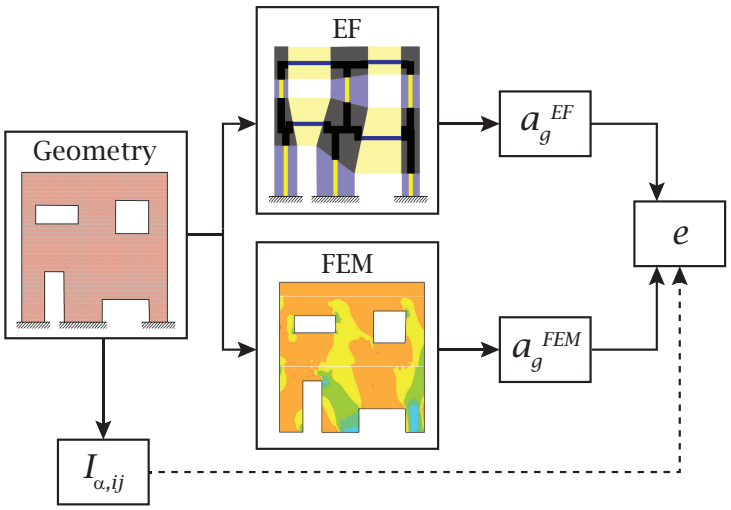

Figure 4.4: Scheme of the analysis procedure.

by the EF model on the seismic vulnerability. To this end, the procedure described below is used (Fig. 4.4).

Given a specific wall geometry, the irregularity indexes are calculated according to the method described in Section 4.2. The wall is analyzed through two modeling strategies: the EF method and the macromodeling technique, where masonry is treated as a homogenized continuum and the boundary-valued problem is solved by finite element discretization. Both models were initially calibrated on experimental data for a regular wall.

The error between the two models is evaluated under the assumption that the FEM model is an extension of the experimental results. Therefore, the difference between the two results can be taken to measure the EF error.

The procedure aimed to determine the EF error on a given-geometry wall has been automatized to perform numerous analyses and obtain statistically-relevant results through the Monte Carlo method. The automated procedure contains:

- A pre-processor, to calculate wall irregularity indexes and algorithmically generate meshes for the EF and FEM solvers;
- An ad-hoc-developed EF solver adopting improved pier and spandrel models;
- An input/output interface to the FEM solver;
- A post-processor, for obtaining, by N2 method, the corresponding seismic capacities, and the relative difference.

The main feature that has allowed to build the automated procedure is the development of the EF solver, which permits to be launched in batch mode, differently from what has been done in the previous paper on the same topic (Berti et al. 2017), where a commercial program that can be used only via the graphical interface was employed. Besides, the use of an ad-hoc-developed EF solver allows getting rid of the IBC doubtful prescriptions on piers and spandrels and the adoption of more refined strength and failure criteria taken from literature.

4.4 Numerical models

4.4.1 Reference experimental test

The numerical models have been calibrated on the experimental test results performed at the University of Pavia (Magenes, Kingsley, et al. 1995) on a full-scale two-story masonry building, consisting of four solid brick walls with 250 mm thickness, with plan dimensions 6.0 m x 4.4 m, and height 6.4 m (Fig. 4.5a). The seismic forces were simulated by the cyclic quasi-static application of four concentrated horizontal forces, through displacement-controlled screw jacks, applied at the two longitudinal walls at the floor levels. The amplitude of each cycle was progressively increased by controlling the wall drift, i.e., the top floor displacement divided by the height of the top actuator.

The structural response is summarized in plots of base shear versus top displacement (Fig. 4.5b). We restrict our attention to the wall "D", also known as Pavia Door Wall (PDW), which is taken as a reference for the model calibration. It is worth noting that PDW is not connected at the corners with the orthogonal walls, and it can be considered an isolated wall in the structure. The specimen was subjected to seven cycles, reaching a drift of 0.4%, corresponding to a top displacement of 23.08 mm. Cracks started forming at a drift of 0.1%, and the maximum base shear of about 150 kN was reached at a drift of 0.2%. Initially, cracks developed in the first-floor spandrels, decreasing the coupling between piers; eventually, spandrels stopped damaging, and the failure mechanism became the one dominated by diagonal-cracking shear in the central pier. At the maximum drift level, external piers failed in shear, exhibiting a diagonal crack only in one direction, due to the compression increase in the piers located downhill with respect to the horizontal force direction (Figure 4.5c).

4.4.2 Equivalent-Frame model

The Equivalent-Frame (EF) method relies on modeling a masonry wall with openings as a frame composed of columns and beams. Let us consider a wall with openings in a masonry building. By virtually extending the lines of opening edges, we can identify vertical and horizontal stripes of masonry, which are defined respectively as "piers" and "spandrels". The panels at the intersection of piers and spandrels are defined as "node" panels.

Once the subdivision of the masonry wall in macroelements is made, the reliable prediction of its overall behavior relies on the proper modeling of each member response. The nonlinear behavior is usually concentrated in piers and spandrels. Node panels are considered zones where damage cannot occur, and they are modeled as infinitely stiff and resistant. Therefore, the choice of the discretization scheme, namely the definition of the effective height of pier and spandrel elements plays a key role for the development of an EF model. Several solutions have been proposed in the literature.

FEMA 156 (FEMA 2000) adopted the "strong spandrels and weak piers" assumption, which allows to consider the pier height as equal to the ones of the adjacent openings, implying that spandrel have great rigidity and strength. Although it can be suitable for new constructions, this assumption seems not appropriate for existing structures, as highlighted in Siano, Sepe, et al. 2017.

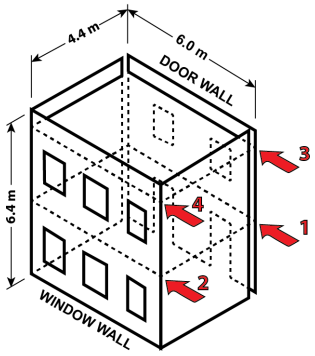

(a) Geometry of the experimental test.

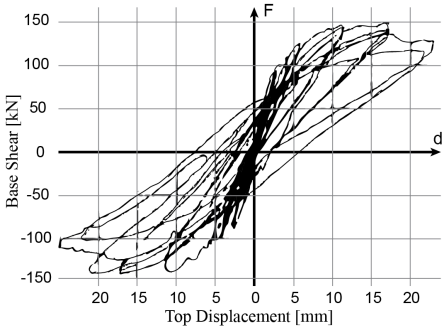

(b) Experimental cyclic response for the PDW.

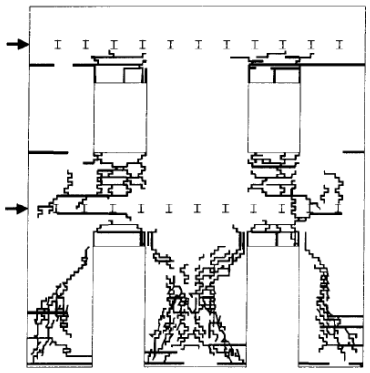

(c) Crack distributions at the end of the test for the PDW.

Figure 4.5: Experimental test on a full-scale masonry building (from Magenes, Kingsley, et al. 1995).

One of the widest-adopted criterion for EF discretization is the one proposed by Dolce 1991, which develops a simplified formula for the effective heights of piers, based on numerical and experimental tests. Dolce found that the effective height can be found by considering a line inclined of 30° starting from the adjacent openings.

Other methods have been proposed accounting for the seismic load direction. In fact, experimental evidences show that the effective portion of piers is determined by the opening located downstream with respect to the seismic action. The models proposed by Moon and coworkers (Moon et al. 2006) and Augenti (Augenti 2006; Parisi and Augenti 2013) take into account this issue. In their discretization methods, the effective height of a pier is defined as the height over which a compression strut is likely to develop. This leads to a different EF discretization depending on the seismic action direction.

Once the subdivision is made, we need to assign a proper constitutive model to each frame member. The simplest and the most common approach, which is implemented in a large number of EF solvers (Lagomarsino et al. 2013), is the piecewise-linear model, in which we first linearly compute the elastic internal forces through the Timoshenko-beam stiffness matrix. Then, some verifications are made aiming to correct the internal forces. It is checked whether the pier has reached the compression limit or a certain drift threshold, after which the pier is considered as collapsed. The internal forces are then corrected to prescribed cap values if certain strength criteria are exceeded.

The definition of proper strength and failure threshold is of central importance for predicting the overall response. However, some of the IBC criteria for the strength and failure of piers and spandrels are questionable. The drift capacity of masonry piers is defined as a fixed value depending only on the failure mode, i.e., 0.4% for panels failing in shear and 0.8% for rocking or toe-crushing. This leads to two issues.

The first one is related to the drift capacity overestimation of panels failing for crushing, which is predicted as double of a panel failing in shear. Contrarily, many analytical and numerical studies (see Chapter 5 and Orlando et al. 2016) show that for high compression loads, to which the crushing failure mode is associated, the drift capacity strongly decreases. The issue of displacement capacity is addressed also in other papers (Salvatori, Marra, et al. 2015, Salvatori, Marra, et al. 2017, Bartoli et al. 2017, Marra et al. 2017).

The second issue is related to the discontinuous variation of the pier ultimate drift as it exhibits a strong jump when the failure mechanism passes from shearing to flexural. Since masonry piers play a key role in determining the overall response, this leads to a strong variation of the drift capacity of the whole structure even for a small variation of boundary conditions or material properties, which is an undesirable characteristic.

Another controversial aspect of IBC prescriptions is the failure criterion for spandrels, considered as a pier rotated by a right angle. Moreover, no shear strength is associated with spandrels in the absence of tensile-resistant elements. In fact, experimental tests (Calderoni et al. 2011) show that spandrels have shear strength due to the activation of a diagonal strut, whose resistance can be limited by compressive strength (toe crushing) or by frictional shear strength (horizontal sliding failure) or by tensile strength in its middle zone (diagonal cracking).

Commercial EF programs have implemented the IBC criteria for piers and

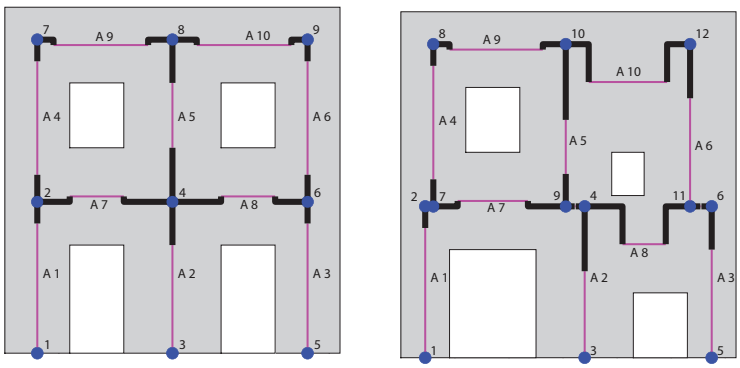

(a) Regular wall. (b) Irregular wall.

Figure 4.6: EF discretization.

spandrels, including the most questionable ones. Moreover, commercial programs do not usually allow their use in batch mode, as they can be launched only via the graphical interface. In contrast, for a study on the reliability of EF models in the case of irregular masonry walls, it is desirable to use an EF model characterized by:

- Reliable strength and failure criteria for piers and spandrels, preferably without jumps leading to strong response variations for small changes in the structure;
- The possibility to be launched in batch mode to perform many analyses and obtain statistically relevant results.

In this work, we have developed a new EF solver based on the linear beam model to address these issues. More refined strength and displacement criteria than those present in building codes and commercial programs have been introduced.

The EF discretization of masonry walls is based on the following rules. Beam nodes are defined at the intersections of the grid formed by storey heights and pier panel center lines. Pier and spandrels are modeled as beams constituted of three parts: two outer rigid offsets, which accounts for the infinitely stiff and resistant node panel, and a central deformable part, in which linearity and nonlinearity are concentrated. The deformable part direction is vertical for piers and horizontal for spandrels and it is located at the macroelement center. Appropriate transversal rigid offsets are inserted in case the spandrel axis does not coincide with the storey level. The deformable part of pier and spandrels between two openings is defined by the intersection of the beam axis with the virtual lines connecting the edges of the adjacent openings. In case the piers and spandrels are located on a wall edge, the effective length is defined by considering virtual lines which connect the opening edges to storey levels.

An example of application of the dicretization rules expressed above on a regular (PDW) and an irregular wall is shown in Figure 4.6.

The strength criteria for piers are the ones consolidated in the literature. Let us consider a panel of height H and shear span H_0, subjected to a compression load P, and let L and t be the in-plane and out-of-plane dimensions of the cross-section. The shear strength associated with flexural rocking and crushing mechanism is

given by

$$V_{r-tc} = \frac{P}{2}\frac{L}{H_0}\left(1 - \frac{\kappa P}{f_c\, t\, L}\right) \tag{4.10}$$

where f_c is the compression strength and $\kappa = 1/0.85$ is a coefficient that modifies the compression strength of masonry. For the shear mechanism, two different criteria are considered. The shear strength associated with bed-joint sliding is defined as

$$V_{bjs,IBC} = c\, t\, L' + \mu\, P \tag{4.11}$$

where c is the cohesion, $\mu = 0.4$ is the friction coefficient, and L' is the depth of the pier compressed area. The shear strength associated with the diagonal cracking mechanism is based on the Turnšek and Čačovič formulation, namely

$$V_{dc} = \frac{f_t\, t\, L}{b}\sqrt{1 + \frac{P}{f_t\, t\, L}} \tag{4.12}$$

where f_t is the tensile strength and b is defined as

$$b = \min\left(\max\left(\frac{H}{L}; 1.0\right); 1.5\right) \tag{4.13}$$

The adopted failure criterion of piers is based on the formulation proposed by Orlando et al. 2016, where the ultimate drift θ_u is expressed as a function of the aspect ratio $\lambda = H_0/L$ and the normalized axial compression of the panel $p = P/(f_c\, t\, L)$, namely

$$\theta_u = \frac{a_1 + a_2\,\lambda}{p^{a_3}} \tag{4.14}$$

where a_1, a_2, and a_3 are parameters accounting for the material composition of masonry and can be obtained by calibration on experimental tests.

A similar criterion has been recently proposed by Vanin, Penna, et al. 2020, who expressed the displacement capacity as

$$\delta_{u,i} = f_i(p) \cdot \left(\frac{H_0}{H}\right)^{\beta} \tag{4.15}$$

where the index i represent the dependence on the displacement capacity prediction of the strength mechanism which can be determined by shear or flexure, f_i is a user-defined function of the axial load ratio which can be different for the two strength mechanisms, H_0/H is the shear span ratio, and β is a constant.

The two models are similar, and this confirms the validity of two formulations as they both depends on the axial load ration and on the shear span H_0. Differently from the latter, Orlando's model explicitly defines the function $f_i(p)$ on which the displacement capacity depends, the shear span is normalized by the pier length L instead of the pier height H, and its contribution is given by a linear function instead of a power function.

The arched strut model proposed by Calderoni et al. 2011 has been adopted as the spandrel strength criterion. The model is based on the consideration that, under seismic actions, a compressed strut develops in the spandrel. The compressive force tends to diffuse in the middle of the panel and concentrate at its ends, forming a double-arch structure. Failure can occur either for toe crushing, due to excessive

compression at panel edges, or for tensile cracking, due to tension generated by the diffusion of compression loads in the middle of the panel.

The shear strength due to toe crushing is given by

$$V_{s,comp} = f_{c,h}\, t\, \bar{c}\, \tan\alpha \tag{4.16}$$

where $f_{c,h}$ is masonry compression strength in horizontal direction, $\bar{c}$ is the length of the reaction zone which, under the assumption of uniform distribution of compressive stresses, is given by

$$\bar{c} = H - 2e \tag{4.17}$$

and $\tan\alpha = 2e/L$ is the inclination of the diagonal strut axis, where e is the strut eccentricity and L is the spandrel length. Since the possible directions α satisfying spandrel equilibrium are infinite, its definition would require a consistency condition. The authors observed from numerical simulations that the strut direction α is function of the panel geometry only, and gave the following expression

$$\tan\alpha = \frac{2e}{L} = \frac{9H - L}{10L} \tag{4.18}$$

where H is the in-plane cross-section dimension. Obviously, for high, slender spandrels, namely $L > 9H$, the eccentricity e is set to zero, and the shear strength vanishes. Substituting (4.17) and (4.18) into (4.16), we get

$$V_{s,comp} = f_{c,h}\, t \frac{(H + L)(9H - L)}{100L} \tag{4.19}$$

which defines the spandrel shear strength due to toe crushing as a function of the horizontal compression strength and its geometry.

The tensile cracking mechanism is explained by modeling the spandrel as a double-arch structure. The strut compression load is seen as the thrust of two arches subjected to a distributed load. The limit value of the arch thrust is obtained when the distributed load reaches the masonry tensile strength. The resulting shear strength is given by

$$V_{s,tens} = f_{t,d} \frac{t\, L^2\, \sin\alpha}{4\, f\, \cos^2\alpha} \tag{4.20}$$

where $f_{t,d}$ is the tensile strength in diagonal direction, which depends, among other factors, on masonry texture. The arch height f can be expressed as

$$f = k\, \frac{H}{2} \cos\alpha \tag{4.21}$$

where k is a coefficient to be determined on the basis of experimental tests, and in general can be taken as 0.70.

Eventually, the spandrel shear strength V_s is the minimum value between the strength associated to two mechanisms, namely

$$V_s = \min\left(V_{s,comp}\ ;\ V_{s,tens}\right) \tag{4.22}$$

A standard incremental-iterative procedure in indirect displacement control is used for the nonlinear static analyses.

4.4.3 Homogenized continuum model

A more refined model has been chosen to assess the reliability of the EF method for irregular walls. Masonry is treated as a homogenized continuum, and the boundary value problem is solved by the finite element method. In the following, we refer to this kind of modeling with the FEM acronym (as "Finite Element Model").

Walls are discretized by 8-node plane-stress isoparametric quadrilateral elements. The Total Strain Crack Model has been chosen as constitutive law. It belongs to the framework of smeared rotating crack models, where up to two cracks (in two dimensions) can develop, where the crack directions keep aligned with the principal strain directions. The model accounts for both material cracking and crushing through the definition of tensile and compressive stress thresholds. The tensile behavior is assumed with linear softening, while the compressive behavior has a parabolic hardening/softening, both based on fracture energies related to a crack bandwidth.

Nonlinear static analyses were performed using an arc-length incremental procedure, modified Newton-Raphson iterative method, and an energy-based convergence criterion. The pushover curve is obtained by monitoring the displacement of the second story centroid versus the base shear.

4.4.4 Model calibration

The EF and FE models are calibrated on the Pavia Door Wall so that the key parameters of the piecewise linear curves (stiffness, strength, and ultimate displacement) are the closest possible to the ones obtained from the shear-displacement curve of the experimental test.

The mechanical parameter for the EF model obtained from the calibration are: a Young modulus $E = 787$ MPa, a compressive strength $f_c = 1.16$ MPa, a tensile strength $f_t = 0.08$ MPa. The parameters $a_1 = 0.0017$, $a_2 = 0.0013$, and $a_3 = 0.82$ related to the drift capacity criterion have been obtained from a numerical calibration on a set of nine masonry piers having different compression loads and aspect ratios. The horizontal compressive strength is taken as $f_{c,h} = f_c/2$ and the diagonal tensile strength is considered equal to f_t.

Figure 4.7a shows the failure pattern of the EF model at the end step, where solid squares at the beam ends represent flexural inelasticity, while double dashes in beam center, shear inelasticity; yellow color denote sections outside the elastic limit, red, sections at failure. The figure shows that failure occurs due to bending in the central and downhill first-story piers (the seismic action is directed to the right).

FE model calibration leads to $E = 1029$ MPa, $f_c = 1.18$ MPa, $f_t = 0.08$ MPa, a compressive fracture volume energy $G_c/h = 40$ kJ/m^3, being h the crack bandwidth size, and a tensile fracture area energy $G_t = 70$ J/m^2. Figure 4.7b shows the compressive principal stresses pattern at the last step of the analysis, from which we can see the formation of two struts in the central and right first-story piers.

Figure 4.8 shows, from left to right, the shear-displacement curves and the corresponding outlines as piecewise linear curves of the experimental test, the EF and the FE models, respectively. The parameters of the piecewise linear curves are reported in Table 4.1.

To ensure that the EF model can effectively reproduce the lateral behavior of regular walls, other four tests on various geometries have been carried out. The

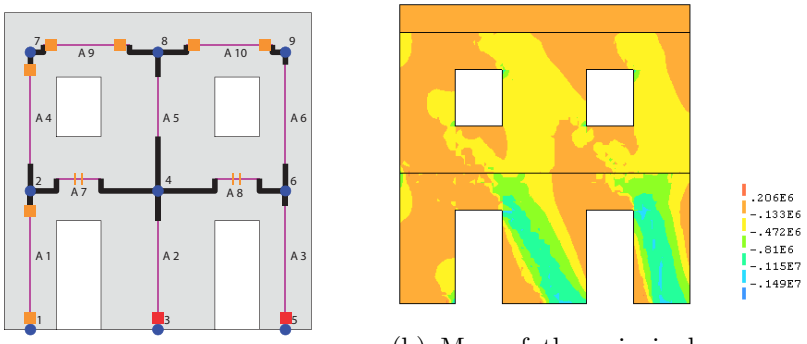

(a) Failure pattern at the last step in the EF model.

(b) Map of the principal compression stresses at the last step of the analysis in the FE model.

Figure 4.7: Calibration of the numerical models on the PDW.

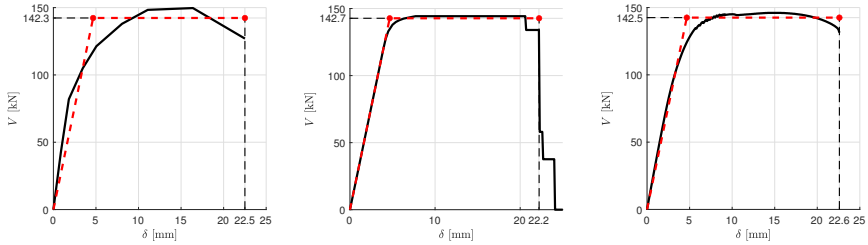

(a) Experimental test. (b) EFM. (c) FEM.

Figure 4.8: Pushover curves for PDW.

	K_s [kN/mm]	V_y [kN]	δ_u [mm]
Exp. Test	30.5	142.3	22.5
EFM	30.6 (+0.3%)	142.7 (+0.3%)	22.2 (-1.3%)
FEM	30.5 (+0.0%)	142.5 (+0.1%)	22.6 (+0.4%)

Table 4.1: Bilinear curve parameters of numerical models compared with PDW test.

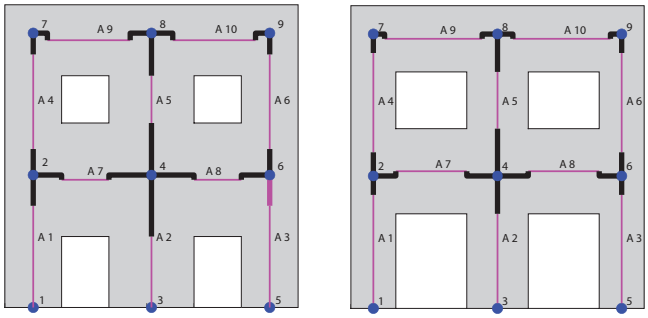

(a) Test 1.

(b) Test 2

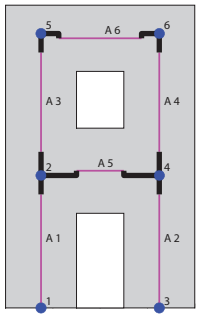

(c) Test 3.

(d) Test 4.

Figure 4.9: Tests on regular walls - Geometries.

mechanical parameters of both models are kept equal as the ones obtained from the calibration on the Pavia Door Wall.

The first two tests have been performed on regular walls based on the Pavia Door Wall where the opening dimensions have been slightly changed. Test 1 (Figure 4.9a) is characterized by the heights of the doors and windows of 1.5 m and 1.0 m instead of 2.0 m and 1.2 m, respectively; Test 2 (Figure 4.9b) has the opening width of 1.5 m instead of 1.0 m. Test 3 (Figure 4.9c) is characterized by having just one opening per storey and by a smaller wall width so that the pier length is kept equal as the one of the piers of the Pavia Door Wall. Test 4 (Figure 4.9d) is based on a single pier of height H=2.5 m, length L=1.25 m, thickness t=0.32 m, subjected to a vertical load of 56 kN (p=0.125), under a double-bending static scheme.

Figure 4.10 shows the maps of minimum principal stresses at the last step of the analyses in the FE model, where red color corresponds to zero and blue color corresponds to compression strength f_c. Figure 4.11 shows the comparison of the response of the EF and FE model in terms of shear-displacement curves for Tests 1-4. The parameters of the piecewise linear curves and the corresponding PGA capacity are reported in Table 4.2. These results demonstrate that the EF model can well reproduce the lateral response of regular masonry walls.

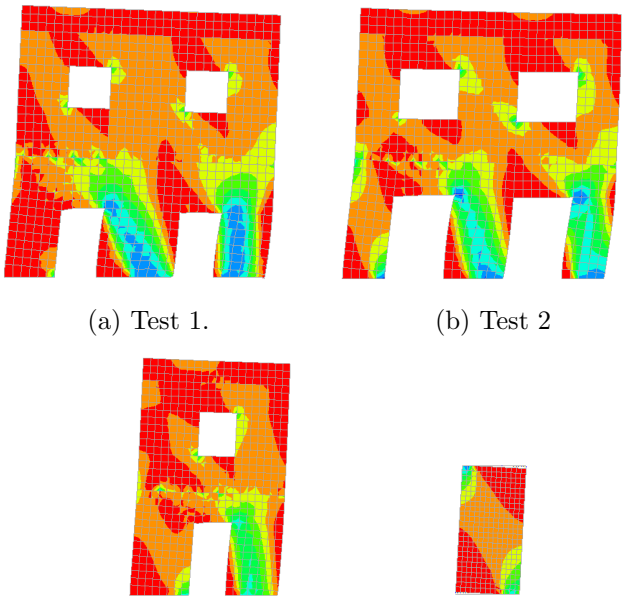

(a) Test 1. (b) Test 2

(c) Test 3. (d) Test 4.

Figure 4.10: Tests on regular walls - Minimum principal stresses.

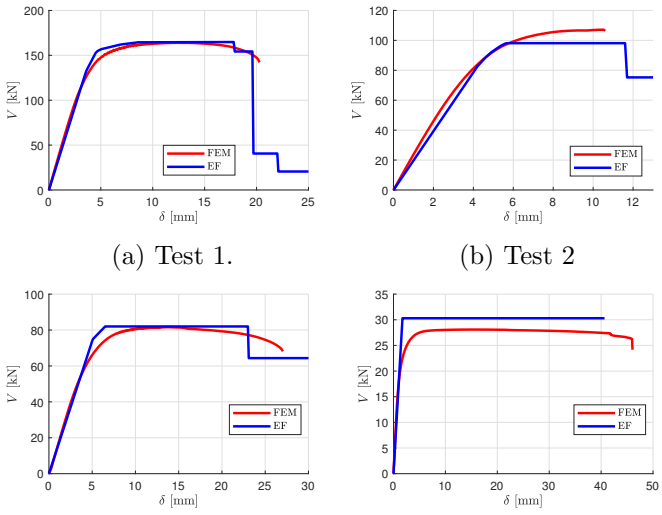

(a) Test 1. (b) Test 2

(c) Test 3. (d) Test 4.

Figure 4.11: Tests on regular walls - Pushover curves.

	K_s [kN/mm]			V_y [kN]		
	FEM	EFM	Err.	FEM	EFM	Err.
Test 1	36.99	36.97	-0.1%	159.0	161.9	+1.8%
Test 2	21.04	19.65	-6.6%	103.6	97.5	-5.9%
Test 3	14.43	14.77	+2.4%	78.4	81.8	+4.3%
Test 4	15.94	17.50	+9.8%	27.6	30.3	+9.7%

	δ_u [mm]			$a_{g,c}$ [m/s^2]		
	FEM	EFM	Err.	FEM	EFM	Err.
Test 1	20.28	19.62	-3.3%	2.71	2.65	-2.2%
Test 2	10.6	11.69	+10.2%	1.14	1.16	+1.8%
Test 3	27.03	23.09	-14.6%	2.54	2.27	-10.6%
Test 4	46.04	40.66	-11.7%	10.16	9.82	-3.3%

Table 4.2: Tests on regular walls - Parameters of the piecewise linear curves.

4.5 Results on irregularities

4.5.1 Calibration of the irregularity-error model

In Section 4.2 we have quantitatively defined four kind of geometric irregularities, that are horizontal ($I_{X,ij}$) and vertical ($I_{Y,ij}$) misalignment, and irregularity in width ($I_{W,ij}$) and in height ($I_{H,ij}$), where the subscript ij refers to the opening located at the row i, with $i \in \{1, ..., M\}$, and column j, with $j \in \{1, ..., N\}$. Each irregularity index may differently influence the error committed by the EF method. Moreover, the same irregularity type may have different importance depending on the opening ij with respect to which is computed. Therefore, it is worth investigating the influence of each irregularity index type applied to each of the four openings of the reference specimen. The aim is to find a relation between these indexes and the error committed by the EF method on an irregular masonry wall, which we define as

$$e = \frac{|a_g^{EF} - a_g^{FEM}|}{a_g^{FEM}} \tag{4.23}$$

where a_g^{EF} and a_g^{FEM} are the PGA capacity estimated by the N2 method (Fajfar and Fischinger 1988), using the capacity curves obtained by the EF method and the finite element model (FEM), respectively.

A group of analyses is performed by varying a single irregularity for each of the PDW four openings. For each case, the analyses have been repeated by increasing the irregularity magnitude in subsequent steps. The results obtained can be summarized in sixteen graphs (four types of irregularities for each of the four wall openings) showing the error e as a function of the irregularity indices. As an

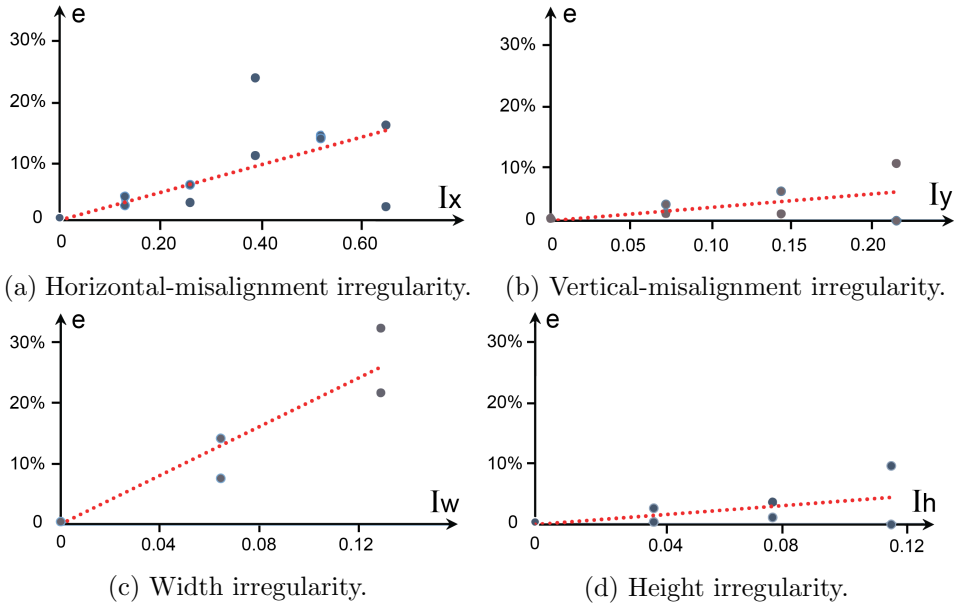

(a) Horizontal-misalignment irregularity. (b) Vertical-misalignment irregularity.

(c) Width irregularity. (d) Height irregularity.

Figure 4.12: Linear regression on data for the different irregularity type on the first-level uphill opening ($i = 1, j = 1$).

example, the results obtained for the ground floor opening positioned uphill of the seismic action are reported in Fig. 4.12.

The error grows as the anomaly increases, as shown by linear regressions performed on the vulnerability prediction error. The different slopes of the regressions indicate that each type of irregularity on each opening affects the global error with a different intensity. In Figure 4.13 and Table 4.3, we represent the slope values of the sixteen graphs obtained in the first group of analyses. The figure shows that the most significant irregularities are mainly those in width for the openings at the ground level and secondarily those in height for all the openings.

As the results show linear influence trends of each anomaly on the error, it is natural to define the relation between the error e and the irregularity indices $I_{\alpha,ij}$ as

$$e = \frac{1}{M}\frac{1}{N}\sum_{i=1}^{M}\sum_{j=1}^{N}\sum_{\alpha\in\{X,Y,W,H\}} w_{\alpha,ij} I_{\alpha,ij} \tag{4.24}$$

where $w_{\alpha,ij}$ are the trend line slopes that act as weights that calibrate the influence of each irregularity index on the error. Then, the error results to be defined as a weighted linear combination of the irregularity indices.

4.5.2 Statistical analysis

The application of the EF method to masonry walls characterized by an irregular layout of openings is questionable, as discussed in the previous sections. The seismic vulnerability assessment performed through the EF method may then be affected by errors. Nevertheless, it can be useful to find a way to keep analyzing irregular

	Opening ij			
	11	21	12	22
I_X	0.227	1.759	0.303	0.271
I_Y	0.220	0.368	0.097	0.206
I_W	2.024	1.185	0.197	0.072
I_H	0.417	0.673	0.722	0.597

Table 4.3: Trend line slope values for each opening and each kind of irregularity.

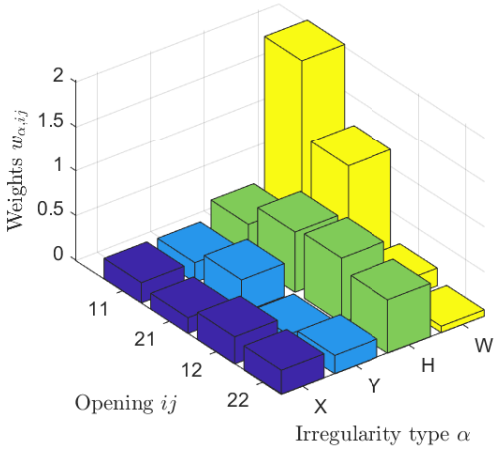

Figure 4.13: Trend line slope values for each opening and each kind of irregularity.

masonry structures through the EF method since it is the most used model in professional practice.

In the previous section, a relation (Eq. 4.24) between the error e committed by the EF method and the irregularity indices $I_{\alpha,ij}$ has been proposed. The linear combination weights $w_{\alpha,ij}$ have been calibrated on the PDW varying each irregularity type for each opening. Under the assumption that the relation (4.24) is valid in general, we can predict the error e committed by the EF method compared to a more refined model.

Proposal of a confidence factor on geometry

For irregular geometries, the EF model can still be used as long as the computed seismic response does not overestimate the more reliable one obtained with more refined models. The idea is to penalize the seismic vulnerability computed by EF according to the error due to geometric irregularity predicted by (4.24). We can define a "geometric confidence factor" as

$$FC_G = 1 + e \tag{4.25}$$

and correct the vulnerability computed by EF as

$$a_{g,mod}^{EF} = \frac{a_g^{EF}}{FC_G} \tag{4.26}$$

The geometric confidence factor FC_G is conceived in analogy to the confidence factors on the mechanical parameters of materials in existing buildings, which are already present in building codes and accounts for the epistemic error of the analysis method. Unlike the material confidence factor, which is aimed to modify material strength design values, the correction through FC_G is made at the end of the analysis by penalizing the vulnerability.

Validation of the proposed approach

A second group of analyses has been designed to test the effectiveness of the confidence factor definition. A total of 600 randomly-generated geometries have been studied through both the EF method and the finite element model. The high number of analyses was aimed to obtain statistically-relevant results through the Monte Carlo method.

The generated geometries are characterized by the same total length L, total height H, and the number of stories and openings of the PDW. The opening size and position have been randomly varied according to uniform distributions (Fig. 4.14). The variation intervals of opening positions and dimensions have been chosen in such a way as to keep openings within the wall and avoid opening overlapping.

Each randomly-generated geometry has been analyzed through the EF and FE method, and the PGA vulnerabilities through the N2 method have been computed (respectively a_g^{EF} and a_g^{FEM}). The 600 analysis results have been represented in a $a_g^{EF} - a_g^{FEM}$ diagram. The point cloud of the analysis series is represented in Figure 4.15a. The line whose slope represents the median of the ratio a_g^{FEM}/a_g^{EF} almost lies on the bisector of the axes, which means that approximately 50% of the EF predictions are on the unsafe side (excessive estimate of the capacity PGA by EF compared to FEM). By correcting the EF predictions by the confidence factor as in

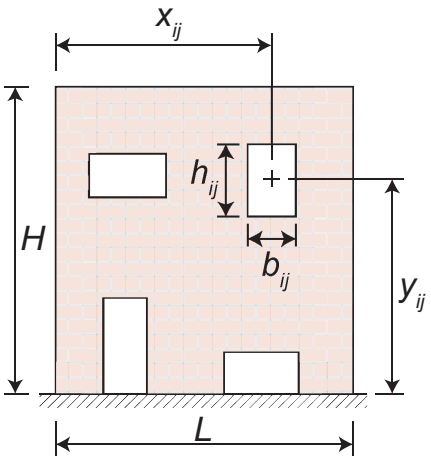

Figure 4.14: Walls with random distribution of openings.

(4.26), the point cloud moves, as shown in Figure 4.15b. After the correction, the cloud is above the quadrant bisector, the safe-side area for EF model analyses. In particular, the fractile 84% of the point cloud is over the quadrant bisector, which means that only a small portion of EF predictions are unsafe. After the correction introduced, the probability $P(a_g^{EF} > a_g^{FEM})$ to have an unsafe estimate by EF drops from 0.53 to 0.10. Moreover, the variation coefficient of the ratio a_g^{EF}/a_g^{FEM} decreases from 22.9% to 18.3%, indicating that the most irregular structures are corrected more effectively, i.e., the proposed confidence factor acts selectively. Both facts are also evident in the graph of Fig. 4.16, where the probability densities of the ratio a_g^{EF}/a_g^{FEM} before (in blue) and after (in red) the correction are represented.

4.6 Remarks

The issue of irregularity was treated by comparing equivalent-frame results with finite-element ones, which are assumed to represent the actual behavior of irregular walls better. The strength and failure criteria for piers and spandrels, provided by building codes and implemented in commercial computer programs, represent an issue in the EF models. This was overcome by developing an equivalent-frame solver implementing more refined criteria for the failure of masonry piers and strength for the spandrels than the oversimplified ones suggested by the building codes. For a regular configuration, the EF and FEM model parameters are calibrated so that their nonlinear behavior in terms of stiffness, strength, and displacement capacity is equivalent to an experimental test used as a reference. Automated procedures were used to perform a large number of analyses that are divided into two groups. The first group was intended to determine the influence of each index of irregularity and each of the wall opening on the capacity PGA error. This allowed obtaining an estimate of the error as a function of the irregularity level. The second group of analyses was designed to test the effectiveness of the proposed epistemic confidence factor. It has been shown that by correcting the capacity PGA predictions of the equivalent frame method by the proposed confidence factor, we obtain safer results

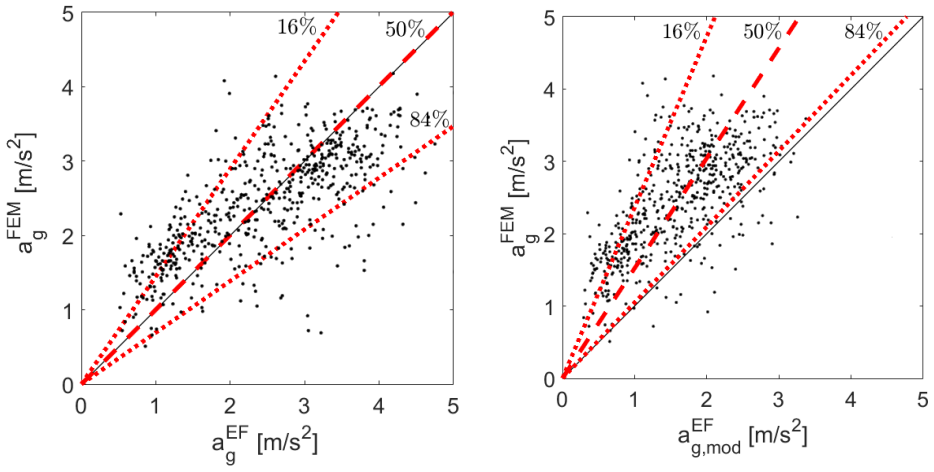

(a) Before the correction by the geometric confidence factor.

(b) After the correction by the geometric confidence factor.

Figure 4.15: Seismic vulnerabilities predicted by EF and FEM.

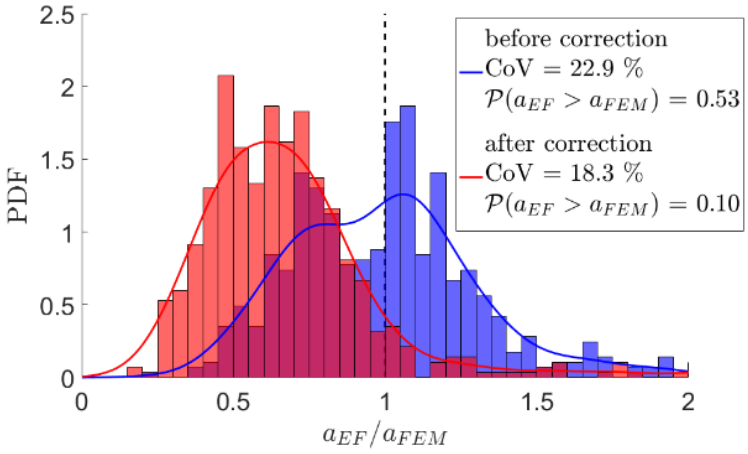

Figure 4.16: PDF of the vulnerability ratios before and after the application of the epistemic confidence factor.

(that would be obvious by considering a factor greater than one) and also less dispersed. This means that the correction acts selectively on the most irregular structures. The most important achievements of this chapter compared to previous publications on the same topic are:

- The development of an equivalent frame solver, which allows getting rid of IBC limits for piers and spandrels by introducing appropriate strength and failure criteria, as well as the ability to automate the analysis (commercial programs do not allow to be launched in batch mode but only via the graphical interface).
- The automation of continuous analysis performed via commercial FEM software whose input and output are generated and post-processed automatically by an ad hoc algorithm for the statistical analyses.

Some aspects still need to be explored in more detail.

Differently from other papers on the same field (Siano, Sepe, et al. 2017; Siano, Roca, et al. 2018) which have compared the results of EF models using different discretization proposals, in this work the discretization scheme is not considered as a variable. It might be interesting to evaluate the different responses of irregular masonry walls by using EF models varying the discretization scheme.

Another open aspect to consider is the influence of the seismic load direction. In this work, seismic vulnerability of each wall, characterized by a given random irregular geometry, has been assessed by considering just one direction of the seismic action. However, the masonry wall response can be different changing the seismic action direction. A case in point is the different influence of the variation of the dimensions of up-hill or down-hill openings on the EF error, as shown in Figure 4.13.

An interesting extension of this work can be the evaluation of the lateral response of irregular masonry walls considering both the possible seismic load directions. In this case, the wall seismic vulnerability is evaluated as the minor of the two directions. Moreover, another variable to evaluate can be the use of a different discretization scheme which accounts for the seismic direction (Moon et al. 2006; Augenti 2006; Parisi and Augenti 2013).

Chapter 5

Nonlinear Static Behavior of Masonry Piers Through Numerical Analysis

Abstract

Nonlinear static analysis through Equivalent-Frame models has become a standard for the seismic vulnerability assessment of masonry structures. In this approach, the modeling effectiveness relies on a proper definition of each macroelement composing the equivalent frame. However, the pier model endorsed by several building codes is highly simplified and does not consider the influence on the displacement capacity of the aspect ratio and the vertical load, which play an important role as testified by experimental tests. In this chapter, the nonlinear static behavior of masonry pier is studied through numerical analyses on a model that has been calibrated on experimental tests. A parametric analysis, varying the aspect ratio and the actual compression-to-compressive strength ratio, are performed to explore pier response in a large range of conditions, and the relations between the nonlinear static quantities, namely lateral stiffness, shear strength, and displacement capacity, and the parameters that influence them are obtained and discussed.

5.1 Introduction

Nonlinear static analysis has become a standard procedure for the seismic vulnerability assessment of masonry structures. The analysis is carried out by increasing a predefined pattern of horizontal static forces in indirect displacement control. Then, the displacement capacity obtained from the pushover analysis is compared with the displacement demand to perform the structural vulnerability assessment.

While local effects, such as the out-of-plane vulnerability of walls, are studied with specific models such as limit analysis (Shawa et al. 2012; Doherty et al. 2002; Abrams et al. 2017), the Equivalent-Frame model, generally used in combination with nonlinear static analyses, is still the most used and implemented in commercial

software for global vulnerability assessment (Quagliarini et al. 2017). Reasons for its diffusion are the simplicity of interpreting the results, the fact that the model is based on simplified hypotheses and defined by few mechanical parameters, and its computational efficiency due to the small number of degree of freedom compared to other types of modeling. Moreover, it is also explicitly suggested by some building codes, such as ASCE 41 (Pekelnicky and Poland 2012), Eurocode 8 (EN 1998-3 2005) and the Italian Building Code (IBC 2018). Nevertheless, the rough approximation deriving from interpreting the masonry wall as a frame leads obviously to some issues. A case in point is when the analysis deals with masonry walls with opening layout irregularities. In this case, the reliability of Equivalent-Frame models is questionable since the seismic vulnerability assessment can be badly overestimated (Parisi, Sabella, et al. 2015; Berti et al. 2017; Siano, Sepe, et al. 2017; Pagani, Salvatori, et al. 2017).

According to the Equivalent-Frame model, masonry walls are discretized in three types of panels: piers, spandrels, and node panels. While node panels are considered to have infinite stiffness and strength, piers and spandrels are usually schematized as two-node standard beam elements connected through rigid braces. The elements often present lumped inelasticity localized at the end of the piers and/or spandrels (Lagomarsino et al. 2013; Magenes 2000). In other cases, it can be used a spread nonlinearity approach (Belmouden and Lestuzzi 2009). The effectiveness of Equivalent-Frame models relies on choosing a proper constitutive model of masonry piers and spandrels. The shape of the shear-drift diagram of experimental tests on masonry piers suggests the lateral behavior approximation as a piece-wise linear curve, with a first linear elastic branch followed by a constant-force one. Other authors have adopted multilinear relationships through progressive strength decay in correspondence of assigned drift values (Cattari, Lagomarsino, et al. 2008).

According to this kind of schematization, the lateral behavior of a masonry pier is defined by only three parameters: the lateral stiffness k_s as the slope of the first branch, the shear strength V_y as the ordinate of the second one, and the ultimate displacement δ_u as the abscissa where the second branch ends. The lateral stiffness is estimated by considering the lateral stiffness of the Timoshenko's beam with a reduction of 50% of the elastic moduli. This reduction is aimed to make sure that the lateral stiffness models the secant stiffness of the respective experimental test. The shear strength of a pier is considered as the minimum strength among four failure mechanisms: rocking, crushing, bed-joint sliding, and diagonal cracking. The estimation of the pier displacement capacity, which plays a key role in determining the displacement capacity of the whole structure, is often treated simplistically by building codes. In fact, it is based only on the pier height and failure mode; it does not take into account other important parameters such as the aspect ratio and the compression ratio (Frumento, Magenes, and Morandi 2009; Orlando et al. 2016).

The study of pier seismic behavior through experimental tests has been developed during the last three decades. The experimental test of reference is the shear-compression test (Figure 5.1). A masonry pier is put on a rigid concrete foundation and subjected to actions imposed by three servo-hydraulic actuators on a stiff steel beam positioned on the pier top (Wilding, Dolatshahi, et al. 2018). Two vertical actuators control the top boundary conditions and the vertical load, maintained constant during the test. The horizontal actuator imposes the hori-

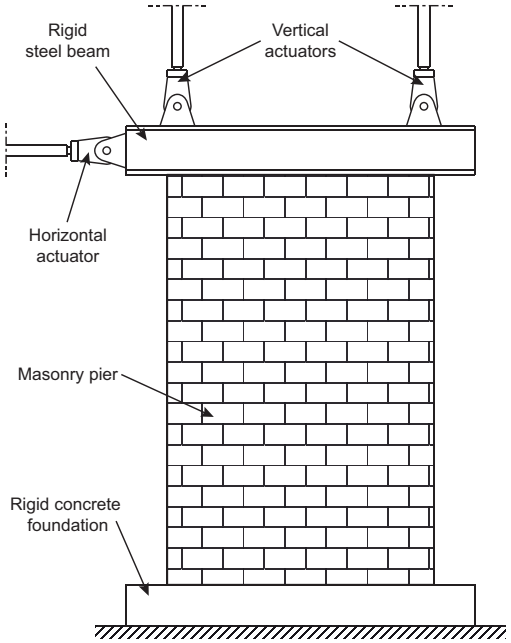

Figure 5.1: Shear-compression test on a masonry pier.

zontal displacement according to a specific loading protocol (often cyclic). The main result of the test is the top displacement - base shear diagram registered by the horizontal actuator. The study conducted by Wilding, Dolatshahi, et al. 2017 shows that the loading protocol may influence the drift capacity of masonry walls, in particular those failing in shear. On the other hand, the shear strength is not sensitive to the loading history according to this study.

While piers are generally tested with a double-bending moment static scheme (Magenes and Calvi 1997; Anthoine et al. 1995; Magenes, Galasco, et al. 2010), in some cases, they were tested in a cantilever system (free rotation at the top, as in Magenes, Morandi, et al. 2008) or in intermediate schemes with different shear span heights (Petry and Beyer 2014). The imposition of the boundary condition is often realized in mixed control of the actuators, checking that, during the test, the sum of the vertical forces remains constant and equal to the prescribed axial load and that the displacements of the two vertical actuators remain equal (Wilding, Dolatshahi, et al. 2018). It is worth noting that, according to two shear-compression test databases (Vanin, Zaganelli, et al. 2017; Morandi et al. 2018), piers have not been tested under high levels of compression. Namely, the compression ratio p, i.e., the ratio between the compression load and compression strength, varies in the interval $0 < p < 0.6$ in the experimental tests taken from that databases. It follows that pier lateral behavior in the presence of axial loads close to the compressive strength is not well known and deserves a thorough study.

As already explained, force-displacement diagrams of experimental tests on masonry piers are usually outlined through a piece-wise linear curve characterized by an initial elastic branch followed by a limited constant-force one. The nonlinear behavior is then described by three quantities: the secant stiffness k_s, the shear

strength V_y, and the displacement capacity δ_u. This approximation is obtained by two procedures: the first one is the determination of a graph representing the ideal monotonous test equivalent to the cyclic one; the second one is the definition of the piece-wise linear curve from the ideal monotonic diagram. Regarding the first procedure, it is generally accepted that the ideal monotonous graph is obtained by connecting the points corresponding to the displacement peak of each loading cycle (Magenes, Galasco, et al. 2010; Vanin, Zaganelli, et al. 2017; Morandi et al. 2018). The second procedure is often taken as the same one used in building codes for shear-displacement diagrams of entire structures (Magenes and Calvi 1997; Frumento, Magenes, and Morandi 2009). Therefore, the construction criterion for piece-wise linearization of the capacity curve is mostly conventional. However, a more rational approach for its definition is desirable since the criterion choice influences the static quantities k_s, V_y, and δ_u.

Among the nonlinear static parameters, the displacement capacity δ_u is the most important one for the seismic vulnerability assessment of masonry structures whose lateral behavior mainly depends on the one of masonry piers. Nevertheless, some of the building code prescriptions on the displacement capacity are still not strongly corroborated by experimental tests and analytical models. Eurocode 8 and IBC express the capacity in terms of ultimate drift θ_u, defined as the ratio between the ultimate lateral displacement δ_u and the height of the pier h, and it shows a constant trend varying aspect ratio and compression ratio. Moreover, it exhibits a discontinuity at the transition between the failure modes as its near-collapse value jumps from 1.0% in the case of rocking failure to 0.5% in the case of shear failure. The fact that the level of compression assumes an important role in determining the failure mode and the displacement capacity has been highlighted by some experimental campaigns (Frumento, Magenes, and Morandi 2009; Magenes, Galasco, et al. 2010; Caballero González et al. 2005; Fehling et al. 2007). Nevertheless, its influence has been taken into account into building codes only recently (IBC 2018). Moreover, the results are influenced by other factors such as the aspect ratio and boundary conditions, which are neglected in some of the building codes.

Only few parametric and numerical studies on the factors that influence the lateral behavior of masonry piers are present in the literature. Recently, Dolatshahi et al. 2018 found that the axial load ratio and the shear span ratio play a key role for the drift capacity. Furthermore, they observed the influence of the wall size in case of panels characterized by toe-crushing failure.

In the present chapter, parametric numerical analyses on masonry piers varying axial load ratio and aspect ratio are carried out. The masonry element is considered in a macro-modeling approach as a homogenized continuum, and the boundary-value problem is solved through the finite element method. The model is calibrated on an experimental campaign on two masonry piers with the same geometrical properties, same material, same static scheme but different compression load so that they exhibit different failure mechanisms: the one with lower axial compression shows a rocking failure, while the other shows a shear failure. It is shown how the main parameters that describe the nonlinear static behavior of masonry piers vary by varying the compression and aspect ratios. Moreover, it is shown that the choice of the linearization criterion could affect the results, especially in masonry pier structures, which show a tensile peak strength in the pushover curve in case of rocking failure. Hence, a new procedure in determining the piece-wise linear curve from the shear-displacement diagram is proposed. The relations between the

nonlinear static quantities k_s, V_y, and θ_u and the parameters that influence them (axial compression ratio p and aspect ratio λ) have been obtained and discussed.

This chapter is organized as follows. In Section 5.2 the interpretation of the pier lateral behavior by some of the building codes is reviewed. In Section 5.3 the description of the numerical model used for the parametric analysis is given, and its calibration on two different experimental tests on undressed double-leaf stone walls (Magenes, Galasco, et al. 2010) is shown. The issues about piece-wise linearization of the shear-displacement diagrams endorsed by the building codes and a new proposal of linearization procedure are exposed in Section 5.4. In Section 5.5, the results of the parametric analysis are shown, and eventually concluding remarks are given in Section 5.6.

5.2 Pier models in the building codes

The pier is a masonry parallelepiped of length L, thickness t, and height H, subjected to a set of actions (compression P, shear force V and bending moment M) on its top surface (Figure 5.2a). Let H_0 be the shear span, i.e. the distance between the bottom surface and the section having zero bending moment, and let η be the span ratio defined as

$$\eta = \frac{H_0}{H} \tag{5.1}$$

The quantities M, V and H_0 are related by rotational equilibrium, namely

$$M = V(H - H_0) = VH(1 - \eta) \tag{5.2}$$

The aspect ratio λ is the ratio between shear span and wall length, namely

$$\lambda = \frac{H_0}{L} \tag{5.3}$$

and the compression ratio p as the ratio between current axial load and the maximum bearing load in compression, that is

$$p = \frac{P}{f_c\, t\, L} \tag{5.4}$$

where f_c is compression strength of masonry. The displacement capacity is often expressed in terms of drift θ, that is the ratio between lateral displacement and the height of the pier, namely

$$\theta = \frac{\delta}{H} \tag{5.5}$$

The relation between the shear force V and the top lateral displacement δ of masonry piers can be experimentally studied through shear-compression tests, whose main result is a graph in which the base shear is plotted against the top displacement. In many of the building codes, the shear-displacement diagram is outlined by a piece-wise linear constitutive model, so that only three parameters suffice for its definition: secant stiffness k_s, shear strength V_y and displacement capacity δ_u, as shown in Figure 5.2b. Hence, the pier behavior is approximated as linear elastic in the first branch, with a slope equivalent to the secant lateral stiffness, until the force reaches the effective yield strength, from which starts the

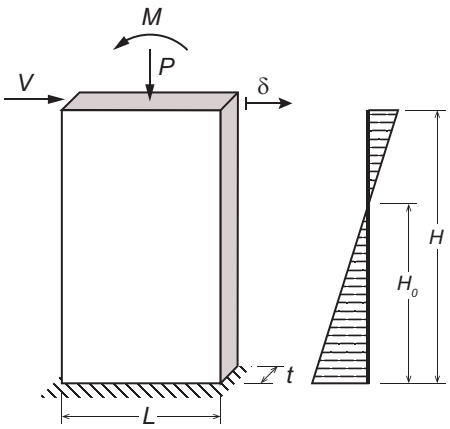

(a) Geometry and loads.

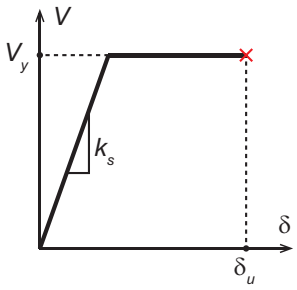

(b) Lateral behavior idealization.

Figure 5.2: Lateral behavior of masonry piers.

second constant-force branch that ends when the displacement reaches its ultimate value.

This section reports the estimations of the three quantities (k_s, V_y and $\theta_u = \delta_u/H$) that describe the nonlinear static lateral behavior of masonry piers provided by some building codes.

5.2.1 Lateral secant stiffness

The lateral stiffness of a masonry pier is evaluated as the one of a Timoshenko beam, taking into account both bending and shear stiffness, namely

$$k_{el} = \left(\left(\frac{n\,E\,t\,L^3}{H^3} \right)^{-1} + \left(\frac{G\,t}{1.2}\frac{L}{H} \right)^{-1} \right)^{-1} \tag{5.6}$$

where E and G are respectively the Young and shear moduli and n is the restraint parameter, that depends on the static scheme (n=3 for cantilever, n=12 for double-fixed panel). It can be shown that the restraint parameter n is function of the shear span ratio η (Wilding and Beyer 2018):

$$n = \frac{6}{3\eta - 1} \tag{5.7}$$

so that the lateral stiffness can be evaluated also in case of intermediate static schemes between cantilever and double-bending.

Since the lateral stiffness is considered to be representative of the secant stiffness of the shear-displacement diagram from experimental tests, the elastic moduli should take into account the cracking of the pier, which is usually achieved by considering a 50% reduction of the elastic moduli.

5.2.2 Shear Strength

Shear failure can occur according to different mechanisms: the flexural ones, i.e., rocking and crushing, and the shearing ones, i.e., shear sliding or diagonal ten-

sile cracking. Consequently, the shear strength value is the minimum among the considered failure mechanisms.

In the two most recent versions of the Italian Building Code (IBC 2008; IBC 2018), three mechanisms are considered: rocking - toe crushing, bed-joint sliding, and diagonal cracking.

The shear strength associated to rocking - toe crushing mechanism is

$$V_{r-tc,IBC} = \frac{P}{2}\frac{L}{H_0}\left(1 - \frac{\kappa P}{f_c t L}\right) \tag{5.8}$$

where κ is a coefficient that modify the compression strength of masonry, that is taken as

$$\kappa = \frac{1}{0.85} \tag{5.9}$$

The bed-joint sliding shear strength is defined as

$$V_{bjs,IBC} = c\,t\,L' + 0.4\,P \tag{5.10}$$

where c is the cohesion and L' is the depth of the compressed area of the pier.

The shear strength associated to diagonal cracking mechanism is

$$V_{dc,IBC} = \frac{f_t t L}{b}\sqrt{1 + \frac{P}{f_t t L}} \tag{5.11}$$

where f_t is the tensile strength and b is defined as

$$b = \min\left(\max\left(\frac{H}{L}; 1.0\right); 1.5\right) \tag{5.12}$$

In Eurocode 8 (EN 1998-3 2005) only rocking - toe crushing and bed-joint sliding mechanisms are defined. The expression of the latter mechanism is the same as for IBC (5.10), while the expression of the former one has just a slight modification in the definition of the parameter κ that is

$$\kappa = 1.15 \tag{5.13}$$

The ASCE 41 (Pekelnicky and Poland 2012) defines four strength mechanisms, divided in two categories: ductile and fragile mechanisms. The ductile mechanisms are rocking and bed-joint sliding, defined as:

$$V_{r,ASCE} = 0.9\,\frac{P}{2}\frac{L}{H_0} \tag{5.14}$$

$$V_{bjs,ASCE} = 0.375\,c\,t\,L + 0.5\,P \tag{5.15}$$

It is worth noting that this building code associates to the bed-joint sliding mechanism a residual value after decohesion given by the frictional term only, namely

$$V_{bjs-f,ASCE} = 0.5\,P \tag{5.16}$$

that is the strength value after the attainment of bed-joint sliding strength peak, justified by experimental tests as explained in Section 2.2.3.

The fragile mechanisms are diagonal cracking and toe crushing, having the same formulation as in the IBC with the only difference on the parameter κ for the toe-crushing mechanism that is

$$\kappa = \frac{1}{0.70} \tag{5.17}$$

5.2.3 Drift capacity

The ultimate displacement of piers is expressed in terms of drift so that the drift capacity is defined as

$$\theta_u = \frac{\delta_u}{H} \tag{5.18}$$

where δ_u is the ultimate displacement of the top of the pier and H is its height. In order to make comparisons between building codes, the near-collapse expression of drift capacity of piers in existing buildings will be considered. The influence of axial load ratio p, aspect ratio λ and the shear span ratio η, shown in experimental tests (Caballero González et al. 2005; Fehling et al. 2007; Magenes and Calvi 1997; Zilch et al. 2008; Atkinson et al. 1989; Magenes 2010; Frumento, Magenes, Morandi, and Calvi 2009) and confirmed in some numerical parametrical analyses (Orlando et al. 2016), is neglected in most of the building codes formulation.

The previous version of IBC (IBC 2008) defined the drift capacity accounting for the type of failure mechanism. Moreover, the drift capacity took into account the influence of the static scheme by means of the shear span H_0. Namely,

$$\theta_{u,NTC08} = \frac{4}{3}\begin{cases} 0.012\, H_0/H & \text{flexural failure} \\ 0.004 & \text{shear failure} \end{cases} \tag{5.19}$$

In the most recent version of IBC (IBC 2018), the drift capacity depends only on the failure mode, although its explicative annex suggests to consider the influence of the axial compression load in case of flexural mechanism.

$$\theta_{u,NTC18} = \begin{cases} \min\left(0.0125\left(1 - \frac{P}{f_c t L}\right); 0.010\right) & \text{flexural failure} \\ 0.005 & \text{shear failure} \end{cases} \tag{5.20}$$

As well as the NTC 2008, the drift capacity defined in Eurocode 8 depends only on the failure mechanism, but it takes into account the influence of the aspect ratio λ in case of rocking - toe crushing.

$$\theta_{u,EC8} = \frac{4}{3}\begin{cases} 0.008\, H_0/L & \text{flexural failure} \\ 0.004 & \text{shear failure} \end{cases} \tag{5.21}$$

While ASCE 41 gives explicit values for drift capacity in case of bed-joint sliding (0.4% at the strength peak and 1.0% at failure), no prescriptions are given about deformation capacity associated with the onset of toe crushing. In this case, ASCE 41 suggests computing the ultimate drift through a moment-curvature approach. Thus, the drift capacity is given by

$$\theta_{u,ASCE} = \begin{cases} \delta_{r-tc}/H & \text{rocking failure} \\ 0.01 & \text{bed-joint sliding failure} \end{cases} \tag{5.22}$$

where δ_{r-tc} is the ultimate displacement associated to rocking - toe crushing mechanism.

5.3 Numerical modeling

Shear-compression tests consist in imposing a constant vertical load through two vertical actuators on a stiff steel beam positioned on the top of the masonry pier and

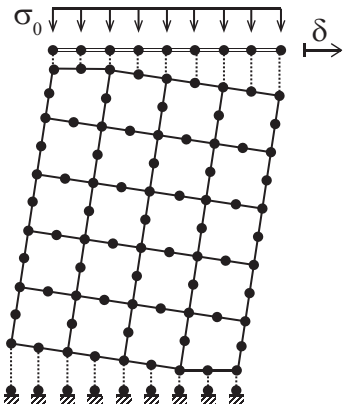

Figure 5.3: Finite element model of the masonry pier.

a cyclic lateral displacement through a horizontal actuator. In the most common case of double-rotation-fixed static scheme, the forces and displacements of the two vertical actuators are controlled to keep constant the sum of their forces and maintain equal their vertical displacements (Wilding, Dolatshahi, et al. 2018).

Here, piers are modeled as a homogenized continuum discretized by isoparametric quadrilateral 8-node plane-stress elements. The chosen constitutive model is the total strain rotating crack model (Vecchio and Collins 1986) implemented in DIANA FEA software (Diana 2012). Several publications have demonstrated the ability of this constitutive model to represent the macroscopic behavior of masonry (Lotfi and Shing 1991; Billi et al. 2019; Pagani, Salvatori, et al. 2017). A parabolic and a linear hardening/softening curve have been selected respectively for compression and tension, both based on fracture energy. Moreover, the lateral crack influence on compressive strength (Vecchio and Collins 1993) has been considered.

The boundary condition at the top is reproduced through multi-degree-of-freedom contraints enforcing the equality of the vertical and horizontal displacements of the top surface nodes. The interactions between the masonry pier and the steel beam on the top and the concrete foundation at the bottom are simulated through nonlinear no-tensile interfaces. These interfaces reproduce the stress-free separation surface in the tension zone, allowing the correct modeling of the rocking behavior.

Nonlinear static analyses are carried out in displacement control using the modified Newton-Raphson iterative method with a convergence criterion based on the out-of-balance force norm. Analyses are performed by imposing a horizontal displacement at one of the top nodes. Pushover curves are obtained by monitoring the target node displacement and the base-shear reaction (Figure 5.3).

5.3.1 Calibration

The model is calibrated on the results of an experimental campaign of cyclic shear-compression tests on undressed double-leaf stone walls (Magenes, Galasco, et al. 2010, Figure 5.4). The experimental test results are summarized in plots of base shear versus top displacement. The numerical model is calibrated on the ideal

Figure 5.4: Experimental test apparatus (from Magenes, Galasco, et al. 2010).

monotonic graph obtained by connecting the points corresponding to the displacement peak of each load cycle.

Among the pier tested in that experimental campaign, two specimens (CS00 and CS01), which exhibit different failure mechanisms, were chosen to calibrate the model. Both specimens have the same doubly rotation-fixed static scheme and have the same geometry: a thickness of 320 mm with no through stones connecting the two leaves, a length of 1.25 m, and a height of 2.50 m; they differ in terms of applied axial load and failure mechanisms exhibited. While the first specimen (CS00) was subjected to a compressive stress of 0.2 MPa and showed a clear rocking failure, the second one (CS01) had a higher level of compression (0.5 MPa)and failed in shear, exhibiting the typical diagonal crack pattern.

The calibration leads to an elastic modulus $E = 1650$ MPa, a compression strength $f_c = 4.0$ MPa, a tensile strength $f_t = 0.07$ MPa, a compression fracture volume energy $G_c/h = 100$ kJ/m^3, being h the crack bandwidth size, and a tensile fracture area energy $G_t = 200$ J/m^2. The model with this set of parameters is able to reproduce both CS00 and CS01 in terms of pushover curve (Figures 5.5 and 5.7) and failure mechanism (Figures 5.6 and 5.8).

As reported in Tab.5.1, the calibrated mechanical parameters are comparable with the results of the characterization tests made on the same material of the specimens (Magenes, Penna, Galasco, et al. 2010).

Sensitivity analyses have been carried out in order to verify that a small variation in mechanical parameters does not cause a large variation in the structure response (Figures 5.9 and 5.10). It is worth noting that the response of the pier exhibiting rocking failure is mostly determined by compression strength and energy, while tensile parameters influence the one characterized by shear failure.

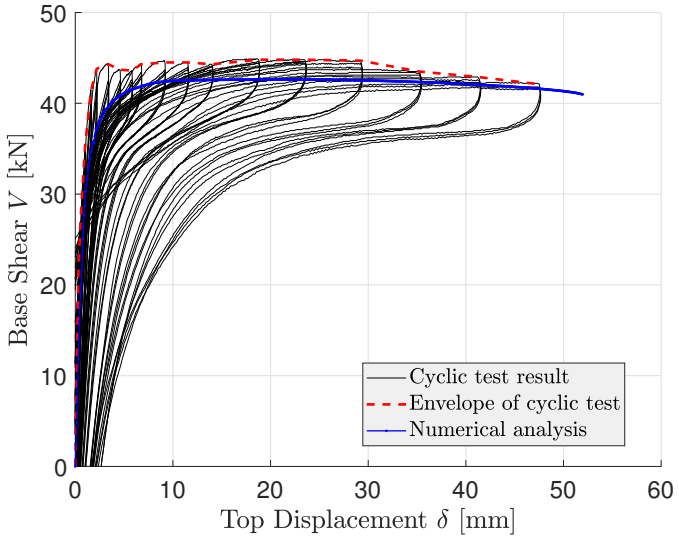

Figure 5.5: Capacity curve (CS00).

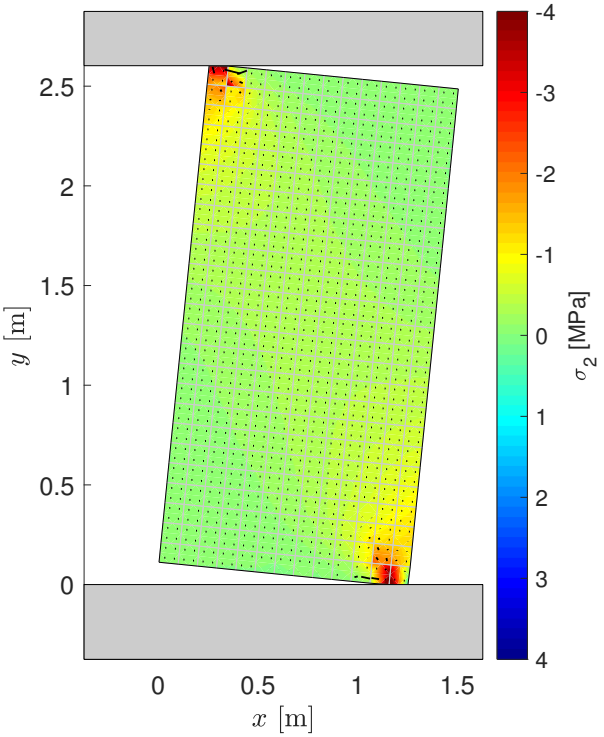

Figure 5.6: Deformed shape and stress-crack pattern (CS00).

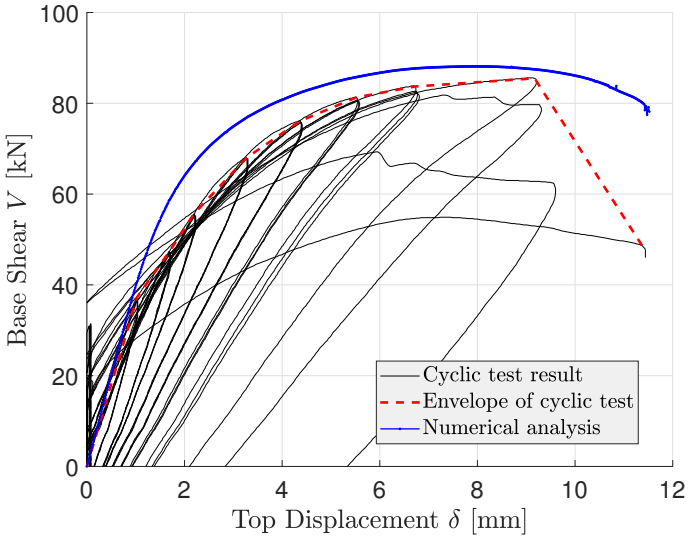

Figure 5.7: Capacity curve (CS01).

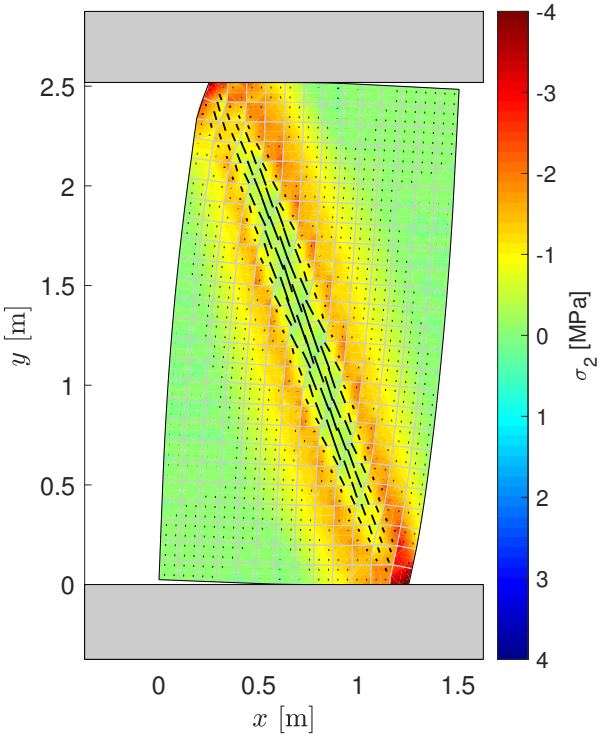

Figure 5.8: Deformed shape and stress-crack pattern (CS01).

	Exp.	Model
E [MPa]	2550	1650
G [MPa]	840	825
f_c [MPa]	3.28	4.00
f_t [MPa]	0.137	0.06
G_c [J/m^2]	-	10000
G_t [J/m^2]	-	170

Table 5.1: Comparison of mechanical parameters between experimental test and model calibration.

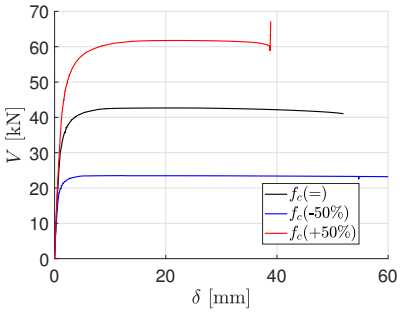

(a) Sensitivity analysis on f_c.

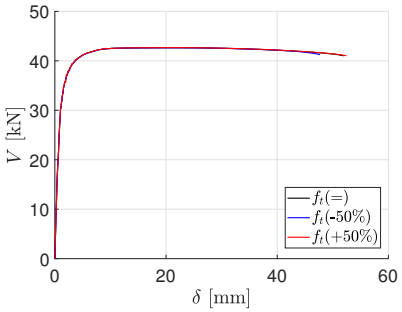

(b) Sensitivity analysis on f_t.

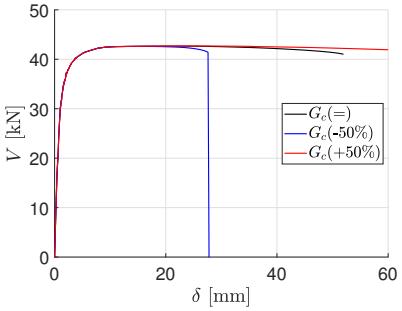

(c) Sensitivity analysis on G_c.

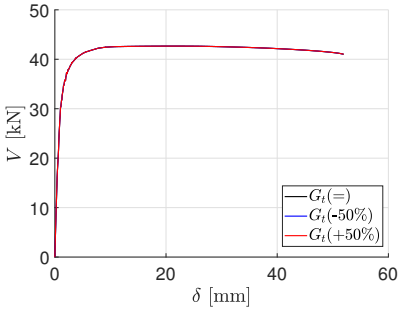

(d) Sensitivity analysis on G_t.

Figure 5.9: Sensitivity analysis (CS00).

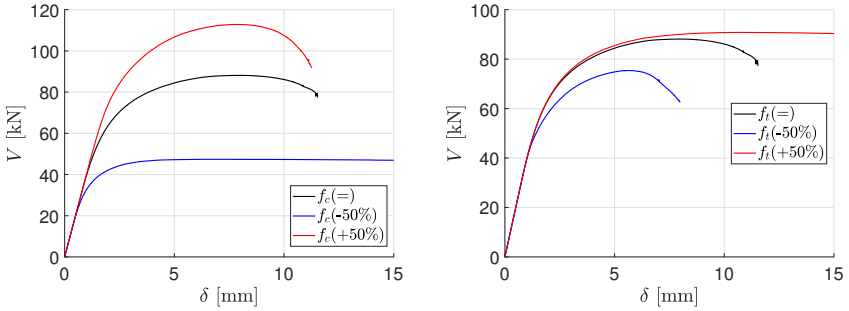

(a) Sensitivity analysis on f_c.

(b) Sensitivity analysis on f_t.

(c) Sensitivity analysis on G_c.

(d) Sensitivity analysis on G_t.

Figure 5.10: Sensitivity analysis (CS01).

The capacity curves obtained from numerical simulations calibrated on the selected specimens does not show a clear after-peak strength drop. This could lead to think that this model cannot be used to predict the displacement capacity of piers. However, the absence of softening in the capacity curves for the selected experimental tests is due to the fragile failure of the compressed pier toe. The reacting part of the base and top sections is small since the compression load applied on the piers is low (5% and 12.5% of the compression strength). Therefore, at the ultimate state, there is a high concentration of compression in a relatively small region. Once the compression stress has reached the compressive strength in an integration point of the toe region, the pier fails and the lateral strength abruptly drops to zero. The fragile behavior is more severe for the rocking pier (CS00) where in the nonlinear branch the shear strength is almost constant until failure, while the pier failing in shear (CS01) exhibits a small lateral strength decrease, due to the diagonal crack opening.

On the other hand, the pier exhibits a clearer softening branch if the compression ratio is higher. Figure 5.11 shows the shear-displacement curve of nine piers characterized by compression ratios of 0.05, 0.50, or 0.95, and by aspect ratios of 0.5, 1.0, or 2.0. The values of the relevant static quantities are reported in Table 5.2.

Figure 5.11 show that panels with high compression ratios and low aspect ratios exhibit more extended softening branches and noticeable strength decreases. As discussed before, this is due to the increase of reacting portion of the base sections. In this case, the pier equilibrium can be found even after the failure in compression of some finite elements located at the base.

We can conclude that the model can predict the after-peak behavior of masonry piers. In some cases, for instance for slender and low-compressed piers, the behavior is almost fragile due to the base section partialization and the shear strength tends to suddenly drop to zero when the panel toe crushes in compression. Conversely, for higher level of compression and for squat piers, we observe smoother strength decrease.

5.3.2 Parametric analyses

Experimental test campaigns have not explored all possible combinations of geometries and load cases typical of piers in masonry structures. In particular, their behavior under a high level of axial compression, namely for compression ratios greater than 0.6, has never been tested (Vanin, Zaganelli, et al. 2017; Morandi et al. 2018). A systematic assessment of the nonlinear static behavior of masonry piers in the whole range of variation of the leading quantities is possible only through numerical simulations, under the assumption that they could be interpreted as an extension of experimental results.

A parametric series of nonlinear static analyses of the calibrated model is carried out by varying the axial compression ratio p and the aspect ratio λ in the following ranges:

$$p = 0.05, 0.15, ..., 0.95 \tag{5.23}$$

$$\lambda = 0.25, 0.30, ..., 0.50, 0.60, ..., 1.00, 1.25, ..., 2.00, 2.50, 3.00 \tag{5.24}$$

These ranges are chosen in such a way to cover almost all possible conditions.

A nonlinear static analysis is performed for each couple (p, λ). From each shear - displacement curve, the secant stiffness k_s, shear strength V_y, and ultimate drift

K_s [kN/mm]	$\lambda = 0.5$	$\lambda = 1.0$	$\lambda = 2.0$
$p = 0.05$	83.35	25.62	4.79
$p = 0.50$	120.39	34.42	5.77
$p = 0.95$	76.08	16.53	2.50

V_y [kN]	$\lambda = 0.5$	$\lambda = 1.0$	$\lambda = 2.0$
$p = 0.05$	76.72	41.97	23.01
$p = 0.50$	217.29	115.09	89.09
$p = 0.95$	37.78	16.76	3.94

δ_u [mm]	$\lambda = 0.5$	$\lambda = 1.0$	$\lambda = 2.0$
$p = 0.05$	16.97	51.79	91.15
$p = 0.50$	3.18	6.97	21.89
$p = 0.95$	0.88	1.68	2.26

Table 5.2: Analyses for a limited range of compression and aspect ratios - Parameters of the piecewise linear curves.

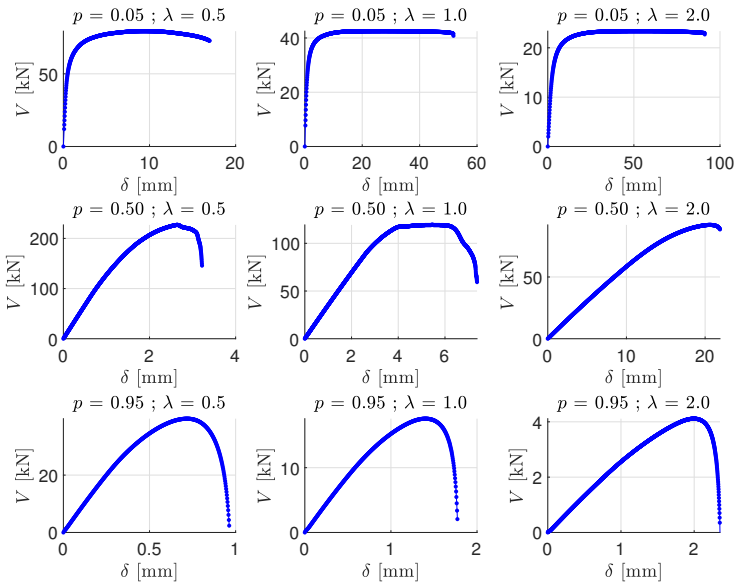

Figure 5.11: Analyses for a limited range of compression and aspect ratios - Pushover curves.

θ_u are obtained through a linearization procedure. Thus, the relationships between these quantities and the parameters that influence them (axial compression ratio p and aspect ratio λ) are obtained.

5.4 Piece-wise linearization of capacity curves

The main result of nonlinear static analyses is the force-displacement diagram representing the relationship between base shear and displacement of a controlled node of the structure. A common approach for the nonlinear static behavior assessment is to idealize the pushover curve as a piece-wise linear curve. This procedure is mainly applied to the capacity curve of a whole structure, but it could also be used for single parts of the structures, such as the masonry piers (Magenes and Calvi 1997; Frumento, Magenes, and Morandi 2009; Magenes, Galasco, et al. 2010; Vanin, Zaganelli, et al. 2017; Morandi et al. 2018).

5.4.1 Piece-wise linearization in building codes

Different piece-wise linearization procedures can be found in building codes. Let k_s be the secant lateral stiffness, V_{peak} the peak value of the shear strength, V_y the effective shear strength, and δ_u the capacity displacement of the structure.

In the Italian Building Code, the capacity curve is replaced by a two-branch piece-wise linear curve (Figure 5.12a). The first branch passes from the point corresponding to 0.7 V_{peak} (0.6 V_{peak} for non-masonry structures) in the increasing part of the actual diagram. The second branch is then defined by the capacity

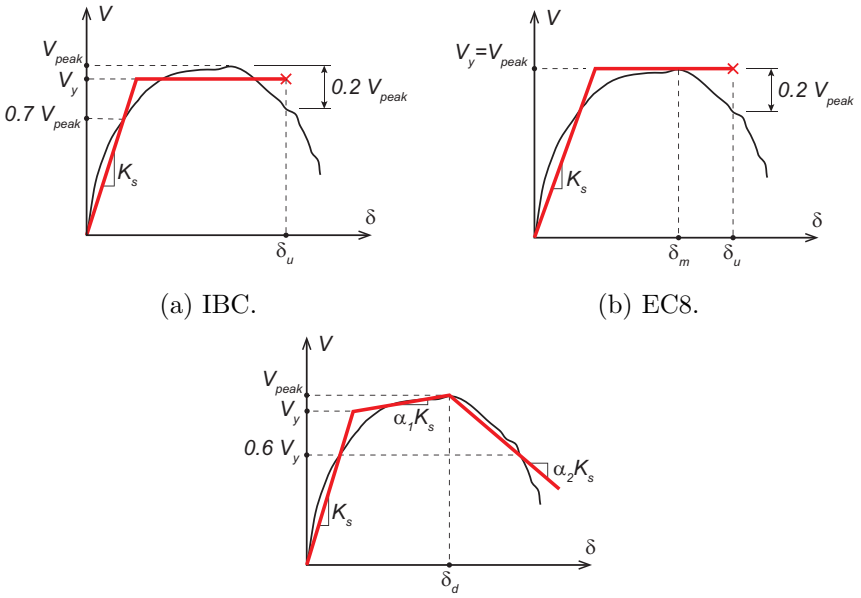

(a) IBC. (b) EC8.

(c) ASCE 41.

Figure 5.12: Piece-wise linearization in some building codes.

displacement δ_u corresponding to a strength reduction of 0.20 V_{peak} (0.15 V_{peak} for non-masonry structures) in the softening branch and by the equivalent yield strength V_y determined with an energy equivalence criterion.

According to Eurocode 8, the capacity curve is a piece-wise linear curve, the first of which represents the linear elastic branch, while the second one is characterized by a constant force, equal to the peak shear force (Figure 5.12b). Bing δ_m the displacement at which the base shear reaches its peak, the initial stiffness is determined in such a way that the areas under the actual and linearized curve in the displacement range from 0 to δ_m are equal. The ultimate displacement capacity is then taken as the one at which the base shear drops below 80% of the peak strength V_{peak}.

In ASCE 41 the shear-displacement diagram is reshaped through a three-piece-linearization (Figure 5.12c). The first segment has a slope representing the effective lateral stiffness of the structure; it begins at the origin and passes through the point corresponding to $0.6V_y$ in the increasing branch. The second segment represents the positive post-yield slope ($\alpha_1 k_s$); it is defined by passing through the point corresponding to the maximum base shear and having a slope determined with an energy equivalence criterion. The third segment, characterized by a negative post-yield slope ($\alpha_2 k_s$), starts from the second segment ending point and passes at $0.6V_y$ in the softening branch.

5.4.2 Issues of the IBC piece-wise linearization criterion

A widely used approach for interpreting the pier pushover curve from experimental tests is to apply the IBC criterion for masonry buildings, as described in Frumento,

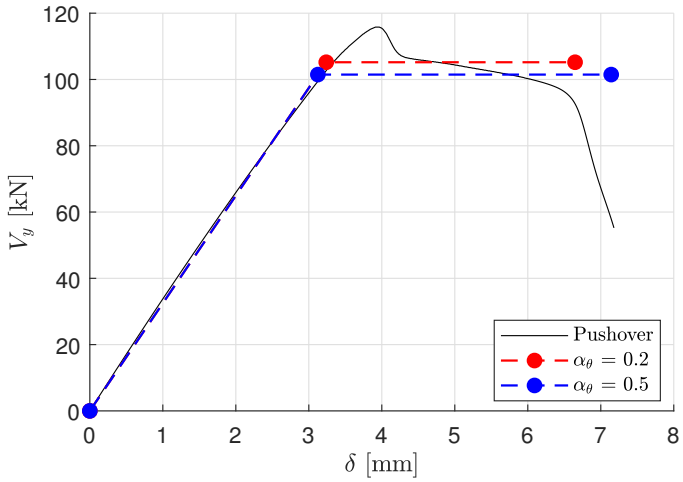

Figure 5.13: Variation of the piece-wise linearization varying α_θ on the same pushover curve.

Magenes, and Morandi 2009. As already mentioned, the pushover curve is simplified in a two-piece-wise linear curve, where the slope of the first segment is defined such that it passes at the point having an ordinate value of 70% of the peak strength in the increasing part of the curve. The horizontal second line ends when the shear force decreases to the value of 80% of strength peak. The choice of this criterion is purely conventional, it is not supported by any rational reasoning, and its application to masonry walls is made by analogy with whole masonry buildings.

A desirable criterion property should be that a small variation of its parameters would not lead to a strong variation of the results while keeping constant the input data.

IBC linearization rule applied to masonry piers does not respect these requirements in case of high ductile behavior, typical of piers characterized by low axial load level and medium-to-high aspect ratio. In fact, a small variation in the constant-branch stop threshold leads to a strong variation in the displacement capacity evaluation since the pushover curve is almost horizontal.

The question is whether there exists a criterion that does not influence the nonlinear static quantities definition. If we keep fixed the IBC criterion framework characterized by its two-piece-wise linear curve, the question reduces to the determination of the parameters that define this schematization. Let α_k be the parameter that defines the percentage of the strength peak at which the first slope intersects the capacity curve and let α_θ be the one at which the constant-force curve is stopped. The parameter values are α_k=0.7 and α_θ=0.8 in the standard criterion.

Observing nonlinear static quantities variability on the criterion parameters, no issue has been observed for the parameter α_k. In contrast, the parameter α_θ has a strong influence on the determination of shear strength and displacement capacity (Figure 5.13). Consequently, in the following study, the parameter α_k is kept as a constant, with the same value as in the IBC criterion ($\alpha_k = 0.70$). The problem reduces to the assessment of the optimized value of α_θ to maximize the linearization criterion objectivity.

5.4.3 Assessment on the piece-wise linearization criterion

The pushover curves from the parametric analysis are linearized varying α_θ from 0.10 to 0.90 in order to obtain the relations

$$k_s = \tilde{k}_s(\alpha_\theta) \tag{5.25}$$
$$V_y = \tilde{V}_y(\alpha_\theta) \tag{5.26}$$
$$\theta_u = \tilde{\theta}_u(\alpha_\theta) \tag{5.27}$$

In particular, their derivative with respect to α_θ are meaningful and the optimized choice of the parameter α_θ is the one for which the value of these derivative is low. Figure 5.14 reports the graphs of the derivative of the nonlinear static parameters with respect to α_θ as a function of α_θ itself. The values reported are the maximum, minimum, and mean over 17×19=323 analyses described in Section 5.3.2.

Figure 5.14a shows that the secant stiffness is not affected by variation with α_θ, as it can be predictable since its definition does not depend on that parameter (it depends on the other one, α_k). However, the shear strength and the ultimate displacement derivatives depends on α_θ as Figures 5.14b and 5.14c show. It can be seen that a variation in α_k in the range $(0.10\,,\,0.45)$ could induce a variation up to 10% on the mentioned quantities. The sensitivity regarding the linearization criterion parameter tends to zero, starting from $\alpha_\theta = 0.50$.

5.4.4 Proposal

The linearization procedure on masonry pier pushover curves exhibited sensitivity on the chosen criterion for the definition of the constant-strength-segment end due to the pushover curve shape, characterized by post-peak shallow softening. To avoid this undesirable feature, a different value of α_θ, the percentage of strength degradation at which the ultimate displacement is defined, should be used. The study carried out above suggested the value $\alpha_\theta = 0.50$, different from the value of 0.20, prescripted by IBC for masonry structures.

5.5 Interpretation of the parametric analyses

The pushover curves obtained through the parametric analysis described in Section 5.3.2 are linearized through the piece-wise linearization procedure proposed in Section 5.4.4. The values of secant stiffness k_s, shear strength V_y and ultimate drift θ_u have been obtained for each couple (p,λ) in the range studied (Eq. 5.23-5.24). In the following subsections, the dependence of each nonlinear static parameter on the compression and aspect ratio is reported and commented.

5.5.1 Secant stiffness

The numerical secant stiffness K_{num}, normalized with respect to the analytical elastic stiffness K_{el} (obtained through Eq.5.6) is represented in Figures 5.15a and 5.15b. It shows that the secant stiffness, except few cases for slender high-compression piers, is always between the 40% and 100% of the value of the elastic lateral stiffness (evaluated with "uncracked" elastic moduli). This result agrees with the building codes prescription, which suggests taking "cracked" moduli as 50% of the "uncracked" corresponding values. In particular, the prescription leads to a lower

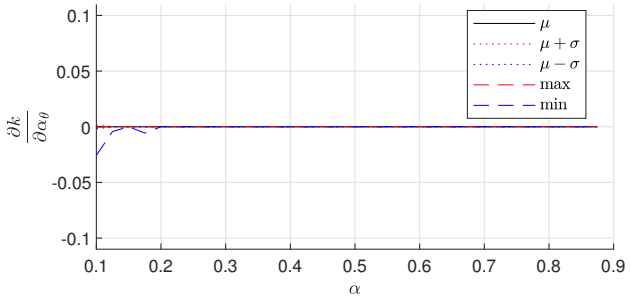

(a) Variation of the secant stiffness k_s.

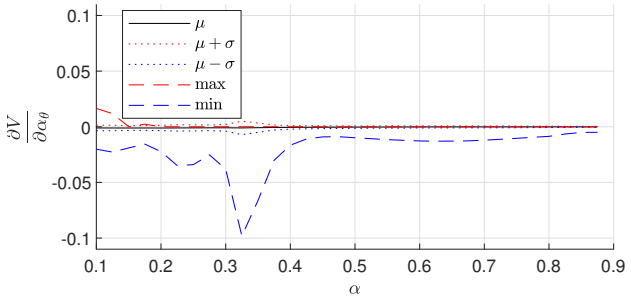

(b) Variation of the shear strength V_y.

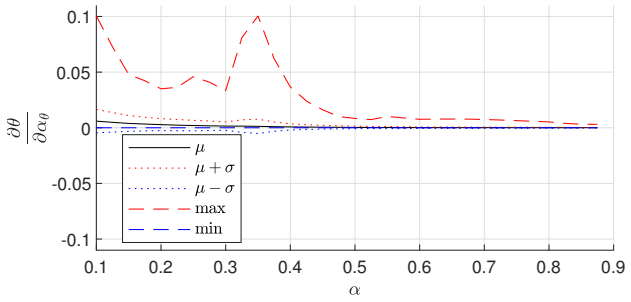

(c) Variation of the drift capacity θ_u.

Figure 5.14: Variation of nonlinear static parameters varying α_θ.

bound prediction of the secant lateral stiffness, except for very slender and highly compressed piers. However, a more refined secant stiffness definition should account for the influence of the compression ratio. The aspect ratio influence is instead limited to the case of high-compression piers, e.g., varying the aspect ratio λ for $p = 0.95$, the ratio K_{num}/K_{el} decreases from 0.6 to 0.25.

5.5.2 Equivalent strength

The numerical shear strength (V_{num}), normalized with respect to the IBC shear strength associated to rocking - toe crushing mechanism (V_{r-tc}) with $\kappa = 1.00$ (Eq. 5.8) is represented in Figures 5.16a-5.16b. The IBC prediction for very slender piers ($\lambda > 1.50$) and $p < 0.6$ is almost correct because the ratio $V_y/V_{r-tc,IBC}$ is close to the unity, while for squat piers the ratio tends to move away from the unity since the failure mechanism becomes the shear one. However, the criterion overestimates the shear strength for highly compressed piers ($p \geq 0.85$) since the lateral strength tends to drop to zero for compression ratios close to the unity. This confirms the validity of taking the parameter κ (which reduces the effective compression strength of masonry) as 0.85.

5.5.3 Drift capacity

The drift capacity trend with respect to compression ratio p and aspect ratio λ is represented in Figures 5.17a and 5.17b, respectively. The graph reported in Figure 5.17a shows that the drift capacity decrease for increasing value of p. It is a result that is confirmed by other numerical tests on masonry piers (Orlando et al. 2016), and it has the physical reason that, in case of higher compression ratios, the compression strain limit is reached sooner as the lateral displacement increases. Among the building codes analyzed in Section 5.2.3, the dependence of θ_u on p is explicitly taken into account only in the recent version of IBC (Eq. 5.20). On the contrary, in its previous version (Eq. 5.19) and EC8 (Eq. 5.21), the drift capacity for rocking and toe-crushing mechanisms, typical for low or high values of compression ratios respectively, is considered as the same, with a large overestimation of θ_u in case of toe-crushing.

Figure 5.17b shows an increase of θ_u for an increasing aspect ratio in the range $0.50 < \lambda < 3.00$, while the behavior is the opposite for very squat piers with $0.25 < \lambda < 0.50$. This is not true for highly compressed piers ($p = 0.95$) for which the ultimate drift decrease with increasing aspect ratios.

5.6 Remarks

A correct assessment of lateral stiffness, shear strength, and displacement capacity of masonry piers is of central interest since they are the main elements that affect the behavior of a masonry structure under horizontal actions. Experimental test campaigns have studied a limited range of the parameters that influence the nonlinear static quantities, such as the compression ratio and the aspect ratio. In the present chapter, a parametric analysis varying these two parameters in a wide range has been carried out through a numerical model previously calibrated on two different experimental tests that exhibited two different failure mechanisms (rocking and shear failure).

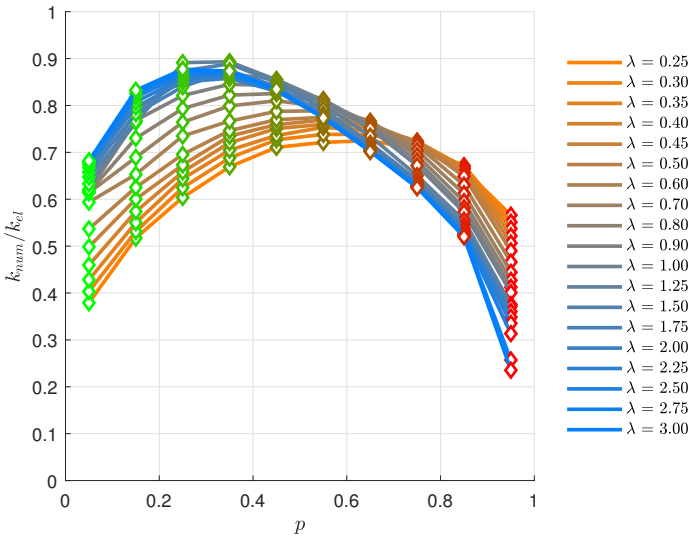

(a) K_{num}/K_{el} as a function of the compression ratio p.

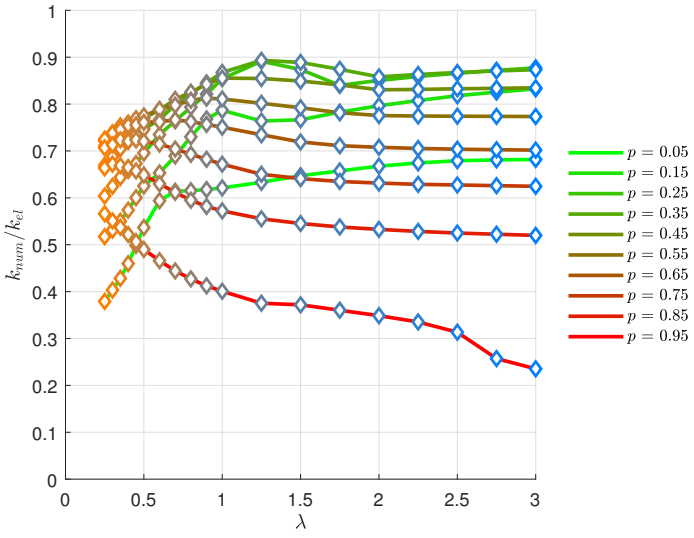

(b) K_{num}/K_{el} as a function of the aspect ratio λ.

Figure 5.15: Normalized secant stiffness obtained from the parametric analysis.

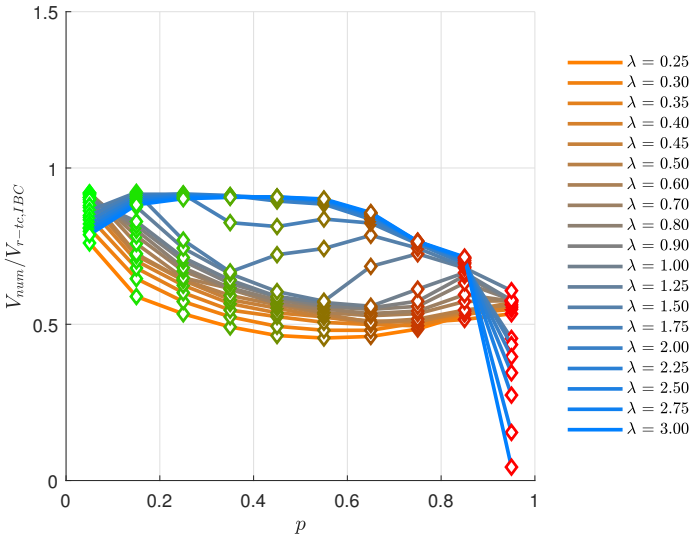

(a) V_{num}/V_{r-tc} as a function of the compression ratio p.

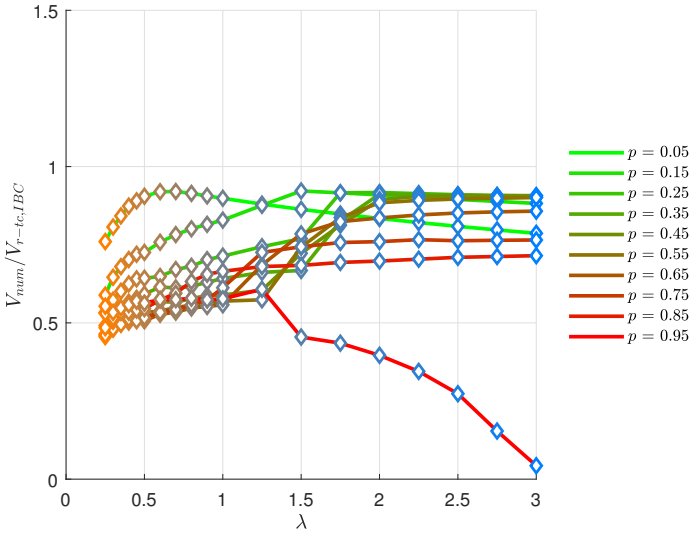

(b) V_{num}/V_{r-tc} as a function of the aspect ratio λ.

Figure 5.16: Normalized shear strength obtained from the parametric analysis.

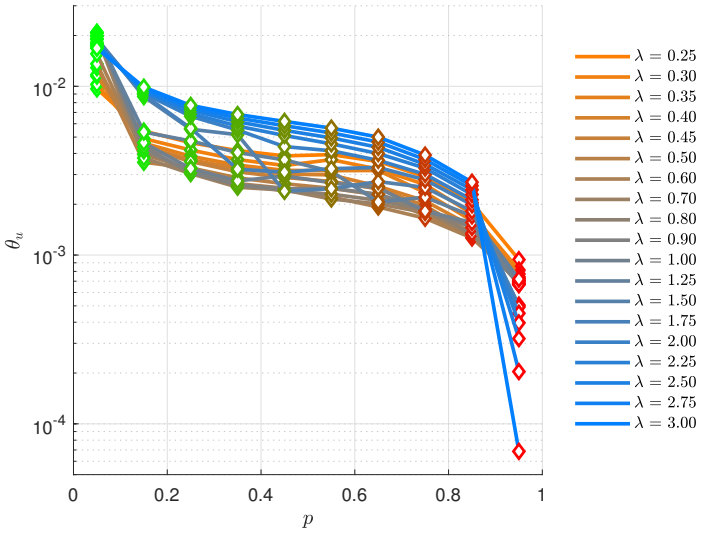

(a) θ_u as a function of the compression ratio p.

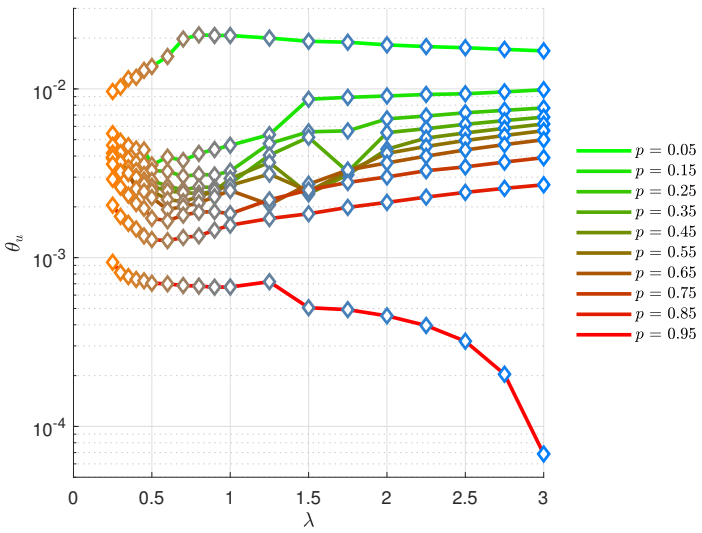

(b) θ_u as a function of the aspect ratio λ.

Figure 5.17: Ultimate drift obtained from the parametric analysis.

Displacement-controlled nonlinear static analyses have been performed to obtain the pier pushover curves. The quantities that describe the lateral behavior of masonry piers have been obtained through a piece-wise linearization criterion. The shear strength and drift capacity showed sensitivity on the piece-wise linearization procedure in the case of long shallow softening, which is typical of low-compression piers. Therefore, the nonlinear static quantities have been obtained according to an improved criterion that increases linearization objectivity, and their dependence on the compression and aspect ratio has been shown.

It was observed that the building code suggestion to consider the "cracked" elastic moduli as the 50% of the uncracked ones for estimating the lateral secant stiffness is a lower-bound estimation, except for very slender and high-compression piers, for which the corresponding percentage decreases to 30%. As to the shear strength, the IBC rocking-toe crushing prediction is correct for very slender piers and is too safety preserving for high-compression piers. Finally, drift capacity exhibits a strong dependence on both aspect and compression ratios. It was highlighted that the dependence on the compression ratio had been implemented only recently in IBC, while the aspect ratio influence is still not considered. These results can be useful for the derivation of analytical formulas for the stiffness, strength, and displacement capacity prediction and as a benchmark for the macroelement design aimed to model the lateral behavior of masonry piers.

Chapter 6

Localization Analysis of an Orthotropic Multisurface Plasticity Model

Abstract

Numerical simulations of masonry structures are often based on continuum macro-modeling approaches that need constitutive laws able to phenomenologically reproduce the behavior of the material. To capture the deformation process up to failure, appropriate softening laws are needed to take into account the contraction of the yield stress domain caused by cracking and crushing. It is well known that softening may lead to localization of inelastic strain.

This chapter focuses on localization analysis of an orthotropic macroscale model in the framework of multi-surface plasticity, which describes the in-plane behavior of masonry structures. The localization properties of Lourenço's model has been determined under uniaxial stress and some biaxial stress states. The theoretical predictions have been compared to numerical simulations, showing a perfect match in terms of localization surface directions.

6.1 Introduction

Different strategies can be adopted for numerical simulations of the behavior of masonry structures. Among others, continuum macro-modeling is a frequently used approach, in which masonry structures are treated as homogenized continua and, in general, discretized by the finite element method. This kind of modeling needs the choice of a constitutive model, which could be formulated within the framework of nonlinear elasticity, plasticity, damage mechanics, smeared crack models, or their combinations, and its aim is to phenomenologically reproduce the average behavior of masonry.

To capture the deformation process up to failure, appropriate softening laws are needed to take into account the contraction of the yield stress domain caused

by cracking and crushing. It is well known that softening may lead to localization of inelastic strain and pathological mesh sensitivity of the numerical solution.

Therefore, it is important to understand the conditions under which localization can occur in order to determine whether a localization regularization procedure in the numerical model is needed. Furthermore, localization analysis can be interpreted as a tool for the macroscopic model evaluation by checking if the theoretically-predicted localization band directions match with the ones obtained from experimental tests.

The classical necessary condition for localization, as inspired by the early works of Hadamard 1903 and Hill 1958, corresponds to the singularity of the localization tensor, under the assumption of the same tangent stiffness tensor on both sides of the discontinuity. For constitutive laws in the framework of plasticity, the localization condition was later extended by Rice and Rudnicki 1980 removing the latter assumption. Borré and Maier 1989 analyzed strain localization in elastoplasticity under the small-strain regime and they found the conditions for localization also in the case that plastic yielding takes place on one side and elastic unloading on the other side of the discontinuity surface. Studies on the localization properties on constitutive models based on orthotropic plasticity have been conducted by Steinmann et al. 1994 and recently by Cervera et al. 2020.

The objective of this chapter is to analyze and characterize localization properties of the orthotropic plasticity model for masonry proposed by Lourenço 1995. More refined but computationally more demanding approaches take into account the microscale heterogeneity of masonry by explicitly considering the geometrical arrangement of bricks and mortar, which are then treated as two different materials. A comparison of localization conditions predicted by microscale simulations and those derived for the macroscopic model will be presented in Chapter 7.

The present analysis will be based on well-established conditions that link the incipient weak discontinuity to the localization tensor (sometimes called the acoustic tensor), which is obtained by contracting the fourth-order material tangent stiffness tensor from the left and from the right with a unit vector that represents the normal to a potential discontinuity surface.

In this chapter, the localization analysis of the presented macro-model is carried out under the condition of uniaxial stress in tension and in compression, and for biaxial stress states. Conditions for the onset of localization are derived and preferential directions of the emerging weak discontinuity are evaluated.

The chapter is structured as follows. The governing equations of Lourenço's model are reported in Section 6.2. In Section 6.3, we describe the localization conditions, first in a simplified approach by assuming the same tangent stiffness at both sides of the discontinuity surfaces, then the localization analysis has been refined by removing the preceding assumption. In Section 6.4 and 6.5, we assess the localization properties of Lourenço's model under uniaxial and biaxial stress states respectively. Finally, we report some concluding remarks in Section 6.6.

6.2 Basic equations of Lourenço's model for masonry

The macroscopic constitutive model for masonry considered here was developed for plane-stress analysis of regular masonry walls, which have two clearly defined axes

of orthotropy, further denoted as axes x and y (horizontal and vertical). The model was formulated within the framework of multi-surface elastoplasticity. It uses two yield surfaces that are linked to tensile and compressive failure modes. The general structure of the model equations is conveniently presented in the matrix form. The stress-strain law can be written as

$$\boldsymbol{\sigma} = \boldsymbol{D}_e \left(\boldsymbol{\varepsilon} - \boldsymbol{\varepsilon}_p \right) \tag{6.1}$$

where $\boldsymbol{\sigma} = (\sigma_x, \sigma_y, \tau_{xy})^T$ is the column matrix of stress components, $\boldsymbol{D}_e$ is the elastic material stiffness matrix, and $\boldsymbol{\varepsilon} = (\varepsilon_x, \varepsilon_y, \gamma_{xy})^T$ and $\boldsymbol{\varepsilon}_p = (\varepsilon_{px}, \varepsilon_{py}, \gamma_{pxy})^T$ are the column matrices of total and plastic strain components. The elastic material stiffness matrix for an orthotropic material under plane-stress conditions can be presented in the form

$$\boldsymbol{D}_e = \frac{1}{1 - \nu_{xy}\nu_{yx}} \begin{pmatrix} E_x & \nu_{yx}E_x & 0 \\ \nu_{xy}E_y & E_y & 0 \\ 0 & 0 & (1 - \nu_{xy}\nu_{yx})G_{xy} \end{pmatrix} \tag{6.2}$$

where E_x and E_y are elastic moduli that correspond to the directions of orthotropy x and y, G_{xy} is the shear modulus and ν_{xy} and ν_{yx} are Poisson's ratios. Only four out of these five elastic constants are independent, because of the symmetry constraint $\nu_{yx}E_x = \nu_{xy}E_y$.

The evolution of plastic strain is described by the flow rule,

$$\dot{\boldsymbol{\varepsilon}}_p = \dot{\lambda}_t \frac{\partial g_t(\boldsymbol{\sigma}, \boldsymbol{q}_t)}{\partial \boldsymbol{\sigma}} + \dot{\lambda}_c \frac{\partial f_c(\boldsymbol{\sigma}, \boldsymbol{q}_c)}{\partial \boldsymbol{\sigma}} \tag{6.3}$$

combined with the Karush-Kuhn-Tucker conditions

$$f_t(\boldsymbol{\sigma}, \boldsymbol{q}_t) \le 0, \qquad f_c(\boldsymbol{\sigma}, \boldsymbol{q}_c) \le 0 \tag{6.4}$$

$$\dot{\lambda}_t \ge 0, \qquad \dot{\lambda}_c \ge 0 \tag{6.5}$$

$$\dot{\lambda}_t f_t(\boldsymbol{\sigma}, \boldsymbol{q}_t) = 0, \qquad \dot{\lambda}_c f_c(\boldsymbol{\sigma}, \boldsymbol{q}_c) = 0 \tag{6.6}$$

Here, $\dot{\lambda}_t$ and $\dot{\lambda}_c$ are the rates of plastic multipliers related to the tensile and compressive mechanisms, f_t and f_c are yield functions, g_t is the plastic potential and $\boldsymbol{q}_t$ and $\boldsymbol{q}_c$ are stress-like internal hardening/softening variables. According to (6.3), the tension-related part of plastic flow is non-associated, because it is derived from a plastic potential g_t which is in general different from the yield function f_t. The compression-related part of plastic flow is associated, i.e., the flow direction is determined by the gradient of the yield function, f_c.

For the model proposed by Lourenço, the stress-like internal variables have only normal components (with respect to the orthotropy axes x and y), but for easier notation we present them as column matrices $\boldsymbol{q}_t = (\sigma_{tx}, \sigma_{ty}, 0)^T$ and $\boldsymbol{q}_c = (\sigma_{cx}, \sigma_{cy}, 0)^T$. This makes it possible to present the yield functions and plastic potential in the compact form

$$f_t(\boldsymbol{\sigma}, \boldsymbol{q}_t) = \sqrt{(\boldsymbol{\sigma} - \boldsymbol{q}_t)^T \boldsymbol{P}_t (\boldsymbol{\sigma} - \boldsymbol{q}_t)} + \boldsymbol{\pi}^T (\boldsymbol{\sigma} - \boldsymbol{q}_t) \tag{6.7}$$

$$f_c(\boldsymbol{\sigma}, \boldsymbol{q}_c) = \sqrt{\boldsymbol{\sigma}^T \boldsymbol{P}_c(\sigma_{cx}, \sigma_{cy}) \boldsymbol{\sigma}} - \sqrt{\sigma_{cx}\sigma_{cy}} \tag{6.8}$$

$$g_t(\boldsymbol{\sigma}, \boldsymbol{q}_t) = \sqrt{(\boldsymbol{\sigma} - \boldsymbol{q}_t)^T \boldsymbol{P}_g (\boldsymbol{\sigma} - \boldsymbol{q}_t)} + \boldsymbol{\pi}^T (\boldsymbol{\sigma} - \boldsymbol{q}_t) \tag{6.9}$$

with auxiliary matrices

$$\boldsymbol{P}_t = \begin{pmatrix} 1/4 & -1/4 & 0 \\ -1/4 & 1/4 & 0 \\ 0 & 0 & \alpha \end{pmatrix}, \qquad \boldsymbol{P}_g = \begin{pmatrix} 1/4 & -1/4 & 0 \\ -1/4 & 1/4 & 0 \\ 0 & 0 & 1 \end{pmatrix} \tag{6.10}$$

$$\boldsymbol{P}_c(\sigma_{cx}, \sigma_{cy}) = \begin{pmatrix} \sigma_{cy}/\sigma_{cx} & \beta/2 & 0 \\ \beta/2 & \sigma_{cx}/\sigma_{cy} & 0 \\ 0 & 0 & \gamma \end{pmatrix} \qquad \boldsymbol{\pi} = \begin{pmatrix} 1/2 \\ 1/2 \\ 0 \end{pmatrix} \tag{6.11}$$

Here, α, β and γ are dimensionless parameters.

Stress-like internal variables control the size and shape of the yield surface. They are uniquely linked to strain-like internal variables κ_t and κ_c, which are identified here with the plastic multipliers. This is formally described by evolution equations

$$\dot{\kappa}_t = \dot{\lambda}_t \tag{6.12}$$

$$\dot{\kappa}_c = \dot{\lambda}_c \tag{6.13}$$

and by the hardening-softening laws

$$\boldsymbol{q}_t = \boldsymbol{h}_t(\kappa_t) \tag{6.14}$$

$$\boldsymbol{q}_c = \boldsymbol{h}_c(\kappa_c) \tag{6.15}$$

For tension, exponential softening is used, and the component-wise form of equation (6.14) is

$$\sigma_{ti} = h_{ti}(\kappa_t) = f_{ti} \exp\left(-\frac{h_b f_{ti}}{G_{fti}} \kappa_t\right), \qquad i = x, y \tag{6.16}$$

in which f_{tx} and f_{ty} are uniaxial tensile strengths in directions x and y, and G_{ftx} and G_{fty} are the corresponding fracture energies. The softening law is adjusted depending on the estimated size h_b of the computationally resolved localized band (typically obtained by projecting the finite element onto the direction normal to the band).

For compression, parabolic hardening is followed by parabolic and later exponential softening, described by

$$\sigma_{ci} = h_{ci}(\kappa_c) = \begin{cases} \sigma_{0i} + (\sigma_{pi} - \sigma_{0i}) \sqrt{\frac{2\kappa_c}{\kappa_p} - \frac{\kappa_c^2}{\kappa_p^2}} & \text{if } \kappa_c \leq \kappa_p \\ \sigma_{pi} + (\sigma_{mi} - \sigma_{pi}) \left(\frac{\kappa_c - \kappa_p}{\kappa_{mi} - \kappa_p}\right)^2 & \text{if } \kappa_p < \kappa_c \leq \kappa_{mi} \\ \sigma_{ri} + (\sigma_{mi} - \sigma_{ri}) \exp\left(\frac{2(\kappa_c - \kappa_{mi})(\sigma_{mi} - \sigma_{pi})}{(\kappa_{mi} - \kappa_p)(\sigma_{mi} - \sigma_{ri})}\right) & \text{if } \kappa_{mi} < \kappa_c \end{cases} \tag{6.17}$$

in which again subscript i can take values x or y. This law, graphically presented in Fig. 6.1, contains parameters κ_p, κ_{mx} and κ_{my} that correspond to characteristic values of internal variable κ_c (e.g., κ_p is the value of κ_c at the peak, i.e., at transition from hardening to softening), and also parameters σ_{0x} and σ_{0y}, which are the initial values of yield stress in directions x and y, σ_{px} and σ_{py}, which are the peak values of yield stress, σ_{mx} and σ_{my}, which are the values of yield stress at transition from parabolic to exponential softening, and σ_{rx} and σ_{ry}, which are the values of residual yield stress.

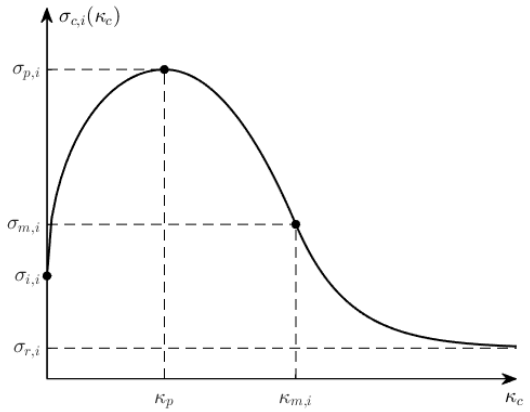

Figure 6.1: Hardening/softening law for compression

In absence of specific experimental tests, the characteristic yield stress values can be set to

$$\sigma_{pi} = f_{ci} \ , \qquad \sigma_{0i} = \frac{1}{3} f_{ci} \ , \qquad \sigma_{mi} = \frac{1}{2} f_{ci} \ , \qquad \sigma_{ri} = \frac{1}{10} f_{ci} \tag{6.18}$$

as suggested by Lourenço 1995. The value of the equivalent plastic strain κ_p at peak is considered to be an additional parameter of the model. The value of κ_{mi} depends on the estimated crack band width h_b (related to the finite element mesh) and is given by (Lourenço 1995)

$$\kappa_{mi} = \frac{75}{67} \frac{G_{fci}}{h_b f_{ci}} + \kappa_p \tag{6.19}$$

6.3 Localization analysis

In the previous section, the basic equations of the constitutive model were introduced in the matrix notation. For the purpose of localization analysis, it is useful to switch to tensorial notation. Stress and strain will now be considered as second-order tensors and the material stiffness as a fourth-order tensor. The strain-like internal variables, κ_t and κ_c, are just two scalars, while the stress-like internal variables, $\boldsymbol{q}_t$ and $\boldsymbol{q}_c$, are treated as second-order tensors, even though not fully general ones, since they have only two independent components each.

In tensorial notation, subscripts x and y will be replaced by 1 and 2. For instance, the tensorial internal variable $\boldsymbol{q}_t$ could be presented in the form $\boldsymbol{q}_t = \sigma_{t1} \boldsymbol{e}_1 \otimes \boldsymbol{e}_1 + \sigma_{t2} \boldsymbol{e}_2 \otimes \boldsymbol{e}_2$ where $\sigma_{t1} \equiv \sigma_{tx}$, $\sigma_{t2} \equiv \sigma_{ty}$, and $\boldsymbol{e}_1$ and $\boldsymbol{e}_2$ are unit vectors aligned with axes x and y.

6.3.1 Rate equations and elastoplastic tangent stiffness

Suppose that plastic yielding takes place with only one yield surface activated. To simplify notation, we will drop the index t or c referring to the tensile or compres-

sive mechanism. For instance, the yield function and the plastic potential will be denoted as f and g instead of f_t and g_t for tension (or f_c and f_c for compression).

The rate of the (activated) plastic multiplier can be computed from the consistency condition

$$\dot{f} = \frac{\partial f}{\partial \boldsymbol{\sigma}} : \dot{\boldsymbol{\sigma}} + \frac{\partial f}{\partial \boldsymbol{q}} : \dot{\boldsymbol{q}} = f_{\boldsymbol{\sigma}} : \dot{\boldsymbol{\sigma}} + f_{\boldsymbol{q}} : \dot{\boldsymbol{q}} = 0 \tag{6.20}$$

where the rate of variable $\boldsymbol{q}$ can be expressed as

$$\dot{\boldsymbol{q}} = \frac{\partial \boldsymbol{h}}{\partial \kappa}\dot{\kappa} = \boldsymbol{h}_\kappa \dot{\kappa} = \boldsymbol{h}_\kappa \dot{\lambda} \tag{6.21}$$

Substituting the flow rule (6.3) (with only one yield mechanism activated) into the rate form of (6.1), we get

$$\dot{\boldsymbol{\sigma}} = \boldsymbol{D}_e : \left(\dot{\boldsymbol{\varepsilon}} - \dot{\lambda}\, g_{\boldsymbol{\sigma}}\right) \tag{6.22}$$

Here, $g_{\boldsymbol{\sigma}} = \partial g / \partial \boldsymbol{\sigma}$ is the derivative of the plastic potential with respect to the stress tensor. For the compressive mechanism, the flow rule is associated, and so $g_{\boldsymbol{\sigma}} = f_{\boldsymbol{\sigma}}$. Specific expressions for tensors $f_{\boldsymbol{\sigma}}$, $g_{\boldsymbol{\sigma}}$ and $\boldsymbol{h}_\kappa$ obtained for Lourenço's model by differentiation of (6.7)–(6.9) and (6.16)–(6.17) are worked out in Appendix 6.A.

Making use of (6.21) and (6.22), we can convert the consistency condition (6.20) into an equation with a single unknown rate,

$$f_{\boldsymbol{\sigma}} : \boldsymbol{D}_e : \left(\dot{\boldsymbol{\varepsilon}} - \dot{\lambda}\, g_{\boldsymbol{\sigma}}\right) + f_{\boldsymbol{q}} : \boldsymbol{h}_\kappa\, \dot{\lambda} = 0 \tag{6.23}$$

from which it is possible to express the rate of the plastic multiplier

$$\dot{\lambda} = \frac{f_{\boldsymbol{\sigma}} : \boldsymbol{D}_e : \dot{\boldsymbol{\varepsilon}}}{f_{\boldsymbol{\sigma}} : \boldsymbol{D}_e : g_{\boldsymbol{\sigma}} - f_{\boldsymbol{q}} : \boldsymbol{h}_\kappa} \tag{6.24}$$

Substitution of this result back into (6.22) leads to the rate form of the elasto-plastic stress-strain law

$$\dot{\boldsymbol{\sigma}} = \left(\boldsymbol{D}_e - \frac{\boldsymbol{D}_e : g_{\boldsymbol{\sigma}} \otimes f_{\boldsymbol{\sigma}} : \boldsymbol{D}_e}{f_{\boldsymbol{\sigma}} : \boldsymbol{D}_e : g_{\boldsymbol{\sigma}} - f_{\boldsymbol{q}} : \boldsymbol{h}_\kappa}\right) : \dot{\boldsymbol{\varepsilon}} \tag{6.25}$$

where the expression in parentheses is the elastoplastic stiffness tensor, $\boldsymbol{D}_{ep}$. To further simplify notation, let us introduce an auxiliary variable

$$h = f_{\boldsymbol{\sigma}} : \boldsymbol{D}_e : g_{\boldsymbol{\sigma}} - f_{\boldsymbol{q}} : \boldsymbol{h}_\kappa \tag{6.26}$$

The elastoplastic stiffness tensor can then be presented in the form

$$\boldsymbol{D}_{ep} = \boldsymbol{D}_e - \frac{1}{h}\boldsymbol{D}_e : g_{\boldsymbol{\sigma}} \otimes f_{\boldsymbol{\sigma}} : \boldsymbol{D}_e \tag{6.27}$$

Let us mention that uniqueness of the response on the local level (in the sense that the strain rate uniquely determines the stress rate and the rate of internal variables) is guaranteed if and only if the auxiliary variable h defined in (6.26) is positive. In what follows, we will assume that this condition is always satisfied.

6.3.2 Simplified localization analysis

At the onset of localization, all field variables are still continuous but their rates are not. The discontinuity in stress and strain rates is not completely arbitrary because, even after the formation of a weak discontinuity surface, displacements are assumed to remain continuous and tractions on the opposite sides of the discontinuity surface must be the same, by virtue of the law of action and reaction.

Traction equilibrium leads to the condition

$$\boldsymbol{n} \cdot \dot{\boldsymbol{\sigma}}^{+} = \boldsymbol{n} \cdot \dot{\boldsymbol{\sigma}}^{-} \tag{6.28}$$

where $\boldsymbol{n}$ is a unit vector normal to the discontinuity surface and $\dot{\boldsymbol{\sigma}}^{+}$ and $\dot{\boldsymbol{\sigma}}^{-}$ are the stress rates on one and the other side of the surface. Displacement continuity leads to a special form of strain rate jump that can be characterized by a vector written as $\boldsymbol{m}\dot{e}$, where $\boldsymbol{m}$ is a unit vector and $\dot{e} > 0$. The strain rates on opposite sides of the discontinuity surface are linked by the relation

$$\dot{\boldsymbol{\varepsilon}}^{+} = \dot{\boldsymbol{\varepsilon}}^{-} + (\boldsymbol{n} \otimes \boldsymbol{m})_{sym}\dot{e} \tag{6.29}$$

The simplest way to derive the localization condition is based on the assumption that the processes taking place on both sides of the discontinuity are governed by the same tangent stiffness, $\boldsymbol{D}_{ep}$, which means that the stress and strain rates are linked by constitutive equations

$$\dot{\boldsymbol{\sigma}}^{+} = \boldsymbol{D}_{ep} : \dot{\boldsymbol{\varepsilon}}^{+} \tag{6.30}$$

$$\dot{\boldsymbol{\sigma}}^{-} = \boldsymbol{D}_{ep} : \dot{\boldsymbol{\varepsilon}}^{-} \tag{6.31}$$

Making use of (6.29)–(6.31), we can transform (6.28) into

$$\boldsymbol{n} \cdot \boldsymbol{D}_{ep} : \dot{\boldsymbol{\varepsilon}}^{-} + \boldsymbol{n} \cdot \boldsymbol{D}_{ep} : (\boldsymbol{n} \otimes \boldsymbol{m})_{sym}\dot{e} = \boldsymbol{n} \cdot \boldsymbol{D}_{ep} : \dot{\boldsymbol{\varepsilon}}^{-} \tag{6.32}$$

which can be rewritten as

$$\boldsymbol{Q}_{ep} \cdot \boldsymbol{m}\dot{e} = \boldsymbol{0} \tag{6.33}$$

where

$$\boldsymbol{Q}_{ep} = \boldsymbol{n} \cdot \boldsymbol{D}_{ep} \cdot \boldsymbol{n} = \boldsymbol{n} \cdot \boldsymbol{D}_{e} \cdot \boldsymbol{n} - \frac{1}{h}\boldsymbol{n} \cdot \boldsymbol{D}_{e} : g_{\boldsymbol{\sigma}} \otimes f_{\boldsymbol{\sigma}} : \boldsymbol{D}_{e} \cdot \boldsymbol{n} \tag{6.34}$$

is the elastoplastic localization tensor. Equation (6.33) can have a nontrivial solution $\boldsymbol{m}\dot{e} \neq \boldsymbol{0}$ only if the localization tensor is singular. This is the standard localization condition.

In terms of auxiliary tensors

$$\boldsymbol{Q}_{e} = \boldsymbol{n} \cdot \boldsymbol{D}_{e} \cdot \boldsymbol{n}, \qquad \boldsymbol{a} = \boldsymbol{n} \cdot \boldsymbol{D}_{e} : f_{\boldsymbol{\sigma}}, \qquad \boldsymbol{b} = \boldsymbol{n} \cdot \boldsymbol{D}_{e} : g_{\boldsymbol{\sigma}} \tag{6.35}$$

the elastoplastic localization tensor can be presented as

$$\boldsymbol{Q}_{ep} = \boldsymbol{Q}_{e} - \frac{1}{h}\boldsymbol{b} \otimes \boldsymbol{a} \tag{6.36}$$

which means that it is a rank-one modification of the elastic localization tensor $\boldsymbol{Q}_{e}$. After some calculations, it can be shown that singularity of the elastoplastic localization tensor is equivalent to the condition

$$-f_{\boldsymbol{q}} : \boldsymbol{h}_{\kappa} = \boldsymbol{a} \cdot \boldsymbol{Q}_{e}^{-1} \cdot \boldsymbol{b} - f_{\boldsymbol{\sigma}} : \boldsymbol{D}_{e} : g_{\boldsymbol{\sigma}} \tag{6.37}$$

We consider normals $\boldsymbol{n} = (n_1, n_2)^T$, characterized by two components, $n_1 \equiv n_x$ and $n_2 \equiv n_y$.

Taking into account symmetries of the orthotropic elastic stiffness tensor and the plane-stress condition, the quantities entering into (6.37) can be simplified. The orthotropic elastic localization tensor is represented by the matrix

$$\boldsymbol{Q}_e = \begin{pmatrix} D_{1111}\, n_1^2 + D_{1212}\, n_2^2 & (D_{1122} + D_{1212})\, n_1\, n_2 \\ (D_{1122} + D_{1212})\, n_1\, n_2 & D_{1212}\, n_1^2 + D_{2222}\, n_2^2 \end{pmatrix} \tag{6.38}$$

where

$$D_{1111} = \frac{E_x}{1 - \nu_{xy}\,\nu_{yx}} \qquad D_{2222} = \frac{E_y}{1 - \nu_{xy}\,\nu_{yx}} \tag{6.39}$$

$$D_{1122} = \frac{\nu_{yx}\,E_x}{1 - \nu_{xy}\,\nu_{yx}} \qquad D_{1212} = G_{xy} \tag{6.40}$$

are tensorial components of the elastic material stiffness, $\boldsymbol{D}_e$. Other relevant quantities are evaluated as follows:

$$f_{\boldsymbol{\sigma}} : \boldsymbol{D}_e : g_{\boldsymbol{\sigma}} = D_{1111}\, f_{\boldsymbol{\sigma},11}\, g_{\boldsymbol{\sigma},11} + D_{1122}(f_{\boldsymbol{\sigma},11}\, g_{\boldsymbol{\sigma},22} + f_{\boldsymbol{\sigma},22}\, g_{\boldsymbol{\sigma},11}) + \\ + 4\, D_{1212}\, f_{\boldsymbol{\sigma},12}\, g_{\boldsymbol{\sigma},12} + D_{2222}\, f_{\boldsymbol{\sigma},22}\, g_{\boldsymbol{\sigma},22} \tag{6.41}$$

$$\boldsymbol{a} = \begin{bmatrix} (D_{1111}\, f_{\boldsymbol{\sigma},11} + D_{1122}\, f_{\boldsymbol{\sigma},22})\, n_1 + 2\, D_{1212}\, f_{\boldsymbol{\sigma},12}\, n_2 \\ 2\, D_{1212}\, f_{\boldsymbol{\sigma},12}\, n_1 + (D_{1122}\, f_{\boldsymbol{\sigma},11} + D_{2222}\, f_{\boldsymbol{\sigma},22})\, n_2 \end{bmatrix} \tag{6.42}$$

$$\boldsymbol{b} = \begin{bmatrix} (D_{1111}\, g_{\boldsymbol{\sigma},11} + D_{1122}\, g_{\boldsymbol{\sigma},22})\, n_1 + 2\, D_{1212}\, g_{\boldsymbol{\sigma},12}\, n_2 \\ 2\, D_{1212}\, g_{\boldsymbol{\sigma},12}\, n_1 + (D_{1122}\, g_{\boldsymbol{\sigma},11} + D_{2222}\, g_{\boldsymbol{\sigma},22})\, n_2 \end{bmatrix} \tag{6.43}$$

where $f_{\boldsymbol{\sigma},ij}$ and $g_{\boldsymbol{\sigma},ij}$ are derivatives of the yield function and the plastic potential with respect to stress components σ_{ij}.

6.3.3 Refined localization analysis

The advantage of the localization condition based on singularity of the localization tensor is that it is easy to derive and has the same general form $\det \boldsymbol{Q}_t = 0$ for any constitutive model—it suffices to use the properly derived tangent stiffness tensor $\boldsymbol{D}_t$ and transform it into the corresponding localization tensor $\boldsymbol{Q}_t = \boldsymbol{n} \cdot \boldsymbol{D}_t \cdot \boldsymbol{n}$. The drawback is that the derivation uses a key assumption that the same tangent stiffness applies on both sides of the discontinuity surface. It is not immediately clear whether this is indeed the most critical case. One can easily imagine localized solutions for which plastic yielding takes place on one side and elastic unloading on the other side, and then the stiffness tensors are obviously different.

For the flow theory of plasticity with a smooth yield surface and smooth plastic potential, it is possible to perform a more general analysis that does not make any additional restrictive assumptions. The rates of the plastic multiplier in regions separated by the discontinuity surface are expressed as

$$\dot{\lambda}^+ = \frac{1}{h}\langle \boldsymbol{f}_{\boldsymbol{\sigma}} : \boldsymbol{D}_e : \dot{\boldsymbol{\varepsilon}}^+ \rangle \tag{6.44}$$

$$\dot{\lambda}^- = \frac{1}{h}\langle \boldsymbol{f}_{\boldsymbol{\sigma}} : \boldsymbol{D}_e : \dot{\boldsymbol{\varepsilon}}^- \rangle \tag{6.45}$$

where $\langle x \rangle$ denotes the positive part of x, which is equal to x if $x > 0$ and to zero otherwise. The corresponding stress rates are then

$$\dot{\boldsymbol{\sigma}}^{+} = \boldsymbol{D}_e : \dot{\boldsymbol{\varepsilon}}^{+} - \frac{1}{h} \langle \boldsymbol{f}_{\boldsymbol{\sigma}} : \boldsymbol{D}_e : \dot{\boldsymbol{\varepsilon}}^{+} \rangle \boldsymbol{D}_e : \boldsymbol{g}_{\boldsymbol{\sigma}} \tag{6.46}$$

$$\dot{\boldsymbol{\sigma}}^{-} = \boldsymbol{D}_e : \dot{\boldsymbol{\varepsilon}}^{-} - \frac{1}{h} \langle \boldsymbol{f}_{\boldsymbol{\sigma}} : \boldsymbol{D}_e : \dot{\boldsymbol{\varepsilon}}^{-} \rangle \boldsymbol{D}_e : \boldsymbol{g}_{\boldsymbol{\sigma}} \tag{6.47}$$

and the traction equilibrium condition can be written in the form

$$\begin{aligned} &\boldsymbol{n} \cdot \boldsymbol{D}_e : \dot{\boldsymbol{\varepsilon}}^{+} - \frac{1}{h} \langle \boldsymbol{f}_{\boldsymbol{\sigma}} : \boldsymbol{D}_e : \dot{\boldsymbol{\varepsilon}}^{+} \rangle \boldsymbol{n} \cdot \boldsymbol{D}_e : \boldsymbol{g}_{\boldsymbol{\sigma}} = \\ &= \boldsymbol{n} \cdot \boldsymbol{D}_e : \dot{\boldsymbol{\varepsilon}}^{-} - \frac{1}{h} \langle \boldsymbol{f}_{\boldsymbol{\sigma}} : \boldsymbol{D}_e : \dot{\boldsymbol{\varepsilon}}^{-} \rangle \boldsymbol{n} \cdot \boldsymbol{D}_e : \boldsymbol{g}_{\boldsymbol{\sigma}} \end{aligned} \tag{6.48}$$

Substituting from (6.29) and making use of the auxiliary tensors introduced in (6.35), we can rewrite condition (6.48) as

$$\boldsymbol{Q}_e \cdot \boldsymbol{m}\dot{e} = \frac{1}{h} \left(\langle \boldsymbol{f}_{\boldsymbol{\sigma}} : \boldsymbol{D}_e : \dot{\boldsymbol{\varepsilon}}^{-} + \boldsymbol{a} \cdot \boldsymbol{m}\dot{e} \rangle - \langle \boldsymbol{f}_{\boldsymbol{\sigma}} : \boldsymbol{D}_e : \dot{\boldsymbol{\varepsilon}}^{-} \rangle \right) \boldsymbol{b} \tag{6.49}$$

Note that $\boldsymbol{Q}_e$ is a regular (invertible) tensor and the right-hand side of (6.49) is a scalar multiple of vector $\boldsymbol{b}$. Therefore, if the problem has a nontrivial solution, the solution must have the form

$$\boldsymbol{m}\dot{e} = c\, \boldsymbol{Q}_e^{-1} \cdot \boldsymbol{b} \tag{6.50}$$

where c is some suitable scalar. Substituting the potential solution (6.50) into the governing equation (6.49), we obtain

$$c\, \boldsymbol{b} = \frac{1}{h} \left(\langle \boldsymbol{f}_{\boldsymbol{\sigma}} : \boldsymbol{D}_e : \dot{\boldsymbol{\varepsilon}}^{-} + c\, \boldsymbol{a} \cdot \boldsymbol{Q}_e^{-1} \cdot \boldsymbol{b} \rangle - \langle \boldsymbol{f}_{\boldsymbol{\sigma}} : \boldsymbol{D}_e : \dot{\boldsymbol{\varepsilon}}^{-} \rangle \right) \boldsymbol{b} \tag{6.51}$$

which is satisfied if

$$h\, c = \langle \boldsymbol{f}_{\boldsymbol{\sigma}} : \boldsymbol{D}_e : \dot{\boldsymbol{\varepsilon}}^{-} + c\, \boldsymbol{a} \cdot \boldsymbol{Q}_e^{-1} \cdot \boldsymbol{b} \rangle - \langle \boldsymbol{f}_{\boldsymbol{\sigma}} : \boldsymbol{D}_e : \dot{\boldsymbol{\varepsilon}}^{-} \rangle \tag{6.52}$$

Up to here, the analysis has covered all possible combinations of processes taking place in the regions around the discontinuity surface (plastic yielding or elastic unloading). To be able to express c, we need to proceed with the analysis case by case. Recall that the first Macauley bracket in (6.52) corresponds to $h\dot{\lambda}^{+}$ and the second to $h\dot{\lambda}^{-}$; see (6.44)–(6.45). Since $h > 0$, the first term is nonzero if $\dot{\lambda}^{+} > 0$, i.e., if the process that takes place on the positive side of the discontinuity is plastic yielding, and the second term is nonzero if $\dot{\lambda}^{-} > 0$, i.e., if plastic yielding takes place on the negative side.

Elastic^{+}/elastic^{-}: If the rate of plastic multiplier vanishes on both sides of the discontinuity, equation (6.52) reduces to

$$h\, c = 0 \tag{6.53}$$

which leads to $c = 0$ and $\boldsymbol{m}\dot{e} = \boldsymbol{0}$, but this does not correspond to a localized solution. This is an expected result, since the elastic localization tensor $\boldsymbol{Q}_e$ is positive definite, and so equation (6.49) cannot have a nontrivial solution if its right-hand side is set to zero.

Plastic$^+$/elastic$^-$: If $\dot\lambda^+ > 0$ and $\dot\lambda^- = 0$, then equation (6.52) gives

$$h\,c = \boldsymbol{f_\sigma} : \boldsymbol{D}_e : \dot{\boldsymbol{\varepsilon}}^- + c\,\boldsymbol{a}\cdot\boldsymbol{Q}_e^{-1}\cdot\boldsymbol{b} \tag{6.54}$$

which leads to

$$c = \frac{\boldsymbol{f_\sigma} : \boldsymbol{D}_e : \dot{\boldsymbol{\varepsilon}}^-}{h - \boldsymbol{a}\cdot\boldsymbol{Q}_e^{-1}\cdot\boldsymbol{b}} \tag{6.55}$$

$$\boldsymbol{m}\dot e = \frac{\boldsymbol{f_\sigma} : \boldsymbol{D}_e : \dot{\boldsymbol{\varepsilon}}^-}{h - \boldsymbol{a}\cdot\boldsymbol{Q}_e^{-1}\cdot\boldsymbol{b}}\boldsymbol{Q}_e^{-1}\cdot\boldsymbol{b} \tag{6.56}$$

The solution is admissible if $\boldsymbol{f_\sigma} : \boldsymbol{D}_e : \dot{\boldsymbol{\varepsilon}}^- \le 0$ and $\boldsymbol{f_\sigma} : \boldsymbol{D}_e : \dot{\boldsymbol{\varepsilon}}^- + c\,\boldsymbol{a}\cdot\boldsymbol{Q}_e^{-1}\cdot\boldsymbol{b} \ge 0$, the latter condition being equivalent to $\boldsymbol{f_\sigma} : \boldsymbol{D}_e : \dot{\boldsymbol{\varepsilon}}^+ \ge 0$. For "reasonable" plasticity models, the product $\boldsymbol{a}\cdot\boldsymbol{Q}_e^{-1}\cdot\boldsymbol{b}$ is always positive, and so c must be positive, which is possible only if the denominator in (6.55) is negative (because the numerator is non-positive). The resulting condition is thus

$$h < \boldsymbol{a}\cdot\boldsymbol{Q}_e^{-1}\cdot\boldsymbol{b} \tag{6.57}$$

Recall that h defined in (6.26) depends only on the current state while tensors $\boldsymbol{a}$, $\boldsymbol{b}$ and $\boldsymbol{Q}_e$ depend on the unit normal $\boldsymbol{n}$, which is arbitrary. Therefore, this type of localization can occur if there exists a unit vector $\boldsymbol{n}$ for which (6.57) holds, in other words, if

$$-\boldsymbol{f_q}\cdot\boldsymbol{h}_\kappa < \max_{\boldsymbol{n}}\left(\boldsymbol{a}\cdot\boldsymbol{Q}_e^{-1}\cdot\boldsymbol{b}\right) - \boldsymbol{f_\sigma} : \boldsymbol{D}_e : \boldsymbol{g_\sigma} \tag{6.58}$$

where the maximum is taken over all unit vectors.

Elastic$^+$/plastic$^-$: Since the choice which side of the discontinuity is referred to as "positive" is arbitrary, this case must be analogous to the previous case and the resulting localization condition must be the same.

Plastic$^+$/plastic$^-$: If the rates of the plastic multiplier on both sides of the discontinuity are positive, then equation (6.52) gives

$$h\,c = c\,\boldsymbol{a}\cdot\boldsymbol{Q}_e^{-1}\cdot\boldsymbol{b} \tag{6.59}$$

which has a nontrivial solution $c \neq 0$ only if

$$h = \boldsymbol{a}\cdot\boldsymbol{Q}_e^{-1}\cdot\boldsymbol{b} \tag{6.60}$$

This can be written as

$$-\boldsymbol{f_q}\cdot\boldsymbol{h}_\kappa = \max_{\boldsymbol{n}}\left(\boldsymbol{a}\cdot\boldsymbol{Q}_e^{-1}\cdot\boldsymbol{b}\right) - \boldsymbol{f_\sigma} : \boldsymbol{D}_e : \boldsymbol{g_\sigma} \tag{6.61}$$

If this is the case, equation (6.59) is satisfied for an arbitrary c, so we can only determine the unit vector

$$\boldsymbol{m} = \frac{\boldsymbol{Q}_e^{-1}\cdot\boldsymbol{b}}{\|\boldsymbol{Q}_e^{-1}\cdot\boldsymbol{b}\|} \tag{6.62}$$

while the magnitude $\dot e$ remains undetermined. The solution is admissible if $\boldsymbol{f_\sigma} : \boldsymbol{D}_e : \dot{\boldsymbol{\varepsilon}}^- \ge 0$ and $\boldsymbol{f_\sigma} : \boldsymbol{D}_e : \dot{\boldsymbol{\varepsilon}}^- + c\,\boldsymbol{a}\cdot\boldsymbol{Q}_e^{-1}\cdot\boldsymbol{b} \ge 0$. The first condition can always be satisfied by a suitable choice of $\dot{\boldsymbol{\varepsilon}}^-$. Since c is arbitrary and $\boldsymbol{a}\cdot\boldsymbol{Q}_e^{-1}\cdot\boldsymbol{b} > 0$, the

second condition is then satisfied for all $c > 0$, and, depending on the particular choice of $\dot{\boldsymbol{\varepsilon}}^-$, it can even be satisfied by a limited range of negative values of c. If c is indeed negative, the fraction on the right-hand side of (6.62), which determines the polarization vector, should be preceded by a negative sign. The cases when $c > 0$ and $\boldsymbol{m}$ is given by (6.62) correspond to higher rates of plastic yielding on the positive side of the discontinuity (as compared to the negative side), while cases when $c < 0$ and $\boldsymbol{m}$ is given by (6.62) with a negative sign correspond to higher rates of plastic yielding on the negative side of the discontinuity. Since the choice of the positive and negative side is arbitrary, we can restrict attention to cases when $c > 0$ and $\boldsymbol{m}$ is given by (6.62), without loss of generality.

Based on the foregoing refined analysis, we can conclude that the general localization condition for the present class of plasticity models reads

$$H \leq H_{crit} \tag{6.63}$$

where

$$H = -\boldsymbol{f}_{\boldsymbol{q}_i} \cdot \boldsymbol{h}_\kappa \tag{6.64}$$

is the generalized plastic modulus and

$$H_{crit} = \max_{\boldsymbol{n}} \left(\boldsymbol{a} \cdot \boldsymbol{Q}_e^{-1} \cdot \boldsymbol{b} \right) - \boldsymbol{f}_{\boldsymbol{\sigma}} : \boldsymbol{D}_e : \boldsymbol{g}_{\boldsymbol{\sigma}} \tag{6.65}$$

is the critical value of the generalized plastic modulus. Both H and H_{crit} may depend on the current state and in general they evolve. As long as H remains above H_{crit}, localization is impossible. When $H = H_{crit}$, there exists one or more special directions $\boldsymbol{n}$ such that a weak discontinuity across a surface with normal $\boldsymbol{n}$ can arise, with plastic yielding on both sides but at different rates of the plastic multiplier. When H becomes smaller than H_{crit}, there is a range of directions for which localization can occur with plastic yielding on one side and elastic unloading on the other.

Alternative expression for the critical hardening modulus Expression (6.65) can be rearranged in an alternative form that turns to be useful for further analysis, in particular when we refer to the plane stress condition.

Substituting the definition of the auxiliar tensors $\boldsymbol{a}$ and $\boldsymbol{b}$ from (6.35) into (6.65), we get

$$H_{crit} = \max_{\boldsymbol{n}} \left(\boldsymbol{f}_{\boldsymbol{\sigma}} : \boldsymbol{D}_e \cdot \boldsymbol{n} \cdot \boldsymbol{Q}_e^{-1} \cdot \boldsymbol{n} \cdot \boldsymbol{D}_e : \boldsymbol{g}_{\boldsymbol{\sigma}} - \boldsymbol{f}_{\boldsymbol{\sigma}} : \boldsymbol{D}_e : \boldsymbol{g}_{\boldsymbol{\sigma}} \right) \tag{6.66}$$

where we have extended the maximization to the second term since it does not depend on the normal $\boldsymbol{n}$. The last expression can be simplified as

$$H_{crit} = \max_{\boldsymbol{n}} \left(\boldsymbol{f}_{\boldsymbol{\sigma}} : \boldsymbol{A}(\boldsymbol{n}) : \boldsymbol{g}_{\boldsymbol{\sigma}} \right) \tag{6.67}$$

where

$$\boldsymbol{A}(\boldsymbol{n}) = \boldsymbol{D}_e \cdot \boldsymbol{n} \cdot \boldsymbol{Q}_e^{-1} \cdot \boldsymbol{n} \cdot \boldsymbol{D}_e - \boldsymbol{D}_e \tag{6.68}$$

is a fourth-order tensor that depends only on the elastic properties and the normal $\boldsymbol{n}$.

If we define the quantity $\mathcal{H}$ as

$$\mathcal{H} = \boldsymbol{f}_{\boldsymbol{\sigma}} : \boldsymbol{A}(\boldsymbol{n}) : \boldsymbol{g}_{\boldsymbol{\sigma}} \tag{6.69}$$

the determination of the critical hardening modulus reduces to maximization of $\mathcal{H}$ over all unit vectors $\boldsymbol{n}$, namely

$$H_{crit} = \max_{\boldsymbol{n}} \left(\mathcal{H}(\boldsymbol{n})\right) \tag{6.70}$$

Simple expressions of the tensor $\boldsymbol{A}$ can be derived under the assumption of plane stress condition. In the case of isotropic material, the elastic stiffness tensor, expressed in subscript notation, is given by

$$\boldsymbol{D}_{e,ijkl} = G\left(\frac{2\nu}{1-\nu}\delta_{ij}\delta_{kl} + \delta_{ik}\delta_{jl} + \delta_{jk}\delta_{il}\right) \tag{6.71}$$

where the indices i, j, k, and l take values 1 and 2. In this case, the inverse of the localization tensor is

$$\left(\boldsymbol{Q}_e^{-1}\right)_{ij} = \frac{1}{G}\left(\delta_{ij} - \frac{1+\nu}{2}n_i n_j\right) \tag{6.72}$$

from which we obtain

$$\begin{aligned}\left[(\boldsymbol{D}_e \cdot \boldsymbol{n}) \cdot \boldsymbol{Q}_e^{-1} \cdot (\boldsymbol{n} \cdot \boldsymbol{D}_e)\right]_{ijpq} = G\Bigg[&\frac{2\nu^2}{1-\nu}\delta_{ij}\delta_{pq} + 2\nu\left(\delta_{ij}n_p n_q + \delta_{pq}n_i n_j\right) + \\ &+ \delta_{iq}n_j n_p + \delta_{ip}n_j n_q + \delta_{jq}n_i n_p + \delta_{jp}n_i n_q - 2(1+\nu)n_i n_j n_p n_q\Bigg]\end{aligned} \tag{6.73}$$

and

$$\begin{aligned}\boldsymbol{A}_{ijpq} = G\Big[&\delta_{iq}n_j n_p + \delta_{ip}n_j n_q + \delta_{jq}n_i n_p + \delta_{jp}n_i n_q - \delta_{ip}\delta_{jq} - \delta_{iq}\delta_{jp} + \\ &- 2\nu\left(\delta_{ij}\delta_{pq} - \delta_{ij}n_p n_q - \delta_{pq}n_i n_j\right) - 2(1+\nu)n_i n_j n_p n_q\Big]\end{aligned} \tag{6.74}$$

If we express the normal $\boldsymbol{n}$ as function of the angle θ that $\boldsymbol{n}$ forms with the x-axis,

$$\boldsymbol{n} = \begin{bmatrix} \cos\theta \\ \sin\theta \end{bmatrix} = \begin{bmatrix} c \\ s \end{bmatrix} \tag{6.75}$$

the matrix representation for the tensor $\boldsymbol{A}$ is then

$$\boldsymbol{A}(\theta) = -2G(1+\nu)\begin{bmatrix} s^4 & c^2s^2 & -cs^3 \\ c^2s^2 & c^4 & -c^3s \\ -cs^3 & -c^3s & c^2s^2 \end{bmatrix} \tag{6.76}$$

In the case of orthotropic and plane stress material, the elastic stiffness matrix in the plane stress case is given by (6.2) and the matrix representation of tensor $\boldsymbol{A}$ is

$$\boldsymbol{A}(\theta) = -\xi(\theta)\begin{bmatrix} s^4 & c^2s^2 & -cs^3 \\ c^2s^2 & c^4 & -c^3s \\ -cs^3 & -c^3s & c^2s^2 \end{bmatrix} \tag{6.77}$$

where

$$\xi(\theta) = \left(\frac{1}{E_{xx}} s^4 + \left(\frac{1}{G_{xy}} - \frac{2\nu_{xy}}{E_{xx}} \right) s^2 c^2 + \frac{1}{E_{yy}} c^4 \right)^{-1} \tag{6.78}$$

In both cases of isotropic or orthotropic material, therefore, the tensor $\boldsymbol{A}$ has the same structure with the only difference of the parameter ξ, which in the isotropic case is given by

$$\xi = 2G(1+\nu) \tag{6.79}$$

while in the orthotropic case is given by (6.78).

The quantity $\mathcal{H}$ in the general case of orthotropic material under plane stress assumption is given by

$$\mathcal{H} = \boldsymbol{f}_{\boldsymbol{\sigma}}^T \, \boldsymbol{A} \, \boldsymbol{g}_{\boldsymbol{\sigma}} \tag{6.80}$$

where $\boldsymbol{f}_{\boldsymbol{\sigma}}$ and $\boldsymbol{g}_{\boldsymbol{\sigma}}$ are expressed in vectorial form as

$$\boldsymbol{f}_{\boldsymbol{\sigma}} = \begin{bmatrix} f_{\boldsymbol{\sigma},11} \\ f_{\boldsymbol{\sigma},22} \\ 2f_{\boldsymbol{\sigma},12} \end{bmatrix} \qquad \boldsymbol{g}_{\boldsymbol{\sigma}} = \begin{bmatrix} g_{\boldsymbol{\sigma},11} \\ g_{\boldsymbol{\sigma},22} \\ 2g_{\boldsymbol{\sigma},12} \end{bmatrix} \tag{6.81}$$

Therefore, its expression reduces to

$$\mathcal{H}(\theta) = -\xi(\theta) \left(f_{\boldsymbol{\sigma},11} \, s^2 - 2f_{\boldsymbol{\sigma},12} \, s \, c + f_{\boldsymbol{\sigma},22} \, c^2 \right) \left(g_{\boldsymbol{\sigma},11} \, s^2 - 2g_{\boldsymbol{\sigma},12} \, s \, c + g_{\boldsymbol{\sigma},22} \, c^2 \right) \tag{6.82}$$

which, in case of associated flow rule, simplifies in

$$\mathcal{H}(\theta) = -\xi(\theta) \left(f_{\boldsymbol{\sigma},11} \, s^2 - 2f_{\boldsymbol{\sigma},12} \, s \, c + f_{\boldsymbol{\sigma},22} \, c^2 \right)^2 \tag{6.83}$$

6.4 Localization analysis for uniaxial stress states

For uniaxial stress, the stress tensor matrix in the Oxy reference frame, where x and y are the orthotropy axes, is given by

$$\boldsymbol{\sigma}(\bar{\sigma}, \phi) = \boldsymbol{Q} \, \hat{\boldsymbol{\sigma}} \, \boldsymbol{Q}^T \tag{6.84}$$

where

$$\hat{\boldsymbol{\sigma}} = \begin{bmatrix} \bar{\sigma} & 0 \\ 0 & 0 \end{bmatrix} \qquad \boldsymbol{Q} = \begin{bmatrix} \cos\phi & -\sin\phi \\ \sin\phi & \cos\phi \end{bmatrix} \tag{6.85}$$

Here, $\bar{\sigma}$ is the magnitude of the uniaxial stress and ϕ is the angle that the stress direction forms with the x-axis.

The localization analysis for uniaxial stresses is carried out separately for tension and compression as follows. For every loading direction ϕ, the stress magnitude $\bar{\sigma}$ is determined as the one which activates plastic flow, i.e., the one which satisfies the condition $f_i = 0$, where f_i is yield function for tension ($i = t$) or compression ($i = c$), respectively. Once the stress state is defined, one can maximize the hardening modulus spectrum given by (6.82) over all angles $\theta \in [0, \pi)$ and determine the critical hardening modulus H_{crit}. Then it must be checked whether the current hardening modulus is lower than or equal to the critical one. If the localization condition is fulfilled, the "natural" localization angle θ_{loc} is determined as the one corresponding to the critical hardening modulus. The polarization vector

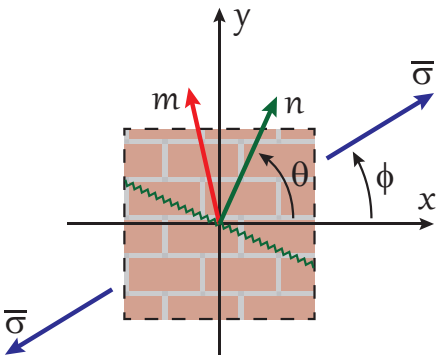

Figure 6.2: Localization ($\boldsymbol{n}$) and polarization ($\boldsymbol{m}$) vectors for uniaxial stress $\bar{\sigma}$ inclined by ϕ with respect the material x-axis

$\boldsymbol{m}$, namely the eigenvector of the elastoplastic localization tensor corresponding to the zero eigenvalue, characterizes the failure mode, ranging from tensile splitting (mode I) with $\boldsymbol{m} = \boldsymbol{n}$ to shear slip (mode II) with $\boldsymbol{m}$ perpendicular to $\boldsymbol{n}$ to crushing (compaction, compressive mode I) with $\boldsymbol{m} = -\boldsymbol{n}$. According to this procedure, the sign of $\boldsymbol{m}$ is lost since eigenvectors are determined up to a multiplicative constant. The sign of $\boldsymbol{m}$ can be recovered by imposing the condition that the work produced by the actual stress on the strain jump is positive, namely

$$\boldsymbol{\sigma} : (\dot{\boldsymbol{\varepsilon}}^{+} - \dot{\boldsymbol{\varepsilon}}^{-}) = \boldsymbol{\sigma} : (\boldsymbol{n} \otimes \boldsymbol{m})_{sym} > 0 \tag{6.86}$$

If the current hardening modulus is exactly equal to the critical one, localization is usually possible only for one angle θ in the interval $[0, \pi)$. However, if the current hardening modulus is strictly lower than the critical one, there exists a range of values of θ for which the localization condition is satisfied. In an idealized problem when the localized solution bifurcates from a uniform one, the actual band direction is arbitrary within this range. The ambiguity could be removed by postulating a variational principle, but its justification is somewhat questionable for models dealing with non-associated flow rules.

In a real problem with nonuniform stress, the localized band often evolves gradually and its trajectory can be constrained by boundary conditions. The range of angles θ for which the localization condition is satisfied provides some additional information on potential directions of the localized band.

In case of uniaxial stress along the material axes, the expression of the hardening modulus spectrum (6.82) further simplifies. For tension along x-axis, the derivative of the yield function and the plastic potential with respect to the stress (at the onset of plastic flow) are given by

$$\boldsymbol{f}_{\boldsymbol{\sigma}} = \boldsymbol{g}_{\boldsymbol{\sigma}} = \begin{bmatrix} 1 \\ 0 \\ 0 \end{bmatrix} \tag{6.87}$$

Therefore, the expression (6.82) reduces to

$$\mathcal{H}_{t,x}(\theta) = -\xi(\theta)\, \sin^4 \theta \tag{6.88}$$

Analogously, for tension along the y-axis the stress derivatives are given by

$$\boldsymbol{f}_{\boldsymbol{\sigma}} = \boldsymbol{g}_{\boldsymbol{\sigma}} = \begin{bmatrix} 0 \\ 1 \\ 0 \end{bmatrix} \tag{6.89}$$

and the expression (6.82) reduces to

$$\mathcal{H}_{t,y}(\theta) = -\xi(\theta)\, \cos^4 \theta \tag{6.90}$$

For compression along the x-axis, the derivative $\boldsymbol{f}_{\boldsymbol{\sigma}}$ at the onset of plastic flow is given by

$$\boldsymbol{f}_{\boldsymbol{\sigma}} = \boldsymbol{g}_{\boldsymbol{\sigma}} = \begin{bmatrix} 1/\mu \\ \beta\, \mu/2 \\ 0 \end{bmatrix} \tag{6.91}$$

where

$$\mu = \sqrt{\frac{\sigma_{c,x}}{\sigma_{c,y}}} \tag{6.92}$$

Therefore, the expression (6.83) reduces to

$$\mathcal{H}_{c,x}(\theta) = -\xi(\theta) \left(\frac{1}{\mu} \sin^2 \theta + \frac{\beta\mu}{2} \cos^2 \theta \right)^2 \tag{6.93}$$

On the other hand, for compression along the y-axis the stress derivatives are

$$\boldsymbol{f}_{\boldsymbol{\sigma}} = \boldsymbol{g}_{\boldsymbol{\sigma}} = \begin{bmatrix} \beta/(2\mu) \\ \mu \\ 0 \end{bmatrix} \tag{6.94}$$

and the hardening modulus spectrum is

$$\mathcal{H}_{c,y}(\theta) = -\xi(\theta) \left(\frac{\beta}{2\mu} \sin^2 \theta + \mu\, \cos^2 \theta \right)^2 \tag{6.95}$$

The graphs of the hardening modulus spectra for uniaxial tension and compression along x- and y-axis as function of the angle θ are shown in Figure 6.3.

The material parameters considered are the ones reported in Table 6.1, which have been calibrated by Lourenço (Lourenço 1995) on an experimental test on a hollow clay brick masonry wall (Ganz and Thurlimann 1983). In those cases, the critical hardening modulus is equal to zero. Therefore, localization can occur at the onset of plastic flow for tension, since the tensile behavior is characterized by abrupt exponential softening, and starting from the peak of the compressive yield stress for compression.

For uniaxial tension, the value of the critical hardening modulus is obtained for $\theta = 0$ for $\phi = 0$ (tension along x-axis) and for $\theta = \pi/2$ for $\phi = \pi/2$ (tension along y-axis). On the other hand, for uniaxial compression, the maximum value of the hardening modulus is attained for two angles θ, which are symmetric with respect to the stress angle ϕ. In particular, for uniaxial compression along x-axis ($\phi = 0$), the localization angles are $\theta_{loc} \simeq \pm\pi/8$, while for uniaxial compression along y-axis ($\phi = \pi/2$), the localization angles are $\theta_{loc} \simeq \pi/2 \pm 5/16\pi$.

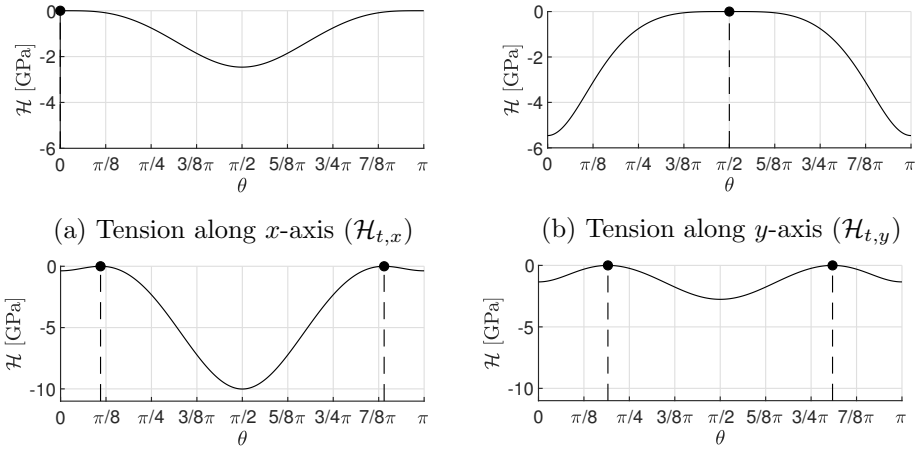

(a) Tension along x-axis ($\mathcal{H}_{t,x}$)

(b) Tension along y-axis ($\mathcal{H}_{t,y}$)

(c) Compression along x-axis ($\mathcal{H}_{c,x}$)

(d) Compression along y-axis ($\mathcal{H}_{c,y}$)

Figure 6.3: Hardening modulus spectra for uniaxial stresses aligned with the material axes

Elastic parameters				**Tensile parameters**				
E_{xx} [GPa]	E_{yy} [GPa]	ν_{xy} [-]	G_{xy} [GPa]	$f_{t,x}$ [MPa]	$f_{t,y}$ [MPa]	$G_{t,x}$ [N/mm]	$G_{t,y}$ [N/mm]	α [-]
2.46	5.46	0.18	1.13	0.28	0.05	0.02	0.02	1.73

Compressive parameters						
$f_{c,x}$ [MPa]	$f_{c,y}$ [MPa]	$G_{c,x}$ [N/mm]	$G_{c,y}$ [N/mm]	β [-]	γ [-]	κ_p [-]
1.87	7.61	5.0	10.0	-1.05	1.20	$8{\cdot}10^{-4}$

Table 6.1: Mechanical parameters considered for localization analysis

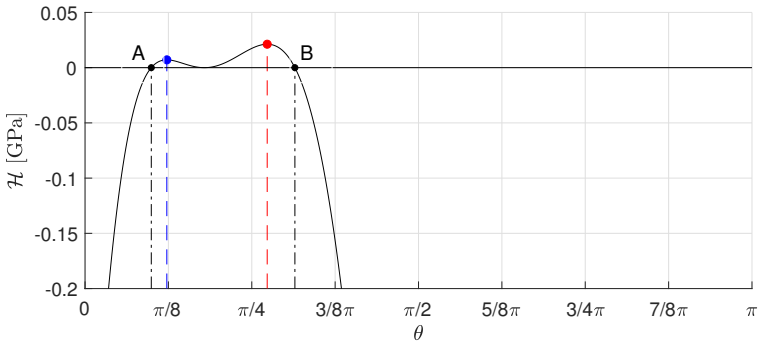

Figure 6.4: Hardening modulus spectrum for uniaxial tension for $\phi = \pi/32$

The localization analysis is then extended to the generic case of uniaxial tension or compression inclined by an angle ϕ with respect to the x-axis, with $\phi \in [0, \pi/2]$. Except for the particular case of uniaxial tension along the material axes, the critical hardening moduli always exhibit two local maxima which are greater than zero in the case of uniaxial tension (Figure 6.6), and equal to zero in the case of uniaxial compression, due to the associated plastic flow in compression. Figure 6.4 shows the particular case of uniaxial tension with $\phi = \pi/32$, where the blue and red dots highlight the location of the two local maxima, and the black dots labeled with A and B pointed out the angle range where the hardening modulus is positive.

For **uniaxial tension**, the influence of the stress angle ϕ on the localization angle is shown in Figure 6.5, where the localization angles corresponding to the two peaks are pointed out with solid blue and red lines. The fan between the dash-dotted lines denote the range of localization angles for which the hardening moduli are greater than zero, and the isolines give additional information about the hardening modulus values for each couple $(\phi\,;\,\theta)$. Figure 6.6 represents the value of the critical hardening modulus for each stress angle ϕ, from which we can see that the critical hardening modulus functions associated to the two solutions differs. The two graphs intersect at $\phi_0 \simeq 13\pi/256$. For $0 < \phi < \phi_0$ the red line, which corresponds to the second maximum (H_2), is above the other one (H_1), and viceversa for $\phi_0 < \phi < \pi/2$. This gives information on the most likely localization angle, which is associated to the solution having the highest critical hardening modulus.

The vectors normal to the two possible weak discontinuity surfaces are inclined with respect to the tension angle, as we can see from Figure 6.7 that represents the difference between the localization angle θ and the stress angle ϕ varying the stress angle. Polarization vectors for both surfaces are close to the corresponding normals since their scalar product is close to the unity for every tension angle (Figure 6.8).

Figure 6.9 gives a visual representation of the localization band directions and polarization vectors for a selected set of stress angles.

In the case of **uniaxial compression**, the hardening modulus spectrum is given by (6.83), here reported for convenience

$$\mathcal{H}(\theta) = -\xi(\theta)\left(f_{\boldsymbol{\sigma},11}\, s^2 - 2 f_{\boldsymbol{\sigma},12}\, s\, c + f_{\boldsymbol{\sigma},22}\, c^2\right)^2 \tag{6.96}$$

Since the parameter $\xi(\theta)$ is non-negative for the chosen set of mechanical parame-

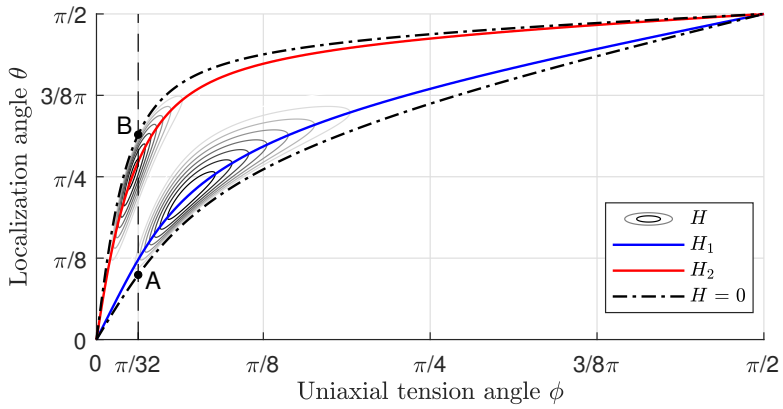

Figure 6.5: Localization angles for uniaxial tension varying stress angle ϕ

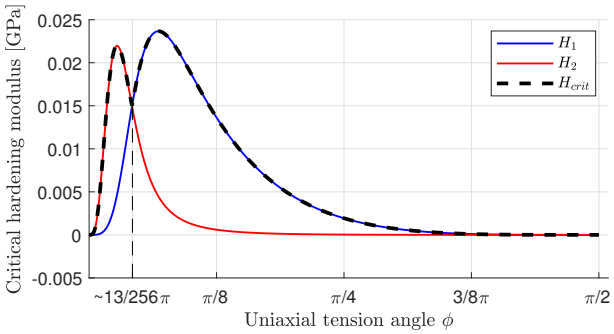

Figure 6.6: Critical hardening moduli for uniaxial tension varying stress angle ϕ

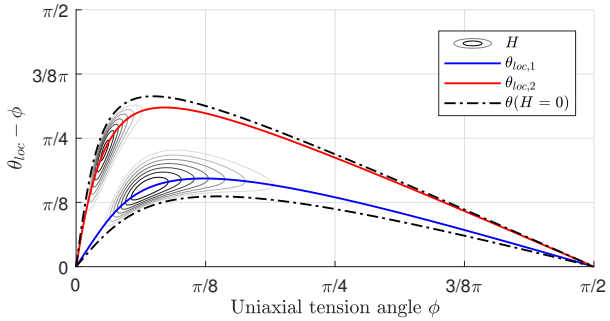

Figure 6.7: Difference between localization angle and stress angle for uniaxial tension

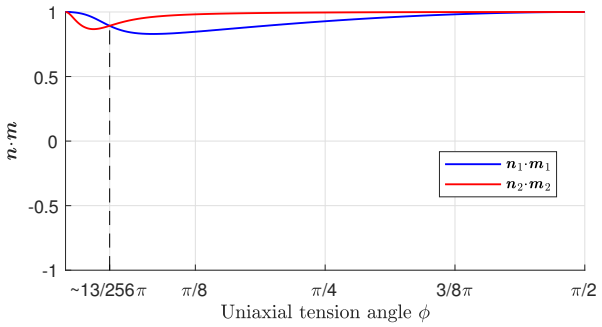

Figure 6.8: Scalar product between normal $\boldsymbol{n}$ and polarization vector $\boldsymbol{m}$ for uniaxial tension

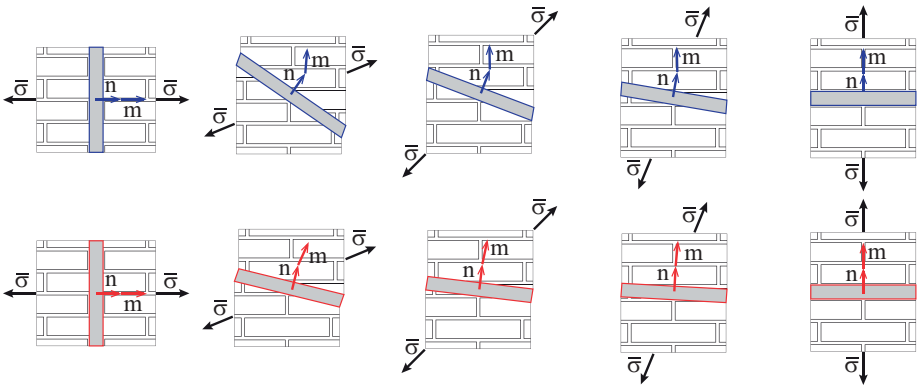

Figure 6.9: Localization bands for uniaxial tension, $\phi = \{0, \pi/8, \pi/4, 3/8\pi, \pi/2\}$

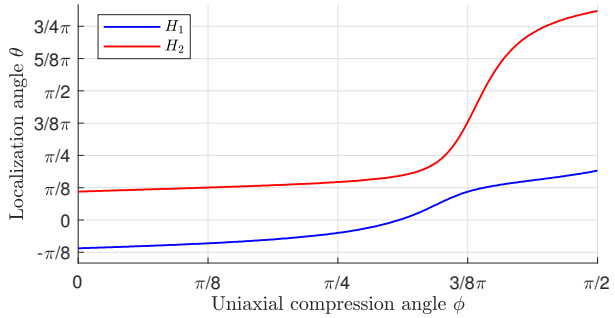

Figure 6.10: Localization angles for uniaxial compression varying stress angle ϕ

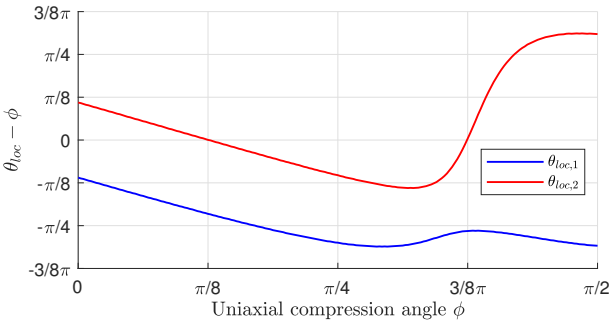

Figure 6.11: Difference between localization angle and stress angle for uniaxial compression

ters, the quantity is always non-positive. Therefore, the maxima of the hardening modulus spectrum are also non-positive.

Figure 6.10 shows the dependence of localization angles on the uniaxial compression angle, where the two localization angles are plotted with solid blue and red lines.

The difference between the localization angles and the uniaxial compression angle is reported in Figure 6.11.

Figure 6.12 shows that the scalar products between the vectors $\boldsymbol{n}$ and polarization vectors $\boldsymbol{m}$ corresponding to the two discontinuity surfaces coincide. Moreover, one can see that the product $\boldsymbol{n} \cdot \boldsymbol{m}$ turns out to be positive for stress angles close to $\pi/2$, which means that the we may have dilating shear bands under compression.

Eventually, we report a visual representation of the localization band directions and polarization vectors for some selected values of stress angles in Figure 6.13.

The theoretically predicted localization band directions have been compared to the ones obtained from numerical simulations on rectangular specimens composed of 61×121 finite elements. The specimen bottom nodes are fixed in the vertical direction, while only the left bottom node is fixed in the horizontal direction. The specimens are loaded by prescribed vertical displacements at the top to generate uniform states of vertical tension or compression. The horizontal and vertical mate-

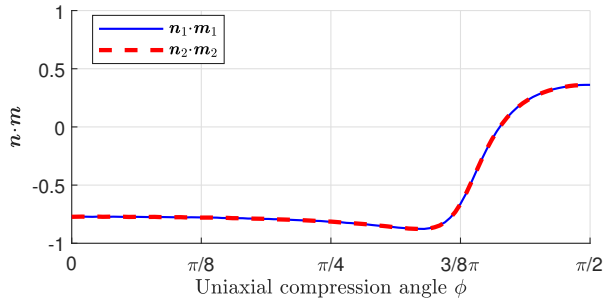

Figure 6.12: Scalar product between normal $\boldsymbol{n}$ and polarization vector $\boldsymbol{m}$ for uniaxial compression

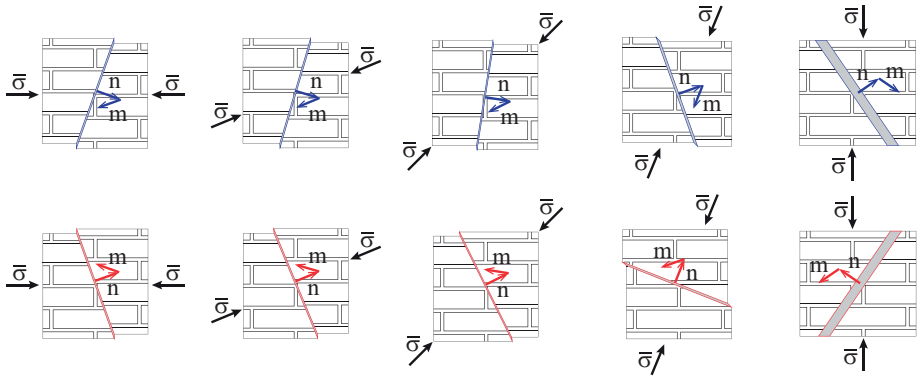

Figure 6.13: Localization bands for uniaxial compression, $\phi = \{0, \pi/8, \pi/4, 3/8\pi, \pi/2\}$

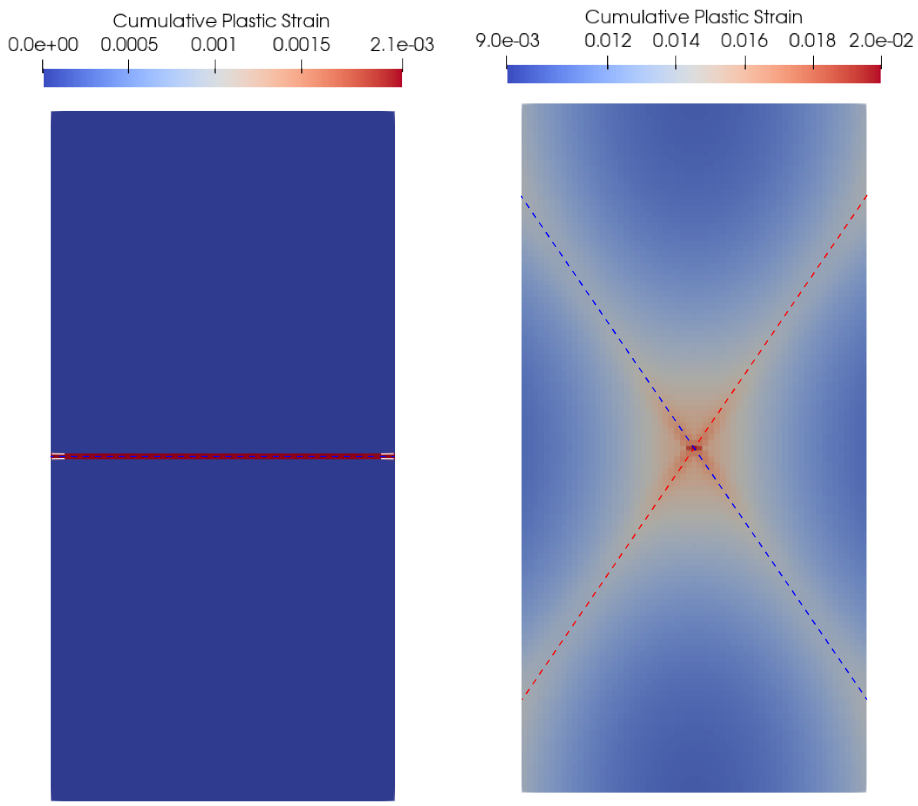

(a) Vertical tension (b) Vertical compression

Figure 6.14: Numerical simulations on a specimen composed of 61 × 121 finite elements.

rial axes coincide with the corresponding global directions. The material properties are uniform in the specimen, except for the central finite element having 10% lower yield strength to trigger the localization.

We perform the numerical simulations through the OOFEM finite element code (Patzák and Bittnar 2001). The implementation of Lourenço's constitutive model into the OOFEM code has been part of the work.

The theoretic localization bands are $\theta_{loc} = 0$ for vertical tension, while for vertical compression we have a double solution $\theta_{loc,1} \simeq 3\pi/16$ and $\theta_{loc,2} \approx 13\pi/16$. For both tensile (Figure 6.14a) and compression (Figure 6.14b) cases, we report the plot of the cumulative plastic strain whose localization exhibit a perfect match with ones predicted theoretically, reported in Figure 6.14 with dashed lines.

6.5 Localization analysis for biaxial stress states

In case of biaxial stress states, we characterize the stress state by the ratio between principal stresses and by the rotation of the principal axes with respect to the material. It is useful to express the ratio between principal stresses as the tangent

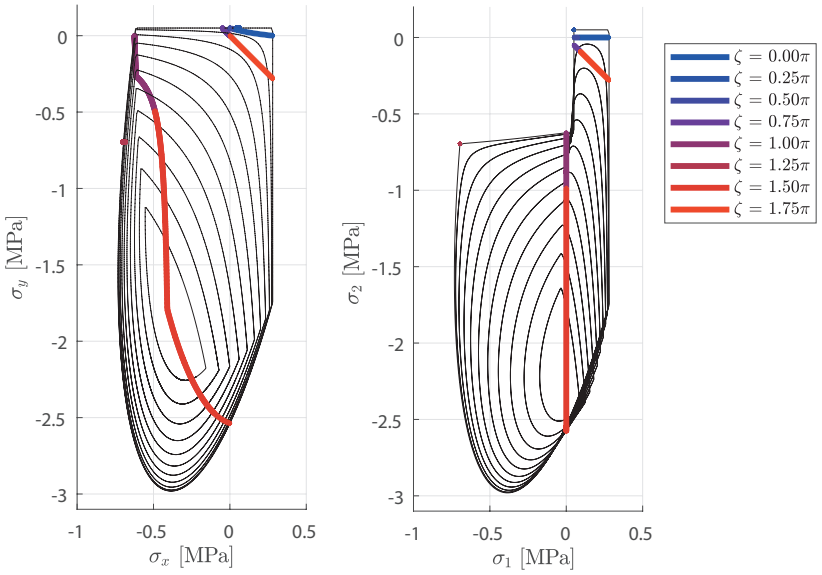

Figure 6.15: Yielding surfaces representations in the plane σ_{xx}-σ_{yy} and σ_1-σ_2

of an angle, which is called the biaxiality angle, namely

$$\tan\zeta = \frac{\sigma_2}{\sigma_1} \tag{6.97}$$

so that one can write

$$\sigma_1 = \bar{\sigma}\cos(\zeta) \tag{6.98}$$
$$\sigma_2 = \bar{\sigma}\sin(\zeta) \tag{6.99}$$

where $\bar{\sigma}$ is the stress magnitude. The matrix representation of the stress state in the Oxy reference frame is given by

$$\boldsymbol{\sigma}\,(\bar{\sigma},\zeta,\phi) = \boldsymbol{Q}(\phi)\,\hat{\boldsymbol{\sigma}}(\bar{\sigma},\zeta)\,\boldsymbol{Q}(\phi)^T \tag{6.100}$$

where

$$\hat{\boldsymbol{\sigma}}(\bar{\sigma},\zeta) = \begin{bmatrix} \sigma_1 & 0 \\ 0 & \sigma_2 \end{bmatrix} \qquad \boldsymbol{Q}(\phi) = \begin{bmatrix} \cos\phi & -\sin\phi \\ \sin\phi & \cos\phi \end{bmatrix} \tag{6.101}$$

The classical representation of the failure surfaces is in the plane of the normal stress components σ_{xx} and σ_{yy}, for fixed values of the tangential stress τ_{xy}. However, it is useful to represent the yield surfaces in the plane of principal stresses for various values of the angle ϕ. Figure 6.15 represents, in both reference frames, the yielding surface and the stress state trajectories for fixed values of biaxiality angles ζ varying the stress angle ϕ.

The localization analysis procedure is developed as in the uniaxial stress case by determining the value of $\bar{\sigma}$ at the onset of plastic flow for any given biaxiality and stress angle. In order to determine the range of variation of these parameters, we can restrict the stress angle in the range $0 \leq \phi \leq \pi/4$ and we can say that

the first principal axis is the one that is closer to the horizontal direction, and this also determines how the principal stresses are numbered. Consequently, we have to relax the constraint $\sigma_1 \geq \sigma_2$ and the biaxiality angle can be taken in the range $0 \leq \zeta < 2\pi$.

Figure 6.16a shows the dependence of the localization angle on the stress state angle ϕ computed for several biaxiality angles ζ, while in Figure 6.16b the critical hardening modulus values are represented, and the scalar product between normal $\boldsymbol{n}$ and polarization vector $\boldsymbol{m}$ in reported in Figure 6.16c. The chosen values of ζ correspond to the special cases of uniaxial tension ($\zeta \in \{0, \pi/2\}$), uniaxial compression ($\zeta \in \{\pi, 3\pi/2\}$), biaxial tension ($\zeta = \pi/4$), biaxial compression ($\zeta = 7\pi/4$). Moreover, the special cases of opposite principal stresses having the same magnitude, namely $\zeta \in \{3\pi/4, 5\pi/4\}$, are considered.

These results, although difficult to read, lead to the conclusion that failure occurs mainly due to tensile limit attainment, while we have failure in compression only for some specific cases. From uniaxial stress analysis we know that localization due to tensile failure is characterized by a positive hardening modulus and a $\boldsymbol{n} \cdot \boldsymbol{m}$ product close to the unity. Moreover, the critical hardening moduli for compressive failure cannot be positive due to the associated plastic flow. The graphs shown in Figure 6.16b and 6.16c verify that tensile failure occurs for most of the considered cases. Compressive failure occurs just for $\zeta = \pi$ (for $0 < \phi < \pi/6$), for $\zeta = 5\pi/4$ (for any ϕ), and for $\zeta = 3\pi/2$ (for $0 < \phi < 3\pi/16$).

In particular, tensile failure can happen even in the case of uniaxial compression. Figures 6.17 and 6.18 show the trajectories of uniaxial compression stress states for κ_c equal to 0 and κ_p, respectively. The figures show that tensile failure occurs for a certain range of uniaxial compression angles ϕ. The range further increases at the hardening variable peak ($\kappa_c = \kappa_p$) when the compressive surface expands to its maximum size.

6.6 Remarks

In this chapter, a localization analysis of Lourenço's model has been performed. The study has been restricted to the case of a regular point on the yielding surface, where the yield function gradient and the plastic flow direction are uniquely defined. The special cases of the vertex of the tensile surface and the intersection of yielding surfaces will be treated in a future work.

The necessary condition for localization has been formulated first through a simplified procedure, under the assumption that the same tangent stiffness is applied at both sides of the discontinuity. However, this assumption is not always verified as localized solutions can also occur in the case of plastic loading on one side and elastic unloading on the other side, and it is not immediately clear which case is the most critical. Then, the analysis was extended by removing the aforementioned assumption. A more general localization condition for the present class of plasticity models has been elaborated, based on the comparison between the current plastic modulus and the critical one.

The localization properties of Lourenço's model have first been determined under uniaxial stress states. The closed-form expressions of the critical hardening moduli were found in the case of uniaxial stresses aligned with the material axes. It was observed that, except for the particular case of uniaxial tension along the material axes, the critical hardening modulus, as a function of the normal to the

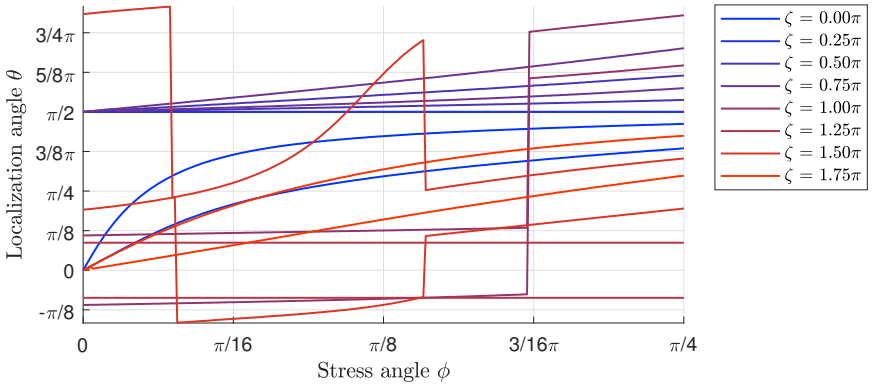

(a) Localization angles varying stress angle ϕ

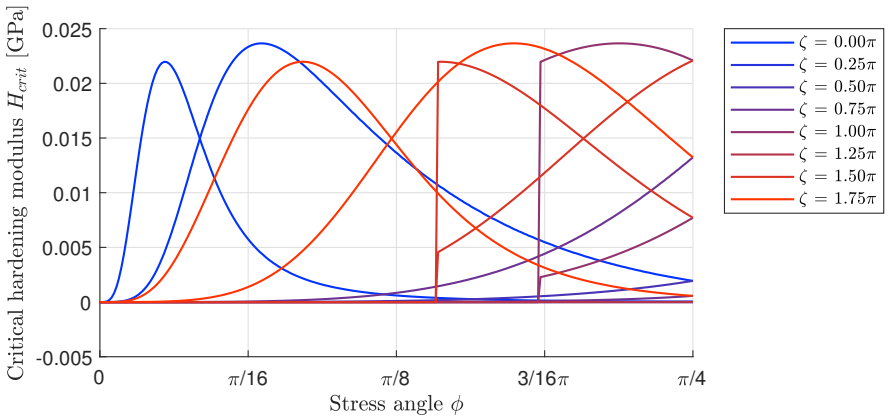

(b) Critical hardening modulus varying stress angle ϕ

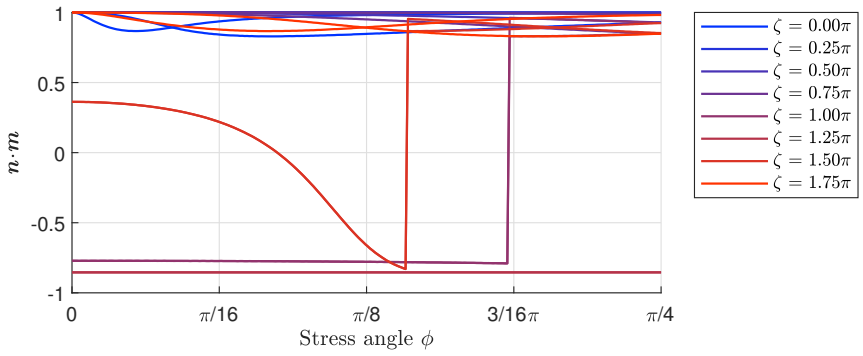

(c) Scalar product between normal $\boldsymbol{n}$ and polarization vector $\boldsymbol{m}$

Figure 6.16: Localization analysis for biaxial stress states for several angles ζ

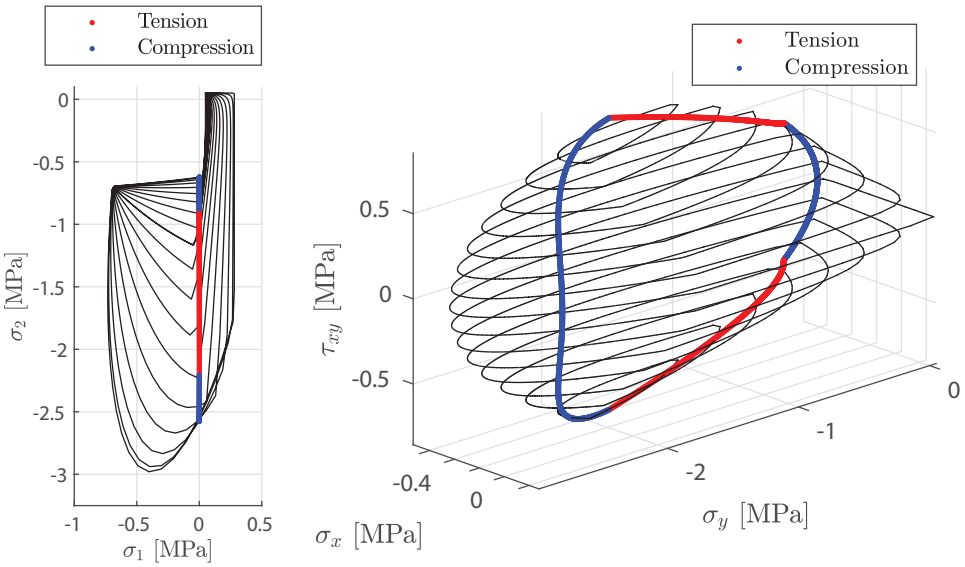

Figure 6.17: Uniaxial compression stress trajectory on the yielding surfaces for $\kappa_c = 0$

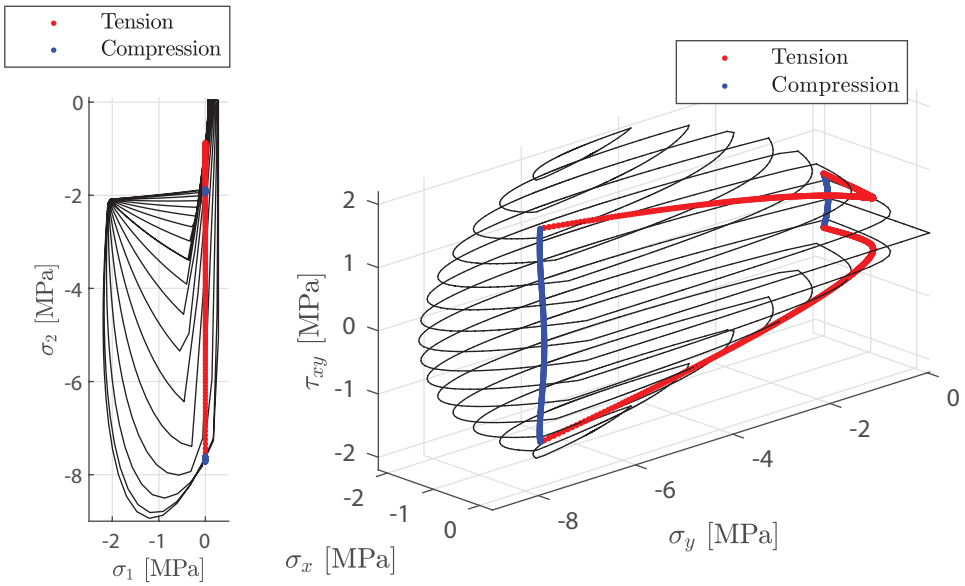

Figure 6.18: Uniaxial compression stress trajectory on the yielding surfaces for $\kappa_c = \kappa_p$

discontinuity surface, has two local maxima which lead to two possible localization angle. The normals to the discontinuity surfaces are almost aligned with the stress directions in the case of uniaxial tension, while two inclined bands tend to form for uniaxial compression. It was noticed that dilating bands can form even for compression when the stress direction is close to the vertical axis, i.e., the strong axis.

The theoretical predictions have been compared to numerical simulations. Lourenço's model has been implemented into OOFEM, an open-source finite element solver. Numerical simulations on virtual specimens subjected to vertical tension and compression show a perfect match in terms of localization surface directions.

The study was then extended to biaxial stress states. It has been shown that the results are not far from the ones obtained for uniaxial tension. This is mainly caused by the associate plastic flow rule for the compressive surface, combined with the hardening law in compression, which has an initial hardening branch, followed by a softening part. Since localization for associate plastic flow can occur only after the hardening peak, it turns out that the most likely mechanism is the tensile one, which can occur starting from the onset of plastic flow.

6.A Derivatives of plastic flow tensors for Lourenço's model

The model equations of the general formulation of multi-surface elastoplasticity are reported in the following.

Elastic-plastic split:

$$\boldsymbol{\varepsilon} = \boldsymbol{\varepsilon}_e + \boldsymbol{\varepsilon}_p \tag{6.102}$$

Stress-strain law for the elastic part:

$$\boldsymbol{\sigma} = \boldsymbol{D}_e \, \boldsymbol{\varepsilon}_e \tag{6.103}$$

Plastic admissibility conditions:

$$f_t(\boldsymbol{\sigma}, \boldsymbol{q}_t) \leq 0, \qquad f_c(\boldsymbol{\sigma}, \boldsymbol{q}_c) \leq 0 \tag{6.104}$$

Flow rule:

$$\dot{\boldsymbol{\varepsilon}}_p = \dot{\lambda}_t \frac{\partial g_t(\boldsymbol{\sigma}, \boldsymbol{q}_t)}{\partial \boldsymbol{\sigma}} + \dot{\lambda}_c \frac{\partial f_c(\boldsymbol{\sigma}, \boldsymbol{q}_c)}{\partial \boldsymbol{\sigma}} \tag{6.105}$$

$$\dot{\lambda}_t \geq 0, \qquad \dot{\lambda}_c \geq 0 \tag{6.106}$$

Complementarity conditions:

$$\dot{\lambda}_t f_t(\boldsymbol{\sigma}, \boldsymbol{q}_t) = 0, \qquad \dot{\lambda}_c f_c(\boldsymbol{\sigma}, \boldsymbol{q}_c) = 0 \tag{6.107}$$

Hardening law:

$$\dot{\kappa}_t = \dot{\lambda}_t \tag{6.108}$$

$$\dot{\kappa}_c = \dot{\lambda}_c \tag{6.109}$$

$$\boldsymbol{q}_t = \boldsymbol{h}_t(\kappa_t) \tag{6.110}$$

$$\boldsymbol{q}_c = \boldsymbol{h}_c(\kappa_c) \tag{6.111}$$

The strain-like hardening variables can be recast in the following vector

$$\boldsymbol{\kappa} = \begin{bmatrix} \kappa_t \\ \kappa_c \end{bmatrix} \tag{6.112}$$

and the yield functions, plastic potential, and functions that describe the hardening-softening behavior are given by

$$f_t(\boldsymbol{\sigma}, \boldsymbol{q}_t) = \left((\boldsymbol{\sigma} - \boldsymbol{q}_t)^T \boldsymbol{P}_t (\boldsymbol{\sigma} - \boldsymbol{q}_t)\right)^{1/2} + \boldsymbol{\pi}^T (\boldsymbol{\sigma} - \boldsymbol{q}_t) \tag{6.113}$$

$$f_c(\boldsymbol{\sigma}, \boldsymbol{q}_c) = \left(\boldsymbol{\sigma}^T \boldsymbol{P}_c(\boldsymbol{q}_c) \boldsymbol{\sigma}\right)^{1/2} - \sqrt{\sigma_{c,x}\sigma_{c,y}} \tag{6.114}$$

$$g_t(\boldsymbol{\sigma}, \boldsymbol{q}_t) = \left((\boldsymbol{\sigma} - \boldsymbol{q}_t)^T \boldsymbol{P}_g (\boldsymbol{\sigma} - \boldsymbol{q}_t)\right)^{1/2} + \boldsymbol{\pi}^T (\boldsymbol{\sigma} - \boldsymbol{q}_t) \tag{6.115}$$

$$\boldsymbol{h}_t(\kappa_t) = \begin{bmatrix} \sigma_{t,x}(\kappa_t) \\ \sigma_{t,y}(\kappa_t) \\ 0 \end{bmatrix} \tag{6.116}$$

$$\boldsymbol{h}_c(\kappa_c) = \begin{bmatrix} \sigma_{c,x}(\kappa_c) \\ \sigma_{c,y}(\kappa_c) \\ 0 \end{bmatrix} \tag{6.117}$$

in which

$$\sigma_{t,i}(\kappa_t) = f_{t,i} \exp\left(-\frac{h f_{t,i}}{G_{ft,i}} \kappa_t\right) \tag{6.118}$$

$$\sigma_{c,i}(\kappa_c) = \begin{cases} \sigma_{i,i} + (\sigma_{p,i} - \sigma_{i,i}) \sqrt{\dfrac{2\kappa_c}{\kappa_p} - \dfrac{\kappa_c^2}{\kappa_p^2}} & \kappa_c < \kappa_p \\ \sigma_{p,i} + (\sigma_{m,i} - \sigma_{p,i}) \left(\dfrac{\kappa_c - \kappa_p}{\kappa_{m,i} - \kappa_p}\right)^2 & \kappa_p < \kappa_c < \kappa_{m,i} \\ \sigma_{r,i} + (\sigma_{m,i} - \sigma_{r,i}) \exp\left(2 \dfrac{(\kappa_c - \kappa_{m,i})(\sigma_{m,i} - \sigma_{p,i})}{(\kappa_{m,i} - \kappa_p)(\sigma_{m,i} - \sigma_{r,i})}\right) & \kappa_c > \kappa_{m,i} \end{cases} \tag{6.119}$$

Auxiliary matrices $\boldsymbol{P}_t$, $\boldsymbol{P}_g$, $\boldsymbol{P}_c$ and $\boldsymbol{\pi}$ are defined as

$$\boldsymbol{P}_t = \begin{bmatrix} 1/4 & -1/4 & 0 \\ -1/4 & 1/4 & 0 \\ 0 & 0 & \alpha \end{bmatrix} \qquad \boldsymbol{P}_g = \begin{bmatrix} 1/4 & -1/4 & 0 \\ -1/4 & 1/4 & 0 \\ 0 & 0 & 1 \end{bmatrix} \tag{6.120}$$

$$\boldsymbol{P}_c = \begin{bmatrix} \dfrac{\sigma_{c,y}(\kappa_c)}{\sigma_{c,x}(\kappa_c)} & \beta/2 & 0 \\ \beta/2 & \dfrac{\sigma_{c,x}(\kappa_c)}{\sigma_{c,y}(\kappa_c)} & 0 \\ 0 & 0 & \gamma \end{bmatrix} \qquad \boldsymbol{\pi} = \begin{bmatrix} 1/2 \\ 1/2 \\ 0 \end{bmatrix} \tag{6.121}$$

The numerical scheme deals with the following derivatives:

$$\frac{\partial f_t}{\partial \boldsymbol{\sigma}} = \frac{\boldsymbol{P}_t(\boldsymbol{\sigma} - \boldsymbol{q}_t)}{\left((\boldsymbol{\sigma} - \boldsymbol{q}_t)^T \boldsymbol{P}_t (\boldsymbol{\sigma} - \boldsymbol{q}_t)\right)^{1/2}} + \boldsymbol{\pi} \tag{6.122}$$

$$\frac{\partial g_t}{\partial \boldsymbol{\sigma}} = \frac{\boldsymbol{P}_g(\boldsymbol{\sigma} - \boldsymbol{q}_t)}{\left((\boldsymbol{\sigma} - \boldsymbol{q}_t)^T \boldsymbol{P}_g (\boldsymbol{\sigma} - \boldsymbol{q}_t)\right)^{1/2}} + \boldsymbol{\pi} \tag{6.123}$$

$$\frac{\partial f_c}{\partial \boldsymbol{\sigma}} = \frac{\boldsymbol{P}_c \boldsymbol{\sigma}}{(\boldsymbol{\sigma}^T \boldsymbol{P}_c \boldsymbol{\sigma})^{1/2}} \tag{6.124}$$

$$\frac{\partial^2 g_t}{\partial \boldsymbol{\sigma}^2} = \frac{\boldsymbol{P}_g}{((\boldsymbol{\sigma}-\boldsymbol{q}_t)^T \boldsymbol{P}_g (\boldsymbol{\sigma}-\boldsymbol{q}_t))^{1/2}} - \frac{\boldsymbol{P}_g (\boldsymbol{\sigma}-\boldsymbol{q}_t)(\boldsymbol{\sigma}-\boldsymbol{q}_t)^T \boldsymbol{P}_g}{((\boldsymbol{\sigma}-\boldsymbol{q}_t)^T \boldsymbol{P}_g (\boldsymbol{\sigma}-\boldsymbol{q}_t))^{3/2}} \tag{6.125}$$

$$\frac{\partial^2 f_c}{\partial \boldsymbol{\sigma}^2} = \frac{\boldsymbol{P}_c}{(\boldsymbol{\sigma}^T \boldsymbol{P}_c \boldsymbol{\sigma})^{1/2}} - \frac{\boldsymbol{P}_c \boldsymbol{\sigma} \boldsymbol{\sigma}^T \boldsymbol{P}_c}{(\boldsymbol{\sigma}^T \boldsymbol{P}_c \boldsymbol{\sigma})^{3/2}} \tag{6.126}$$

$$\frac{\partial f_t}{\partial \boldsymbol{\kappa}} = \begin{bmatrix} \partial f_t/\partial \kappa_t & 0 \end{bmatrix} \qquad \frac{\partial g_t}{\partial \boldsymbol{\kappa}} = \begin{bmatrix} \partial g_t/\partial \kappa_t & 0 \end{bmatrix} \tag{6.127}$$

$$\frac{\partial f_c}{\partial \boldsymbol{\kappa}} = \begin{bmatrix} 0 & \partial f_c/\partial \kappa_c \end{bmatrix} \tag{6.128}$$

$$\frac{\partial f_t}{\partial \kappa_t} = -\frac{\partial \boldsymbol{q}_t}{\partial \kappa_t} \left(\frac{\boldsymbol{P}_t (\boldsymbol{\sigma}-\boldsymbol{q}_t)}{((\boldsymbol{\sigma}-\boldsymbol{q}_t)^T \boldsymbol{P}_t (\boldsymbol{\sigma}-\boldsymbol{q}_t))^{1/2}} + \boldsymbol{\pi} \right) \tag{6.129}$$

$$\frac{\partial g_t}{\partial \kappa_t} = -\frac{\partial \boldsymbol{q}_t}{\partial \kappa_t} \left(\frac{\boldsymbol{P}_g (\boldsymbol{\sigma}-\boldsymbol{q}_t)}{((\boldsymbol{\sigma}-\boldsymbol{q}_t)^T \boldsymbol{P}_g (\boldsymbol{\sigma}-\boldsymbol{q}_t))^{1/2}} + \boldsymbol{\pi} \right) \tag{6.130}$$

$$\frac{\partial f_c}{\partial \kappa_c} = \frac{\boldsymbol{\sigma}^T \frac{d\boldsymbol{P}_c}{d\kappa_c} \boldsymbol{\sigma}}{2\sqrt{\boldsymbol{\sigma}^T \boldsymbol{P}_c \boldsymbol{\sigma}}} - \frac{\frac{d\sigma_{c,x}}{d\kappa_c}\sigma_{c,y} + \sigma_{c,x}\frac{d\sigma_{c,y}}{d\kappa_c}}{2\sqrt{\sigma_{c,x}\sigma_{c,y}}} \tag{6.131}$$

$$\frac{d\boldsymbol{P}_c}{d\kappa_c} = \frac{\partial \boldsymbol{P}_c}{\partial \sigma_{c,x}} \frac{d\sigma_{c,x}}{d\kappa_c} + \frac{\partial \boldsymbol{P}_c}{\partial \sigma_{c,y}} \frac{d\sigma_{c,y}}{d\kappa_c} \tag{6.132}$$

$$\frac{\partial \boldsymbol{P}_c}{\partial \sigma_{c,x}} = \begin{bmatrix} -\frac{\sigma_{c,y}}{\sigma_{c,x}^2} & 0 & 0 \\ 0 & \frac{1}{\sigma_{c,y}} & 0 \\ 0 & 0 & 0 \end{bmatrix} \qquad \frac{\partial \boldsymbol{P}_c}{\partial \sigma_{c,y}} = \begin{bmatrix} \frac{1}{\sigma_{c,x}} & 0 & 0 \\ 0 & -\frac{\sigma_{c,x}}{\sigma_{c,y}^2} & 0 \\ 0 & 0 & 0 \end{bmatrix} \tag{6.133}$$

$$\frac{\partial^2 g_t}{\partial \boldsymbol{\sigma} \partial \boldsymbol{\kappa}} = \begin{bmatrix} \frac{\partial^2 g_t}{\partial \boldsymbol{\sigma} \partial \kappa_t} & \mathbf{0} \end{bmatrix} \tag{6.134}$$

$$\frac{\partial^2 f_c}{\partial \boldsymbol{\sigma} \partial \boldsymbol{\kappa}} = \begin{bmatrix} \mathbf{0} & \frac{\partial^2 f_c}{\partial \boldsymbol{\sigma} \partial \kappa_c} \end{bmatrix} \tag{6.135}$$

$$\frac{\partial^2 g_t}{\partial \boldsymbol{\sigma} \partial \kappa_t} = \left[-\frac{\boldsymbol{P}_g}{((\boldsymbol{\sigma}-\boldsymbol{q}_t)^T \boldsymbol{P}_g (\boldsymbol{\sigma}-\boldsymbol{q}_t))^{1/2}} + \frac{\boldsymbol{P}_g (\boldsymbol{\sigma}-\boldsymbol{q}_t)(\boldsymbol{\sigma}-\boldsymbol{q}_t)^T \boldsymbol{P}_g}{((\boldsymbol{\sigma}-\boldsymbol{q}_t)^T \boldsymbol{P}_g (\boldsymbol{\sigma}-\boldsymbol{q}_t))^{3/2}} \right] \frac{d\boldsymbol{h}_t}{d\kappa_t} \tag{6.136}$$

$$\frac{\partial^2 f_c}{\partial \boldsymbol{\sigma} \partial \kappa_c} = \frac{\frac{d\boldsymbol{P}_c}{d\kappa_c}\boldsymbol{\sigma}}{(\boldsymbol{\sigma}^T \boldsymbol{P}_c \boldsymbol{\sigma})^{1/2}} - \frac{\boldsymbol{P}_c \boldsymbol{\sigma} \left(\boldsymbol{\sigma}^T \frac{d\boldsymbol{P}_c}{d\kappa_c} \boldsymbol{\sigma} \right)}{2\left(\boldsymbol{\sigma}^T \boldsymbol{P}_c \boldsymbol{\sigma}\right)^{3/2}} \tag{6.137}$$

$$\frac{\partial \boldsymbol{\kappa}}{\partial \boldsymbol{\lambda}} = \begin{bmatrix} 1 & 0 \\ 0 & 1 \end{bmatrix} \tag{6.138}$$

$$\frac{d\boldsymbol{h}_t}{d\kappa_t} = \begin{bmatrix} d\sigma_{t,x}/d\kappa_t \\ d\sigma_{t,y}/d\kappa_t \\ 0 \end{bmatrix} \qquad \frac{d\boldsymbol{h}_c}{d\kappa_c} = \begin{bmatrix} d\sigma_{c,x}/d\kappa_c \\ d\sigma_{c,y}/d\kappa_c \\ 0 \end{bmatrix} \tag{6.139}$$

where

$$\frac{d\sigma_{t,i}}{d\kappa_t} = -\frac{hf_{t,i}^2}{G_{ft,i}} \exp\left(-\frac{hf_{t,i}}{G_{ft,i}}\kappa_t\right) \tag{6.140}$$

$$\frac{d\sigma_{c,i}}{d\kappa_c} = \begin{cases} \dfrac{(\sigma_p - \sigma_i)(\kappa_p - \kappa_c)}{\kappa_p\sqrt{\kappa_c(2\kappa_p - \kappa_c)}} & \kappa_c < \kappa_p \\ \dfrac{2(\sigma_m - \sigma_p)(\kappa_c - \kappa_p)}{(\kappa_m - \kappa_p)^2} & \kappa_p < \kappa_c < \kappa_{m,i} \\ 2\,\dfrac{\sigma_m - \sigma_p}{\kappa_m - \kappa_p} \exp\left(2\dfrac{(\kappa_c - \kappa_m)(\sigma_m - \sigma_p)}{(\kappa_m - \kappa_p)(\sigma_m - \sigma_r)}\right) & \kappa_c > \kappa_{m,i} \end{cases} \tag{6.141}$$

It is useful to evaluate the norm of the plastic strain rate caused by tensile yielding. In tensor notation, it would be given by $\|\dot{\boldsymbol{\varepsilon}}_p\| = \sqrt{\dot{\boldsymbol{\varepsilon}}_p : \dot{\boldsymbol{\varepsilon}}_p}$ but in engineering notation we must write

$$\|\dot{\boldsymbol{\varepsilon}}_p\| = \sqrt{\dot{\boldsymbol{\varepsilon}}_p^T \boldsymbol{P}^{-1} \dot{\boldsymbol{\varepsilon}}_p} = \dot{\lambda}_t \sqrt{\left(\frac{\partial g_t}{\partial \boldsymbol{\sigma}}\right)^T \boldsymbol{P}^{-1} \frac{\partial g_t}{\partial \boldsymbol{\sigma}}} \tag{6.142}$$

where

$$\boldsymbol{P}^{-1} = \begin{bmatrix} 1 & 0 & 0 \\ 0 & 1 & 0 \\ 0 & 0 & 1/2 \end{bmatrix} \tag{6.143}$$

is a suitable scaling matrix that converts a strain-like column matrix into a stress-like column matrix. It is worth noting that

$$\boldsymbol{P}_g^T \boldsymbol{P}^{-1} \boldsymbol{P}_g = \frac{1}{2}\boldsymbol{P}_g \tag{6.144}$$

$$\boldsymbol{P}_g^T \boldsymbol{P}^{-1} \boldsymbol{\pi} = \boldsymbol{0} \tag{6.145}$$

$$\boldsymbol{\pi}^T \boldsymbol{P}^{-1} \boldsymbol{\pi} = \frac{1}{2} \tag{6.146}$$

Based on these relations, it is easy to evaluate

$$\begin{aligned} \left(\frac{\partial g_t}{\partial \boldsymbol{\sigma}}\right)^T \boldsymbol{P}^{-1} \frac{\partial g_t}{\partial \boldsymbol{\sigma}} &= \frac{(\boldsymbol{\sigma} - \boldsymbol{q}_t)^T \boldsymbol{P}_g^T \boldsymbol{P}^{-1} \boldsymbol{P}_g (\boldsymbol{\sigma} - \boldsymbol{q}_t)}{(\boldsymbol{\sigma} - \boldsymbol{q}_t)^T \boldsymbol{P}_g (\boldsymbol{\sigma} - \boldsymbol{q}_t)} + \\ &\quad + 2\frac{(\boldsymbol{\sigma} - \boldsymbol{q}_t)^T \boldsymbol{P}_g^T \boldsymbol{P}^{-1} \boldsymbol{\pi}}{\left((\boldsymbol{\sigma} - \boldsymbol{q}_t)^T \boldsymbol{P}_g (\boldsymbol{\sigma} - \boldsymbol{q}_t)\right)^{1/2}} + \boldsymbol{\pi}^T \boldsymbol{P}^{-1} \boldsymbol{\pi} = \\ &= \frac{1}{2} + 0 + \frac{1}{2} = 1 \end{aligned} \tag{6.147}$$

and (6.142) simplifies to

$$\|\dot{\boldsymbol{\varepsilon}}_p\| = \dot{\lambda}_t \tag{6.148}$$

Of course, $\dot{\boldsymbol{\varepsilon}}_p$ is only the part of the plastic strain rate caused by tensile yielding.

It can be demonstrated that also the rate of the maximum principal plastic strain is equal to the rate of the plastic multiplier related to the tensile failure surface. It can be expressed as

$$\dot{\varepsilon}_{P,1} = \frac{\dot{\varepsilon}_{P,x} + \dot{\varepsilon}_{P,y}}{2} + \frac{1}{2}\sqrt{\left(\dot{\varepsilon}_{P,x} - \dot{\varepsilon}_{P,y}\right)^2 + \dot{\gamma}_{P,xy}^2} \tag{6.149}$$

which can also be recast in matrix form as

$$\dot{\varepsilon}_{P,1} = \sqrt{\dot{\boldsymbol{\varepsilon}}_P^T \boldsymbol{P}_1 \dot{\boldsymbol{\varepsilon}}_P} + \boldsymbol{\pi}^T \dot{\boldsymbol{\varepsilon}}_P \tag{6.150}$$

where $\boldsymbol{P}_1$ is the following auxiliary matrix

$$\boldsymbol{P}_1 = \begin{bmatrix} 1/4 & -1/4 & 0 \\ -1/4 & 1/4 & 0 \\ 0 & 0 & 1/4 \end{bmatrix} \tag{6.151}$$

and $\dot{\boldsymbol{\varepsilon}}_P$ is the vector of plastic strain in Voigt notation, related to the plastic potential through the flow rule,

$$\dot{\boldsymbol{\varepsilon}}_P = \dot{\lambda}_t \frac{\partial g_t}{\partial \boldsymbol{\sigma}} = \dot{\lambda}_t \left(\frac{\boldsymbol{P}_g(\boldsymbol{\sigma} - \boldsymbol{q}_t)}{\sqrt{(\boldsymbol{\sigma} - \boldsymbol{q}_t)^T \boldsymbol{P}_g (\boldsymbol{\sigma} - \boldsymbol{q}_t)}} + \boldsymbol{\pi} \right) \tag{6.152}$$

so that (6.149) can be rewritten as

$$\dot{\varepsilon}_{P,1} = \dot{\lambda}_t \left(\frac{\boldsymbol{\pi}^T \boldsymbol{P}_g \left(\boldsymbol{\sigma} - \boldsymbol{q}_t\right)}{\sqrt{(\boldsymbol{\sigma} - \boldsymbol{q}_t)^T \boldsymbol{P}_g (\boldsymbol{\sigma} - \boldsymbol{q}_t)}} + \boldsymbol{\pi}^T \boldsymbol{\pi} + \right.$$
$$\left. + \sqrt{\left(\frac{\boldsymbol{P}_g(\boldsymbol{\sigma} - \boldsymbol{q}_t)}{\left((\boldsymbol{\sigma} - \boldsymbol{q}_t)^T \boldsymbol{P}_g (\boldsymbol{\sigma} - \boldsymbol{q}_t)\right)^{1/2}} + \boldsymbol{\pi} \right)^T \boldsymbol{P}_1 \left(\frac{\boldsymbol{P}_g(\boldsymbol{\sigma} - \boldsymbol{q}_t)}{\left((\boldsymbol{\sigma} - \boldsymbol{q}_t)^T \boldsymbol{P}_g (\boldsymbol{\sigma} - \boldsymbol{q}_t)\right)^{1/2}} + \boldsymbol{\pi} \right)} \right) \tag{6.153}$$

It is worth noting that

$$\boldsymbol{\pi}^T \boldsymbol{P}_g = \boldsymbol{0} \tag{6.154}$$
$$\boldsymbol{\pi}^T \boldsymbol{P}_1 = \boldsymbol{0} \tag{6.155}$$
$$\boldsymbol{P}_g^T \boldsymbol{P}_1 \boldsymbol{P}_g = \frac{1}{4} \boldsymbol{P}_g \tag{6.156}$$
$$\boldsymbol{\pi}^T \boldsymbol{\pi} = \frac{1}{2} \tag{6.157}$$

Then it is easy to evaluate the rate of the maximum principal plastic strain as

$$\dot{\varepsilon}_{P,1} = \dot{\lambda}_t \left(0 + \frac{1}{2} + \sqrt{\frac{1}{4} + 0 + 0 + 0} \right) = \dot{\lambda}_t \tag{6.158}$$

Chapter 7

Localization Analysis of Masonry RVEs

Abstract

Numerical simulations of masonry structures are often based on continuum macro-modeling approaches that need constitutive laws able to phenomenologically reproduce the behavior of the material. The constitutive model developed by Lourenço in the framework of orthotropic multi-surface plasticity represents one notable example.

Macroscopic models cannot take into account the microstructure heterogeneities typical of masonry, at least not directly, and may fail in reproducing failure mechanisms and localization directions of inelastic strains when compared to experimental tests. To address this issue, we need to increase the detailing level by performing microscale analyses, where we separately model blocks and mortar and assign to each constituent a proper constitutive law.

In this chapter, a microstructural analysis of a masonry unit cell under periodic boundary conditions has been performed. A simple unit cell model in the framework of plasticity is developed and its ability to reproduce most behaving typical of regular masonry is assessed. The localized inelastic strains resulting from macro- and micro-scale models are compared in terms of predicted localization angles for uniaxial tension. Moreover, the influence of the size of the representative element and periodicity directions on localization is assessed.

7.1 Introduction

Numerical analysis of masonry structures is performed by using models with different detailing levels.

At large scale, masonry buildings could be seen as a set of walls and slabs, where each wall could be further decomposed in macroelements that are masonry piers, spandrels, and node panels. In the *macroelement* approach (Magenes 2000; Lagomarsino et al. 2013; Caliò et al. 2012) the detailing level stops at this point by assigning a mechanical behavior to each panel. The equivalent-frame method is one

example of this group of models, and it consists of treating each macroelement as an equivalent beam having suitable moment-curvature relationships. This method is widely used in engineering practice for its advantages, namely the small computational cost for the small number of degrees of freedom involved, and its explicit endorsement by several building codes. Nevertheless, macroelement models present several drawbacks. For instance, macroelements subdivisions are not uniquely determined in the case of irregular opening layouts, and lateral displacement capacity is often taken as a certain percentage of the height of panels without considering material characteristics.

The detailing level could be increased by considering each macroelement as a *homogeneized continuum* (Lourenço, De Borst, et al. 1997; Berto et al. 2002; Addessi, Marfia, et al. 2002). In this case, we assign at each material point average mechanical properties and a proper constitutive law that should phenomenologically reproduce the response. Numerous attempts have been made for simulating macroscopic masonry behavior by using stress-strain relations in the framework of nonlinear elasticity, plasticity, damage mechanics, or smeared cracking. However, the definition of a constitutive relationship is not an easy task. In fact, masonry behavior strongly depends on its microstructure composed of two different materials, blocks and mortar, each with its own properties, and the way they are arranged.

Hence, there might be a need to get to a finer scale and take into account the material heterogeneity by performing a *microscale* analysis, in which we model each constituent separately and assign to each one a proper constitutive law. In this case, the stress-strain relation of each constituent could be directly calibrated on elementary experimental tests. This approach is the most detailed way of representing the mechanical properties of masonry that makes sense in structural analysis. However, it has the drawback of being highly expensive in terms of computational costs, particularly when applied to the analysis of a whole structure.

Some authors label this level of representation as *mesoscopic*, borrowing this term from the study of concrete structures. For concrete, in fact, numerous scales of representation can be defined. While at the macroscopic scale concrete may be represented as a homogenized continuum, at the mesoscopic scale concrete is regarded to as a three-phase composite consisting of coarse aggregate, mortar matrix, and interfacial zones. The detailing level can be increased by analyzing concrete at the microscale, or even at the nanoscale, where the prefixes indicate the dimensions in meters of the particle characteristic lengths. For masonry, however, analyzing particles having dimensions that are smaller than the mortar layer thickness is not relevant from a structural point of view. Therefore, we consider two detailing levels only: the scale at which masonry is regarded as a homogenized continuum (macroscale) and the scale at which we model the constituents separately (microscale). This will be the terminology used throughout this chapter.

The micromodeling approach can be used for large-scale simulations. Alternatively, the microscale model response can be used just to pre-calculate the parameters of a homogenized continuum model (Sejnoha et al. 2008; Cavalagli et al. 2011), or it can be used simultaneously with a macroscale model, which interactively obtains macroscopic stresses from the microscale during the analysis, realizing a proper multiscale model (Massart et al. 2007; Salerno and De Felice 2009; De Bellis and Addessi 2011).

In *multiscale* models, the structure is modeled as a continuum where, instead of assigning a specific constitutive law, the material point behavior is obtained through

the homogenization of the response of a Representative Volume Element (RVE), in which the microstructure is explicitly modeled. The homogenization procedure is done in a fully nested way through the so-called "FE-square" approach. This model advantage is to maintain a high detailing level while simultaneously speeding up numerical analysis compared to a microscale analysis applied to the whole structure.

The choice of the RVE dimensions is the key aspect of the homogenization procedure. The RVE should be large enough to contain all the material heterogeneities and, at the same time, the smallest possible to limit the computation burden. The RVE must then geometrically reproduce the whole body by repeating its pattern in its neighborhood along specific periodicity directions, if any are present. Moreover, the constitutive law for the materials within the RVE must be chosen properly to reproduce the masonry mechanics of the microstructure.

The more direct approach for microscale modeling considers bricks and mortar as a continuum and requires a stress-strain law for each constituent. A case in point is the model proposed by Massart et al. 2007 in which an isotropic damage model was adopted for both bricks and mortar. However, the most common approach is to consider the mortar joints as an interface where all the nonlinearities are concentrated. This consideration leads to models where bricks are represented as linear elastic or rigid bodies, and the attention is focused on the formulation of the interface stress-strain law. Interface models can be formulated in the framework of damage mechanics (Gambarotta and Lagomarsino 1997), multisurface plasticity (Lourenço and Rots 1997), coupled damage-plasticity (Minga et al. 2018), or can be based on phase transition with a constitutive model depending on the interface state (Salvatori and Spinelli 2018).

The smallest RVE for regular-masonry texture is composed of one brick and one vertical and one horizontal mortar layer, and it has been extensively used for the microstructural analysis of masonry (Massart et al. 2004; La Malfa Ribolla et al. 2020; Mercatoris et al. 2009). Alternatively, a cell composed of a brick surrounded by two brick quarters on each horizontal side has been considered (Sacco 2009; Milani 2011; De Bellis and Addessi 2011).

In general, the RVE response may change varying its size, especially in its localization properties. With bigger RVE sizes, the unit cell is featured by several mortar layers, and it may have more freedom to develop different localization paths. Moreover, large-size RVEs may allow different sets of periodicity directions whose choice may further influence localization, as shown in Stransky and Jirásek 2011.

In this chapter, we carry out a study on the localization properties of masonry RVEs. A microscale model for masonry is proposed, treating bricks and mortar as continua with a Rankine plasticity model. The model effectiveness to reproduce the microstructural mechanics of masonry is assessed under basic stress scenarios. A comparison between the RVE localization properties and the ones of a macroscale constitutive model widely used for masonry (Lourenço, De Borst, et al. 1997) is performed. A study of the response of the RVEs varying their size and periodicity directions is explored under selected stress states.

The chapter is organized as follows. The homogenization procedure to relate the microscopic stresses and strains to the macroscopic ones is described in Section 7.2. Some detailing aspects about masonry RVEs, regarding the unit-cell geometries, enforcement of restraints and periodicity constraints, and the localization procedure are presented in Section 7.3. The RVE finite element model and the implementation details of Rankine plasticity are discussed respectively in Section 7.4 and 7.5. The

results on the one-brick RVE under basic stress states and the comparison with Lourenço's model in terms of localization properties are reported in Section 7.6. Then, the effect of size and periodicity direction variation are analyzed in Section 7.7. Finally, some concluding remarks are reported in Section 7.8.

7.2 Homogenization procedure

The derivation of the homogenization procedure takes advantage of the divergence theorem and its corollaries, reported in the following.

Green's theorem. *Let V be a regular region having boundary S, and let ϕ, $\boldsymbol{v}$, and $\boldsymbol{T}$ respectively be scalar, vectorial, and tensorial smooth fields in V. Then*

$$\int_S \phi\, \boldsymbol{n}\, \mathrm{d}S = \int_V \nabla\phi\, \mathrm{d}V \tag{7.1}$$

$$\int_S \boldsymbol{v}\cdot\boldsymbol{n}\, \mathrm{d}S = \int_V \nabla\cdot\boldsymbol{v}\, \mathrm{d}V \tag{7.2}$$

$$\int_S \boldsymbol{n}\cdot\boldsymbol{T}\, \mathrm{d}S = \int_V \nabla\cdot\boldsymbol{T}\, \mathrm{d}V \tag{7.3}$$

where $\boldsymbol{n}$ is the outward unit normal field on S, the boundary of the region V.

Three corollaries of this theorem, used for further demonstrations, are the following (Gurtin 1982):

$$\int_S \boldsymbol{n}\otimes\boldsymbol{v}\, \mathrm{d}S = \int_V \nabla\boldsymbol{v}\, \mathrm{d}V \tag{7.4}$$

$$\int_S (\boldsymbol{n}\cdot\boldsymbol{T})\otimes\boldsymbol{v}\, \mathrm{d}S = \int_V \left[(\nabla\cdot\boldsymbol{T})\otimes\boldsymbol{v} + \boldsymbol{T}\cdot\nabla\boldsymbol{v}^T\right] \mathrm{d}V \tag{7.5}$$

$$\int_S \boldsymbol{v}\cdot(\boldsymbol{n}\cdot\boldsymbol{T})\, \mathrm{d}S = \int_V (\boldsymbol{v}\cdot(\nabla\cdot\boldsymbol{T}) + \boldsymbol{T}:\nabla\boldsymbol{v})\, \mathrm{d}V \tag{7.6}$$

In the preceding equations, we make use of the definition of the gradient of a vector $\boldsymbol{v}$, whose ij components are defined as

$$(\nabla\boldsymbol{v})_{ij} = \frac{\partial v_j}{\partial x_i} \tag{7.7}$$

We define the symmetric part of a second-order tensor $\boldsymbol{T}$ as

$$(\boldsymbol{T})_{sym} = \frac{\boldsymbol{T}+\boldsymbol{T}^T}{2} \tag{7.8}$$

7.2.1 Unit-cell kinematics and balance

The displacement field $\boldsymbol{u}$ within the RVE is expressed as the superposition of the macroscale ($\boldsymbol{W}$) and microscale ($\boldsymbol{w}$) contributions, that is

$$\boldsymbol{u}(\boldsymbol{x}) = \boldsymbol{W}(\boldsymbol{x}) + \boldsymbol{w}(\boldsymbol{x}) \tag{7.9}$$

where $\boldsymbol{x}$ is the position vector of a point in the unit cell.

In the case of first-order homogenization, the macroscale contribution is assumed to vary linearly within the RVE, namely

$$\boldsymbol{W}(\boldsymbol{x}) = \boldsymbol{W}(\boldsymbol{x}_R) + \boldsymbol{E} \cdot (\boldsymbol{x} - \boldsymbol{x}_R) \tag{7.10}$$

where $\boldsymbol{x}_R$ is the position of the reference point of the unit cell, and $\boldsymbol{E}$ is the macroscopic strain. If rigid body motion is preserved and if we assume that reference point $\boldsymbol{x}_R$ is restrained and positioned at the origin O of the reference frame, so that

$$\boldsymbol{W}(\boldsymbol{x}_R) = \boldsymbol{W}(O) = \boldsymbol{0} \tag{7.11}$$

the displacement field at the microscale can be expressed as

$$\boldsymbol{u}(\boldsymbol{x}) = \boldsymbol{E} \cdot \boldsymbol{x} + \boldsymbol{w}(\boldsymbol{x}) \tag{7.12}$$

The microscopic strain $\boldsymbol{\varepsilon}$ is the symmetric part of the gradient of the displacement field $\boldsymbol{u}$, namely

$$\boldsymbol{\varepsilon} = (\nabla \boldsymbol{u})_{sym} = \boldsymbol{E} + (\nabla \boldsymbol{w})_{sym} \tag{7.13}$$

We neglect body forces in the unit cell, so the balance equation reduces to

$$\nabla \cdot \boldsymbol{\sigma} = 0 \tag{7.14}$$

7.2.2 Hill-Mandel condition

The scale transition is commonly complemented by the Hill-Mandel condition, according to which we impose the equivalence of the macroscopic virtual work and the volume average of the microscopic one, namely

$$\boldsymbol{\Sigma}_A : \boldsymbol{E}_B = \frac{1}{V} \int_V \boldsymbol{\sigma}_A : \boldsymbol{\varepsilon}_B \, \mathrm{d}V \tag{7.15}$$

where $\boldsymbol{\Sigma}_A$ and $\boldsymbol{\sigma}_A$ are the macroscopic and microscopic stress states, where the microscopic stress is equilibrated

$$\nabla \cdot \boldsymbol{\sigma}_A = 0 \tag{7.16}$$

and $\boldsymbol{E}_B$ and $\boldsymbol{\varepsilon}_B$ are the macroscopic and microscopic strain states, where the microscopic strain field is compatible

$$\boldsymbol{\varepsilon}_B = (\nabla \boldsymbol{u}_B)_{sym} \tag{7.17}$$

We added the subscripts A and B to underline that the stress and strain states are entirely independent of each other. The Hill-Mandel condition, therefore, states that the macroscopic stress $\boldsymbol{\Sigma}$ is the work-conjugate quantity to the macroscopic strain $\boldsymbol{E}$.

7.2.3 Macro-micro transition

Homogenization procedures are usually built so that the macroscopic fields are expressed as the volume average on the unit-cell of the corresponding microscopic quantities, namely

$$\boldsymbol{E} = \frac{1}{V} \int_V \boldsymbol{\varepsilon} \, \mathrm{d}V \tag{7.18}$$

$$\boldsymbol{\Sigma} = \frac{1}{V} \int_V \boldsymbol{\sigma} \, \mathrm{d}V \tag{7.19}$$

However, the previous equalities are not automatically satisfied and proper boundary conditions are needed. Among the numerous possibilities, we consider the three cases of imposing kinematic (i), static (ii), or periodic boundary conditions (iii). In the following derivations, we assume the validity of the Hill-Mandel condition (7.15), an equilibrated microscopic stress field (7.16), and a compatible microscopic strain field (7.17).

Case (i) We impose kinematic constraints by enforcing the vanishing of the fluctuations $\boldsymbol{w}$ on the RVE boundary S, namely

$$\boldsymbol{w} = \boldsymbol{0} \qquad \text{on } S \tag{7.20}$$

that leads to

$$\boldsymbol{u} = \boldsymbol{E} \cdot \boldsymbol{x} \qquad \text{on } S \tag{7.21}$$

which corresponds to the so-called "linear boundary conditions". In this case, the scale-transition condition on the strains (7.18) is fulfilled. In fact, the volume average of the microscopic strains is given by

$$\int_V \boldsymbol{\varepsilon} \, \mathrm{d}V = \int_V \boldsymbol{E} \, \mathrm{d}V + \int_V (\nabla \boldsymbol{w})_{sym} \, \mathrm{d}V \tag{7.22}$$

Considering that the macroscopic strain $\boldsymbol{E}$ is constant over the volume V and applying a corollary of the divergence theorem (7.4), the right-hand side can be further simplified as

$$\int_V \boldsymbol{\varepsilon} \, \mathrm{d}V = \boldsymbol{E} \, V + \int_S (\boldsymbol{n} \otimes \boldsymbol{w})_{sym} \, \mathrm{d}S \tag{7.23}$$

The second term of the right-hand side vanishes by imposing the kinematic constraints (7.20); consequently, we obtain the requested condition

$$\boldsymbol{E} = \frac{1}{V} \int_V \boldsymbol{\varepsilon} \, \mathrm{d}V \tag{7.24}$$

Moreover, we can demonstrate that the kinematic constraints lead to the scale-transition condition on stresses (7.19) through the Hill-Mandel condition, which reads

$$\boldsymbol{\Sigma} : \boldsymbol{E}^* = \frac{1}{V} \int_V \boldsymbol{\sigma} : (\nabla \boldsymbol{u}^*)_{sym} \, \mathrm{d}V \tag{7.25}$$

where the strain fields, marked with asterisks, are considered as virtual, while the stress fields are considered as the actual ones. The right-hand side of the previous equation can be rewritten by using a corollary of the divergence theorem (7.6) as

$$\boldsymbol{\Sigma} : \boldsymbol{E}^* = \frac{1}{V} \int_S (\boldsymbol{n} \cdot \boldsymbol{\sigma}) \cdot \boldsymbol{u}^* \, \mathrm{d}S - \frac{1}{V} \int_V (\nabla \cdot \boldsymbol{\sigma}) \cdot \boldsymbol{u}^* \, \mathrm{d}V \tag{7.26}$$

Substituting (7.16) and (7.21) into (7.26), we obtain

$$\boldsymbol{\Sigma} : \boldsymbol{E}^* = \frac{1}{V} \int_S (\boldsymbol{n} \cdot \boldsymbol{\sigma}) \cdot \boldsymbol{E}^* \cdot \boldsymbol{x} \, \mathrm{d}S \tag{7.27}$$

Taking out the virtual macroscopic strain from the integral, we have

$$\boldsymbol{\Sigma} : \boldsymbol{E}^* = \frac{1}{V} \int_S (\boldsymbol{n} \cdot \boldsymbol{\sigma}) \otimes \boldsymbol{x} \, \mathrm{d}S : \boldsymbol{E}^* \tag{7.28}$$

Then, the surface integral can be transformed into a volume integral by means of (7.5), namely

$$\boldsymbol{\Sigma} : \boldsymbol{E}^* = \frac{1}{V} \int_V \boldsymbol{\sigma} \, \mathrm{d}V : \boldsymbol{E}^* \tag{7.29}$$

Since the previous relation must hold for all virtual macroscopic strain $\boldsymbol{E}^*$, we retrieve the relation between macroscopic and microscopic stresses, that is

$$\boldsymbol{\Sigma} = \frac{1}{V} \int_V \boldsymbol{\sigma} \, \mathrm{d}V \tag{7.30}$$

Case (ii) In this case, tractions are imposed on the boundary of the unit cell, namely

$$\boldsymbol{n} \cdot \boldsymbol{\Sigma} = \boldsymbol{n} \cdot \boldsymbol{\sigma} \qquad \text{on } S \tag{7.31}$$

Conversely to the case (i), the fields considered as virtual in the Hill-Mandel condition are the macroscopic and microscopic stresses, that is

$$\boldsymbol{\Sigma}^* : \boldsymbol{E} = \frac{1}{V} \int_V \boldsymbol{\sigma}^* : (\nabla \boldsymbol{u})_{sym} \, \mathrm{d}V \tag{7.32}$$

The right-hand side can be transformed into a surface integral by using the corollary (7.5) and the unit-cell equilibrium (7.16), namely

$$\boldsymbol{\Sigma}^* : \boldsymbol{E} = \frac{1}{V} \int_S (\boldsymbol{n} \cdot \boldsymbol{\sigma}^*) \cdot \boldsymbol{u} \, \mathrm{d}S \tag{7.33}$$

Substituting the static boundary conditions (7.31) in (7.33), we obtain

$$\boldsymbol{\Sigma}^* : \boldsymbol{E} = \frac{1}{V} \int_S (\boldsymbol{n} \cdot \boldsymbol{\Sigma}^*) \cdot \boldsymbol{u} \, \mathrm{d}S \tag{7.34}$$

where the virtual macroscopic stress $\boldsymbol{\Sigma}^*$ can be taken out from the integral, namely

$$\boldsymbol{\Sigma}^* : \boldsymbol{E} = \boldsymbol{\Sigma}^* : \frac{1}{V} \int_S \boldsymbol{n} \otimes \boldsymbol{u} \, \mathrm{d}S \tag{7.35}$$

Considering the symmetry of $\boldsymbol{\Sigma}^*$, we can rewrite the previous identity as

$$\boldsymbol{\Sigma}^* : \boldsymbol{E} = \boldsymbol{\Sigma}^* : \frac{1}{V} \int_S (\boldsymbol{u} \otimes \boldsymbol{n})_{sym} \, \mathrm{d}S \tag{7.36}$$

which reduces to the kinematic scale transition condition since the previous equation must hold for all $\boldsymbol{\Sigma}^*$, namely

$$\boldsymbol{E} = \frac{1}{V} \int_V \boldsymbol{\varepsilon} \, \mathrm{d}V \tag{7.37}$$

where we have used again a corollary of the divergence theorem (7.4). As it has been already demonstrated in the case (i), the combination of the previous relation with the Hill-Mandel condition (7.15) leads to the static scale transition equation, that is

$$\boldsymbol{\Sigma} = \frac{1}{V} \int_V \boldsymbol{\sigma} \, \mathrm{d}V \tag{7.38}$$

Case (iii) The imposition of periodic boundary conditions represents an alternative solution that has shown to provide a reliable estimation of the RVE behavior (Coenen et al. 2012). In this approach, the RVE boundary is partitioned into two sets: an image part S^+ and a mirror part S^-, so that $S = S^+ \cup S^-$ and $S^+ \cap S^- = \varnothing$. The two sets are associated with each other through a one-to-one function $\varphi : S^+ \to S^-$, called "mirror function", that maps each point of the image part to one of the mirror part, namely

$$\varphi(\boldsymbol{x}^+) = \boldsymbol{x}^- \tag{7.39}$$

The couple of points $\boldsymbol{x}^+ \in S^+$ and $\boldsymbol{x}^- \in S^-$ linked by (7.39) are said to be corresponding points. The normals to the surface of the RVE associated with two corresponding points are opposite, namely

$$\boldsymbol{n}(\boldsymbol{x}^+) = -\boldsymbol{n}\left(\varphi(\boldsymbol{x}^+)\right) \qquad \forall \boldsymbol{x}^+ \in S^+ \tag{7.40}$$

Periodic boundary conditions are imposed by means of the equivalence of the fluctuations associated with corresponding points along the RVE boundary, that is

$$\boldsymbol{w}(\boldsymbol{x}^+) = \boldsymbol{w}\left(\varphi(\boldsymbol{x}^+)\right) \qquad \forall \boldsymbol{x}^+ \in S^+ \tag{7.41}$$

The previous condition guarantees the respect of the kinematic scale transition condition (7.20). In fact, we can demonstrate that the second term of the right-hand side of (7.23) vanishes by splitting the surface integral into two integrals over the image and mirror part, namely

$$\int_S (\boldsymbol{w} \otimes \boldsymbol{n})_{sym} \, \mathrm{d}S = \int_{S^+} \left(\boldsymbol{w}(\boldsymbol{x}^+) \otimes \boldsymbol{n}(\boldsymbol{x}^+)\right)_{sym} \mathrm{d}S + \int_{S^-} \left(\boldsymbol{w}(\boldsymbol{x}^-) \otimes \boldsymbol{n}(\boldsymbol{x}^-)\right)_{sym} \mathrm{d}S \tag{7.42}$$

Substituting the periodicity conditions (7.41) and the relation between the normals of corresponding points (7.40), we have

$$\int_S (\boldsymbol{w} \otimes \boldsymbol{n})_{sym} \, \mathrm{d}S = \int_{S^+} \left(\boldsymbol{w}(\boldsymbol{x}^+) \otimes \left[\boldsymbol{n}(\boldsymbol{x}^+) + \boldsymbol{n}(\varphi(\boldsymbol{x}^+))\right]\right)_{sym} \mathrm{d}S = 0 \tag{7.43}$$

which leads to

$$\boldsymbol{E} = \frac{1}{V} \int_V \boldsymbol{\varepsilon} \, \mathrm{d}V \tag{7.44}$$

Moreover, the periodicity conditions induce a link between displacements of corresponding points, which are given by

$$\boldsymbol{u}(\boldsymbol{x}^+) = \boldsymbol{E} \cdot \boldsymbol{x}^+ + \boldsymbol{w}(\boldsymbol{x}^+) \tag{7.45}$$

$$\boldsymbol{u}(\boldsymbol{x}^-) = \boldsymbol{E} \cdot \boldsymbol{x}^- + \boldsymbol{w}(\boldsymbol{x}^-) \tag{7.46}$$

Subtracting (7.46) from (7.45) and taking into account (7.41), we obtain

$$\boldsymbol{u}(\boldsymbol{x}^+) - \boldsymbol{u}(\boldsymbol{x}^-) = \boldsymbol{E} \cdot (\boldsymbol{x}^+ - \boldsymbol{x}^-) \tag{7.47}$$

which represents a linear constraint between corresponding points.

In the previous cases, the boundary-valued problem is well-posed due to the imposition of kinematic or static boundary conditions. Conversely, the imposition of periodic displacements on the RVE boundary (7.41) is not sufficient for the well-posedness since it represents an internal constraint between corresponding points

on the boundary. The problem must be complemented by another condition, that is the antiperiodicity of tractions, namely

$$\boldsymbol{n}(\boldsymbol{x}^+) \cdot \boldsymbol{\sigma}(\boldsymbol{x}^+) + \boldsymbol{n}(\boldsymbol{x}^-) \cdot \boldsymbol{\sigma}(\boldsymbol{x}^-) = \boldsymbol{0} \tag{7.48}$$

To retrieve the scale transition relation on stresses, let us evaluate the integral over the RVE volume of the microscopic work that the actual stresses produce on the virtual strains. The virtual displacement field must be compatible (7.17) and satisfy the periodicity condition (7.47).

The virtual microscopic work can be transformed into a surface integral in the usual way as

$$\int_V \boldsymbol{\sigma} : \boldsymbol{\varepsilon}^* \, \mathrm{d}V = \int_S (\boldsymbol{n} \cdot \boldsymbol{\sigma}) \cdot \boldsymbol{u}^* \, \mathrm{d}S \tag{7.49}$$

where the microscopic stresses and strains are the actual ones. The surface integral on the right-hand side can be split in two over the image and mirror part as

$$\int_V \boldsymbol{\sigma} : \boldsymbol{\varepsilon}^* \, \mathrm{d}V = \int_{S^+} (\boldsymbol{n}^+ \cdot \boldsymbol{\sigma}^+) \cdot \boldsymbol{u}^{*+} \, \mathrm{d}S + \int_{S^-} (\boldsymbol{n}^- \cdot \boldsymbol{\sigma}^-) \cdot \boldsymbol{u}^{*-} \, \mathrm{d}S \tag{7.50}$$

where the plus and the minus sign as superscript indicate fields evaluated in points of the image and mirror part, respectively. Introducing the conditions on periodic displacements (7.47) and antiperiodic tractions (7.48), we can write

$$\int_V \boldsymbol{\sigma} : \boldsymbol{\varepsilon}^* \, \mathrm{d}V = \int_{S^+} (\boldsymbol{n}^+ \cdot \boldsymbol{\sigma}^+) \cdot \boldsymbol{E}^* \cdot (\boldsymbol{x}^+ - \boldsymbol{x}^-) \, \mathrm{d}S \tag{7.51}$$

Taking out the macroscopic strain from the integral, we get

$$\int_V \boldsymbol{\sigma} : \boldsymbol{\varepsilon}^* \, \mathrm{d}V = \int_{S^+} (\boldsymbol{n}^+ \cdot \boldsymbol{\sigma}^+) \otimes (\boldsymbol{x}^+ - \boldsymbol{x}^-) \, \mathrm{d}S : \boldsymbol{E}^* \tag{7.52}$$

Then, rearranging the surface integral and using again the antiperiodicity condition on the tractions (7.48), we obtain

$$\begin{aligned} \int_V \boldsymbol{\sigma} : \boldsymbol{\varepsilon}^* \, \mathrm{d}V &= \left(\int_{S^+} (\boldsymbol{n}^+ \cdot \boldsymbol{\sigma}^+) \otimes \boldsymbol{x}^+ \, \mathrm{d}S - \int_{S^-} (\boldsymbol{n}^- \cdot \boldsymbol{\sigma}^-) \otimes \boldsymbol{x}^- \, \mathrm{d}S \right) : \boldsymbol{E}^* = \\ &= \int_S (\boldsymbol{n} \cdot \boldsymbol{\sigma}) \otimes \boldsymbol{x} \, \mathrm{d}S : \boldsymbol{E}^* \end{aligned} \tag{7.53}$$

that could be transformed back to a volume integral by means of the corollary (7.5) as

$$\int_V \boldsymbol{\sigma} : \boldsymbol{\varepsilon}^* \, \mathrm{d}V = \int_V \boldsymbol{\sigma} \, \mathrm{d}V : \boldsymbol{E}^* \tag{7.54}$$

Finally, substituting the previous relation in the Hill-Mandel condition (7.15),

$$\boldsymbol{\Sigma} : \boldsymbol{E}^* = \frac{1}{V} \int_V \boldsymbol{\sigma} : \boldsymbol{\varepsilon}^* \, \mathrm{d}V \tag{7.55}$$

it reduces to

$$\boldsymbol{\Sigma} : \boldsymbol{E}^* = \frac{1}{V} \int_V \boldsymbol{\sigma} \, \mathrm{d}V : \boldsymbol{E}^* \tag{7.56}$$

that leads to the scale transition on stresses, namely

$$\boldsymbol{\Sigma} = \frac{1}{V} \int_V \boldsymbol{\sigma} \, \mathrm{d}V \tag{7.57}$$

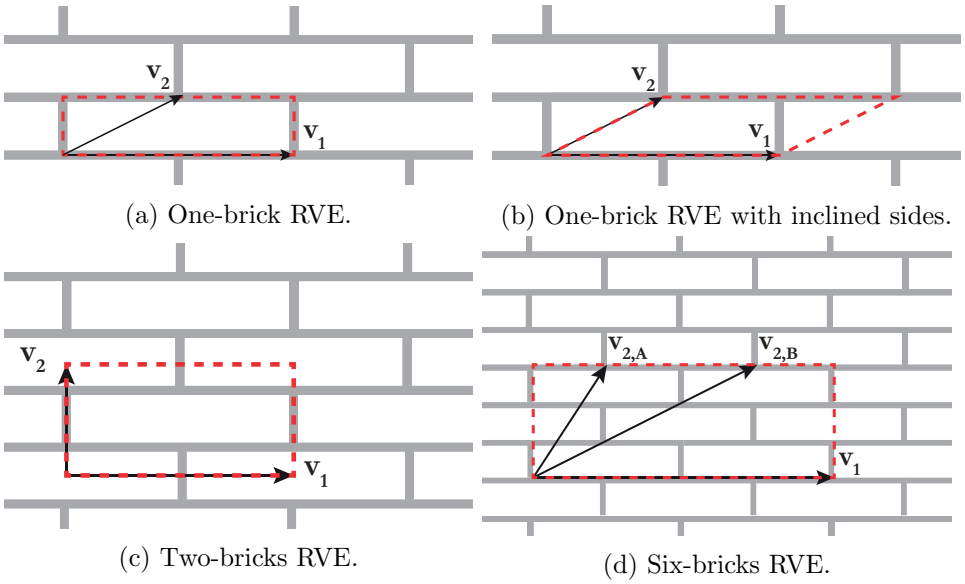

(a) One-brick RVE.

(b) One-brick RVE with inclined sides.

(c) Two-bricks RVE.

(d) Six-bricks RVE.

Figure 7.1: Geometries of different masonry RVEs.

7.3 Masonry RVEs

7.3.1 Unit-cell dimensions and periodicity directions

In this chapter, we restrict our attention to the case of masonry characterized by regular-textured running bond brickwork, which is made of rows of identical blocks placed next to each other, and each row is shifted by the size of half a block with respect to those above and below. Head and bed mortar joints fill respectively vertical and horizontal interfaces between blocks. We indicate as L_b and H_b the length and height of bricks, and as L_m and H_m the thickness of respectively head and bed joints of mortar. We define L and H as

$$L = L_b + L_m \tag{7.58}$$

$$H = H_b + H_m \tag{7.59}$$

In the case of regular masonry, it is worth finding a pattern that repeats itself along certain directions. We call this volume partition as Representative Volume Element (RVE) and these directions as periodicity directions, which can be expressed as

$$\boldsymbol{v}_i = \alpha_i \, \boldsymbol{e}_1 + \beta_i \, \boldsymbol{e}_2 \tag{7.60}$$

where $\boldsymbol{e}_1$ and $\boldsymbol{e}_2$ are the Cartesian axis unit vectors and α_i and β_i are scalars defining the i-th periodicity direction. For the analysis of the in-plane behavior of masonry structures, plane stress or plane strain assumptions are adopted, restricting the computation into two dimensions. Therefore, we are concerned to define a bi-dimensional RVE and identify two periodicity directions, $\boldsymbol{v}_1$ and $\boldsymbol{v}_2$.

The periodicity directions $\boldsymbol{v}_1$ and $\boldsymbol{v}_2$ need to satisfy the condition that, by shifting the RVE by an integer multiple of $\boldsymbol{v}_1$ and by an integer multiple of $\boldsymbol{v}_2$, we obtain a periodic image of the RVE with the same microstructure. If we repeat this

shifting operation using all possible combinations of integer multipliers different from zero, we obtain the whole plane without any gaps or overlaps.

Since finite element calculations are to be performed on the cell, it is worth choosing the one having the least area. One of the possible choices is the RVE made up of one brick surrounded by half mortar joints (Figure 7.1a), characterized by the following periodicity directions

$$\boldsymbol{v}_1 = L\,\boldsymbol{e}_1 \tag{7.61}$$

$$\boldsymbol{v}_2 = \frac{L}{2}\,\boldsymbol{e}_1 + H\,\boldsymbol{e}_2 \tag{7.62}$$

which are non-orthogonal. The study conducted in Anthoine 1995 was one of the first attempts to make use of this choice of the unit cell, and it was aimed to determine its in-plane elastic properties. In particular, the author took advantage of the properties of periodicity and symmetry to reduce the computations to a quarter cell. Massart et al. 2004 adopted the one-brick unit cell representing bricks and mortar as a continuum with a scalar damage model based on a non-local implicit gradient framework. Recently, La Malfa Ribolla et al. 2020 developed a meshless model assuming the block as elastic and the mortar joints as zero-thickness Mohr-Coulomb interfaces with a tension cut-off. An alternative one-brick RVE can be obtained by inclining the vertical sides, aligning them to the periodicity vector $\boldsymbol{v}_2$, as done in Mercatoris et al. 2009 (Figure 7.1b). The result is an equivalent RVE since the periodicity vectors and the number of bricks and mortar layers are the same.

Sacco 2009 and Milani 2011 considered a cell composed of a brick surrounded by two quarters of a brick on each horizontal side (Figure 7.1c), having orthogonal periodicity directions

$$\boldsymbol{v}_1 = L\,\boldsymbol{e}_1 \tag{7.63}$$

$$\boldsymbol{v}_2 = 2H\,\boldsymbol{e}_2 \tag{7.64}$$

In both papers, nonlinearities were concentrated on mortar joint interfaces, in one case (Sacco 2009) accounting for the coupling of damage and friction, based on the interface model developed by Alfano and Sacco 2006, while in the other one (Milani 2011) a constitutive law with frictional behavior and limited tensile and compression strength was considered. The same unit cell was considered by De Bellis and Addessi 2011 to develop a Cosserat-based multiscale model.

In this chapter, we first consider a one-brick RVE similar to the one adopted in the aforementioned papers, with the difference of having the whole bed and head joints on the top and the right RVE sides. The reason for this modification of the RVE will be explained in Section 7.4, where the finite element model will be described. Masonry nonlinearities are taken into account by adopting Rankine plasticity with exponential softening for all components, differentiating the mechanical parameters for bricks, head joint, and bed joint.

Then, the mechanical behavior of the one-brick RVE will be compared to the one of the two-brick RVE and to the one of a bigger RVE, composed of a total of six bricks and three bed joint layers (Figure 7.1d). The latter cell, in particular, admits two different sets of periodicity directions which differ in vector $\boldsymbol{v}_2$. The

first set, "set A", has the following periodicity directions

$$\boldsymbol{v}_{1,A} = 2\,L\,\boldsymbol{e}_1 \tag{7.65}$$

$$\boldsymbol{v}_{2,A} = \frac{L}{2}\,\boldsymbol{e}_1 + 3H\,\boldsymbol{e}_2 \tag{7.66}$$

while the second set, "set B", is characterized by

$$\boldsymbol{v}_{1,B} = 2(L_b + L_m)\,\boldsymbol{e}_1 \tag{7.67}$$

$$\boldsymbol{v}_{2,B} = \frac{3}{2}L\,\boldsymbol{e}_1 + 3H\,\boldsymbol{e}_2 \tag{7.68}$$

The purpose of these analyses is to investigate the influence of RVE size and the choice of periodicity directions on stress-strain diagrams and localization of inelastic strains (Stransky and Jirásek 2011; Svenning et al. 2017).

7.3.2 Prevention of rigid body motions in two-dimensional unit cells

Restricting our attention to two-dimensional cells and considering a Cartesian coordinate system $0xy$, the position vector can be expressed as

$$\boldsymbol{x} = \begin{bmatrix} x \\ y \end{bmatrix} \tag{7.69}$$

In the first order homogenization, the macroscopic strain field $\boldsymbol{E}$ imposes a macroscopic displacement field $\boldsymbol{W}$ that is linear with respect to the position vector $\boldsymbol{x}$ as stated in (7.10), reported here for convenience:

$$\boldsymbol{W}(\boldsymbol{x}) = \boldsymbol{W}(\boldsymbol{x}_R) + \boldsymbol{E}\cdot(\boldsymbol{x} - \boldsymbol{x}_R) \tag{7.70}$$

The matrix form of the macroscopic strain tensor $\boldsymbol{E}$ is given by

$$\boldsymbol{E} = \begin{bmatrix} E_{xx} & \Gamma_{xy} \\ \Gamma_{xy} & E_{yy} \end{bmatrix} \tag{7.71}$$

If we consider the reference point as positioned in the reference-frame origin, we have

$$\boldsymbol{x}_R = \begin{bmatrix} 0 \\ 0 \end{bmatrix} \tag{7.72}$$

Let W_x and W_y be the x and y components of $\boldsymbol{W}$. We can rewrite (7.70) in matrix form as

$$\begin{bmatrix} W_x(x,y) \\ W_y(x,y) \end{bmatrix} = \begin{bmatrix} W_x(0,0) \\ W_y(0,0) \end{bmatrix} + \begin{bmatrix} E_{xx} & \Gamma_{xy} \\ \Gamma_{xy} & E_{yy} \end{bmatrix} \begin{bmatrix} x \\ y \end{bmatrix} \tag{7.73}$$

or, equivalently, we can express separately the components of the macroscopic displacements as

$$W_x(x,y) = W_x(0,0) + E_{xx}\,x + \Gamma_{xy}\,y \tag{7.74}$$

$$W_y(x,y) = W_y(0,0) + \Gamma_{xy}\,x + E_{yy}\,y \tag{7.75}$$

The macroscopic displacement field has still an underdetermination of order two, corresponding to the two traslational rigid body motions[1].

Rigid body translation are prevented by restraining the vertical and horizontal displacement of one node. For simplicity, taking the reference-frame origin $\boldsymbol{x}_R$ as the supported node, we get

$$W_x(0,0) = 0 \tag{7.76}$$
$$W_y(0,0) = 0 \tag{7.77}$$

The resulting macroscopic displacement field is given by

$$\boldsymbol{W} = \boldsymbol{E} \cdot \boldsymbol{x} \tag{7.78}$$

It is worth noting that the support position is not mandatory: it could be changed if needed, and $\boldsymbol{W}$ would change accordingly.

7.3.3 Periodicity constraints

The assumption of periodic boundary conditions is equivalent to imposing (7.47), here reported for convenience:

$$\boldsymbol{u}(\boldsymbol{x}^+) - \boldsymbol{u}(\boldsymbol{x}^-) = \boldsymbol{E} \cdot (\boldsymbol{x}^+ - \boldsymbol{x}^-) \qquad \forall\, \boldsymbol{x}^- \in \Gamma^- \tag{7.79}$$

where $\boldsymbol{x}^+$ and $\boldsymbol{x}^-$ are the position vectors in the image and mirrored part respectively, $\boldsymbol{u}$ is the displacement vector, and $\boldsymbol{E}$ is the macroscopic strain matrix.

The periodicity directions that define the correspondence between points of the image and the mirrored part of the RVE boundary are strictly related to the problem of interest. In the case of a one-brick RVE, the RVE is a rectangle having the image side divided into three parts: the first two (Γ_1 and Γ_2) are half the horizontal side, and the third one (Γ_3) is the whole vertical side. While the mirrored part of the vertical side is the opposite one, the mirrored parts of the horizontal sides are crossed, as shown in Figure 7.2a.

If we solve the boundary-valued problem through the finite element method, the body is discretized in finite elements, and we need to link degrees of freedom of nodes on the periodic parts according to (7.47). When imposing the constraints, one has to pay attention that the number of periodicity constraint equations must be equal to the number of degrees of freedom of mirrored boundary nodes. In the case of crossed mirrored parts, i.e., for the one-brick RVE, the definition of these equations might not be trivial. To show an application example, we consider an RVE discretized in eight four-nodes elements arranged in two rows. In Figure 7.2b, the link between degrees of freedom of nodes of corresponding surfaces is pointed out through solid lines of different colors, one for each boundary part. Particular attention must be paid to degrees of freedom of nodes belonging to two surfaces, i.e., the ones at the intersections of different boundary parts, in order not to build an under- or over-constrained set of equations. In Figure 7.2b, the link between nodes 5 and 13 is missing since it is redundant, as it can be obtained as a linear combination of the constraints between nodes 1 and 13 and nodes 1 and 5. Analogously, imposing links between nodes 3 and 11 and nodes 3 and 15 implies a link between nodes 11 and 15.

[1] Rigid body rotation is automatically prevented by the symmetry of the macroscopic strain tensor.

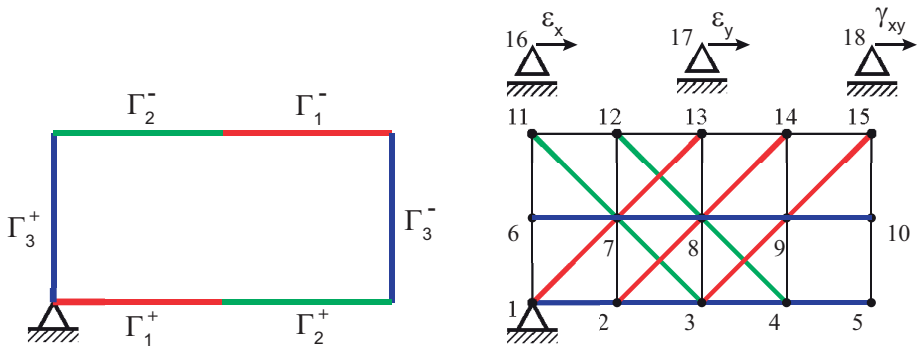

(a) Division of the RVE boundary in image and mirrored parts.

(b) Scheme of the enforced internal constraints.

Figure 7.2: Imposition of periodicity constraints in the RVE.

One can come up with a general rule. Let Γ^+ be the image (master) boundary part and Γ^- be the mirrored (slave) boundary part, which can be composed of a set of sub-boundaries. Every node in the internal part of Γ^+ must be the master of the corresponding slave nodes belonging to Γ^-. If a node belongs to two different sub-boundaries of Γ^+, then it is the master of two slave nodes. The external nodes of the boundary Γ^+ have to be excluded, as they are slaves of other master nodes.

It is worth mentioning an implementation detail. The macroscopic strain components are usually represented as degrees of freedom of fictitious nodes in the finite element model of the RVE. This representation is useful because we can impose macroscopic strains on the RVE by imposing displacements of the fictitious nodes, and read the macroscopic stress components as the corresponding reactions. Conversely, we can release a fictitious node degree of freedom and prescribe forces, representing macroscopic stress components imposed on the RVE; the corresponding macroscopic strains are then determined by reading the fictitious node displacements. In the example of Figure 7.2b, we define three nodes (16, 17, and 18) whose horizontal displacement represents respectively ε_{xx}, ε_{yy}, and γ_{xy}. Therefore, the periodic boundary conditions (7.47) reduce to linear tyings between degrees of freedom of the system, which can be imposed through a multi-master-slave approach.

We report here the implementation technique for multi-master-slave constraints of the finite element solver used in this chapter. Internal constraints represent supplementary equations that must be fulfilled in addition to the standard equilibrium equations, which can be written in matrix form for the linearized case as

$$\boldsymbol{K}\,\boldsymbol{u} = \boldsymbol{f} \tag{7.80}$$

where $\boldsymbol{u}$ and $\boldsymbol{f}$ are respectively the vectors of degrees of freedom and external forces, and $\boldsymbol{K}$ is the stiffness matrix. Linear constraints between degrees of freedom can be denoted in matrix form (Felippa 2004) as

$$\boldsymbol{A}\,\boldsymbol{u} = \boldsymbol{b} \tag{7.81}$$

where $\boldsymbol{A}$ is a matrix of coefficients having size $m \times n$, m is the number of constraint equations, and n is the number of degrees of freedom. To take into account the constraints (7.81), the assembled master equations (7.80) must be changed.

The i-th row of (7.81), namely

$$A_{ij} u_j = b_j \tag{7.82}$$

represents the i-th constraint equation. For a given equation i, if the number n_0 of non-zero elements of A_{ij} is less than or equal to 2, the constraint can be imposed as a usual external restraint ($n_0 = 1$) or through a single master-slave approach ($n_0 = 2$). However, if n_0 is greater than 2, the constraint imposition needs a more general method.

For each constraint equation, we label a degree of freedom as the "slave" while the remaining ones are labeled as "master". The internal constraint equations (7.81) may be rewritten as

$$\boldsymbol{A}_m \, \boldsymbol{u}_m + \boldsymbol{u}_s = \boldsymbol{b} \tag{7.83}$$

We can solve for the slave degrees of freedom and get

$$\boldsymbol{u}_s = -\boldsymbol{A}_m \, \boldsymbol{u}_m + \boldsymbol{b} \tag{7.84}$$

The system (7.80) can be partitioned as

$$\begin{bmatrix} \boldsymbol{K}_{mm} & \boldsymbol{K}_{ms} \\ \boldsymbol{K}_{sm} & \boldsymbol{K}_{ss} \end{bmatrix} \begin{bmatrix} \boldsymbol{u}_m \\ \boldsymbol{u}_s \end{bmatrix} = \begin{bmatrix} \boldsymbol{f}_m + \boldsymbol{r}_m \\ \boldsymbol{f}_s + \boldsymbol{r}_s \end{bmatrix} \tag{7.85}$$

where $\boldsymbol{r}_m$ and $\boldsymbol{r}_s$ are the constraint reactions, acting respectively on the master and slave degrees of freedom. We assume that the internal constraints are smooth, i.e., the reactions do not develop power on the displacement increment, namely

$$\dot{\boldsymbol{u}}_m^T \, \boldsymbol{r}_m + \dot{\boldsymbol{u}}_s^T \, \boldsymbol{r}_s = 0 \qquad \forall \, \dot{\boldsymbol{u}}_s, \dot{\boldsymbol{u}}_m \tag{7.86}$$

From (7.84) we get

$$\dot{\boldsymbol{u}}_s = -\boldsymbol{A}_m \, \dot{\boldsymbol{u}}_m \tag{7.87}$$

which can be substituted into (7.86) to obtain

$$\dot{\boldsymbol{u}}_m^T \, \boldsymbol{r}_m - \dot{\boldsymbol{u}}_m^T \, \boldsymbol{A}_m^T \, \boldsymbol{r}_s = 0 \qquad \forall \, \dot{\boldsymbol{u}}_m \tag{7.88}$$

Since the previous equation must hold for all $\dot{\boldsymbol{u}}_m$, we get

$$\boldsymbol{r}_m = \boldsymbol{A}_m^T \, \boldsymbol{r}_s \tag{7.89}$$

Solving the second equation of (7.85) in terms of $\boldsymbol{r}_s$ and substituting it into (7.89), we obtain

$$\boldsymbol{r}_m = \boldsymbol{A}_m^T \, (\boldsymbol{K}_{sm} \, \boldsymbol{u}_m + \boldsymbol{K}_{ss} \, \boldsymbol{u}_s - \boldsymbol{f}_s) \tag{7.90}$$

which can substitute into the first equation of (7.85) and get the reduced system

$$\tilde{\boldsymbol{K}} \, \boldsymbol{u}_m = \tilde{\boldsymbol{f}} \tag{7.91}$$

where

$$\tilde{\boldsymbol{K}} = \boldsymbol{K}_{mm} - \boldsymbol{A}_m^T \boldsymbol{K}_{sm} - \boldsymbol{K}_{ms} \, \boldsymbol{A}_m + \boldsymbol{A}_m^T \boldsymbol{K}_{ss} \, \boldsymbol{A}_m \tag{7.92}$$

$$\tilde{\boldsymbol{f}} = \boldsymbol{f}_m - \boldsymbol{A}_m^T \boldsymbol{f}_s - \Big(\boldsymbol{K}_{ms} - \boldsymbol{A}_m^T \boldsymbol{K}_{ss} \Big) \, \boldsymbol{b} \tag{7.93}$$

We have obtained a new solving system with a reduced number of equations and unknowns by removing the slave degrees of freedom from the vector of unknowns $\boldsymbol{u}$.

7.3.4 Localization analysis

The study of localization properties of inelastic strains is of central importance for failure modeling. When localization occurs, inelastic strain increments localize in narrow bands while the remaining part of the body unloads elastically. The displacement field remains continuous across the separation surfaces, while the strain field may have a jump. In numerical analysis, this leads to a pathological sensitivity of the results with respect to the spatial discretization.

The classical necessary condition for localization, as inspired by the early works of Hadamard 1903 and Hill 1958, corresponds to the singularity of the localization tensor, under the assumption of the same tangent stiffness tensor on both sides of the discontinuity. This condition was later extended removing the latter assumption (Rice and Rudnicki 1980), obtaining the following localization condition

$$\exists \boldsymbol{v} : \boldsymbol{v} \cdot \boldsymbol{Q} \cdot \boldsymbol{v} \leq 0 \tag{7.94}$$

i.e., the loss of positive definiteness of the localization tensor, which is given by

$$\boldsymbol{Q} = \boldsymbol{n} \cdot \boldsymbol{D} \cdot \boldsymbol{n} \tag{7.95}$$

where $\boldsymbol{D}$ is the tangent stiffness tensor and $\boldsymbol{n}$ is the normal to the weak discontinuity surface.

In the homogenization of an RVE, it is interesting to analyze its localization properties considering the RVE as a macroscopic material point. For this purpose, we have to determine consistently the stiffness tensor that relates stresses and strains at the macroscopic level. The system of equations of the RVE takes into account the equilibrium equations of all the microscopic degrees of freedom, together with the constraint equations coming from the imposition of the periodic boundary conditions which connects the microscopic degrees of freedom to the macroscopic ones. If we rearrange the total RVE system of equations to the form (V. Kouznetsova et al. 2001)

$$\begin{bmatrix} \boldsymbol{D}_{ee} & \boldsymbol{D}_{ei} \\ \boldsymbol{D}_{ie} & \boldsymbol{D}_{ii} \end{bmatrix} \begin{bmatrix} \delta \boldsymbol{u}_e \\ \delta \boldsymbol{u}_i \end{bmatrix} = \begin{bmatrix} \delta \boldsymbol{f}_e \\ \boldsymbol{0} \end{bmatrix} \tag{7.96}$$

where $\boldsymbol{D}_{ee}$, $\boldsymbol{D}_{ei}$, $\boldsymbol{D}_{ie}$, and $\boldsymbol{D}_{ii}$ are partitions of the tangent stiffness matrix of the whole system, while $\delta \boldsymbol{u}_e$ and $\delta \boldsymbol{f}_e$ are the variations of displacements and forces that refer to the external degrees of freedom, i.e., the macroscopic strains, and $\delta \boldsymbol{u}_i$ correspond to the variations of the microscopic displacements. By condensation of (7.96), we obtain the macroscopic tangent stiffness matrix $\boldsymbol{D}_M$ which relates the variations of displacements $\delta \boldsymbol{u}_e$ and forces $\delta \boldsymbol{f}_e$ of the macroscopic degrees of freedom, namely

$$\boldsymbol{D}_M = \boldsymbol{D}_{ee} - \boldsymbol{D}_{ei} \boldsymbol{D}_{ii}^{-1} \boldsymbol{D}_{ie} \tag{7.97}$$

The localization condition reduces to finding the set of vectors $\boldsymbol{n}$ for which the following condition is satisfied,

$$\lambda_{min} \leq 0 \tag{7.98}$$

where λ_{min} is the minimum eigenvalue of the macroscopic localization tensor, defined as

$$\boldsymbol{Q}_M = \boldsymbol{n} \cdot \boldsymbol{D}_M \cdot \boldsymbol{n} \tag{7.99}$$

As explained in Chapter 6, the eigenvector associated to $\lambda_m in$ represents the direction of material instability and it is called "polarization vector" and denoted with the symbol $\boldsymbol{m}$.

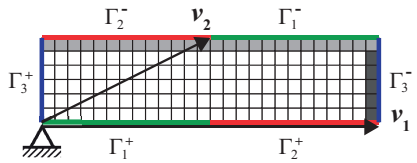

(a) One-brick RVE (RVE-1).

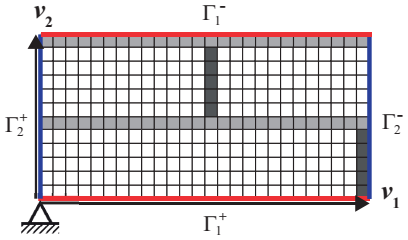

(b) Two-bricks RVE (RVE-2).

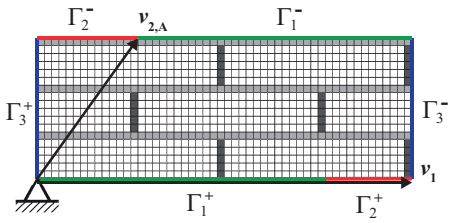

(c) Six-bricks RVE, case A (RVE-6a).

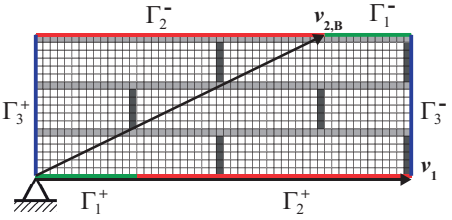

(d) Six-bricks RVE, case B (RVE-6b).

Figure 7.3: Masonry RVEs analyzed.

7.4 Finite element model of the RVE

The boundary-value problem of the RVE is solved through the finite element method. The body is considered as two-dimensional and discretized by 4-node isoparametric finite elements with 2x2 Gauss integration scheme under plane stress conditions.

To assess the different responses of masonry RVEs changing their size and the periodicity directions, we consider three different geometries, one of which allows two sets of periodicity directions, leading to a total of four different RVE types. First, we consider an RVE composed of one brick and one head and bed mortar layers (RVE-1, Figure 7.3a). This unit cell is characterized by an inclined periodicity direction, which links the bottom-left corner to the mid-point of the top side. Then, we consider the two-bricks RVE composed of a brick and two half ones and characterized by orthogonal periodicity directions (RVE-2, Figure 7.3b). Finally, we study the response of a bigger RVE, composed of five bricks plus two half ones and three horizontal mortar layers. This unit cell admits two possible sets of periodicity directions, what we denote by the letters A and B; see Figures 7.3c (RVE-6a) and 7.3d (RVE-6b).

The constitutive law assigned to all materials inside the RVE is Rankine elasto-plasticity, which can reproduce the tensile failure of both bricks and mortar layers. The Rankine yield function reads

$$f(\boldsymbol{\sigma}, \kappa) = \sigma_I - \sigma_Y(\kappa) \tag{7.100}$$

where σ_I is the maximum principal stress. We assume an exponential softening given by

$$\sigma_Y(\kappa) = f_t \, \exp\left(-\frac{f_t}{g}\kappa\right) \tag{7.101}$$

	Bricks	Bed Joints	Head joints
E_Y [GPa]	5.0	1.0	0.5
ν [-]	0.15	0.35	0.35
f_t [MPa]	2.500	0.250	0.125
g [N·m/m^3]	700	250	60

Table 7.1: Mechanical parameters (strong-bricks scenario)

where f_t is the tensile strength, g is the dissipated energy per unit volume, i.e., the ratio between the dissipated energy per unit area and the finite element characteristic length, and κ the hardening variable. The latter is equal among all finite elements, since the RVE is discretized in finite elements of the same size (squares with side 1.0 cm). More details regarding Rankine plasticity model implemented in the numerical solver are reported in Section 7.5.

Different mechanical parameters, reported in Table 7.1, are assigned to bricks, head joints, and bed joints. In addition to the symbols already defined, we denote with E_Y and ν the Young modulus and Poisson ratio, respectively. In particular, we consider two different scenarios: strong bricks, in which bricks have higher tensile strength, and weak bricks, where bricks and mortar have similar tensile strength. In the latter case, the mechanical parameters are the same as reported in Table 7.1, with the only difference of a value of brick tensile strength of 0.5 MPa. The elastic moduli have been chosen as typical ones taken from literature.

The mortar bed and head joints are discretized, respectively, by only one row and column of elements to force the inelastic strain localization into the entire joint thickness. The RVE is subjected to isostatic restraints for preventing rigid body motions. To retrieve the macroscopic stresses and strains associated to the RVE, we perform the homogenization procedure described in the preceding section, which consists in imposing the periodic boundary conditions over RVE boundary parts. The periodicity directions define the correspondence between points on the boundary parts. The displacements of the corresponding points are linked by linear internal constraints that depend on their relative position and the macroscopic strains, as expressed by (7.47). In the numerical model, it is useful to interpret the macroscopic strain components as degrees of freedom of a fictitious node. This way, we can impose macroscopic strains on the RVE by imposing displacements of the fictitious node, and the corresponding reactions, multiplied by the RVE volume, represent the macroscopic stress components. Conversely, we can release a degree of freedom of the fictitious node and prescribe a force, which now represents a macroscopic stress component. The corresponding macroscopic strains are determined by reading the fictitious node displacements.

In Section 7.6 and 7.7, we analyze the RVE under uniaxial and shear-compression stresses. Analyses are performed in indirect displacement control (Jirásek and Bažant 2001), in which the RVE is subjected to a set of loads, a function of a scalar multiplier. The scalar multiplier represents an additional unknown determined by monitoring the monotonic increase of a linear combination of controlled degrees of freedom during the process. We consider a linear loading program, characterized by

$$\boldsymbol{f}_{ext}(\mu) = \boldsymbol{f}_0 + \mu \boldsymbol{f}_1 \tag{7.102}$$

where $\boldsymbol{f}_0$ is the part of external forces kept constant during the process, and $\boldsymbol{f}_1$ is

the scaled component.

The discretized equation of equilibrium reads

$$\boldsymbol{f}_{int}(\boldsymbol{d}) = \boldsymbol{f}_{ext}(\mu) \tag{7.103}$$

where $\boldsymbol{d}$ is the nodal displacement vector. Since this equation is nonlinear, an incremental-iterative procedure must be used. We start at step number (n) with the known quantities $\boldsymbol{d}^{(n-1)}$ and $\mu^{(n-1)}$, and we are looking for the values

$$\boldsymbol{d}^{(n)} = \boldsymbol{d}^{(n-1)} + \Delta\boldsymbol{d} \qquad \mu^{(n)} = \mu^{(n-1)} + \Delta\mu \tag{7.104}$$

so that

$$\boldsymbol{f}_{int}(\boldsymbol{d}^{(n)}) = \boldsymbol{f}_0 + \mu^{(n)}\boldsymbol{f}_1 \tag{7.105}$$

The scalar multiplier μ is an additional unknown which can be determined by the condition

$$\boldsymbol{c}^T\Delta\boldsymbol{d} = \Delta l \tag{7.106}$$

where Δl is a constant which determines the step size, and $\boldsymbol{c}$ is a column matrix containing coefficients at individual nodal displacements. The linearized equation at a given iteration i reads

$$\boldsymbol{f}_{int}^{(n,i-1)} + \boldsymbol{K}^{(n,i-1)}\,\delta\boldsymbol{d}^{(n,i)} = \boldsymbol{f}_0 + \mu^{(n,i-1)}\boldsymbol{f}_1 + \delta\mu^{(n,i)}\boldsymbol{f}_1 \tag{7.107}$$

where $\delta\boldsymbol{d}^{(n,i)}$ and $\delta\mu^{(n,i)}$, which represent the unknowns of the system, are respectively the correction of the displacement increment $\Delta\boldsymbol{d}$ and the load parameter increment $\Delta\mu$. We can separately solve the equations

$$\boldsymbol{K}^{(n,i-1)}\,\delta\boldsymbol{d}_0 = \boldsymbol{f}_0 + \mu^{(n,i-1)}\boldsymbol{f}_1 - \boldsymbol{f}_{int}^{(n,i-1)} \tag{7.108}$$

$$\boldsymbol{K}^{(n,i-1)}\,\delta\boldsymbol{d}_f = \boldsymbol{f}_1 \tag{7.109}$$

and express the correction as

$$\delta\boldsymbol{d}^{(n,i)} = \delta\boldsymbol{d}_0 + \delta\mu^{(n,i)}\delta\boldsymbol{d}_f \tag{7.110}$$

In order to determine the load multiplier correction, we can use the constraint equation

$$\boldsymbol{c}^T\left(\Delta\boldsymbol{d}^{(n,i-1)} + \delta\boldsymbol{d}^{(n,i)}\right) = \Delta l \tag{7.111}$$

which combined with (7.110) gives

$$\delta\mu^{(n,i)} = \frac{\Delta l - \boldsymbol{c}^T\,\Delta\boldsymbol{d}^{(n,i-1)} - \boldsymbol{c}^T\,\delta\boldsymbol{d}_0}{\boldsymbol{c}^T\,\delta\boldsymbol{d}_f} \tag{7.112}$$

In summary, at the given step n, we impose a displacement increment Δl of the controlled node, and, for each iteration, we find the correction of the displacement and the load parameter increment by (7.110) and (7.112) respectively. The iterations stop when a selected convergence criterion is fulfilled for the equilibrium equations (7.105).

7.5 Rankine plasticity

It is useful to write the model equations in the standard form corresponding to a general formulation of plasticity. The Voigt notation will be used in the following.

Elastic-plastic split:

$$\boldsymbol{\varepsilon} = \boldsymbol{\varepsilon}_e + \boldsymbol{\varepsilon}_p \tag{7.113}$$

Stress-strain law for the elastic part:

$$\boldsymbol{\sigma} = \boldsymbol{D}_e \, \boldsymbol{\varepsilon}_e \tag{7.114}$$

Admissibility condition:

$$f(\boldsymbol{\sigma}, \kappa) \leq 0 \tag{7.115}$$

Associated flow rule:

$$\dot{\boldsymbol{\varepsilon}}_p = \dot{\lambda} \boldsymbol{f} \tag{7.116}$$

$$\dot{\lambda} \geq 0 \tag{7.117}$$

where

$$\boldsymbol{f} = \frac{\partial f(\boldsymbol{\sigma}, \kappa)}{\partial \boldsymbol{\sigma}} \tag{7.118}$$

Loading-unloading condition:

$$\dot{\lambda} f(\boldsymbol{\sigma}, \kappa) = 0 \tag{7.119}$$

The Rankine yield function reads

$$f(\boldsymbol{\sigma}, \kappa) = \sigma_I - \sigma_Y(\kappa) \tag{7.120}$$

where σ_I is the first principal stress and $\sigma_Y(\kappa)$ is the yielding stress, function of the hardening variable κ. In the plane stress case, we can express the first principal stress in terms of the plane stress components σ_{xx}, σ_{yy}, and τ_{xy}, namely

$$f(\boldsymbol{\sigma}, \kappa) = \frac{\sigma_x + \sigma_y}{2} + \sqrt{\left(\frac{\sigma_x - \sigma_y}{2}\right)^2 + \tau_{xy}^2} - \sigma_Y(\kappa) \tag{7.121}$$

which can be rewritten in matrix form as

$$f(\boldsymbol{\sigma}, \kappa) = \boldsymbol{\delta}^T \boldsymbol{\sigma} + \sqrt{\boldsymbol{\sigma}^T \boldsymbol{P} \boldsymbol{\sigma}} - \sigma_Y(\kappa) \tag{7.122}$$

where the stress $\boldsymbol{\sigma}$ is expressed in the Voigt notation as

$$\boldsymbol{\sigma} = \begin{bmatrix} \sigma_x \\ \sigma_y \\ \tau_{xy} \end{bmatrix} \tag{7.123}$$

and the auxiliary matrices $\boldsymbol{P}$ and $\boldsymbol{\delta}$ are defined as

$$\boldsymbol{P} = \begin{bmatrix} 1/4 & -1/4 & 0 \\ -1/4 & 1/4 & 0 \\ 0 & 0 & 1 \end{bmatrix} \qquad \boldsymbol{\delta} = \begin{bmatrix} 1/2 \\ 1/2 \\ 0 \end{bmatrix} \tag{7.124}$$

The numerical scheme deals with the following derivatives:

$$\boldsymbol{f} = \boldsymbol{\delta} + \frac{\boldsymbol{P}\boldsymbol{\sigma}}{\sqrt{\boldsymbol{\sigma}^T \boldsymbol{P} \boldsymbol{\sigma}}} \tag{7.125}$$

$$\frac{\partial \boldsymbol{f}}{\partial \boldsymbol{\sigma}} = \frac{\boldsymbol{P}}{\sqrt{\boldsymbol{\sigma}^T \boldsymbol{P} \boldsymbol{\sigma}}} + \frac{(\boldsymbol{P}\boldsymbol{\sigma})\,(\boldsymbol{P}\boldsymbol{\sigma})^T}{\sqrt{(\boldsymbol{\sigma}^T \boldsymbol{P} \boldsymbol{\sigma})^3}} \tag{7.126}$$

$$\frac{\partial \boldsymbol{f}}{\partial \kappa} = \boldsymbol{0} \tag{7.127}$$

$$\frac{\partial f}{\partial \kappa} = -\frac{\partial \sigma_Y}{\partial \kappa} \tag{7.128}$$

We consider an exponential softening law given by

$$\sigma_Y = f_t \, \exp(-\frac{f_t}{g}\kappa) \tag{7.129}$$

where f_t is the initial value of the tensile strength and g is the dissipated energy per unit volume.

We define the hardening parameter κ in the strain-hardening hypothesis, namely

$$\dot{\kappa} = \|\dot{\boldsymbol{\varepsilon}}_p\| \tag{7.130}$$

It is useful to evaluate the norm of the plastic strain rate in Rankine plasticity. In tensor notation, it would be given by $\|\dot{\boldsymbol{\varepsilon}}_p\| = \sqrt{\dot{\boldsymbol{\varepsilon}}_p : \dot{\boldsymbol{\varepsilon}}_p}$. In the Voigt notation we must write

$$\|\dot{\boldsymbol{\varepsilon}}_p\| = \sqrt{\dot{\boldsymbol{\varepsilon}}_p^T \boldsymbol{Q}^{-1} \dot{\boldsymbol{\varepsilon}}_p} = \dot{\lambda} \sqrt{\boldsymbol{f}^T \boldsymbol{Q}^{-1} \boldsymbol{f}} \tag{7.131}$$

where

$$\boldsymbol{Q}^{-1} = \begin{bmatrix} 1 & 0 & 0 \\ 0 & 1 & 0 \\ 0 & 0 & 1/2 \end{bmatrix} \tag{7.132}$$

is a suitable scaling matrix that converts a strain-like column matrix into a stress-like column matrix. It is worth noting that

$$\boldsymbol{P}^T \boldsymbol{Q}^{-1} \boldsymbol{P} = \frac{1}{2}\boldsymbol{P} \tag{7.133}$$

$$\boldsymbol{P}^T \boldsymbol{Q}^{-1} \boldsymbol{\delta} = \boldsymbol{0} \tag{7.134}$$

$$\boldsymbol{\delta}^T \boldsymbol{Q}^{-1} \boldsymbol{\delta} = \frac{1}{2} \tag{7.135}$$

Based on these relations, it is easy to evaluate

$$\begin{aligned} \boldsymbol{f}^T \boldsymbol{Q}^{-1} \boldsymbol{f} &= \frac{\boldsymbol{\sigma}^T \boldsymbol{P}^T \boldsymbol{Q}^{-1} \boldsymbol{P} \boldsymbol{\sigma}}{\boldsymbol{\sigma}^T \boldsymbol{P} \boldsymbol{\sigma}} + 2\frac{\boldsymbol{\sigma}^T \boldsymbol{P}^T \boldsymbol{Q}^{-1} \boldsymbol{\delta}}{\sqrt{\boldsymbol{\sigma}^T \boldsymbol{P} \boldsymbol{\sigma}}} + \boldsymbol{\delta}^T \boldsymbol{Q}^{-1} \boldsymbol{\delta} = \\ &= \frac{1}{2} + 0 + \frac{1}{2} = 1 \end{aligned} \tag{7.136}$$

and (7.131) simplifies to

$$\|\dot{\boldsymbol{\varepsilon}}_p\| = \dot{\lambda} \tag{7.137}$$

which gives also

$$\dot{\kappa} = \dot{\lambda} \tag{7.138}$$

7.5.1 Comment on vertex of the yield surface

The expression for the gradient of the yield function, given in (7.125), contains a fraction, and the denominator of this fraction vanishes if

$$\boldsymbol{\sigma}^T \boldsymbol{P}\, \boldsymbol{\sigma} = 0 \tag{7.139}$$

Due to the structure of matrix $\boldsymbol{P}$ specified in (7.124), this can happen only if $\sigma_x = \sigma_y$ and $\tau_{xy} = 0$, i.e., the stress tensor in spherical. This condition corresponds to a certain line in the stress space, passing through the origin. We are concerned only about the point at the intersection of this line with the yield surface, which is located at

$$\sigma_x = \sigma_Y \tag{7.140}$$
$$\sigma_y = \sigma_Y \tag{7.141}$$
$$\tau_{xy} = 0 \tag{7.142}$$

The yield surface is actually a surface in the three-dimensional stress space, and the singularity appears at one point only, so it corresponds to a vertex. For any nonzero value of the shear stress, the section remains smooth.

The normal to the yield surface at the vertex is not uniquely defined. Instead, one can characterize the normal cone, consisting of all vectors that are normal to planes that pass through the vertex and do not intersect the elastic domain (i.e., the interior of the yield surface). A vector $\boldsymbol{s}$ belongs to the normal cone if

$$\boldsymbol{s} \cdot \Delta\boldsymbol{\sigma} \leq 0 \tag{7.143}$$

for all vectors $\Delta\boldsymbol{\sigma}$ that represents the difference between an arbitrary point on the yield surface and the vertex point. Let us now find an explicit description of the normal cone.

Suppose that the stress state at the vertex is changed by $\Delta\boldsymbol{\sigma}$ such that the resulting state remains on the yield surface. The yield condition written for this modified state reads

$$\frac{\Delta\sigma_x + \Delta\sigma_y}{2} + \sqrt{\left(\frac{\Delta\sigma_x - \Delta\sigma_y}{2}\right)^2 + \Delta\tau_{xy}^2} = 0 \tag{7.144}$$

This condition can be rewritten as

$$\sqrt{\left(\frac{\Delta\sigma_x - \Delta\sigma_y}{2}\right)^2 + \Delta\tau_{xy}^2} = -\frac{\Delta\sigma_x + \Delta\sigma_y}{2} \tag{7.145}$$
$$\left(\Delta\sigma_x - \Delta\sigma_y\right)^2 + 4\Delta\tau_{xy}^2 = \left(\Delta\sigma_x + \Delta\sigma_y\right)^2 \tag{7.146}$$
$$-2\Delta\sigma_x\Delta\sigma_y + 4\Delta\tau_{xy}^2 = 2\Delta\sigma_x\Delta\sigma_y \tag{7.147}$$
$$\Delta\tau_{xy} = \pm\sqrt{\Delta\sigma_x\Delta\sigma_y} \tag{7.148}$$

For an admissible change of normal stresses, it is possible to evaluate the corresponding change of shear stress such that the modified state satisfies the yield condition. The magnitude of the shear stress is obtained from (7.148) but the sign remains arbitrary. By admissible changes of normal stresses we mean nonpositive ones, because the square root in (7.148) can be evaluated only if $\Delta\sigma_x\Delta\sigma_y \geq 0$

and the yield condition (7.144) can be satisfied only if $\Delta\sigma_x + \Delta\sigma_y \leq 0$, which in effect leads to constraints $\Delta\sigma_x \leq 0$ and $\Delta\sigma_y \leq 0$. It is convenient to characterize admissible stress changes by

$$\Delta\sigma_x = -\Delta\sigma\cos\beta \tag{7.149}$$

$$\Delta\sigma_y = -\Delta\sigma\sin\beta \tag{7.150}$$

$$\Delta\tau_{xy} = \pm\sqrt{\Delta\sigma_x\Delta\sigma_y} = \pm\Delta\sigma\sqrt{\cos\beta\sin\beta} \tag{7.151}$$

where $\Delta\sigma \geq 0$ and $\beta \in [0, \pi/2]$.

Now let us substitute the admissible stress changes into condition (7.143):

$$s_x\Delta\sigma_x + s_y\Delta\sigma_y + s_{xy}\Delta\tau_{xy} \leq 0 \tag{7.152}$$

$$-s_x\Delta\sigma\cos\beta - s_y\Delta\sigma\sin\beta \pm s_{xy}\Delta\sigma\sqrt{\cos\beta\sin\beta} \leq 0 \tag{7.153}$$

$$s_x\cos\beta + s_y\sin\beta \pm s_{xy}\sqrt{\cos\beta\sin\beta} \geq 0 \tag{7.154}$$

The magnitude of the stress change has disappeared and only the "direction", characterized by angle β, has remained. Condition (7.154) should be satisfied for all $\beta \in [0, \pi/2]$. Special cases $\beta = 0$ and $\beta = \pi/2$ directly lead to $s_x \geq 0$ and $s_y \geq 0$. If we set both s_x and s_y to zero, condition (7.154) cannot be satisfied for both signs, unless $s_{xy} = 0$, but this would give a zero vector $\boldsymbol{s}$. Now we can select s_x and s_y such that one of them is positive and the other at least nonnegative, and we can look for the admissible range of values of s_{xy} such that (7.154) holds for both signs. This condition can be rewritten as

$$\pm s_{xy}\sqrt{\cos\beta\sin\beta} \leq s_x\cos\beta + s_y\sin\beta \tag{7.155}$$

$$|s_{xy}| \leq \frac{s_x\cos\beta + s_y\sin\beta}{\sqrt{\cos\beta\sin\beta}} \tag{7.156}$$

Since β is an arbitrary angle between 0 and $\pi/2$, the right-hand side needs to be minimized with respect to β. A simple calculation shows that the partial derivative of the fraction on right-hand side with respect to β vanishes if $s_x\cos\beta = s_y\sin\beta$, and the corresponding value of the fraction is $2\sqrt{s_x s_y}$. The normal cone is thus characterized by conditions

$$s_x \geq 0 \tag{7.157}$$

$$s_y \geq 0 \tag{7.158}$$

$$|s_{xy}| \leq 2\sqrt{s_x s_y} \tag{7.159}$$

Any vector with components s_x, s_y, and s_{xy} satisfying these conditions is a generalized "normal" to the yield surface at the vertex. The same arguments can be used for the plastic potential since it is equal to the yield function for the present model.

For a stationary (non-evolving) yield surface, it would be easy to check whether the stress return algorithm should end up at the vertex. One would simply take the difference between the trial stress and the stress at the vertex, transform it into strain by applying the elastic compliance operator, and then check whether the resulting vector corresponds to one of the potential flow directions at the vertex. Since the yield surface is evolving, the check is somewhat more complicated because the stresses at the vertex after softening during the current step are not known in advance. One needs to find iteratively the increment of the hardening variable κ, assuming that the stress state at the end of the increment is at the vertex, and only then check whether the direction of plastic flow is admissible.

7.5.2 Stress return to a regular point

The standard stress-return algorithm used here is based on the backward Euler scheme. This means that the flow direction is determined for the state at the end of the step. Let us denote $\boldsymbol{\sigma}^{(n)}$ the stress at the beginning of the increment. The stress state at the end of the increment can be expressed as

$$\boldsymbol{\sigma} = \boldsymbol{\sigma}^{(n)} + \boldsymbol{D}_e \left(\Delta\boldsymbol{\varepsilon} - \Delta\boldsymbol{\varepsilon}_p\right) = \boldsymbol{\sigma}^{(tr)} - \boldsymbol{D}_e \Delta\boldsymbol{\varepsilon}_p \tag{7.160}$$

where

$$\boldsymbol{\sigma}^{(tr)} = \boldsymbol{\sigma}^{(n)} - \boldsymbol{D}_e \Delta\boldsymbol{\varepsilon}_p \tag{7.161}$$

is the trial stress and $\Delta\boldsymbol{\varepsilon}_p$ is the (unknown) plastic strain increment. The flow rule is approximated by

$$\Delta\boldsymbol{\varepsilon}_p = \Delta\kappa\, \boldsymbol{f}(\boldsymbol{\sigma}, \kappa^{(n)} + \Delta\kappa) \tag{7.162}$$

where $\boldsymbol{f}$ denotes the flow direction evaluated as the gradient of the yield function at the end of the step and $\Delta\kappa$ is the increment of the hardening variable, which is equal to the increment of the plastic multiplier (for the present model).

In a regular stress return, one would iteratively solve equations

$$\begin{aligned} \boldsymbol{\sigma} + \Delta\kappa\, \boldsymbol{D}_e\, \boldsymbol{f}(\boldsymbol{\sigma}, \kappa^{(n)} + \Delta\kappa) &= \boldsymbol{\sigma}^{(tr)} && (7.163)\\ f(\boldsymbol{\sigma}, \kappa^{(n)} + \Delta\kappa) &= 0 && (7.164) \end{aligned}$$

with unknowns $\boldsymbol{\sigma}$ and $\Delta\kappa$.

The previous set of nonlinear equations (7.163-7.164) is cast in a format of residuals at the integration point level:

$$\begin{aligned} \boldsymbol{r}_{\boldsymbol{\sigma}} &= \boldsymbol{\sigma} - \boldsymbol{\sigma}^{(tr)} + \Delta\kappa\, \boldsymbol{D}_e\, \boldsymbol{f}(\boldsymbol{\sigma}, \kappa) && (7.165)\\ r_f &= f(\boldsymbol{\sigma}, \kappa) && (7.166) \end{aligned}$$

The system can be solved using the Newton-Raphson method:

$$\begin{bmatrix} \boldsymbol{\sigma}^{k+1} \\ \kappa^{k+1} \end{bmatrix} = \begin{bmatrix} \boldsymbol{\sigma}^{k} \\ \kappa^{k} \end{bmatrix} - \begin{bmatrix} \dfrac{\partial \boldsymbol{r}_{\boldsymbol{\sigma}}}{\partial \boldsymbol{\sigma}} & \dfrac{\partial \boldsymbol{r}_{\boldsymbol{\sigma}}}{\partial \kappa} \\ \dfrac{\partial r_f}{\partial \boldsymbol{\sigma}} & \dfrac{\partial r_f}{\partial \kappa} \end{bmatrix}^{-1} \begin{bmatrix} \boldsymbol{r}_{\boldsymbol{\sigma}}{}^{k} \\ r_f{}^{k} \end{bmatrix} \tag{7.167}$$

where the superscript k denotes the iteration counter of the method at the integration point level. The differentials in (7.167) can be elaborated as

$$\begin{aligned} \frac{\partial \boldsymbol{r}_{\boldsymbol{\sigma}}}{\partial \boldsymbol{\sigma}} &= \boldsymbol{I} + \Delta\kappa\, \boldsymbol{D}_e\, \frac{\partial \boldsymbol{f}}{\partial \boldsymbol{\sigma}} && (7.168)\\ \frac{\partial \boldsymbol{r}_{\boldsymbol{\sigma}}}{\partial \kappa} &= \boldsymbol{D}_e\, \boldsymbol{f} + \Delta\kappa\, \boldsymbol{D}_e\, \frac{\partial \boldsymbol{f}}{\partial \kappa} && (7.169)\\ \frac{\partial r_f}{\partial \boldsymbol{\sigma}} &= \boldsymbol{f} && (7.170)\\ \frac{\partial r_f}{\partial \kappa} &= \frac{\partial f}{\partial \kappa} && (7.171) \end{aligned}$$

Tangent stiffness operator is given by differentiating (7.163-7.164), which gives

$$\begin{aligned} \dot{\boldsymbol{\sigma}} + \Delta\kappa\, \boldsymbol{D}_e\, \frac{\partial \boldsymbol{f}}{\partial \boldsymbol{\sigma}}\, \dot{\boldsymbol{\sigma}} + \boldsymbol{D}_e\, \boldsymbol{f}\, \dot{\kappa} + \Delta\kappa\, \boldsymbol{D}_e\, \frac{\partial \boldsymbol{f}}{\partial \kappa} \dot{\kappa} &= \boldsymbol{D}_e\, \dot{\boldsymbol{\varepsilon}} && (7.172)\\ \boldsymbol{f}^T \dot{\boldsymbol{\sigma}} + \frac{\partial f}{\partial \kappa} \dot{\kappa} &= 0 && (7.173) \end{aligned}$$

By defining the following auxiliary quantities

$$\boldsymbol{m} = \boldsymbol{f} + \Delta\kappa \frac{\partial \boldsymbol{f}}{\partial \kappa} \tag{7.174}$$

$$\boldsymbol{A} = \boldsymbol{I} + \Delta\lambda \boldsymbol{D}_e \frac{\partial \boldsymbol{f}}{\partial \boldsymbol{\sigma}} \tag{7.175}$$

$$h = -\frac{\partial f}{\partial \kappa} \tag{7.176}$$

we can rewrite (7.172-7.173) as

$$\boldsymbol{A}\,\dot{\boldsymbol{\sigma}} = \boldsymbol{D}_e\,(\dot{\boldsymbol{\varepsilon}} - \boldsymbol{m}\,\dot{\kappa}) \tag{7.177}$$

$$\boldsymbol{f}^T \dot{\boldsymbol{\sigma}} = h\,\dot{\kappa} \tag{7.178}$$

Substituting the expression of $\dot{\boldsymbol{\sigma}}$ obtained from (7.177)

$$\dot{\boldsymbol{\sigma}} = \boldsymbol{A}^{-1}\,\boldsymbol{D}_e\,(\dot{\boldsymbol{\varepsilon}} - \boldsymbol{m}\,\dot{\kappa}) \tag{7.179}$$

into (7.178), we have

$$\dot{\kappa} = \frac{\boldsymbol{f}^T \boldsymbol{A}^{-1}\,\boldsymbol{D}_e\,\dot{\boldsymbol{\varepsilon}}}{h + \boldsymbol{f}^T \boldsymbol{A}^{-1}\,\boldsymbol{D}_e\,\boldsymbol{m}} \tag{7.180}$$

which can be substituted again into (7.179), giving the algorithmic tangential stiffness relation between stress and strain rates

$$\dot{\boldsymbol{\sigma}} = \left(\boldsymbol{A}^{-1} - \frac{\boldsymbol{A}^{-1}\,\boldsymbol{D}_e\,\boldsymbol{m}\,\boldsymbol{f}^T \boldsymbol{A}^{-1}}{h + \boldsymbol{f}^T \boldsymbol{A}^{-1}\,\boldsymbol{D}_e\,\boldsymbol{m}} \right) \boldsymbol{D}_e\,\dot{\boldsymbol{\varepsilon}} \tag{7.181}$$

7.5.3 Stress return to the vertex

In the special case of vertex return, the flow direction is not a unique function of the final stress state but on the other hand the final stress state is a unique function of the hardening variable. We will consider the components of plastic strain increment as primary unknowns, express $\Delta\kappa_t$ as the norm of $\Delta\boldsymbol{\varepsilon}_p$, and then set up equation

$$\boldsymbol{\sigma}^{(vtx)}(\kappa^{(n)} + \|\Delta\boldsymbol{\varepsilon}_p\|) + \boldsymbol{D}_e \Delta\boldsymbol{\varepsilon}_p = \boldsymbol{\sigma}^{(tr)} \tag{7.182}$$

in which $\boldsymbol{\sigma}^{(vtx)}(\kappa)$ denotes the vertex stress state considered as function of the hardening variable, κ. From (7.182), the plastic strain increment can be computed, and then we need to check whether it is included in the normal cone evaluated for the final stress state.

For the specific form of yield function used by this model, equations (7.182) can be expanded component by component into

$$\sigma_x(\kappa^{(n)} + \|\Delta\boldsymbol{\varepsilon}_p\|) + D_{11}\Delta\varepsilon_{px} + D_{12}\Delta\varepsilon_{py} = \sigma_x^{(tr)} \tag{7.183}$$

$$\sigma_y(\kappa^{(n)} + \|\Delta\boldsymbol{\varepsilon}_p\|) + D_{21}\Delta\varepsilon_{px} + D_{22}\Delta\varepsilon_{py} = \sigma_y^{(tr)} \tag{7.184}$$

$$D_{33}\Delta\gamma_{pxy} = \tau_{xy}^{(tr)} \tag{7.185}$$

where D_{ij} denote the components of the elastic stiffness matrix (for simplicity) and

$$\|\Delta\boldsymbol{\varepsilon}_p\| = \sqrt{\Delta\varepsilon_{px}^2 + \Delta\varepsilon_{py}^2 + \Delta\gamma_{pxy}^2/2} \tag{7.186}$$

is the tensorial norm of the plastic strain increment (note the factor 1/2 at the shear term). Equation (7.185) is linear and contains a single unknown. Equations (7.183)–(7.184) are then solved iteratively as two coupled nonlinear equations with unknowns $\Delta\varepsilon_{px}$ and $\Delta\varepsilon_{py}$. Once the solution is found, we need to check whether it satisfies conditions that characterize the normal cone, which are rewritten here as

$$\Delta\varepsilon_{px} \geq 0 \tag{7.187}$$

$$\Delta\varepsilon_{py} \geq 0 \tag{7.188}$$

$$|\Delta\gamma_{px}| \leq 2\sqrt{\Delta\varepsilon_{px}\Delta\varepsilon_{py}} \tag{7.189}$$

In fact, since stiffnesses D_{ij} are positive and σ_i is always nonnegative, one can immediately exclude cases in which at least one of the normal components of trial stress is negative. If this first test is passed, one can perform a refined test, in which the maximum possible increment of hardening variable κ is estimated by solving linear equations

$$D_{11}\Delta\varepsilon_{px} + D_{12}\Delta\varepsilon_{py} = \sigma_x^{(tr)} \tag{7.190}$$

$$D_{21}\Delta\varepsilon_{px} + D_{22}\Delta\varepsilon_{py} = \sigma_y^{(tr)} \tag{7.191}$$

$$D_{33}\Delta\gamma_{pxy} = \tau_{xy}^{(tr)} \tag{7.192}$$

which would describe return to the origin of the stress space (extreme position of the vertex). This largest possible increment is then used to evaluate the minimum possible values of residual strengths σ_x and σ_y, and if at least one of them exceeds the corresponding component of trial stress, the solution cannot be admissible. Based on these checks, one can right away exclude many cases and directly proceed to the regular stress return. On the other hand, if both tests are passed, it is perhaps better to run the vertex return first, and only if the solution is not admissible, proceed to the regular return. The reason is that if the regular return is run for a trial state in the vertex region, convergence problems can be expected because of the high sensitivity of the plastic flow direction to the stress state in the vicinity of a singularity.

7.6 Analysis of the one-brick RVE

The one-brick RVE (Figure 7.3a) is analyzed under basic stress scenarios to test the model reliability with respect to the experimental observations. We recall that the RVE is discretized in finite elements having the thickness of mortar layers as the maximum size. The microscopic response of masonry is simulated through Rankine plasticity for all the constituents, differentiating the mechanical properties among bricks, head and bed joints, as shown in Table 7.1.

We perform nonlinear analysis in indirect displacement control. If we put the fictitious degrees of freedom corresponding to the macroscopic strains as the last three components of the displacement vector $\boldsymbol{d}$, namely

$$\boldsymbol{d} = \begin{bmatrix} \ldots & \varepsilon_{xx} & \varepsilon_{yy} & \gamma_{xy} \end{bmatrix}^T \tag{7.193}$$

the corresponding components of $\boldsymbol{f}_0$ and $\boldsymbol{f}_1$ represent respectively the constant part and the proportionally varying one of the macroscopic stress in the linear loading program defined in (7.102) and here reported for convenience

$$\boldsymbol{f}_{ext}(\mu) = \boldsymbol{f}_0 + \mu\boldsymbol{f}_1 \tag{7.194}$$

where μ is the scalar load multiplier. The increasing strain direction is defined by properly choosing the last three components of the vector $\boldsymbol{c}$, namely

$$\boldsymbol{c} = \begin{bmatrix} ... & \alpha_1 & \alpha_2 & \alpha_3 \end{bmatrix}^T \tag{7.195}$$

where α_1, α_2, and α_3 are coefficients individuating the macroscopic degrees of freedom to be controlled during the nonlinear analysis, while the other components of $\boldsymbol{c}$ are zero.

In the following analyses, vectors $\boldsymbol{f}_1$ and $\boldsymbol{c}$ are equal, i.e., the increasing strain and controlled stress directions are the same. Therefore, analyses are identified by vectors $\boldsymbol{c}$ and $\boldsymbol{f}_0$ only.

In the following paragraphs, we report the evolution of the macroscopic stresses and strains in the direction individuated by the vector $\boldsymbol{c}$. The macroscopic stress Σ is obtained by dividing the multiplier by the RVE volume, namely

$$\Sigma = \frac{\mu}{V_{RVE}} \tag{7.196}$$

while the macroscopic strain E is considered as

$$E = \boldsymbol{c}^T \boldsymbol{d} \tag{7.197}$$

Eventually, the RVE response will be compared to the one of a macroscopic model widely used to analyze masonry, namely Lourenço's model. The differences between the two models in terms of stiffness, strength, and localization properties under uniaxial tensile states will be investigated.

7.6.1 RVE response to basic stress conditions

The one-brick RVE response has been tested under some basic stress states to assess its effectiveness to model microscopic masonry mechanics.

Vertical tension First, the RVE is tested under vertical tension. The corresponding vectors defining the indirect displacement control analysis are

$$\boldsymbol{c} = \begin{bmatrix} ... & 1 & 0 & 0 \end{bmatrix}^T \tag{7.198}$$

$$\boldsymbol{f}_0 = \begin{bmatrix} ... & 0 & 0 & 0 \end{bmatrix}^T \tag{7.199}$$

The RVE exhibits localization of plastic strains in the whole bed joint (Figure 7.9a). The stress-strain graph (Figure 7.4) shows a clean exponential softening. The evolution of the minimum localization tensor eigenvalue exhibits a sudden drop to a negative value when the bed joint starts yielding and its value keeps to be negative, tending to zero. The corresponding localization angle is $\pi/2$, which is consistent with the bed joint localization observed experimentally.

We report here a thorough localization analysis of the RVE under vertical tension. We analyze the step at which we obtain the lowest localization tensor eigenvalue, namely right after the tensile stress peak. After condensation on the macroscopic degrees of freedom, the tangent stiffness reads

$$\boldsymbol{D}_M = \begin{bmatrix} 3895.4 & -185.9 & 0 \\ -185.9 & -1016.9 & 0 \\ 0 & 0 & 994.5 \end{bmatrix} \text{ MPa} \tag{7.200}$$

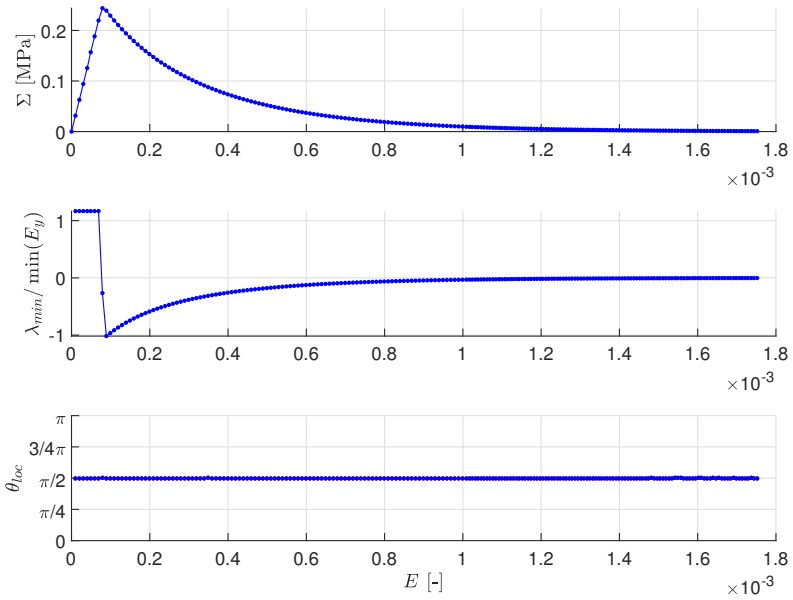

Figure 7.4: Evolution of the stress-strain relation, λ_{min}, and θ_{loc} under vertical tension.

The The minimization of the localization tensor eigenvalues over all possible normals $\boldsymbol{n}$ gives

$$\lambda_{min} = -1016.8\,\text{MPa} \tag{7.201}$$

which is referred to

$$\boldsymbol{n}_{loc} = [\quad 0.00789 \quad 0.99997 \quad]^T \tag{7.202}$$

The localization tensor corresponding to $\boldsymbol{n}_{loc}$ is given by

$$\boldsymbol{Q}(\boldsymbol{n}_{loc}) = \begin{bmatrix} 994.7 & 6.4 \\ 6.4 & -1016.8 \end{bmatrix} \text{MPa} \tag{7.203}$$

and the eigenvector associated to the minimum eigenvalue (polarization vector) is given by

$$\boldsymbol{m} = [\quad -0.00317 \quad 0.99999 \quad]^T \tag{7.204}$$

Therefore, we can conclude that vectors $\boldsymbol{n}$ and $\boldsymbol{m}$ almost coincide and the localization band is horizontal and opens in mode I. Figure 7.5a represents vectors $\boldsymbol{n}$ and $\boldsymbol{m}$ and the localization surface over the RVE plastic strain pattern.

Horizontal tension The test under horizontal tension is performed by choosing the following vectors

$$\boldsymbol{c} = [\ \ldots \quad 0 \quad 1 \quad 0\ ]^T \tag{7.205}$$

$$\boldsymbol{f}_0 = [\ \ldots \quad 0 \quad 0 \quad 0\ ]^T \tag{7.206}$$

$$\tag{7.207}$$

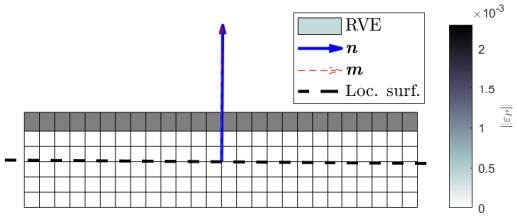

(a) Normal $\boldsymbol{n}$ and polarization vector $\boldsymbol{m}$.

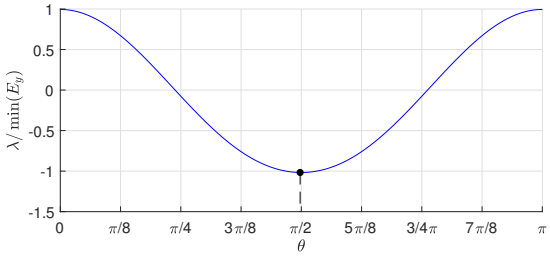

(b) Variation of the minimum localization tensor eigenvalue with the normal $\boldsymbol{n}$.

Figure 7.5: Localization analysis of the RVE under vertical tension.

The RVE is tested with two different sets of mechanical parameters, aimed to model the scenario of strong or weak bricks. In the "strong-bricks scenario", mortar represents the only source of weakness for masonry, and mortar joints are the zones where plastic strains tend to localize. The chosen set of parameters is reported in Table 7.1, and it is characteristic of new masonry construction. In some cases, however, bricks might be weaker, and cracks might propagate through them. To account for this failure mechanism, the RVE has been tested with a different set of mechanical parameters, which we call the "weak-brick scenario", where the brick tensile strength is reduced to 0.5 MPa, while the other parameters are kept equal. The graphs of the stress-strain relation and the localization properties evolution are reported in Figure 7.6. The plastic strain and stress maps at the last step of the analysis are shown in Figure 7.9b-7.9c. In both cases, the head joint starts yielding first, as testified by the slight change in the stress-strain diagram slope. Afterward, the yielding mechanism differs. In the strong-brick case, the block slides along one half of the bed joint, and failure occurs after its complete deterioration. The minimum localization tensor eigenvalue progressively decreases and eventually becomes negative, satisfying the localization condition. The corresponding localization surface confirms the zig-zag pattern as the normal $\boldsymbol{n}$ is inclined by an angle slightly bigger than $\pi/4$. In the weak-brick case, a vertical localized band forms in the middle of the brick, triggered by the head-joint of the adjacent brick layers. The corresponding localization angle is $\theta_{loc} = 0$, which is consistent with the forming vertical band.

Here, we report the RVE localization analysis in the interesting case of horizontal tension in the strong-brick scenario, which shows a zig-zag failure pattern. The analysis step considered is again the one corresponding to the lowest localization

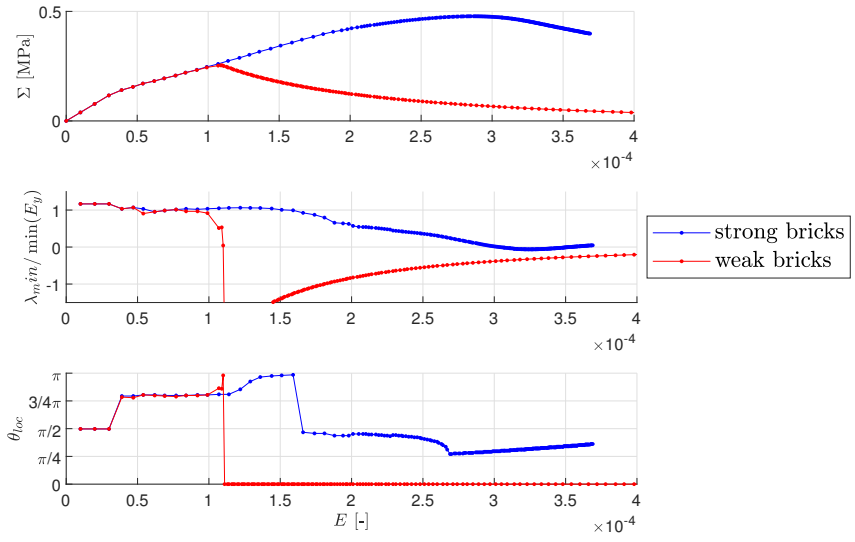

Figure 7.6: Evolution of the stress-strain relation, λ_{min}, and θ_{loc} under horizontal tension for both weak- and strong-bricks scenarios.

tensor eigenvalue registered during the analysis. The macroscopic tangent stiffness matrix is given by

$$\boldsymbol{D}_M = \begin{bmatrix} 1766.7 & -866.5 & 136.0 \\ -866.5 & 441.5 & -196.6 \\ -136.0 & -196.6 & 302.5 \end{bmatrix} \text{MPa} \tag{7.208}$$

The minimization of the localization tensor eigenvalues over all possible normals $\boldsymbol{n}$ gives

$$\lambda_{min} = -61.7\,\text{MPa} \tag{7.209}$$

which is referred to

$$\boldsymbol{n}_{loc} = \begin{bmatrix} 0.54486 & 0.83853 \end{bmatrix}^T \tag{7.210}$$

The localization tensor corresponding to $\boldsymbol{n}_{loc}$ is given by

$$\boldsymbol{Q}(\boldsymbol{n}_{loc}) = \begin{bmatrix} 612.9 & -436.3 \\ -436.3 & 220.5 \end{bmatrix} \text{MPa} \tag{7.211}$$

and the eigenvector associated to the minimum eigenvalue (polarization vector) is given by

$$\boldsymbol{m} = \begin{bmatrix} 0.54310 & 0.83967 \end{bmatrix}^T \tag{7.212}$$

Therefore, we have an inclined band which opens in mode I, since the vectors $\boldsymbol{n}$ and $\boldsymbol{m}$ almost coincide. Figure 7.5a represents vectors $\boldsymbol{n}$ and $\boldsymbol{m}$ and the localization surface over the RVE plastic strain map.

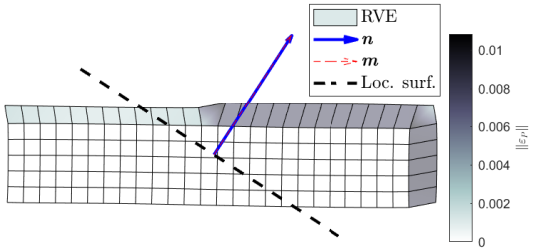

(a) Normal $\boldsymbol{n}$ and polarization vector $\boldsymbol{m}$.

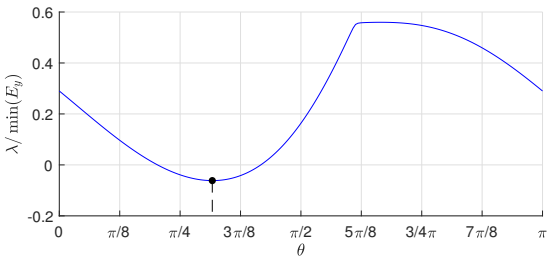

(b) Variation of the minimum localization tensor eigenvalue with the normal $\boldsymbol{n}$.

Figure 7.7: Localization analysis of the RVE under horizontal tension (strong bricks).

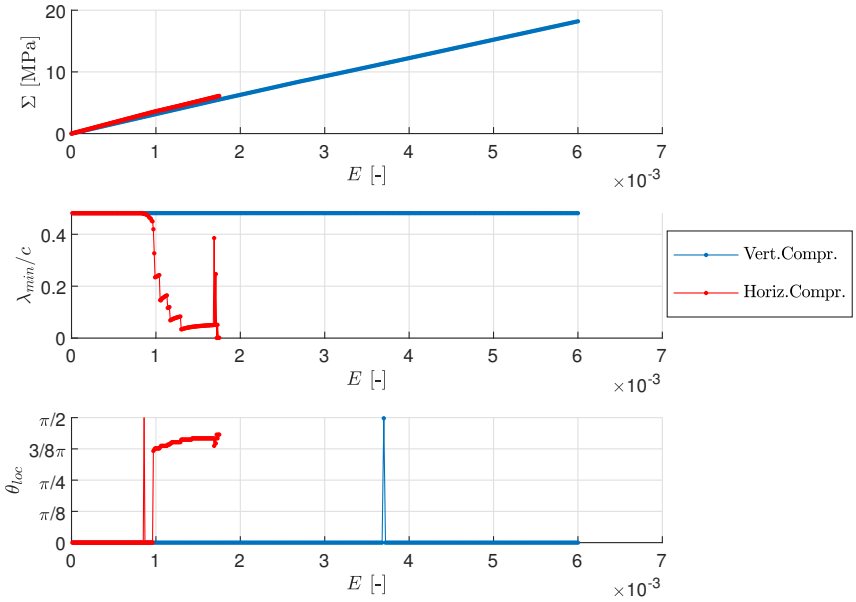

Figure 7.8: Evolution of the stress-strain relation, λ_{min}, and θ_{loc} under vertical and horizontal compression.

Horizontal and vertical compression The RVE is then tested under vertical and horizontal compression. The values of the quantities determining the analysis in indirect displacement control are the same as in (7.198-7.199) and (7.205-7.206), respectively for vertical and horizontal compression, with the only difference of having a negative value of $\Delta\ell$ from (7.106). Although the Rankine yielding criterion is in general not suitable for capturing failure in compression, the RVE model can reproduce the typical failure of a masonry specimen in vertical compression due to tensile strength overcoming in the transversal direction (this mechanism is thoroughly discussed in Section 2.2.1). Figure 7.9d shows the formation of vertical bands in the bricks due to horizontal tension originated by vertical compression. In horizontal compression, inelastic strains are localized in the horizontal bed joints, as shown in Figure 7.9e. The behavior in both vertical and horizontal compression is extremely brittle (Figure 7.8). The angles of the potential localization surfaces are $\theta_{loc} = 0$ for vertical compression, and $\theta_{loc} \simeq 7/16\pi$ for horizontal compression.

Shear-compression tests Finally, the masonry RVE has been tested in shear, by varying vertical compression in the range -1.25 MPa $\leq \sigma_0 \leq 0$. The corresponding vectors of the indirect displacement control analysis are

$$\boldsymbol{c} = \begin{bmatrix} \dots & 0 & 0 & 1 \end{bmatrix}^T \tag{7.213}$$

$$\boldsymbol{f}_0 = \begin{bmatrix} \dots & 0 & \sigma_0 V_{RVE} & 0 \end{bmatrix}^T \tag{7.214}$$

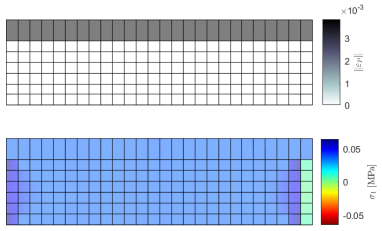

(a) Vertical tension.

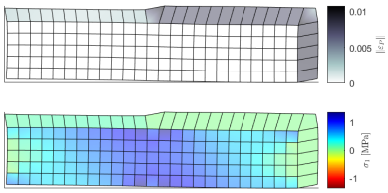

(b) Horizontal tension (strong bricks).

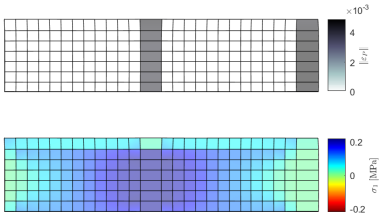

(c) Horizontal tension (weak bricks).

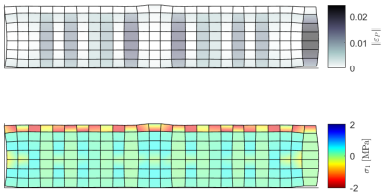

(d) Vertical compression.

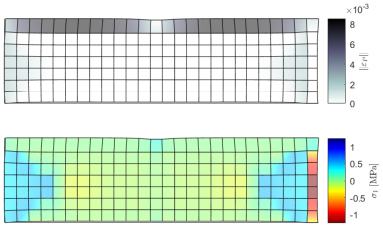

(e) Horizontal compression.

Figure 7.9: Plastic strain and tensile principal stress patterns for vertical and horizontal, tension and compression tests in the one-brick RVE.

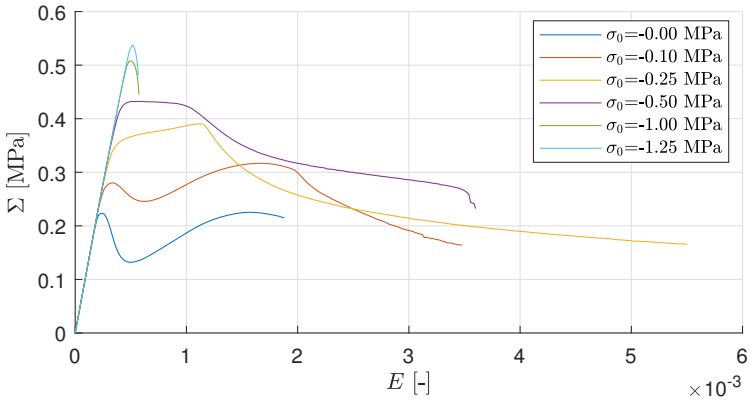

Figure 7.10: Stress-strain graphs for shear-compression tests with varying vertical compression.

The RVE is able to model the typical frictional behavior of masonry under shear stresses as the shear strength increases and the behavior becomes brittler with the increase of the vertical compression (see Figure 7.10). The plastic strain and principal stress map are reported in Figure 7.11. In the absence of vertical compression (Figure 7.11a), we observe a shear-sliding mechanism along the bed joint. By increasing the vertical compression, the failure mode gradually switches to brick cracking. Plastic strains localize into two inclined bands for moderate compressions (Figures 7.11b-7.11d), which successively coalesce into a single vertical band (Figures 7.11e-7.11f).

7.6.2 Localization properties and comparison with Lourenço's model

Masonry structures can be studied by considering their actual microstructure through explicit modeling of each constituent, as done in this chapter, or by defining a macroscopic constitutive law that phenomenologically reproduces the microstructural mechanics, as done in Chapter 6. It is interesting to compare the localization properties predicted with these two modeling techniques.

The macroscopic model chosen as the reference is Lourenço's model (Lourenço, De Borst, et al. 1997), formulated in the orthotropic multi-surface plasticity framework, having a Rankine-type yielding surface in the tensile part and a Hill-type yielding surface for the compressive part. Its localization properties have been studied in Chapter 6 (see also Pagani, Jirásek, et al. 2020). Lourenço's model mechanical parameters are chosen here to match the RVE's elastic stiffness and tensile strength along the two material axes x and y (horizontal and vertical), and they are reported in Table 7.2.

We chose to compare the localization response under uniaxial tension states only since the Rankine plasticity model of the RVE cannot capture failure due to compression properly. Moreover, as discussed in Chapter 6, localization band directions due to compression from Lourenço's model do not well represent the actual compression failure mechanism of masonry, since two inclined localization

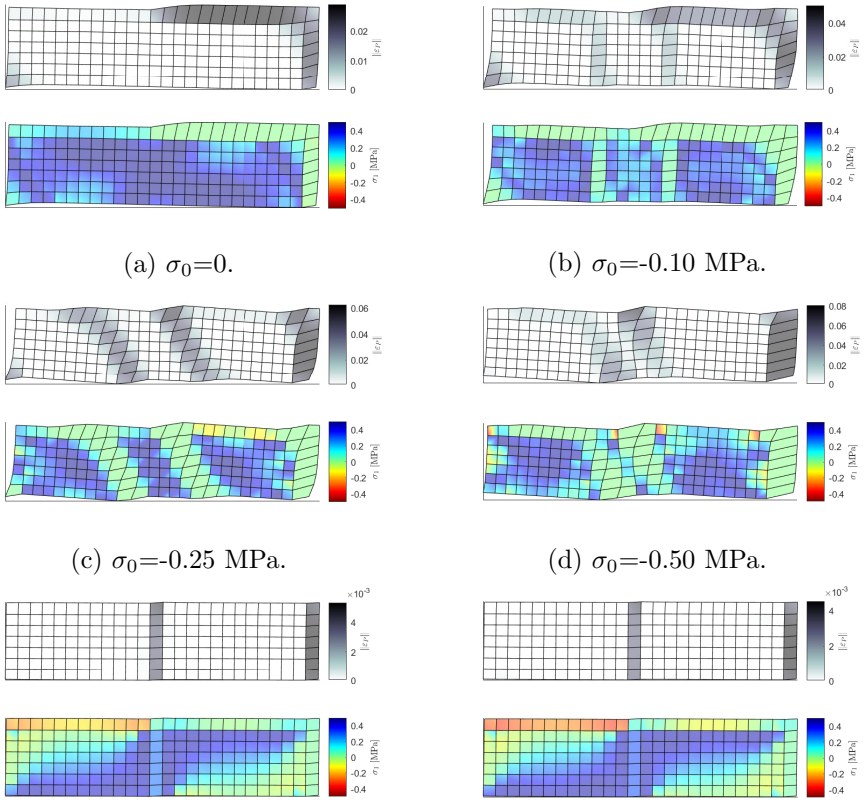

(a) σ_0=0. (b) σ_0=-0.10 MPa.

(c) σ_0=-0.25 MPa. (d) σ_0=-0.50 MPa.

(e) σ_0=-1.00 MPa. (f) σ_0=-1.25 MPa.

Figure 7.11: Plastic strain and tensile principal stress patterns for shear-compression tests in the one-brick RVE.

Elastic parameters				**Tensile parameters**				
E_{xx} [GPa]	E_{yy} [GPa]	ν_{xy} [-]	G_{xy} [GPa]	$f_{t,x}$ [MPa]	$f_{t,y}$ [MPa]	$G_{t,x}$ [N/mm]	$G_{t,y}$ [N/mm]	α [-]
3.56	3.08	0.15	1.50	0.49	0.24	0.02	0.02	1.50

Table 7.2: Mechanical parameters considered for Lourenço's model.

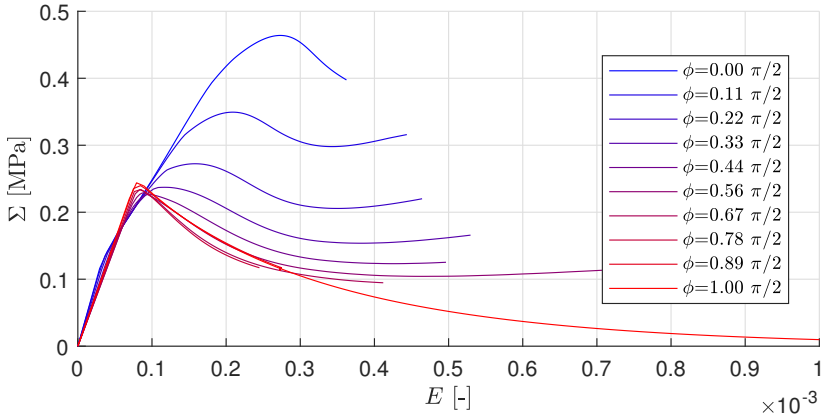

Figure 7.12: Stress-strain graphs and localization-indicator evolution for uniaxial tension tests varying stress direction (RVE).

surfaces are predicted to form in the specimen, instead of a vertical one (due to tensile lateral splitting) as it can be seen in experimental tests. The vectors defining the indirect displacement control analysis are

$$\boldsymbol{c} = \begin{bmatrix} \dots & \cos^2\phi & \sin^2\phi & \cos\phi\sin\phi \end{bmatrix}^T \tag{7.215}$$

$$\boldsymbol{f}_0 = \begin{bmatrix} \dots & 0 & 0 & 0 \end{bmatrix}^T \tag{7.216}$$

where ϕ is the uniaxial tensile stress direction.

The numerical results on the RVE varying the uniaxial stress angle are shown in Figure 7.12 in terms of stress-strain diagrams and in Figure 7.13 in terms of deformed shape and plastic strain map. It can be seen that there is a gradual change of failure mechanism, varying from the brittle bed joint failure for close-to-vertical tensile directions, characterized by lower values of tensile strength, to the frictional behavior for close-to-horizontal tensile angles, with a failure mechanism which involves bed-joint sliding. The yielding activation of the whole bed joint occurs in the case of vertical tension, while in the other cases plastic strains localize in the head and bed joints.

Figure 7.14 shows the comparison between Lourenço's and RVE models under uniaxial tension in terms of initial stiffness, tensile strength, and localization angles. The elastic stiffness variation with the tension direction shows a different trend. In Lourenço's model, the elastic stiffness exhibit a shallow variation with the minimum reached in correspondence of the weaker axis, here the y-axis. Contrarily, the RVE elastic stiffness steeply drops to its minimum value, reached for $\theta \simeq 5/16\pi$, which is 10% lower than the one related to the weaker material axis. Similarly, the RVE's tensile strength exhibits a steeper decrease than Lourenço's model, as the failure mechanism rapidly switches from bed-joint sliding to tensile splitting. The lowest strength value occurs for $\pi \simeq 3/8\pi$.

Figures 7.14c and 7.14d show respectively localization angles and the difference between localization angles and loading angle. In the RVE model, the localization angles are determined as the ones that minimize the lowest eigenvalue of the RVE localization tensor defined in (7.98). Except for tensile angles close to $\pi/2$, i.e.

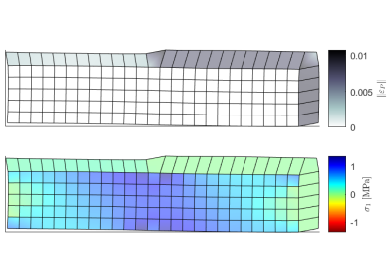

(a) ϕ=0.

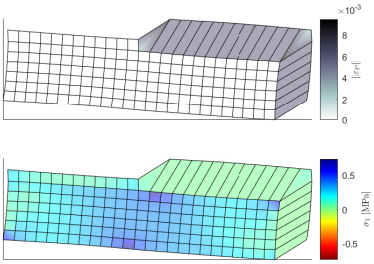

(b) $\phi = \pi/8$.

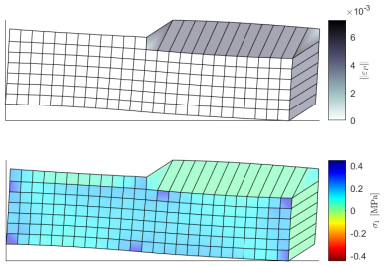

(c) $\phi = \pi/4$.

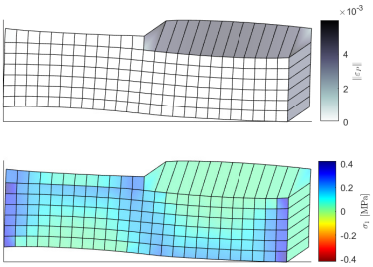

(d) $\phi = 3\pi/8$.

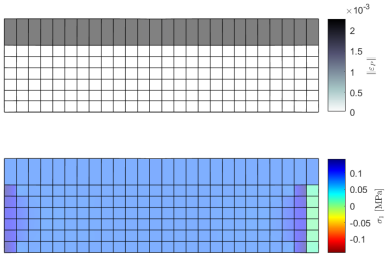

(e) $\phi = \pi/2$.

Figure 7.13: Plastic strain and tensile principal stress patterns for uniaxial tension tests in the one-brick RVE.

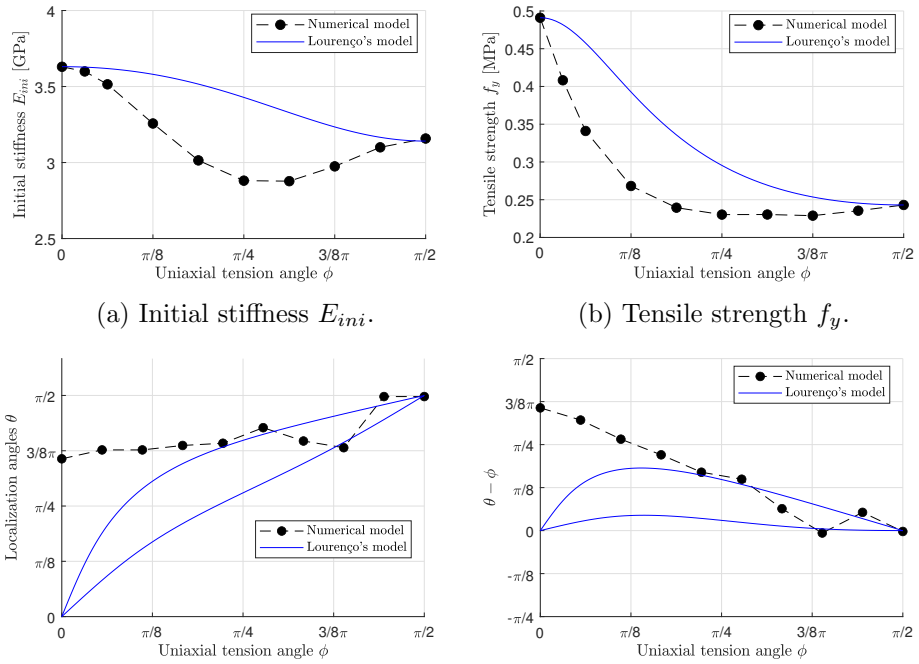

(a) Initial stiffness E_{ini}.

(b) Tensile strength f_y.

(c) Localization angle θ.

(d) Difference between θ and ϕ.

Figure 7.14: Comparison of Lourenço's and RVE model under uniaxial tension tests.

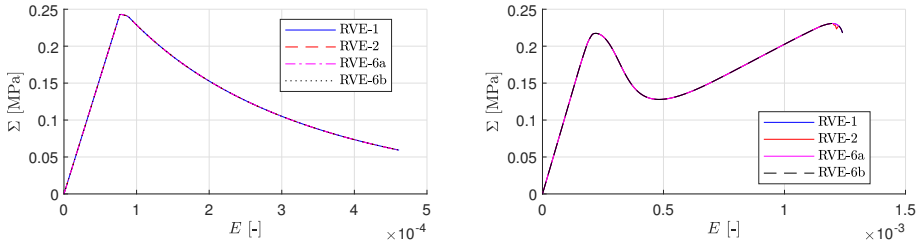

(a) Vertical tension. (b) Shear.

Figure 7.15: Stress-strain graphs varying the RVE size.

quasi-vertical tensile stresses, for which we have localization angles close to $\pi/2$, resulting in horizontal localization surfaces, the value of localization angles is always close to $\phi \simeq 3/8\pi$, resulting in an inclined localization band that reflects the zig-zag pattern of the inelastic strains. On the other hand, Lourenço's model localization angles are closer to the actual tensile angle ϕ, as shown in Figure 7.14d. This highlights that only a refined model that explicitly represents masonry constituents can properly account for the brickwork influence on the localization properties, while a macroscopic model can only phenomenologically reproduce the overall behavior.

7.7 Analysis varying the RVE size and periodicity directions

This section is devoted to studying the effect of variation of size and periodicity directions on the RVE localization properties. In fact, by increasing its size, the RVE might have more freedom for the localization path development due to the presence of a larger number of mortar layers, which are the weaker zone of the masonry microstructure. Moreover, for larger RVEs (see Figures 7.3c-7.3d) it is possible to have multiple sets of periodicity directions. The choice of the periodicity direction may further influence the RVE response, as shown in Stransky and Jirásek 2011. Therefore, it is also interesting to study the difference, if any exists, in inelastic strain localization between two periodicity direction sets within the same RVE.

The RVEs considered in this study are a) the one-brick RVE, b) the two-brick RVE, and c) and d) the six-brick RVE with, respectively, the set A and B of periodicity directions. A representation of their finite element discretization is reported in Figure 7.3. For simplicity, we restricted the analyses to two stress states only, vertical tension and pure shear. Although the obtained results allow some interesting comments, a thorough study of the RVE response varying its size in a wider range of stress scenarios needs to be carried out.

In a first analysis, the RVEs do not behave differently in both vertical tension and shear tests. The stress-strain curves are exactly the same (Figure 7.15), and plastic strains localize in bands (horizontal ones due to vertical tension and stepped bands due to shear, see Figures 7.16 and 7.17), but they repeat themselves along parallel paths. In other words, inelastic strain localization is "smeared" within the RVE.

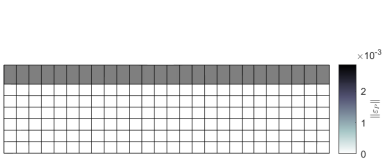

(a) RVE-1.

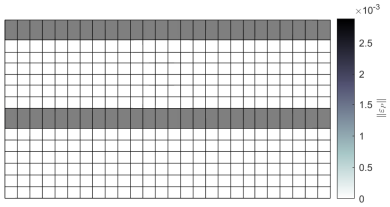

(b) RVE-2.

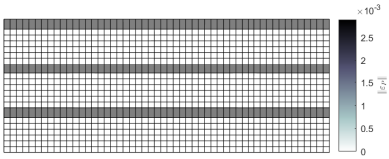

(c) RVE-6a.

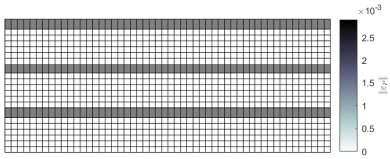

(d) RVE-6b.

Figure 7.16: Plastic strain maps under vertical tension varying RVE size.

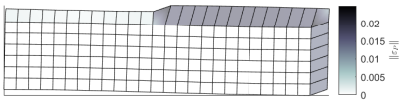

(a) RVE-1.

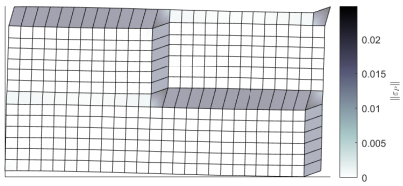

(b) RVE-2.

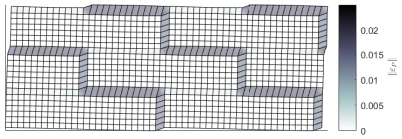

(c) RVE-6a.

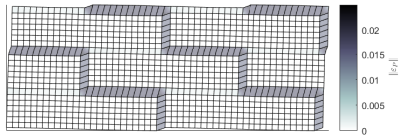

(d) RVE-6b.

Figure 7.17: Plastic strain maps under pure shear varying RVE size.

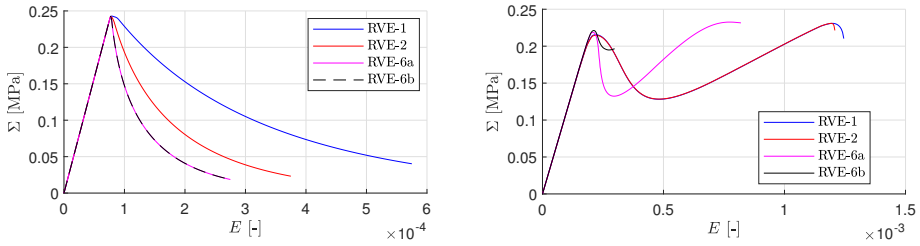

(a) Vertical tension. (b) Pure Shear.

Figure 7.18: Stress-strain graphs varying the RVE size, after the introduction of localization triggering weaknesses.

Then, we introduced material imperfections to trigger localization in the RVE. The elements located at the intersections between head and bed joints have been weakened through a 20% reduction of tensile strength. Consequently, the RVEs started to behave differently. The stress-strain graphs show a brittler response while increasing the RVE size (Figure 7.18), and inelastic strains now localize in a single band within the RVE. In vertical tension, the two six-bricks RVEs (RVE-6a and RVE-6b) do not exhibit any difference both in localization properties (Figure 7.19) and in the stress-strain curve. However, in the shear test, a different percolation path occurs in RVE-6a and RVE-6b, which might be caused by the different periodicity directions. In the two six-bricks RVEs, in fact, localization starts from the element, located in the upper bed-joint layer, which is linked to the origin through the inclined periodicity direction, see Figure 7.3. Therefore, in the case of pure shear, the periodicity direction variation leads only to a change in the element that triggers localization, which results in a variation of its path.

It is worth noting that the assumption of periodic boundary conditions imposes a constraint on the localization formation. The localization bands, in fact, must respect the periodic stacking of the RVE. We can conclude that the need to follow both the brickwork pattern and the periodic displacement boundary conditions strongly limits the development of a strain localization band, despite the size of the RVE.

7.8 Remarks

A microscale model for regular masonry has been developed, treating its constituents as continua with a Rankine plasticity constitutive law. The model has proved to model masonry micromechanics effectively. Vertical tension induces fragile tensile splitting of bed mortar joints; the strength mechanism under horizontal tension is characterized either by bed-joint sliding or brick cracking depending on the relative yielding stress value between bricks and mortar; failure due to vertical compression occurs with the formation of vertical bands; shear-compression tests show the typical frictional mechanism of masonry, with an increase of shear strength with the increase of vertical compression and a failure mechanism gradually switching from bed-joint sliding to diagonal cracking of bricks.

A comparison of the localization properties of masonry has been assessed between models of different scales of representation. The localization angles computed

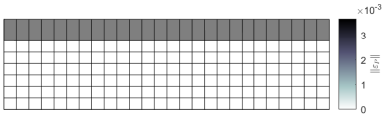

(a) RVE-1.

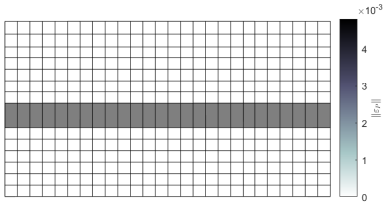

(b) RVE-2.

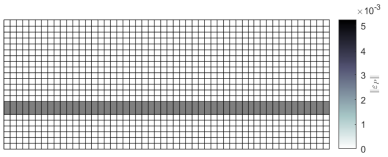

(c) RVE-6a.

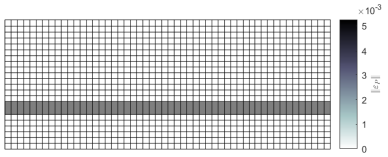

(d) RVE-6b.

Figure 7.19: Plastic strain maps under vertical tension varying RVE size, after the introduction of localization triggering weaknesses.

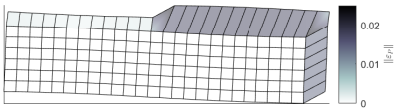

(a) RVE-1.

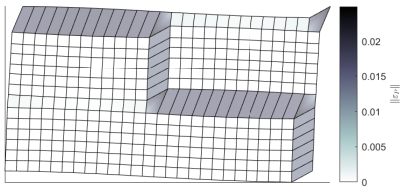

(b) RVE-2.

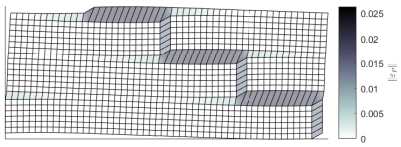

(c) RVE-6a.

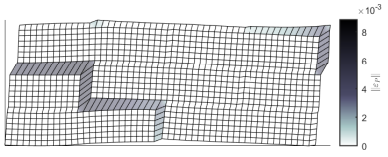

(d) RVE-6b.

Figure 7.20: Plastic strain maps under pure shear varying RVE size, after the introduction of localization triggering weaknesses.

within the RVE have been compared to those of a macroscopic constitutive law suitable for masonry, namely Lourenço's model. The resulting discontinuity surfaces from the RVE model testify that a more detailed representation of the microstructure can better reproduce masonry localization properties.

The RVE behavior varying its size was studied under vertical tension and pure shear. It has been shown that the brickwork regularity strongly limits inelastic strain localization. In fact, localization occurs only after the insertion of weakened elements. The RVE response is obviously more fragile increasing its size. Despite the insertion of triggering points, the localization paths are still highly restrained to mortar joints. Therefore, localization properties do not substantially change by varying the RVE size. Finally, the change of RVE periodicity direction leads to a variation of percolation path position due to the change of element that triggers localization.

Chapter 8

Conclusions

This chapter summarizes the study performed within the thesis, where masonry structures were studied at different detailing levels.

Masonry buildings can be seen as a set of walls, and each wall can be further decomposed into macroelements, namely piers, spandrels, and node panels. In the macroelement approach, the detailing level stops at this point by assigning a mechanical behavior to each panel.

Furthermore, each element can be interpreted as a 2-dimensional continuum, when attention is focused on the in-plane behavior. In this case, a homogenized continuum model is set up. We assign to each material point a proper constitutive law that should be able to reproduce the material response phenomenologically. However, the formulation of a macroscopic constitutive law is not an easy task. Reproducing with a single stress-strain relationship the microstructural mechanics of a heterogeneous material in terms of stiffness, strength, and localization properties is a difficult challenge.

Masonry mechanics at the microstructural level is characterized by a complex behavior. The material is heterogeneous and anisotropic due to the presence of two phases, i.e., bricks and mortar. Restricting our description to regular masonry, it is characterized by an orthotropic symmetry due to the presence of horizontal mortar layers, which determines masonry preferential axes. Moreover, the strength and stiffness properties vary significantly with the orientation of the stress directions with respect to material axes.

Therefore, to effectively account for the microstructure characteristics, we need to get to a finer scale performing microscale analyses, in which we model each constituent separately.

A study on masonry structures at each level of representation, starting from the global building to the masonry microscale, is reported in this manuscript. A summary of the methodologies and obtained results is reported in the following sections.

8.1 Interpretation of cyclic tests on masonry piers

An initial proposal of synthetic parameters for the interpretation of cyclic behavior of panels has been formulated. It accounts for stiffness and strength degradation as well as for the energy dissipation and presence of permanent displacements. This

is a first step toward the formulation of more refined pier models accounting for damage and plasticity.

8.2 Seismic analysis of irregular masonry walls

The Equivalent-Frame (EF) method relies on treating the masonry wall as an assembly of macroelements where piers and spandrels are the columns and beams of an ideal frame. This method has some advantages, in terms of reduced computational time needed and readability of the results. On the other hand, the method has drawbacks, due to the questionable prescriptions by building codes on the strength and failure criteria of piers and spandrels and for its use in case of walls characterized by an irregular layout of openings, since in these cases an equivalent frame is not easy to define.

To assess the effectiveness of the EF method, we compared its seismic response to the one of a more refined model. A new EF model with more reasonable strength and failure criteria for piers and spandrels was developed. The second model treated masonry as a homogenized continuum and assumed a smeared crack formulation as a constitutive law. Both models were calibrated on a full-scale building experimental test performed at the University of Pavia.

An automatic procedure was developed to easily analyze a statistically significant number of masonry walls with a randomly-generated opening layout.

A geometric confidence factor, to be used to penalize the seismic capacity predicted through the EF method, was formulated. The proposed factor brought the analysis to the safe side and acts selectively on the most irregular structures.

8.3 Nonlinear static behavior of masonry piers through numerical analysis

The effectiveness of the EF method relies on a proper modeling of the elements it is composed of. Among the macroelements of EF models, piers play a key role since they are the components that mainly influence the seismic response of masonry structures.

Piers are generally modeled as beams with a piecewise-linear constitutive law. Some of the failure criteria used by current building codes are questionable. A case in point is the ultimate drift threshold, which does not consider the influence of pier aspect ratio and vertical compression load.

To assess the lateral behavior of masonry piers, we performed a series of numerical analyses varying some parameters afflicting the pier response, namely the vertical compression load and the aspect ratio. We developed a finite element model treating masonry as a homogenized continuum adopting a smeared crack model as constitutive law. The model was first calibrated on two panels from the same experimental campaign subjected to different vertical loads, exhibiting different failure types. The model was able to reproduce the shear-displacement response and both the rocking and shear failures of the two specimens.

The calibrated model was used to perform a parametric analysis varying the compression load and the aspect ratio. We assessed the parameter influence on the quantities that characterize the pier lateral behavior, namely stiffness, strength, and displacement capacity. The numerical results were compared with the prescriptions

of some of the building codes. In particular, it was highlighted that the dependence of the displacement capacity on the compression ratio has been captured by a recent modification of the Italian Building Code, while the influence of the aspect ratio is still not considered. The results of the parametric analysis can be used to formulate new strength and failure criteria for piers or as a benchmark for the design of new pier macroelements.

8.4 Localization analysis of Lourenço's model

Different strategies can be adopted for numerical simulations of the behavior of masonry structures. Among others, continuum macro-modeling is a frequently used approach, in which masonry structures are treated as homogenized continua and, in general, discretized by the finite element method. The effectiveness of these models relies on selecting a proper constitutive law that phenomenologically reproduces the stress-strain relation of masonry microstructure from a macroscopic point of view. A notable example of macromodels suitable for masonry structures is Lourenço's model, formulated in the framework of orthotropic multisurface plasticity, with the yield function described as the composition of two different surfaces for the tensile and compressive behavior.

Localization analysis is a useful tool for the assessment of constitutive laws. From the study of the localization properties of a model, we can predict the localization band direction and the expected failure mode. Therefore, localization analysis may represent an indicator of the macroscale model reliability to capture the failure properties of a given material.

The localization analysis of Lourenço's model was performed. The study was restricted to the case of a regular point on the yielding surface, where the yield function gradient and the plastic flow direction are uniquely defined.

The necessary condition for localization was formulated first through a simplified procedure, under the assumption that the same tangent stiffness is applied at both sides of the discontinuity. However, this assumption is not always verified as localized solutions can also occur in the case of plastic loading on one side and elastic unloading on the other side, and it is not immediately clear which case is the most critical. Then, the analysis was extended by removing the aforementioned assumption. A more general localization condition was elaborated for the present class of plasticity models, based on the comparison between the current plastic modulus and the critical one.

The localization properties of Lourenço's model were first determined under uniaxial stress states. The closed-form expressions of the critical hardening moduli were found in the case of uniaxial stresses aligned with the material axes. It was observed that, except for the particular case of uniaxial tension along the material axes, we obtained a double solution in terms of the most likely localization angle. The normals to the discontinuity surfaces were almost aligned with the stress directions in the case of uniaxial tension, while two inclined bands tended to form for uniaxial compression.

The theoretical predictions were compared to numerical simulations. Lourenço's model was implemented into OOFEM, an open-source finite element solver. Numerical simulations on specimens subjected to vertical tension and compression showed a perfect match in terms of localization surface directions.

The study was then extended to biaxial stress states. It was shown that the results were not far from the ones obtained for uniaxial tension. This is mainly caused by the associate plastic flow rule for the compressive surface, combined with the hardening law in compression, which has an initial hardening branch, followed by a softening part. Since localization for associate plastic flow can occur only after the hardening peak, it turned out that the most likely mechanism was the tensile one, which can occur starting from the onset of plastic flow.

8.5 Localization analysis of masonry RVEs

Macroscopic models cannot take into account the microstructure heterogeneities typical of masonry, at least not directly. They may fail in reproducing failure mechanisms and localization directions of inelastic strains when compared to experimental tests. To address this issue, we need to increase the detailing level by performing microscale analyses, where we separately model blocks and mortar and assign to each constituent a proper constitutive law.

A microscale model for regular masonry was set up, modeling bricks and mortar as continua with a Rankine plasticity constitutive law. The analysis was performed on an RVE, and the macroscopic quantities were retrieved through homogenization imposing periodic boundary conditions.

The model was able to reproduce the typical failure mechanisms of the masonry microstructure, such as: (i) the bed-joint tensile splitting for vertical tension, (ii) bed-joint sliding or brick cracking for horizontal tension, (iii) vertical cracks in bricks for vertical compression, and (iv) the frictional mechanism on the bed joint for shear-compression tests, increasing the shear strength with the increase of vertical compression.

A comparison of the localization properties of masonry was assessed between models at different scales of representation. The localization angles computed within the RVE were compared to those of Lourenço's macroscopic model. The RVE discontinuity surfaces turned out to better account for the microstructural characteristics of masonry. A case in point is the analysis under horizontal tension, whose localization surface is inclined by an angle which corresponds to the zig-zag failure pattern. Contrarily, Lourenço's model localization angles tended to gradually vary with the stress angle.

Finally, the effect of the variation of the RVE size and, when meaningful, of the periodicity direction on its response was assessed. In fact, the RVE size choice is a key point in the microscale analysis since the localization path within the RVE may have more freedom to develop in larger RVEs. The results pointed out that the brickwork regularity, in addition to the periodicity conditions, strongly limited inelastic strain localization. To obtain a strong localization within the RVE, material imperfections had to be added. Despite the insertion of imperfections, the localization properties did not substantially vary, varying the RVE size. The change of periodicity direction changed the element that triggered localization.

8.6 Concluding remarks and future developments

In summary, a study of modeling techniques of masonry structures, from the roughest to the most refined one, has been performed throughout this manuscript. The

path began with the EF method, an application-oriented technique which is characterized by a rough interpretation of masonry mechanics and low computation burden. Then, we restricted our attention to the study of masonry piers, which were modeled as homogenized continua with a smeared crack constitutive law. Next, we focused on the material point level by performing the localization analysis of a macroscopic constitutive law suitable for masonry structures, namely Lourenço's model. Finally, we increased the detailing level at the finest scale by developing a microstructural model for regular masonry, where bricks and mortar have been explicitly modeled.

While traveling along this path, we realized at each level the need to get to a finer scale to better capture the upper level mechanics. When analyzing masonry piers as piece-wise linear beams, it turned out that a nonlinear continuum model can better represent their failure characteristics. Analogously, we found out that the definition of a proper constitutive law for masonry treated as homogenized continuum is a challenging task, and that this issue could be overcome only by explicitly considering masonry microstructure.

It could be interesting to retrace this route in the opposite direction. In the following lines, we outline some ideas on the future work that can be done after the experience gained in this travel.

For the *microscale* level, the influence of the RVE size and the periodicity directions on the localization properties of regular masonry RVEs needs to be sistematically clarified. The microscale problem can be handled analytically, adopting certain simplifications suggested by numerical solutions, which shows that mortar layers often deforms in an almost uniform way. A simplified microscale model, which represents mortar layers as interfaces and bricks as rigid bodies, can represent a promising approach. Moreover, more sophisticated constitutive laws for the mortar layers can be used. After the RVE localization property assessment, we need a method to upscale the microscale localization at the macroscale. Several techniques have been explored in literature. The "approximate embedded band model" proposed by Massart et al. 2007 consists in splitting the volume associated to the macroscopic integration point in a localized band and its surrounding unloading volume, and imposing a constant strain in each sub-region. Alternatively, the microscale localization band can be lumped into a macroscopic cohesive crack, accommodated through discontinuity-enriched kinematics at the macroscale (X-FEM), as done by Bosco et al. 2015. Moreover, a possible strategy is to consider a second-order computational homogenization where the gradient of the macroscopic deformation gradient tensor is considered, as proposed by VG Kouznetsova et al. 2004.

At the *macroscale* level, a thorough knowledge of masonry at the microscale can lead to the formulation of a new constitutive model. Experimental tests on masonry show that some failure mechanisms can be represented in the framework of plasticity. From a microscopic point of view, plasticity is due to intergranular displacements. It accounts for inelastic deformations during the loading process, and it can be used to model shear-sliding and crushing mechanisms. However, the tensile mechanism cannot be represented in this framework. In fact, experimental tests show that, in case of tensile failures, either the blocks detach from mortar or a crack forms through blocks, leading to the creation of voids or macro-cracks. In this case, damage mechanics represents a more suitable framework. Therefore, a proper constitutive model for masonry at the macroscale should encompass both plasticity

and damage mechanics, where plasticity is related to the compressive and shear mechanisms, while damage is linked to the growth and coalescence of micro-cracks due to macroscale tensile stress.

At the *wall* level, and for large structures, the EF approach is still the only method that allows analysis with a reasonable computational effort and a simple interpretation of results. To reliably represent the masonry wall mechanics, a proper modeling of masonry piers is needed. Among several possibilities, a beam model with smeared nonlinearities can represent a promising strategy. The flexural-compressive behavior can be modeled through a fiber approach within each beam section, where each fiber has a proper constitutive law, for instance coupled damage-plasticity in compression and fragile low-strength behavior in tension. The shear behavior can be formulated at the section level in the plasticity framework, with shear-sliding effects occurring in the compressed portion of the cross section. The proposed interpretation of cyclic tests can help to dose damage and plastic ingredients in a pier macroelement.

Bibliography

Abrams, D.P., O. AlShawa, P.B. Lourenço, and L. Sorrentino (2017). "Out-of-plane seismic response of unreinforced masonry walls: conceptual discussion, research needs, and modeling issues". In: *International Journal of Architectural Heritage* 11.1, pp. 22–30.

Addessi, D. and V. Ciampi (2007). "A regularized force-based beam element with a damage–plastic section constitutive law". In: *International Journal for Numerical Methods in Engineering* 70.5, pp. 610–629.

Addessi, D., S. Marfia, and E. Sacco (2002). "A plastic nonlocal damage model". In: *Computer methods in applied mechanics and engineering* 191.13-14, pp. 1291–1310.

Addessi, D., A. Mastrandrea, and E. Sacco (2014). "An equilibrated macro-element for nonlinear analysis of masonry structures". In: *Engineering Structures* 70, pp. 82–93.

Alfano, G. and E. Sacco (2006). "Combining interface damage and friction in a cohesive-zone model". In: *International Journal for Numerical Methods in Engineering* 68.5, pp. 542–582.

Almeida, C., J. Guedes, A. Arêde, and A. Costa (2012). "Shear and compression experimental behaviour of one leaf stone masonry walls". In: *15th World Conference Earthquake Engineering, Lisbon, Portugal.*

Angelillo, M. (1994). "A finite element approach to the study of no-tension structures". In: *Finite elements in analysis and design* 17.1, pp. 57–73.

Anthoine, A. (1995). "Derivation of the in-plane elastic characteristics of masonry through homogenization theory". In: *International journal of solids and structures* 32.2, pp. 137–163.

Anthoine, A., G. Magonette, and G. Magenes (1995). "Shear-compression testing and analysis of brick masonry walls". In: *Tenth European Conference on Earthquake Engineering.*

Atkinson, R.H., B.P. Amadei, S. Saeb, and S. Sture (1989). "Response of masonry bed joints in direct shear". In: *Journal of Structural Engineering* 115.9, pp. 2276–2296.

Augenti, N. (2006). "Seismic behaviour of irregular masonry walls". In: *Proceedings of the 1st European conference on earthquake engineering and seismology.*

Bartoli, G., M. Betti, P. Biagini, A. Borghini, A. Ciavattone, M. Girardi, G. Lancioni, A.M. Marra, B. Ortolani, B. Pintucchi, et al. (2017). "Epistemic uncertainties in structural modeling: a blind benchmark for seismic assessment of slender masonry towers". In: *Journal of Performance of Constructed Facilities* 31.5, p. 04017067.

Bažant, Z.P. and P.D. Bhat (1977). "Prediction of hysteresis of reinforced concrete members". In: *ASCE J STRUCT DIV* 103.1, pp. 153–167.

Bazoune, A., Y.A. Khulief, and N.G. Stephen (2003). "Shape functions of three-dimensional Timoshenko beam element". In: *Journal of Sound and Vibration* 259.2, pp. 473–480.

Belmouden, Y. and P. Lestuzzi (2009). "An equivalent frame model for seismic analysis of masonry and reinforced concrete buildings". In: *Construction and Building Materials* 23.1, pp. 40–53.

Berti, M., L. Salvatori, M. Orlando, and P. Spinelli (2017). "Unreinforced masonry walls with irregular opening layouts: reliability of equivalent-frame modelling for seismic vulnerability assessment". In: *Bulletin of earthquake engineering* 15.3, pp. 1213–1239.

Berto, L., A. Saetta, R. Scotta, and R. Vitaliani (2002). "An orthotropic damage model for masonry structures". In: *International Journal for Numerical Methods in Engineering* 55.2, pp. 127–157.

Beyer, K. and A. Dazio (2012). "Quasi-static cyclic tests on masonry spandrels". In: *Earthquake Spectra* 28.3, pp. 907–929.

Beyer, K., S. Petry, M. Tondelli, and A. Paparo (2014). "Towards displacement-based seismic design of modern unreinforced masonry structures". In: *Perspectives on European Earthquake Engineering and Seismology*. Springer, Cham, pp. 401–428.

Billi, L., F. Laudicina, L. Salvatori, M. Orlando, and P. Spinelli (2019). "Forming new steel-framed openings in load-bearing masonry walls: design methods and nonlinear finite element simulations". In: *Bulletin of Earthquake Engineering* 17.5, pp. 2647–2670.

Binda, L., A. Della Fontana, and G. Frigerio (1988). "Mechanical behaviour of brick masonries derived from unit and mortar characteristics". In: *Brick and Block Masonry(8 th IBMAC) London, Elsevier Applied Science,* 1, pp. 205–216.

Borré, G. and G. Maier (1989). "On linear versus nonlinear flow rules in strain localization analysis". In: *Meccanica* 24.1, pp. 36–41.

Borri, A., G. Castori, and M. Corradi (2012). "Evaluation of shear strength of masonry panels through different experimental analyses". In.

Bosco, E, VG Kouznetsova, and MGD Geers (2015). "Multi-scale computational homogenization–localization for propagating discontinuities using X-FEM". In: *International Journal for Numerical Methods in Engineering* 102.3-4, pp. 496–527.

Braga, F. and M. Dolce (1982). "A method for the analysis of antiseismic masonry multi-storey buildings". In: *Sixth International Brick Masonry Conference*, pp. 1088–1098.

Caballero González, A., E. Fehling, and J. Kieker (2005). "ESECMaSE Enhanced Safety and Efficient Construction of Masonry Structures in Europe: Europäisches Gemeinschaftsforschungsvorhaben zum Schubtragverhalten von Mauerwerksbauteilen". In: *Mauerwerk* 9.5, pp. 238–243.

Calderoni, B., E.A. Cordasco, P. Lenza, and G. Pacella (2011). "A simplified theoretical model for the evaluation of structural behaviour of masonry spandrels". In: *International Journal of Materials and Structural Integrity* 5.2-3, pp. 192–214.

Caliò, I., M. Marletta, and B. Pantò (2012). "A new discrete element model for the evaluation of the seismic behaviour of unreinforced masonry buildings". In: *Engineering Structures* 40, pp. 327–338.

Cattari, S., S. Lagomarsino, et al. (2008). "A strength criterion for the flexural behaviour of spandrels in unreinforced masonry walls". In: *Proc. of 14th WCEE*.

Cavalagli, N., F. Cluni, and V. Gusella (2011). "Strength domain of non-periodic masonry by homogenization in generalized plane state". In: *European Journal of Mechanics-A/Solids* 30.2, pp. 113–126.

Cervera, M., J. Wu, M. Chiumenti, and S. Kim (2020). "Strain localization analysis of Hill's orthotropic elastoplasticity: analytical results and numerical verification". In: *Computational Mechanics* 65.2, pp. 533–554.

Coenen, E.W.C., V.G. Kouznetsova, and M.G.D. Geers (2012). "Novel boundary conditions for strain localization analyses in microstructural volume elements". In: *International Journal for Numerical Methods in Engineering* 90.1, pp. 1–21.

De Bellis, M.L. and D. Addessi (2011). "A Cosserat based multi-scale model for masonry structures". In: *International Journal for Multiscale Computational Engineering* 9.5, p. 543.

De Falco, A., M. Mori, and G. Sevieri (2018). "Mazars' damage model for masonry structures: a case study of a church in Italy". In: *2018 COMSOL Conference*. COMSOL Multiphysics.

Dhanasekar, M., A.W. Page, and P.W. Kleeman (1985). "The failure of brick masonry under biaxial stresses." In: *Proceedings of the Institution of Civil Engineers* 79.2, pp. 295–313.

Diamond, S. and E. Landis (2007). "Microstructural features of a mortar as seen by computed microtomography". In: *Materials and Structures* 40.9, pp. 989–993.

Diana, TNO (2012). "Diana finite element analysis user's manual release 9.4. 4". In: *Delft, The Netherlands*.

Doherty, K., M.C. Griffith, N. Lam, and J. Wilson (2002). "Displacement-based seismic analysis for out-of-plane bending of unreinforced masonry walls". In: *Earthquake Engineering and Structural Dynamics*.

Dolatshahi, K.M., M.T. Nikoukalam, and K. Beyer (2018). "Numerical study on factors that influence the in-plane drift capacity of unreinforced masonry walls". In: *Earthquake Engineering & Structural Dynamics* 47.6, pp. 1440–1459.

Dolce, M. (1991). "Schematizzazione e modellazione degli edifici in muratura soggetti ad azioni sismiche". In: *Industria delle costruzioni* 25.242, pp. 44–57.

EN 1998-3 (2005). *Eurocode 8 - Design of structures for earthquake resistance - Part 3: Assesment and retrofitting of buildings.*

Facchini, L. and M. Betti (2016). "Simplified seismic analysis of disordered masonry towers". In: *ASCE-ASME Journal of Risk and Uncertainty in Engineering Systems, Part A: Civil Engineering* 2.2, p. C4015010.

Fajfar, P. and M. Fischinger (1988). "N2-A method for non-linear seismic analysis of regular buildings". In: *Proceedings of the ninth world conference in earthquake engineering.* Vol. 5, pp. 111–116.

Fehling, E., J. Stürz, and A. Emami (2007). "Test results on the behaviour of masonry under static (monotonic and cyclic) in plane lateral loads". In: *ESECMaSE deliverable D* 7.

Felippa, C.A. (2004). *Introduction to finite element methods.* University of Colorado.

FEMA, BSS (2000). *Prestandard and commentary for the seismic rehabilitation of buildings.*

Frumento, S., G. Magenes, and P. Morandi (2009). "Interpretazione di prove cicliche di compressione e taglio eseguite su pannelli di muratura in laterizio". In: *XIII Convegno ANIDIS - "L'INGEGNERIA SISMICA IN ITALIA".*

Frumento, S., G. Magenes, P. Morandi, and G.M. Calvi (2009). *Interpretation of experimental shear tests on clay brick masonry walls and evaluation of q-factors for seismic design.* Iuss Press Pavia.

Gambarotta, L. and S. Lagomarsino (1997). "Damage models for the seismic response of brick masonry shear walls. Part I: the mortar joint model and its applications". In: *Earthquake engineering & structural dynamics* 26.4, pp. 423–439.

Ganz, H.R. and B. Thurlimann (1983). "Strength of brick walls under normal force and shear". In: *8th International Symposium on Load Bearing Brickwork, BCRA, London.*

Gattesco, N., I. Clemente, L. Macorini, and S. Noè (2008). "Experimental investigation on the behaviour of spandrels in ancient masonry buildings". In: *Proc. of the 14th World Conference on Earthquake Engineering.*

Graziotti, F., G. Magenes, and A. Penna (2012). "Experimental cyclic behaviour of stone masonry spandrels". In: *Proceedings of the 15th World Conference on Earthquake Engineering*, pp. 24–28.

Gupta, A.K. and H. Akbar (1984). "Cracking in reinforced concrete analysis". In: *Journal of Structural Engineering* 110.8, pp. 1735–1746.

Gurtin, M.E. (1982). *An introduction to continuum mechanics*. Vol. 158. Academic press.

Hadamard, J. (1903). *Leçons sur la propagation des ondes*. Paris: Librairie Scientifique A. Hermann et Fils.

Hellesland, J. and A. Scordelis (1981). "Analysis of RC bridge columns under imposed deformations". In: *IABSE colloquium*. Delft the Netherlands, pp. 545–559.

Hendry, A.W. (1981). *Structural brickwork*. Springer.

Heyman, J. (1966). "The stone skeleton". In: *International Journal of solids and structures* 2.2, pp. 249–279.

Hill, R. (1958). "A general theory of uniqueness and stability in elastic-plastic solids". In: *Journal of the Mechanics and Physics of Solids* 6.3, pp. 236–249.

Hilsdorf, H.K. (1969). "Investigation into the failure mechanism of brick masonry loaded in axial compression". In: *Designing engineering and constructing with masonry products*, pp. 34–41.

IBC (2008). "Italian Building Code (Norme Tecniche per le Costruzioni)". In: *D.M. 14/01/2008*.

IBC (2018). "Italian Building Code (Aggiornamento delle norme tecniche per le costruzioni)". In: *D.M. 17/01/2018*.

Jirásek, M. and Z.P. Bažant (2001). *Inelastic analysis of structures*. John Wiley & Sons.

Kallioras, S., G. Guerrini, U. Tomassetti, B. Marchesi, A. Penna, F. Graziotti, and G. Magenes (2018). "Experimental seismic performance of a full-scale unreinforced clay-masonry building with flexible timber diaphragms". In: *Engineering Structures* 161, pp. 231–249.

Kouznetsova, V., W.A.M. Brekelmans, and F.P.T. Baaijens (2001). "An approach to micro-macro modeling of heterogeneous materials". In: *Computational mechanics* 27.1, pp. 37–48.

Kouznetsova, VG, Marc GD Geers, and WAM1112 Brekelmans (2004). "Multi-scale second-order computational homogenization of multi-phase materials: a nested finite element solution strategy". In: *Computer methods in applied Mechanics and Engineering* 193.48-51, pp. 5525–5550.

La Malfa Ribolla, E., G. Giambanco, and A. Spada (2020). "Mesoscopic aspects of the computational homogenization with meshless modeling for masonry material". In: *International Journal for Numerical Methods in Engineering*.

Lagomarsino, S., A. Penna, A. Galasco, and S. Cattari (2013). "TREMURI program: An equivalent frame model for the nonlinear seismic analysis of masonry buildings". In: *Engineering Structures*.

Li, H., H. Xiao, J. Yuan, and J. Ou (2004). "Microstructure of cement mortar with nano-particles". In: *Composites part B: engineering* 35.2, pp. 185–189.

Lotfi, H.R. and P.B. Shing (1991). "An appraisal of smeared crack models for masonry shear wall analysis". In: *Computers & structures* 41.3, pp. 413–425.

Lourenço, P.B. (1995). *An orthotropic continuum model for the analysis of masonry structures*. Tech. rep. Delft University of Technology.

Lourenço, P.B., R. De Borst, and J.G. Rots (1997). "A plane stress softening plasticity model for orthotropic materials". In: *International Journal for Numerical Methods in Engineering* 40.21, pp. 4033–4057.

Lourenço, P.B., D.V. Oliveira, P. Roca, and A. Orduña (2005). "Dry joint stone masonry walls subjected to in-plane combined loading". In: *Journal of Structural Engineering* 131.11, pp. 1665–1673.

Lourenço, P.B. and J.G. Rots (1997). "Multisurface interface model for analysis of masonry structures". In: *Journal of engineering mechanics* 123.7, pp. 660–668.

Lucchesi, M., C. Padovani, G. Pasquinelli, and N. Zani (2008). *Masonry constructions: mechanical models and numerical applications*. Springer Science & Business Media.

Magenes, G. (2000). "A method for pushover analysis in seismic assessment of masonry buildings". In: *12th World Conference on Earthquake Engineering (WCEE)*.

Magenes, G. (2010). "Earthquake resistant design of masonry structures : rules , backgrounds , latest findings". In: *Proc. of the 8th International Masonry Conference*.

Magenes, G. and G.M. Calvi (1992). "Cyclic behaviour of brick masonry walls". In: *Proceedings of the 10th world conference on earthquake engineering*, pp. 3517–3522.

Magenes, G. and G.M. Calvi (1996). "Prospettive per la calibrazione di di metodi semplificati per l'analisi sismica di pareti murarie". In: *Atti del Convegno La meccanica delle murature tra teoria e progetto*, pp. 503–512.

Magenes, G. and G.M. Calvi (1997). "In-plane seismic response of brick masonry walls". In: *Earthquake Engineering and Structural Dynamics*.

Magenes, G. and A. Della Fontana (1998). "Simplified non-linear seismic analysis of masonry buildings". In: *Proc. Br. Masonry Soc. No. 8*, pp. 190–195.

Magenes, G., A. Galasco, A. Penna, and M. Da Paré (2010). "In-plane cyclic shear tests of undressed double leaf stone masonry panels". In: *... of the 14th European Conference of ...*

Magenes, G., G.R. Kingsley, and G.M. Calvi (1995). *Seismic testing of a full-scale, two-story masonry building: test procedure and measured experimental response*. Consiglio nazionale delle ricerche, Gruppo nazionale per la Difesa dai terremoti.

Magenes, G., P. Morandi, and A. Penna (2008). "Experimental in-plane cyclic response of masonry walls with clay units". In: *In: Proceedings of the 14th World conference on earthquake engineering*.

Magenes, G., A. Penna, A. Galasco, and M. Rota (2010). "Experimental characterisation of stone masonry mechanical properties". In: *Proceedings of the 8th International Masonry Conference*.

Magenes, G., A. Penna, I.E. Senaldi, M. Rota, and A. Galasco (2014). "Shaking table test of a strengthened full-scale stone masonry building with flexible diaphragms". In: *International Journal of Architectural Heritage* 8.3, pp. 349–375.

Maier, G. and A. Nappi (1990). "A theory of no-tension discretized structural systems". In: *Engineering structures* 12.4, pp. 227–234.

Mann, W. and H. Muller (1982). "Failure of shear-stressed masonry. An enlarged theory, tests and application to shear walls". In: *Proc. Br. Ceram. Soc.* 30, p. 223.

Mann, W. and H. Müller (1977). *Bruchkriterien für querkraftbeanspruchtes Mauerwerk und ihre Anwendung auf gemauerte Windscheiben*. Informationsverbundzentrum Raum und Bau der Fraunhofer-Ges.

Margiacchi, F., L. Salvatori, M. Orlando, M. De Stefano, and P. Spinelli (2016). "Seismic response of masonry-infilled steel frames via multi-scale finite-element analyses". In: *Bulletin of Earthquake Engineering* 14.12, pp. 3529–3546.

Marra, A.M., L. Salvatori, P. Spinelli, and G. Bartoli (2017). "Incremental dynamic and nonlinear static analyses for seismic assessment of medieval masonry towers". In: *Journal of Performance of Constructed Facilities* 31.4, p. 04017032.

Massart, T.J., R.H.J. Peerlings, and M.G.D. Geers (2004). "Mesoscopic modeling of failure and damage-induced anisotropy in brick masonry". In: *European Journal of Mechanics-A/Solids* 23.5, pp. 719–735.

Massart, T.J., R.H.J. Peerlings, and M.G.D. Geers (2007). "An enhanced multi-scale approach for masonry wall computations with localization of damage". In: *International journal for numerical methods in engineering* 69.5, pp. 1022–1059.

Mazars, J., F. Hamon, and S. Grange (2015). "A new 3D damage model for concrete under monotonic, cyclic and dynamic loadings". In: *Materials and Structures* 48.11, pp. 3779–3793.

McNary, W.S. and D.P. Abrams (1985). "Mechanics of masonry in compression". In: *Journal of Structural Engineering* 111.4, pp. 857–870.

Mercatoris, B.C.N., P. Bouillard, and T.J. Massart (2009). "Multi-scale detection of failure in planar masonry thin shells using computational homogenisation". In: *Engineering fracture mechanics* 76.4, pp. 479–499.

Milani, G. (2011). "Simple lower bound limit analysis homogenization model for in-and out-of-plane loaded masonry walls". In: *Construction and Building Materials* 25.12, pp. 4426–4443.

Minga, E., L. Macorini, and B.A. Izzuddin (2018). "A 3D mesoscale damage-plasticity approach for masonry structures under cyclic loading". In: *Meccanica* 53.7, pp. 1591–1611.

Moon, F.L., T. Yi, R.T. Leon, and L.F. Kahn (2006). "Recommendations for seismic evaluation and retrofit of low-rise URM structures". In: *Journal of Structural Engineering* 132.5, pp. 663–672.

Morandi, P., L. Albanesi, F. Graziotti, T. Li Piani, A. Penna, and G. Magenes (2018). "Development of a dataset on the in-plane experimental response of URM piers with bricks and blocks". In: *Construction and Building Materials*.

Neuenhofer, A. and F.C. Filippou (1998). "Geometrically nonlinear flexibility-based frame finite element". In: *Journal of Structural Engineering* 124.6, pp. 704–711.

Oliveira, D.V. and P.B. Lourenço (2004). "Implementation and validation of a constitutive model for the cyclic behaviour of interface elements". In: *Computers & structures* 82.17-19, pp. 1451–1461.

Orlando, M., L. Salvatori, P. Spinelli, and M. De Stefano (2016). "Displacement capacity of masonry piers: parametric numerical analyses versus international building codes". In: *Bulletin of Earthquake Engineering* 14.8, pp. 2259–2271.

Pagani, C., M. Jirásek, and M. Horák (2020). "Localization analysis of an orthotropic multi-surface plasticity model under uniaxial stress". In: *Acta Polytechnica CTU Proceedings* 26, pp. 56–63.

Pagani, C., L. Salvatori, M. Orlando, and P. Spinelli (2017). "Irregular Opening Layouts in Unreinforced Masonry Walls: Equivalent Frame and Finite Element Simulations." In: *ANIDIS 2017, Pistoia(Italy)*, pp. 105–114.

Page, A.W. (1981). "The biaxial compressive strength of brick masonry." In: *Proceedings of the Institution of Civil Engineers* 71.3, pp. 893–906.

Page, A.W., P.W. Kleeman, and M. Dhanasekar (1985). "An in-plane finite element model for brick masonry". In: *New analysis techniques for structural masonry*. ASCE, pp. 1–18.

Parisi, F. and N. Augenti (2013). "Seismic capacity of irregular unreinforced masonry walls with openings". In: *Earthquake Engineering & Structural Dynamics* 42.1, pp. 101–121.

Parisi, F., G. Sabella, and N. Augenti (2015). "Seismic Capacity Prediction for Irregular Masonry Walls with Opening Offsets". In: *Proceedings of the Fifteenth International Conference on Civil, Structural and Environmental Engineering Computing*.

Patzák, B. and Z. Bittnar (2001). "Design of object oriented finite element code". In: *Advances in Engineering Software* 32.10-11, pp. 759–767.

Pekelnicky, R. and C. Poland (2012). "ASCE 41-13: Seismic Evaluation and Retrofit Rehabilitation of Existing Buildings". In: *Citeseer*.

Penna, A., S. Lagomarsino, and A. Galasco (2014). "A nonlinear macroelement model for the seismic analysis of masonry buildings". In: *Earthquake Engineering & Structural Dynamics* 43.2, pp. 159–179.

Petry, S. and K. Beyer (2014). "Influence of boundary conditions and size effect on the drift capacity of URM walls". In: *Engineering Structures* 65, pp. 76–88.

Pina-Henriques, J. and P.B. Lourenço (2006). "Masonry compression: a numerical investigation at the meso-level". In: *Engineering computations*.

Poleni, G. (1748). *Memorie istoriche della gran cupola del Tempio vaticano, e de'danni di essa, e de'ristoramenti loro...*

Pugh, J.S., L.N. Lowes, and D.E. Lehman (2014). "Seismic design of slender concrete walls". In: *Proceedings of the 10th National Conference in Earthquake Engineering*.

Pugi, F. (2000). *PCM: Progettazione di costruzioni in muratura: la teoria*. Alinea.

Quagliarini, E., G. Maracchini, and F. Clementi (2017). "Uses and limits of the Equivalent Frame Model on existing unreinforced masonry buildings for assessing their seismic risk: A review". In: *Journal of Building Engineering* 10, pp. 166–182.

Raka, E., E. Spacone, V. Sepe, and G. Camata (2015). "Advanced frame element for seismic analysis of masonry structures: model formulation and validation". In: *Earthquake Engineering & Structural Dynamics* 44.14, pp. 2489–2506.

Rice, J.R. and J.W. Rudnicki (1980). "A note on some features of the theory of localization of deformation". In: *International Journal of solids and structures* 16.7, pp. 597–605.

Rinaldin, G., C. Amadio, and N. Gattesco (2017). "Review of experimental cyclic tests on unreinforced and strengthened masonry spandrels and numerical modelling of their cyclic behaviour". In: *Engineering Structures* 132, pp. 609–623.

Rinaldin, G., C. Amadio, and L. Macorini (2016). "A macro-model with nonlinear springs for seismic analysis of URM buildings". In: *Earthquake Engineering & Structural Dynamics* 45.14, pp. 2261–2281.

Sacco, E. (2009). "A nonlinear homogenization procedure for periodic masonry". In: *European Journal of Mechanics-A/Solids* 28.2, pp. 209–222.

Salerno, G. and G. De Felice (2009). "Continuum modeling of periodic brickwork". In: *International Journal of Solids and Structures* 46.5, pp. 1251–1267.

Salvatori, L., A.M. Marra, G. Bartoli, and P. Spinelli (2015). "Probabilistic seismic performance of masonry towers: General procedure and a simplified implementation". In: *Engineering Structures* 94, pp. 82–95.

Salvatori, L., A.M. Marra, G. Bartoli, and P. Spinelli (2017). "Role of correlation between mechanical parameters in the probabilistic seismic vulnerability of historical masonry towers". In: *International Journal of Masonry Research and Innovation* 2.2-3, pp. 134–149.

Salvatori, L. and P. Spinelli (2018). "A continuum-discrete multiscale model for in-plane mechanical modeling of masonry panels". In: *Journal of Multiscale Modelling* 9.03, p. 1840004.

Scordelis, A.C. (1984). "Computer models for nonlinear analysis of reinforced and prestressed concrete structures". In: *PCI JOURNAL* 29.6, pp. 116–135.

Scott, M.H. and G.L. Fenves (2006). "Plastic hinge integration methods for force-based beam–column elements". In: *Journal of Structural Engineering* 132.2, pp. 244–252.

Sejnoha, J., M. Sejnoha, J. Zeman, J. Sykora, and J. Vorel (2008). "Mesoscopic study on historic masonry". In: *arXiv preprint arXiv:0804.3262*.

Shawa, O.A., G. De Felice, A. Mauro, and L. Sorrentino (2012). "Out-of-plane seismic behaviour of rocking masonry walls". In: *Earthquake Engineering and Structural Dynamics*.

Shing, P.B., J.L. Noland, E. Klamerus, and H. Spaeh (1989). "Inelastic behavior of concrete masonry shear walls". In: *Journal of structural engineering* 115.9, pp. 2204–2225.

Siano, R., P. Roca, G. Camata, L. Pelà, V. Sepe, E. Spacone, and M. Petracca (2018). "Numerical investigation of non-linear equivalent-frame models for regular masonry walls". In: *Engineering Structures* 173, pp. 512–529.

Siano, R., V. Sepe, G. Camata, E. Spacone, P. Roca, and L. Pelà (2017). "Analysis of the performance in the linear field of equivalent-frame models for regular and irregular masonry walls". In: *Engineering Structures* 145, pp. 190–210.

Silva, B., M. Dalla Benetta, F. da Porto, and C. Modena (2014). "Experimental assessment of in-plane behaviour of three-leaf stone masonry walls". In: *Construction and Building Materials* 53, pp. 149–161.

Spacone, E., F.C. Filippou, and F.F. Taucer (1996). "Fibre beam–column model for non-linear analysis of R/C frames: Part I. Formulation". In: *Earthquake Engineering & Structural Dynamics* 25.7, pp. 711–725.

Steinmann, P., C. Miehe, and E. Stein (1994). "On the localization analysis of orthotropic Hill type elastoplastic solids". In: *Journal of the Mechanics and Physics of Solids* 42.12, pp. 1969–1994.

Stransky, J. and M. Jirásek (2011). "Calibration of particle-based models using cells with periodic boundary conditions". In: *Particle-Based Methods II: Fundamentals and Applications*, pp. 274–285.

Suidan, M. and W.C. Schnobrich (1973). "Finite element analysis of reinforced concrete". In: *Journal of the structural division* 99.st1.

Svenning, E., M. Fagerström, and F. Larsson (2017). "Localization aligned weakly periodic boundary conditions". In: *International Journal for Numerical Methods in Engineering* 111.5, pp. 493–500.

Tassios, T.P. (1986). *Mechanics of masonry*. National Tehnical University: Athens (in greek and italian).

Taucer, F., E. Spacone, and F.C. Filippou (1991). *A fiber beam-column element for seismic response analysis of reinforced concrete structures*. Vol. 91. 17. Earthquake Engineering Research Center, College of Engineering, University ...

Tomaževič, M. (1978). "The computer program POR". In: *Report ZRMK* 846.

Tomaževič, M. (1999). "Correlation between damage and seismic resistance of masonry walls and buildings". In: *Seismic Damage to Masonry Buildings: Proceedings of the International Workshop, Padova, Italy, 25-27 June, 1998*. CRC Press, p. 161.

Tomaževič, M. and M. Lutman (1996). "Seismic behavior of masonry walls: modeling of hysteretic rules". In: *Journal of structural engineering* 122.9, pp. 1048–1054.

Turnšek, V. and F. Čačovič (1971). "Some experimental results on the strength of brick masonry walls". In: *Proc. of the 2nd International Brick Masonry Conference*, pp. 149–156.

Van der Pluijm, R. (1999). "Out-of-plane bending of masonry: behaviour and strength". PhD thesis. Technische Universiteit Eindhoven.

Vanin, F., A. Penna, and K. Beyer (2020). "A three-dimensional macroelement for modelling the in-plane and out-of-plane response of masonry walls". In: *Earthquake Engineering & Structural Dynamics* 49.14, pp. 1365–1387.

Vanin, F., D. Zaganelli, A. Penna, and K. Beyer (2017). "Estimates for the stiffness, strength and drift capacity of stone masonry walls based on 123 quasi-static cyclic tests reported in the literature". In: *Bulletin of Earthquake Engineering* 15.12, pp. 5435–5479.

Vasconcelos, G. and P.B. Lourenço (2009). "In-plane experimental behavior of stone masonry walls under cyclic loading". In: *Journal of structural engineering* 135.10, pp. 1269–1277.

Vásquez, J.A., J.C. de la Llera, and M.A. Hube (2016). "A regularized fiber element model for reinforced concrete shear walls". In: *Earthquake Engineering & Structural Dynamics* 45.13, pp. 2063–2083.

Vecchio, F.J. and M.P. Collins (1986). "The modified compression-field theory for reinforced concrete elements subjected to shear." In: *ACI J.* 83.2, pp. 219–231.

Vecchio, F.J. and M.P. Collins (1993). "Compression response of cracked reinforced concrete". In: *Journal of structural engineering* 119.12, pp. 3590–3610.

Wilding, B.V. and K. Beyer (2018). "The effective stiffness of modern unreinforced masonry walls". In: *Earthquake Engineering & Structural Dynamics* 47.8, pp. 1683–1705.

Wilding, B.V., K.M. Dolatshahi, and K. Beyer (2017). "Influence of load history on the force-displacement response of in-plane loaded unreinforced masonry walls". In: *Engineering Structures* 152, pp. 671–682.

Wilding, B.V., K.M. Dolatshahi, and K. Beyer (2018). "Shear-compression tests of URM walls: Various setups and their influence on experimental results". In: *Engineering Structures* 156, pp. 472–479.

Zepeda, J.A., S.M. Alcocer, and L.E. Flores (2000). "Earthquake-resistant construction with multi-perforated clay brick walls". In: *Twelfth World Conference on Earthquake Engineering*.

Zilch, K., W. Finckh, S. Grabowski, D. Schermer, and W. Scheufler (2008). "Test results on the behaviour of masonry under static cyclic in-plane lateral loads". In: *ESECMaSE deliverable D* 7.

Zimmermann, T., A. Strauss, and R. Wendner (2011). "Old masonry under seismic loads: Stiffness identification and degradation". In: *Structures Congress 2011*, pp. 1736–1747.